THE UNIVERSITY OF
SYDNEY

Characterisation of turbulence in an open channel flow and in a fountain with Tomographic PIV

by

Thomas Earl

A thesis submitted in fulfilment of the

requirements for the degree of

Doctor of Philosophy

THE UNIVERSITY OF

SYDNEY

Faculty of Engineering and Information Technologies

School of *Civil Engineering*

The University of Sydney

2015

Abstract

This work aims to improve the understanding of the fundamental characteristics of environmental flows by interpreting the turbulence in a 3D measurement domain. Environmental flows are dominated by turbulence due to their large geometric length scales. Turbulence is characterised by fluctuating three dimensional (3D) vortices that transfer kinetic energy between scales and modify the mean flow profile. Thus, there is a need to use volumetric measurement techniques, such as TPIV, in order to fully analyse these types of flows. This thesis primarily describes the TPIV technique and the results of three experimental investigations of environmental flows.

Two experiments were conducted in an open channel flow. Five trash rack assemblies divided a 5 m long flume into four sequential, identical pools, where the turbulence in the third pool downstream was analysed. The global characteristics of the flow were analysed and then compared with the TPIV measurements.

The first set of TPIV measurements were in the water column, or intermediate region, in the centre of the pool. The instantaneous structures in the flow were visualised and the turbulent kinetic energy k, energy dissipation ε and vorticity ω were analysed. The measurements showed the decay of k and ε along the streamwise direction. The turbulent scales of the flow, such as Taylor's microscale λ and the integral length scale l_0 were calculated and shown to be anisotropic.

In the subsequent investigation, measurements were made in the same flume along the channel bottom. Two regions in the pool were considered, one at $x/L = 0.5$ and the other $x/L = 0.85$, where x is the streamwise coordinate and L the pool length. Ejections (Q2) and sweeps (Q4) were identified as were coherent vortices in the 3D flow field that appeared to reveal hairpin-like structures. The data yield allowed for the statistical analysis of the Reynolds stress distribution through the boundary layer along with the distribution of the turbulent energy dissipation. The results showed that the turbulence produced by the trash racks dominated the flow in the near wall regions.

A major contribution that resulted from the investigation of the open channel flow

(Chapters 3 and 4) pertains to the correction of vibration of the cameras (which resulted in the publication of Earl et al, 2015). The measurement of high Reynolds number open channel flows with optical methods as the flows generally require high velocity that leads to vibrations. Oftentimes, these vibrations are small enough that 'acceptable' results can be yielded from the data. Several techniques to correct the vibration, with a synthetic model used to further explain and quantify the effects of using correction schemes are presented.

In the third investigation, TPIV measurements were taken of a regime of turbulent, forced fountain flows. The fountains were created by injecting a salt water solution (high density fluid) through a circular opening into the bottom of a reservoir of a water-ethanol solution (low density fluid). Due to the density differences, the upward pointing jet collapses over itself, resulting in a fountain. In order to make these measurements, the refractive indices of both solutions were carefully matched. The initialisation of the fountains along with the fully developed states were considered in the analysis.

The evolution of the fountain in its initial stages was captured and described in a series of chronological measurement volumes. The instantaneous measurements of the fully developed fountains captured the large scale structures in the fountains and the characteristics of the structures were analysed by considering the topology of the invariants of the velocity gradient tensor. The turbulence intensity of the fountains was also investigated to ascertain their Reynolds number dependence and where the turbulent fluctuations were most prominent. This work resulted in the publication of Earl et al (2013), a significant contribution in the study of fountains. Fountains are canonical flows with significant environmental implications. In addition, the TPIV system was designed and built in-house at the University of Sydney.

The experimental investigations described in this work revealed some interesting features of the environmental flows. The applicability and versatility of TPIV for these flows were demonstrated. The measurements allowed for the quantification and visualisation of the turbulence in the flows and hence shed light on the physics behind them.

Contents

Abstract ii

Declaration x

Acknowledgements xi

List of Publications xiii

Nomenclature xv

Introduction 1

1 Turbulent Flows 5

1.1 An overview of turbulence 5

1.2 Governing equations of fluid motion 6

1.3 Reynolds averaged equations 8

1.4 The Reynolds stress equation 9

1.5 The origins of turbulence 11

1.6 Vorticity in turbulent flows 13

1.7 Turbulence properties and length scales 14

1.8 Turbulence kinetic energy and its rate of dissipation 15

1.9 Identification of vortices 18

1.10 Topology of the invariants of the velocity gradient tensor 18

1.10.1 Canonical turbulent flows 20

1.10.2 Grid generated turbulence 20

1.10.3 Wall-bounded flows . . . 21
1.10.4 Fountain flows . . . 23
1.11 Summary of turbulent flows . . . 24

2 Particle Image Velocimetry (PIV) 26
2.1 Introduction . . . 26
2.1.1 Working principle of PIV . . . 27
2.1.2 Technical and economic considerations . . . 28
2.2 Towards three component three dimensional (3C3D) PIV . . . 30
2.2.1 Stereo PIV . . . 30
2.2.2 Multi-plane PIV . . . 32
2.2.3 Scanning PIV . . . 33
2.2.4 Holographic PIV . . . 35
2.2.5 3D Particle Tracking Velocimetry (PTV) . . . 36
2.2.6 Tomographic PIV . . . 38
2.2.7 Other volumetric PIV techniques . . . 39
2.2.8 Summary of 3D PIV methods . . . 41
2.3 Working Principles of TPIV . . . 41
2.3.1 Principle of Reconstruction . . . 42
2.3.2 Camera Calibration . . . 44
2.3.3 Reconstruction Algorithms . . . 45
2.3.4 Volume initialisation . . . 49
2.3.5 Initialisation and reconstruction performance . . . 50
2.3.6 Ghost particles . . . 56
2.3.7 Volumetric cross-correlation . . . 57
2.3.8 Pushing the boundaries of TPIV . . . 59
2.3.9 Limitations and accuracy of TPIV . . . 60
2.3.10 SLIP Library . . . 61
2.4 Summary . . . 61

3 Evaluation of the energy dissipation by tomographic PIV of an open channel flow behind a series of regular grids **62**

3.1 Introduction . . . 62

3.2 Experimental Set-up . . . 65

3.2.1 Trash Rack and Grid Details . . . 66

3.2.2 Flow properties . . . 68

3.2.3 Volumetric Dissipated Power and Energy . . . 68

3.2.4 2D PIV . . . 69

3.3 TPIV Set-up . . . 70

3.3.1 TPIV System . . . 71

3.3.2 Image Processing . . . 73

3.3.3 Volume Reconstruction . . . 74

3.3.4 Vibration Correction with Self-Calibration . . . 75

3.3.5 Velocity field calculation . . . 76

3.3.6 TPIV Resolution . . . 77

3.4 Results . . . 78

3.4.1 Instantaneous Velocity Fields . . . 78

3.4.2 Mean Velocity Fields . . . 79

3.4.3 Spectral Analysis . . . 79

3.4.4 Turbulence Kinetic Energy . . . 84

3.4.5 Dissipation of turbulence energy . . . 87

3.4.6 Comparison of energy dissipation methods . . . 91

3.5 Error analysis . . . 95

3.5.1 Divergence Tests . . . 95

3.6 Closing remarks . . . 100

4 Analysis of Turbulent Boundary Layer with TPIV **102**

4.1 Introduction . . . 102

4.2 Experimental Setup . . . 106

4.2.1 Flow properties . . . 107

4.2.2 Wall region scaling parameters . . . 107

4.2.3 TPIV measurements . . . 110
4.2.4 Image Processing . . . 112
4.2.5 Volume Reconstruction and Vibration Correction . . . 113
4.2.6 Velocity field calculation . . . 113
4.3 Results . . . 114
4.3.1 Mean velocity fields . . . 114
4.3.2 Instantaneous velocity fields . . . 115
4.3.3 Velocity field probability density functions . . . 117
4.3.4 Velocity field joint probability density functions . . . 121
4.3.5 Reynolds stresses . . . 123
4.3.6 Dissipation of turbulence energy . . . 125
4.4 Comparison of energy dissipation methods . . . 127
4.4.1 Boundary layer regions R_1 and R_2 . . . 127
4.4.2 Comparison of R_1 and R_2 and centre pool regions . . . 129
4.5 Concluding remarks . . . 131

5 Tomographic PIV measurements of a turbulent fountain with refraction index matching 133
5.1 Introduction . . . 133
5.1.1 Fountain Flow . . . 133
5.1.2 Experimental measurements of fountain flows . . . 135
5.1.3 Tomographic Particle Image Velocimetry . . . 139
5.2 Experimental Set-up . . . 140
5.2.1 Experimental regime . . . 142
5.2.2 Refraction-Index Matching . . . 142
5.3 TPIV set-up . . . 144
5.3.1 Laser and optical details . . . 144
5.3.2 Reconstruction . . . 147
5.3.3 Reconstruction quality assessment . . . 147
5.3.4 Velocity Field Calculation . . . 149
5.3.5 Computational Time . . . 151

5.4 Results . . . 151
5.4.1 Fountain initialisation velocity fields . . . 151
5.4.2 Fully developed fountain: instantaneous velocity fields . . . 155
5.4.3 Fully developed fountain: mean velocity fields . . . 157
5.4.4 Turbulence properties . . . 163
5.4.5 Characterisation of mixing . . . 165
5.4.6 Error analysis . . . 167
5.4.7 Limitations . . . 169
5.5 Discussion . . . 170

6 Conclusions **172**

Bibliography **176**

A Turbulent channel: experimental set-up and supplementary results **195**
A.1 Materials . . . 195
A.2 Additional information of the apparatus . . . 196
A.3 Supplementary results and curve fitting . . . 199
A.4 Appendix - Technical Details of 2D PIV Measurements . . . 202

B Camera Calibration for TPIV **204**
B.1 Calibration Targets . . . 204
B.2 Determination of the camera calibration matrix **M** . . . 205
B.3 Re-Projection Errors . . . 206
B.4 Volume Self-Calibration . . . 207

C Vibration-Correction Implementations **211**
C.1 Synthetic Model to Study Camera Vibration . . . 214
C.1.1 Implementation . . . 214
C.1.2 Reconstruction and Cross-Correlation Metrics . . . 216
C.1.3 Simulation of Vibration Correction Schemes. . . . 218
C.1.4 Correction Schemes and their Effect on Velocity . . . 219

C.1.5 Correction Schemes and their Affect on Turbulence Statistics 221

D Programme that calculates the approximate lens mounted adapter settings to achieve Scheimpflug condition 224

E Short guide to batch processing TPIV experiments 231

Declaration

I, Thomas Anthony Earl, hereby declare that the work presented in this thesis is solely my own work and to the best of my knowledge is original and contains no material previously published or written by another author, except where due reference to the other author is provided in the text of this thesis. I have read and understood the *University of Sydney Student Plagiarism: Coursework Policy and Procedure* guidelines. I declare that this thesis has been written by me and any help that I have received in my research work has been acknowledged.

No part of this thesis has been submitted or accepted for the award of any other degree or diploma in any university or institution other than the University of Sydney, Australia.

Thomas Earl
February, 2014

Acknowledgements

I would like to begin by extending my sincerest thanks to my thesis supervisor, Dr. Steve Cochard. Steve recognised my enthusiasm for research and fluid mechanics towards the end of my Bachelor degree, and since then has been instrumental in the advancement of my studies in this field (and in the process, rescuing me from the clutches of structural engineering!). Steve has given me some amazing opportunities over the last four years that have taken me across the globe and cemented my drive to study fluid mechanics, to which I am truly indebted. These include arranging a 6 month research position at École Polytechnique de Fedèrale de Lausanne (EPFL), and forging a collaboration with Professor Laurent David which led to me spending 6 months of my doctoral studies in Poitiers. Steve, thank you for your encouragement, the famous Swiss eye to detail, and guidance. A suitable supervisor indeed! I also take this opportunity to thank my co-supervisor, Professor John Patterson for his insights, discussions, dry humour and encouragement.

My sincerest thanks to Professor Laurent David, who gave me an incredible opportunity to work in his lab (not once, but twice!) at the University of Poitiers and who has been a very important figure in advancing my studies. It was a privilege to have been able to work with an expert in volumetric PIV techniques and in fluid mechanics. The patience and trust you gave me are sincerely appreciated. Undoubtedly, I would not be presenting this work if it weren't for your generosity.

Je tiens à remercier toute l'équipe de Poitiers pour leur temps et leur aide: Lionel Thomas, Martin Druon et Benoît Tremblais ainsi qu'à Romain, Patrice et Jocelyn. Mon séjour en Poitou-Charentes a été mémorable grâce à l'accueil chaleureux de Riadh, Sylvain, Adrian, Guillaume, Vincent, Laurent, Remi, Soria, Florence et Badredine; un tout grand merci.

Back in Sydney, a big thanks to Nick Williamson and Sten Stårner for their help with the fountain rig. Thanks to Garry Towel for his support in acquiring lab spaces for the fountain experiments and for the fast tracking of manufacturing various bits and pieces for the experiment. Thanks also to the technical officers in the labs, particularly Theo, Paul

and ‘Oz’, for your help with soldering, machining and building.

To the guys in the Eagle’s Nest, our appropriately named office perched on top of the structural engineering lab. It was great to forge some strong friendships over the course of three years or so. The Eagle’s Nest inhabitants during my studies were: Benjy Marks, Tom Miller, Adam Trouncer, James Reynolds, Joachim (Joe) Pätzold and Francisco Cardoso. I wish you all luck in all your future endeavours, covering a broad base from granular material to thin walled steel structures. A special mention to Joe, who spent many hours with me in the labs helping me to conduct the fountain flow experiments – your help was invaluable, thank you. On a personal level, it was quite a feat to keep so many cafés in the Darlington area in business, but we did it! Besides that daily ritual, Joe has been a great friend and colleague.

Voor mijn heel mooie vrouw, Merel. Waarschijnlijk was mijn werk makkelijker door je liefde, ondersteuning, energie en enthousiasme, zeker is dat mijn leven onmeetbaar en exponentieel beter is door jou. Regarding this thesis, especially in these final months of writing, it was your continuous encouragement for me to persevere that helped get me over the line in the end. Thank you for the final crossing of ‘t’s and dotting of ‘i’s after the examination process.

My warmest thanks to my parents, Michael and Gail, who throughout this thesis and indeed my whole life, would always show interest in my studies and offer me unfaltering love and support. It is indisputable that my modest pursuit of attaining a broad and in depth knowledge of science began and flourished under you. Thank you dad, for taking the time to proof read through the opening chapters. Your suggestions have no doubt markedly improved their readability. Thanks also to my immediate and extended family for their continued support and encouragement.

Finally, I would like to acknowledge the financial support for this project, which was provided through an Australian Postgraduate Award and also an AD McConnell scholarship.

List of Publications

Journal Arcticles

- T.A. Earl, S. Cochard, L. Thomas, B. Tremblais & L. David (2015) Implementation of vibration correction schemes to the evaluation of a turbulent flow in an open channel by tomographic particle image velocimetry. Meas. Sci. Technol. Volume 26. 19pp.

- T.A. Earl, J. Paetzold & S. Cochard (2013) Tomographic PIV measurements of turbulent fountains with refraction index matching. Journal of Flow Visualisation and Image Processing. Volume 20, pp 179–208.

- S. Cochard, C.W. Letchford, T.A. Earl & A. Montlaur. (2012) Formation of tip-vortices on triangular prismatic-shaped cliffs Part 1: A wind tunnel study. Journal of Wind Eng. and Industrial Aerodynamics 109: 9–20.

Conference proceedings

- T.A. Earl, S. Cochard, L. Thomas, B. Tremblais & L. David (2014) Investigation of the turbulent boundary layer and associated energy dissipation in an open channel flow behind a series of regular grids. River Flow International Conference on Fluvial Hydraulics, 3-5 September, Lausanne, Switzerland.

- S. Cochard, J. Paetzold, D. Fletcher, T. A. Earl, M. Mohamad Khairuddi, S. Fathieh (2013). Numerical simulations of the mixing potential of a high-rise inclined building. 16th Australasian Wind Engineering Society Workshop (AWES 2013), 18-19 July, Brisbane, Australia

- T. A. Earl, L. Thomas, S. Cochard, R. Ben Salah, B. Tremblais, L. David (2013) Volumetric Measurements by Tomographic PIV of Grid Generated Turbulence in

an Open Channel Flow. International Symposium on Turbulence and Shear Flow Phenomena (TSFP-8), 28-30 August, Poitiers, France.

- T.A. Earl, S. Cochard, B. Tremblais, L. Thomas & L. David (2013) Evaluation of the Energy Dissipation from Tomographic PIV Measurements in an Open Channel Flow behind Regular Grids. International Association for Hydro-Environment Engineering and Research, IAHR2013, 8-13 September, Chengdu, China.

- T. A. Earl, R. Ben Salah, L. Thomas, B. Tremblais, S. Cochard, L. David (2012) Volumetric Measurements by Tomographic PIV of an Open Channel Flow Behind a Turbulent Grid. 18th Australasian Fluid Mechanics Conference, 3-7 December, Launceston, Australia.

- R. Ben Salah, T. A. Earl, L. Thomas, B. Tremblais, S. Cochard, L. David (2012) Mesure volumique par tomo-PIV dun écoulement dans un canal turbulent de surface libre derrière une grille. 13ième Congrès Francophone de Techniques Laser, 18 21 September, CFTL 2012 - ROUEN, France.

- S. Cochard, C. W. Letchford, T. A. Earl (2011) PIV measurement of the velocity over triangular shaped cliffs. 13th International Conference on Wind Engineering, July 10-15, Amsterdam, The Netherlands.

- D. Marra, T. A. Earl and C. Ancey (2011) Experimental Investigations of Dam Break Flows down an Inclined Channel. 34th International Association for Hydro-Environment Engineering and Research, IAHR 2011, 26 June - 1 July, Brisbane, Australia.

Nomenclature

Acronyms

2D	Two dimensional
3D	Three dimensional
2C	Two components
3C	Three components
ART	Algebraic Reconstruction Technique
AART	Adaptive Algebraic Reconstruction Technique
BiMART	Block Iterative Multiplicative Algebraic Reconstruction Technique
CT	Computed Tomography
DNS	Direct Numerical Simulation
DSR	Dynamic Spatial Range
FFT	Fast Fourier Transform
HPIV	Holographic Particle Image Velocimetry
LDA	Laser Doppler Anemometry
LoS	Line-of-Sight
MENT	Maximum Entropy (reconstruction algorithm)
MinLOS	Minimum Line-of-Sight (volume initialisation algorithm)
MTE	Motion Tracking Enhanced
PIV	Particle Image Velocimetry
ppp	Particles per pixel
ppv	Particles per voxel
PTV	Particle Tracking Velocimetry
ROI	Region of Interest

rms	Root mean square
SAPIV	Synthetic Aperture Particle Image Velocimetry
SMART	Simultaneous Multiplicative Algebraic Reconstruction Technique
SPIV	Stereo Particle Image Velocimetry
TI	Turbulence intensity, $\lvert u_i' \rvert / U$
TKE	Turbulent Kinetic Energy
TPIV	Tomographic Particle Image Velocimetry
WIDIM	Window Displacement Iterative Multigrid

Greek Symbols

Δt	Time between two laser pulses
Δz_0	Laser sheet thickness
μ	Dynamic Viscosity, relaxation paramater
ν	Kinematic viscosity
λ	Taylor microscale
δ	Error; centre-to-centre *IW* or *IV* spacing
δz	Focal depth
$\delta_{i,j}$	Kronecker delta (0 if $i \neq j$, 1 if $i = j$)
ω	Instantaneous vorticity vector
$\omega_x, \omega_y, \omega_z$	Instantaneous components of vorticity about x, y, z axes, respectively
∇	Gradient operator $\left(\frac{\partial}{\partial x} + \frac{\partial}{\partial y} + \frac{\partial}{\partial z} \right)$
ξ	Divergence test
η	Kolmogorov Lengthscale
τ_w	Shear stress at the wall

κ	Wave number; von Kàrmàn's constant
ρ	Density
ε	Energy Dissipation
θ	Slope, Angle between camera lens and sensor
ϕ	Angle between camera lens plane and focal plane
ξ	Divergence quality, $\big(\sum_{i=1,2,3} \partial u_i/\partial x_i\big)^2 / \sum_{i=1,2,3} (\partial u_i/\partial x_i)^2$

Latin symbols

A_{ij}	Velocity Gradient Tensor, $\partial u_i/\partial x_j$
$\mathscr{B}$	Block (in regards to block-iterative computational methods)
c	Camera number
D	Bar width/diameter of a regular grid
D_0	Diameter of jet or fountain nozzle at exit point
d_A	Pixel pitch
E	Energy of reconstructed volume
$E(\mathbf{x}_j)$	Energy of jth voxel in reconstructed volume
$f_\#$	F-number: the ratio of the lens focal length to aperture diameter
Fr	Froude number
G	Trashrack grid type
h	Water depth; fountain height along y axis
h_c	Water depth in channel centre
I	Image intensity distribution
$I(\mathbf{X}_i)$	Intensity of ith pixel
IV	Interrogation volume
IW	Interrogation window
k	Average fluctuating kinetic energy per unit mass; iteration number
L	Streamwise length between trash racks; characteristic length

L_{P}	Total length of a grid's perimeter
l	Length; length scale of vortices
l_0	Integral length scale
M	Bar-to-bar spacing of a regular grid
M_0	Magnification factor of imaging system
Ma	Mach Number
N_c	Number of cameras
N_j	Number of voxels
N_s	Image source density
P	First invariant of A_{ij}; production range of turbulence
P_G	Global volumetric power of the flow from one pool to the next
Q	Second invariant of A_{ij}
Q_f	Local re-projection correlation coefficient
Q_0	Volumetric flow rate
$Q(x)$	Autocorrelation coefficient
Q2	Ejection region
Q4	Sweep region
R	Cross-correlation coefficient; third invariant of A_{ij}; Radius
Re	Reynolds number
Ri	Richardson number
s	Offset distance between parallel laser sheets
T_{ij}	Deviatoric stress tensor
T_{scan}	Duration of laser sheet sweep through a measurement volume
t	Time
$\mathbf{u}$	Instantaneous velocity vector
u_i	Instantaneous velocity vector
u, v, w	Instantaneous components of velocity $\mathbf{u}$ in the x, y, z directions, respectively

U_0	Characteristic velocity; bulk velocity; top hat velocity of a jet.
U_i	Mean components of $\mathbf{u}$
U_*	Friction Velocity
U_V	Average velocity, taken over the measurement region
u_i'	fluctuating components of $\mathbf{u}$
$\langle u \rangle$	Ensemble (spatial and temporal) mean of u
$w_{i,j}$	Weighting matrix for reconstruction algorithms
W	Channel or tank width
$\mathbf{x}_\mathrm{p}$	Vector of particle displacement in real coordinates
$\mathbf{X}_\mathrm{p}$	Vector of particle displacement in image coordinates
x, y, z	Coordinate axis names, where x is in the flow direction
X, Y, Z	Nominal distances in the x, y, z directions, respectively, typically measurement volume dimensions
y^+	Normalised wall coordinate
y^*	Viscous length scale for wall bounded flows
z_m	Mean fountain height

Introduction

The objective of this study is to measure the 3D turbulent structures in both open channel and fountain flows with the aim to increase the understanding of the mixing processes observed in an environmental flow. Environmental flows cover a broad range of flows in both the natural and man-made environments, including the flow in rivers, estuaries, and lakes; flows in the atmosphere and the ocean, and; flows from waste water pipes or industrial chimney stacks. Our quality of life and the health of the environment are intrinsically linked and dependent on these flows.

Environmental flows are predominantly at very large scales and this results in them being dominated by turbulence. Turbulence tends to occur at large scales because the viscous or dampening action of the fluid becomes insignificant compared to its inertia – the larger or faster a flow is, the greater its inertia. The ratio of inertial on viscous forces is known as the Reynolds number, Re. At large Re the inevitable perturbations in the flow caused by a local change in velocity or temperature (for example due to an interaction with a solid boundary or another fluid) propagate through the flow and modify it significantly from its otherwise smooth, laminar state.

An investigation into the physics and behaviours of these turbulent fluctuations is crucial to understand the mixing processes, sediment transport and heat exchange in them. We know that these fluctuations are not chaotic and uncorrelated, but they exist as coherent structures of high vorticity, otherwise called eddies or vortices. One of the greatest difficulties in studying flows with high Re is the wide range of length scales of turbulent motion that affect the flow. At the largest geometric scales, large vortices are formed that characterise the flow field, while at the smallest scales, the vortices become small enough to be broken down by viscosity and dissipated into heat. As Re increases, so too does the range of the smallest to largest vortices. Another significant difficulty in measuring turbulence is that these vortices are three dimensional. Hence, only by considering a flow in the full three dimensions can we hope to understand the underlying physics.

To this end, experimental techniques to measure turbulent flows have evolved steadily over the last hundred or so years. Point measurements conducted by probes, most notably

by hot wires, enabled researchers[1] to develop statistical approaches and theories of turbulence. From these measurements stemmed the theories of 'frozen turbulence' and the isotropic and inertia conserving decay of turbulence energy following Kolmogorov's -5/3 power law until dissipation into internal energy.

Laser diagnostic approaches, namely laser Doppler anemometry (LDA) enabled non-intrusive measurements at very high sampling frequencies with increased accuracy and simpler retrieval of all three components of velocity (compared to an equivalent probe). Despite the improvements to point measurements, the structure of the vortices in the flow could not be analysed. At the same time, flow visualisation techniques were being improved, which were able to give clues as to the underlying features of turbulent flows, however there was no way in quantifying the observations.

Particle image velocimetry (PIV) (Dudderar and Simpkins, 1977; Adrian, 1984; Willert and Gharib, 1991) is a technique that allows the determination of the *instantaneous vector velocity by measuring the displacements of numerous fine particles that accurately follow the motion of the fluid* (Adrian and Westerweel, 2011). PIV offers a deterministic study of turbulence – the ability to investigate coherent vortices. In short, PIV measurements have enabled the quantification of qualitative observations of turbulence by capturing a flow field on a two-dimensional (2D) plane.

Many adaptions of planar PIV have striven towards the ultimate goal of volumetric measurements. Of those, tomographic particle image velocimetry (TPIV) (Elsinga et al, 2006a) emerges as a highly versatile technique. The objective of the tomographic reconstruction is to determine the three dimensional position of the tracer particles. This is achieved by projecting the multiple and simultaneous PIV images back into the measurement domain and calculating the most probable intensity distribution that could have made the images. It follows that regions of high intensity in the field correspond to the particle locations. Finally, the reconstructed particle field is divided into a number of interrogation volumes (IVs), and through a volumetric cross-correlation between corresponding and sequential IVs, the three-dimensional (3D) velocity field is retrieved.

[1] the pioneering researchers in turbulence were O. Reynolds (before hot wires), G. I. Taylor, Prandtl, von Karman and Kolmogorov (Pope, 2000)

Since its inception, the research community appears to have been truly re-invigorated (Scarano, 2013), with a steady stream of new applications, algorithms and data treatment. Despite this, few or no TPIV measurements have been conducted in a turbulent open channel flow. Likewise, the application to measuring fluid flows of differing densities is very much in its infancy. This work addresses these two areas in the context of understanding environmental flows.

Aims and objectives

The aim of this thesis is to understand the fundamental characteristics of environmental flows. Two flows will be be investigated specifically: an open channel flow and a fountain flow, with the following objectives:

1. To analyse the energy dissipation in a pool of an open channel flow behind a trash rack.
2. To measure a series of turbulent fountain flows to obtain the 3D structures within.
3. To visualise and identify the turbulent structures and phenomena in the flows.

This work will show the application of TPIV to measure these flows and in the process, a new TPIV system at the University of Sydney was built in order to demonstrate its application with multi-fluid flows.

Chapter overview

This work is divided into the following six chapters; a synopsis of each is provided below.

Chapter 1 explains the fundamentals of fluid mechanics and the derivation of the equations of motion. The development of turbulence is described not purely by observation, but from the governing equations themselves. A review of turbulence, its origins and the current knowledge is provided, highlighting its 3D nature and specific canonical cases linking turbulence theory to the experimental measurements.

Chapter 2 introduces PIV as an established technique in analysing turbulent flows. A brief review of the method is accompanied by an examination of it's development into a volumetric measurement technique. TPIV has emerged as a highly versatile and promising approach of the volumetric adaptations and is the technique chosen to measure the flows in this work. The working principles of TPIV are presented, along with a review of some of the latest developments in the field.

Chapter 3 describes the experimental investigation of the energy dissipation in a pool of an open channel flow. Each pool was bound by a series of regular grids in the flume. Turbulent structures are visualised and the turbulence in the pool is characterised in terms of anisotropy and fundamental scales. A thorough analysis of the errors based on the divergence and other criteria are presented. The work resulting from this chapter resulted in the publication of Earl et al (2015).

Chapter 4 details a secondary experiment in the open channel flow in a measurement region along the channel floor and at higher resolution. The boundary layer of the open channel flow is analysed and events known as sweeps and ejections are identified. The turbulence generated at the wall is used in order to fully characterise the energy dissipation in the pool. The work resulting from this chapter resulted in the conference proceedings of Earl et al (2014).

Chapter 5 investigates fountain flows using TPIV. Fountain flows appear frequently in the environment, from pyroclastic eruptions to the pumping of wastewater into the ocean. In order to employ TPIV the refractive indices of both fluids were matched. The initial and fully developed periods of the fountain are analysed. The work resulting from this chapter resulted in the publication of Earl et al (2013).

Chapter 6 concludes the work presented in the thesis, highlighting the key findings of the experimental investigations. This chapter also presents opportunities and recommendations for future work, regarding the viability of TPIV to measuring environmental flows. The contributions of this work to the scientific community are discussed.

Chapter 1

Turbulent Flows

Big whorls have little whorls that feed on their velocity, and little whorls have lesser whorls and so on to viscosity – in the molecular sense
— Richardson (1922) p.66

1.1 An overview of turbulence

Turbulence is the unsteady, seemingly chaotic and unpredictable state of fluid motion. The motions are measured as fluctuations from the mean flow velocity and are correlated in space and time by means of coherent structures of vorticity, known as vortices. These vortices are said to exist in a self-similar manner: from the largest length scales of the flow down to the smallest, dissipative scales (Ecke, 2004), transferring kinetic energy to internal energy at the molecular level. However, the self-similarity hypothesis has been shown not to be universal (for example, George and Hussein, 1991; Seoud and Vassilicos, 2007, . See also Section 1.10.1). The larger vortices are a function of the geometric conditions and a generally highly anisotropic. Not until they break down into smaller and smaller vortices can isotropy be achieved. Turbulence is present in every natural flow, from rivers and ocean currents to weather systems – very few exceptions exist. Turbulence is a dominant feature of the open channel and fountain flows that are investigated in this work.

The objective of this study is to measure the 3D turbulent structures in both open channel and fountain flows with the aim to increase the understanding of the mixing processes

observed in an environmental flow. Predicting the behaviour or characteristics of turbulence is notoriously difficult, and this results in having to conduct expensive testing or the use of over-conservative factors for designing new engineering objects. To show why this is the case, and why there must be an emphasis on experimental measurements, this chapter reviews the origins of turbulence and its features, commencing with the derivation of the equations of motion.

1.2 Governing equations of fluid motion

In this text, both vector notation and Einstein index notation for Cartesian tensors are used interchangeably depending on what explains an idea most succinctly. Lower case u_i represents the three instantaneous components of velocity vector $\mathbf{u}$ and capitalised U_i represents the corresponding mean components in Cartesian space x_i.

To derive the equations of motion, we consider an infinitesimal element of fluid (or 'fluid element') in a flow. *Infinitesimal* is smaller than the smallest geometric length scale in a flow, but significantly larger than the free path of the fluid molecules. This means the application of the continuum hypothesis is valid (Pope, 2000).

The equations of motion are derived by application of the conservation of mass and momentum to a fluid element. In the absence of temperature gradients, flow can be considered incompressible (constant density, ρ) when $U_0 < 0.3\text{Ma}$, where Ma is the Mach number and U_0 the characteristic velocity of the flow. As this work only deals with incompressible flows, the conservation of mass equation simplifies to

$$\frac{\partial \rho}{\partial t} + \nabla \cdot \rho \mathbf{u} = 0 \quad \rightarrow \quad \nabla \cdot \mathbf{u} \equiv \frac{\partial u_i}{\partial x_i} = 0 \tag{1.1}$$

which states that when the trace of the velocity gradient tensor of a fluid element is zero, the volume of the element is constant, and hence so too is its mass. A fluid element in a flow can accelerates due to its position and time, $\mathbf{a}(x,y,z,t)$. In an Eulerian frame of reference, the acceleration is defined as:

$$\mathbf{a} = \frac{D\mathbf{u}}{Dt} \equiv \frac{\partial u_i}{\partial t} + u_j \frac{\partial u_i}{\partial x_j} \tag{1.2}$$

The element is subject to the conservation of momentum equations (Newton's 2nd Law, $\mathbf{F} = m\mathbf{a}$). The mass term m is considered as the mass per unit volume, i.e. the density ρ. The forces $\mathbf{F}$ are determined by considering the body forces and surface forces (normal and tangential) acting on a fluid element, so that

$$\rho\left(\frac{\partial u_i}{\partial t} + u_j\frac{\partial u_i}{\partial x_j}\right) = -\frac{\partial p}{\partial x_j} + \frac{\partial \tau_{ij}}{\partial x_j} \tag{1.3}$$

where τ_{ij} is the tensor representing the instantaneous deviatoric stresses and p is the static pressure, which accounts for hydrostatic pressure variation. For a Newtonian fluid, τ_{ij} describes the linearly dependent resistance to deformation of a fluid element as a function of the stresses $s_{ij} = \frac{1}{2}(\partial u_i/\partial x_j + \partial u_j/\partial x_i)$ and its viscosity μ, given by the relation (George, 2013):

$$\tau_{ii} = -2\mu\frac{\partial u_i}{\partial x_i} = 0 \qquad \text{(from Eq. 1.1)} \tag{1.4a}$$

$$\tau_{ij} = 2\mu(s_{ij}) \qquad \text{(when } i \neq j\text{)} \tag{1.4b}$$

where μ is the kinematic viscosity. Substituting Eq. 1.4 into Eq. 1.3 and used in conjunction with the conservation of mass (Eq. 1.1) results in:

$$\rho\left(\frac{\partial u_i}{\partial t} + u_j\frac{\partial u_i}{\partial x_j}\right) = -\frac{\partial p}{\partial x_i} + \mu\left(\frac{\partial^2 u_i}{\partial x_j^2}\right) \tag{1.5}$$

Equation 1.5 is known as the Navier-Stokes equations. In this form, it represents the instantaneous flow field of an incompressible flow. Although the Navier-Sokes equation has been derived from seemingly simple fundamental principles, its behaviour is still poorly understood. To prove its existence and smoothness for a general 3D case in time are one of the seven mathematics problems set in the *Millennium Prize Problems* by the Clay Mathematics Institute[1].

[1]See: http://www.claymath.org/millenium-problems/navier-stokes-equation. At the time of going to press, Kazakh mathematician Mukhtarbay Otelbaev has submitted a paper entitled: *Existence of a strong solution to the Navier-Stokes equation* which claims to have proved its smoothness and existence.

1.3 Reynolds averaged equations

The analysis of the flow in its mean and fluctuating parts can reveal interesting features about the transfer of turbulence energy. What will be seen in the following section is the way in which turbulent energy can transfer between the mean flow field and the fluctuations about the mean. This is achieved by Reynolds decomposition, where the instantaneous velocity is divided into its mean and fluctuating parts:

$$u_i = U_i + u_i' \tag{1.6a}$$

$$p = P + p' \tag{1.6b}$$

$$\tau_{ij} = T_{ij} + \tau_{ij}' \tag{1.6c}$$

where capitalisation represents the mean components and the primes represent the time dependent fluctuations about the mean. Substituting Eqs. 1.6 into Equation 1.3 yields:

$$\rho\left(\frac{\partial(U_i+u_i')}{\partial t} + (U_j+u_j')\frac{\partial(U_i+u_i')}{\partial x_j}\right) = -\frac{\partial(P+p')}{\partial x_i} + \left(\frac{\partial(T_{ij}+\tau_{ij}')}{\partial x_j}\right) \tag{1.7}$$

The ensemble average of Eq. 1.7 gives Eq. 1.8. As the averaging and differentiating operations commute and the average of the fluctuating components are zero, by definition, Eq. 1.7 reduces to:

$$\rho\left(\frac{\partial U_i}{\partial t} + U_j\frac{\partial U_i}{\partial x_j}\right) = -\frac{\partial P}{\partial x_i} + \frac{\partial T_{ij}}{\partial x_j} - \langle u_j'\frac{\partial u_i'}{\partial x_j}\rangle \tag{1.8}$$

It can also be shown that the divergence (Eq. 1.1) is solenoidal (Pope, 2000), and hence applies to both the mean and fluctuating components, so that:

$$\frac{\partial U_i}{\partial x_i} = 0 \tag{1.9a}$$

$$\frac{\partial u_i'}{\partial x_i} = 0 \tag{1.9b}$$

As shown by George (2013), multiplication of Eq. 1.9 by u_i', and substitution into the last term of Eq. 1.8 yields the mean Navier-Stokes equation:

$$\rho\left(\frac{\partial U_i}{\partial t} + U_j\frac{\partial U_i}{\partial x_j}\right) = -\frac{\partial P}{\partial x_i} + \frac{\partial}{\partial x_j}\left[T_{ij} - \rho\langle u_i'u_j'\rangle\right] \tag{1.10}$$

The right hand side of the equation is the mean stress contribution. Further, the term in the angled brackets is called the Reynolds stress. The deviatoric stresses are related directly to the constitutive fluid property of viscosity and the mean motion. The Reynolds stress, on the other hand, is a property of the flow, not the fluid. The implication of this is that as the flow field changes, so do the Reynolds stresses. This equation also shows how the turbulent fluctuations affect the mean flow field. As discussed further by George (2013), the mean flow cannot be considered as the laminar portion of the flow, and the fluctuating component simply superimposed on top – the turbulence feeds back into the mean equations through the Reynolds stress.

An important feature of the Reynolds stress term is that to be inserted into the mean flow requires knowledge of not only the three components of velocity, but all nine gradients of the fluctuating velocity gradient tensor, $A'_{ij} = \partial u'_i / \partial x_j$. It is essentially the Reynolds stress that causes all of the difficulty in computationally modelling turbulent flows because the number of unknown quantities exceed the number of equations. Discussion on the Turbulence Closure Problem that arises from this, and the subsequent modelling techniques implemented to solve the Reynolds averaged Navier-Stokes equation is beyond the scope of this work. Discussion about the various length scales in turbulent flows (which are also a hindrance to modelling flows) is provided in Section 1.7.

1.4 The Reynolds stress equation

Although this thesis is primarily concerned about the measurement of turbulence directly from an experimental technique, it is important to investigate another derivation of the Navier-Stokes equation, the Reynolds stress equation. As will be seen, the Reynolds stress equation shows how the mean velocity field transports energy to the fluctuating terms. In addition, the Reynolds stress equation shows the mechanisms of the turbulent energy dissipation.

The derivation of the Reynolds stress equation is from the fluctuating portion of the Navier-Stokes equations. To obtain the fluctuating Navier-Stokes, Eq. 1.10 is subtracted from Eq. 1.3 to yield:

$$\rho\left(\frac{\partial u_i'}{\partial t}+U_j\frac{\partial u_i'}{\partial x_j}\right)=-\frac{\partial p}{\partial x_i}+\frac{\partial \tau_{ij}'}{\partial x_j}-\underbrace{\rho\left(u_j'\frac{\partial U_i}{\partial x_j}\right)}_{\text{production}}+\rho\left(u_j'\frac{\partial u_i'}{\partial x_j}-\langle u_j'\frac{\partial u_i'}{\partial x_j}\rangle\right) \tag{1.11}$$

One term of the fluctuating Navier-Stokes equations above worthy of discussion is the production term. This term is the way in which the energy from the mean flow is transported to the fluctuating part (George, 2013). When decomposed into the Reynolds stress equation, it can be used to ascertain whether or not the turbulent fluctuations have enough energy to influence the mean flow equations or whether they dampen out. The main driver is the non-linearity of the terms, which is discussed further in Section 1.5.

The decomposition of Eq. 1.11 into the Reynolds Stress equation is beyond the scope of this work. The interested reader should consult the works of Pope (2000), Lesieur (2008) or George (2013) for further discussion. For the purpose of this thesis, it is more appropriate to discuss its main features and that it is a derivation of the fluctuating velocity momentum equation. Hence,

$$\begin{aligned}\frac{\partial}{\partial t}\langle u_i'u_k'\rangle+U_j\frac{\partial}{\partial x_j}\langle u_i'u_k'\rangle &= \underbrace{\langle\frac{p'}{\rho}\left[\frac{\partial u_i'}{\partial x_k}+\frac{\partial u_k'}{\partial x_i}\right]\rangle}_{\text{Pressure strain-rate}}\\ &+ \underbrace{\frac{\partial}{\partial x_j}\Big\{-\frac{1}{\rho}[\langle p'u_k'\rangle\delta_{ij}+\langle p'u_i'\rangle\delta_{kj}]-\langle u_i'u_k'u_j'\rangle+2\nu[\langle s_{ij}'u_k'\rangle+\langle s_{kj}'u_i'\rangle]\Big\}}_{\text{Turbulent Transport}}\\ &- \underbrace{\left[\langle u_i'u_j'\rangle\frac{\partial U_k}{\partial x_j}+\langle u_k'u_j'\rangle\frac{\partial U_i}{\partial x_j}\right]}_{\text{Production}}\\ &- \underbrace{2\nu\left[\langle s_{ij}'\frac{\partial u_k'}{\partial x_j}\rangle+\langle s_{kj}'\frac{\partial u_i'}{\partial x_j}\rangle\right]}_{\text{Dissipation}}\end{aligned} \tag{1.12}$$

is the Reynolds stress equation. The terms on the right hand side are labelled according to their contribution to turbulence. In particular, the dissipation of turbulence energy, the last term, will be investigated in Chapter 3. The dissipation term contains the fluctuating

stress tensor and viscosity, so with this term the fluctuations (at small enough scales) are dissipated into internal energy. It can be seen that the production terms provide energy to the fluctuations via the mean velocity gradients.

1.5 The origins of turbulence

In the previous sections, the Navier-Stokes equation (Eq 1.5) was derived by directly considering the motions and forces on an infinitesimal fluid element. An analysis of these equations by averaging revealed the Reynolds stress, a quantity that enables the transfer of fluctuating energy into the mean flow energy and vice-versa. The development of random fluctuations then stems from two observations (Pope, 2000):

- In all flows, there are unavoidable perturbations or disturbances, often inconceivably small, in initial conditions, boundary conditions and material properties
- Turbulent flows are observed to be highly sensitive to these perturbations

These initial perturbations can be due to, for example, an interaction with a boundary, whether it be liquid or solid, where there is a relative velocity difference, or a local temperature fluctuation due to uneven heating, which results in a change in density. Bailly and Comte-Bellot (2003) showed analytically that by substituting the convective acceleration term with a cosine wave (Eq 1.13) that the non-linear terms result in a superior harmonic series, that is, a divergent result. They consider the one dimensional form of the convective acceleration term

$$\frac{\partial u}{\partial t} + u\frac{\partial u}{\partial x} = 0$$

from the Navier-Stokes equation with the external forces (right hand side terms in Eq. 1.5) omitted and with the initial condition $u(x,t_0) = A\cos(k_x x)$ at $t = t_0$. Then, by way of Taylor expansion, they show:

$$
\begin{aligned}
u(x,t) &= u(x,t_0) + (t-t_0)\frac{\partial u}{\partial t}(x,t_0) + \mathrm{O}(\Delta t^2) \\
&= A\cos(k_x x) - (t-t_0)u\frac{\partial u}{\partial x}(x,t_0) + \ldots \\
&= A\cos(k_x x) + (t-t_0)A^2 k_x \cos(k_x x)\sin(k_x x) + \ldots \\
&= A\cos(k_x x) + \underbrace{(t-t_0)\frac{A^2 k_x}{2}\sin(2k_x x)}_{\text{harmonic series}} + \ldots
\end{aligned} \tag{1.13}
$$

This analysis shows how the non-linear terms in the Navier-Stokes equations are sensitive to perturbations. In the first line, the third term is in the order of $\Delta t^2 \to 0$. In the harmonic series term, the amplitude of the initial perturbation A is squared, and the frequency component has doubled, to $2k_x x$. Therefore, an initially small perturbation of energy A can cause secondary fluctuations that dominate the flow as a result of the non-linearity. This is an appropriate analogy for the development of turbulence fluctuations.

Not all perturbations lead to turbulence - these same disturbances also exist for laminar flows. In the case for laminar flow, the viscous forces in the fluid are strong enough to dampen out the perturbations. For turbulent flows, the inertial forces overcome the dampening effect of viscosity, leading to divergent and random fluctuations superimposed on the mean flow. The defining dimensionless parameter used to characterise turbulent flows is the Reynolds number,

$$
\mathrm{Re} = \frac{UL}{\nu} \tag{1.14}
$$

where L is the characteristic length scale of the flow (often determined by a dominant geometric length or from local scales in the flow), $\nu = \mu/\rho$ is the dynamic viscosity of the fluid and U is a characteristic velocity. For convection driven flows (not considered in this work) it is the Rayleigh-Bénard (Ra) number that determines whether a flow is likely to be laminar or turbulent.

1.6 Vorticity in turbulent flows

It has been mentioned that the turbulence fluctuations exist as coherent structures of vorticity ω, known as vortices. This section provides a brief insight into the transport of vorticity into different energy levels, and demonstrates how vorticity and vortex stretching is a 3D phenomenon. Vorticity is defined as the curl of velocity,

$$\omega = \nabla \times \mathbf{u} \equiv \left(\frac{\partial u_i}{\partial x_j} - \frac{\partial u_j}{\partial x_i} \right) \tag{1.15}$$

which is equivalent to twice the rate-of-rotation vector (Pope, 2000). The equation for the transport of vorticity is obtained by taking the curl of the Navier-Stokes equation Eq. 1.3, so that

$$\frac{\partial \omega_i}{\partial t} + \frac{\partial u_j \omega_i}{\partial x_i} = \underbrace{-\omega_i \frac{\partial u_j}{\partial x_j}}_{\text{divergence}} + \underbrace{\varepsilon_{ijk} \frac{\partial \rho}{\partial x_j} \frac{\partial p}{\partial x_k} / \rho^2}_{\substack{\text{Baroclinic} \\ \text{torque}}} + \underbrace{\omega_j \frac{\partial u_i}{\partial x_j}}_{\substack{\text{vortex} \\ \text{stretching}}} + \underbrace{\frac{1}{\text{Re}} \frac{\partial^2 \omega_i}{\partial x_j^2}}_{\substack{\text{viscous} \\ \text{diffusion}}} \tag{1.16}$$

From Eq. 1.1, the divergence term is zero for incompressible flows. The Baroclinic torque term generates vorticity through unaligned density and pressure gradients. Again, this term also cancels as only incompressible flows at constant temperature are considered. The viscous diffusion tends to dissipate the vorticity energy. The term is multiplied by the inverse of Re – thus at high Re, the viscous diffusion becomes insignificant. In other words, the affect of viscosity on the large scale turbulent structures is relatively small. Finally, the vortex stretching term shows the mechanism by which vorticity is transferred to smaller scales. This is a crucial term that corresponds with the energy cascade discussed in Section 1.7. To explain further, this term is called vortex stretching as its primary action is to *stretch* vortices, that is to elongate them along one axis proportional to a change in rotational velocity, and decrease their radius r along that axis. As the angular momentum (proportional to ωr^2) must be conserved, a reduction in the diameter results in an intensification of the vorticity. This is the mechanism for transferring energy from the large to the small scales, and it is via coherent vortices in the flow.

To see how the vortices obtain their energy, the following decomposition is performed. The vortex stretching term is the vorticity multiplied by the velocity gradient tensor $A_{ij} =$

$\partial u_i/\partial x_j$. A_{ij} can be decomposed into its symmetric (S_{ij}) and antisymmetric (Ω_{ij}) components

$$S_{ij} = \frac{1}{2}\left(\frac{\partial u_i}{\partial x_j} + \frac{\partial u_j}{\partial x_i}\right) \tag{1.17a}$$

$$\Omega_{ij} = \frac{1}{2}\left(\frac{\partial u_i}{\partial x_j} - \frac{\partial u_j}{\partial x_i}\right) \tag{1.17b}$$

to obtain

$$\omega_j \frac{\partial u_i}{\partial x_j} \equiv \omega_j A_{ij} = \omega_j S_{ij} + \omega_j \Omega_{ij} \tag{1.18}$$

The antisymmetric component multiplied by the vorticity is zero, so that

$$\omega_j \frac{\partial u_i}{\partial x_j} = \omega_j S_{ij} \tag{1.19}$$

Eq. 1.19 shows the underlying nature of vorticity amplification or decay. A positive local strain acts to amplify the vorticity in the flow, and if the strain is aligned with the vorticity, will act to stretch it in one direction, resulting in the transfer of vorticity to the smaller length scales. Finally, to show that the vortex mechanism is truly 3D, consider the vorticity equation (Eq. 1.16) in 2D.

$$\frac{\partial \omega_i}{\partial t} + u_j \frac{\partial \omega_i}{\partial x_i} = \nu \frac{\partial^2 \omega_i}{\partial x_j^2} \tag{1.20}$$

It can be seen that the vortex stretching mechanism has canceled out, which means that no mechanism exists in 2D for the transfer of energy from the large to the small vortices. In 2D, the vorticity can exist only about an axis normal to the flow plane and acts as a passive scalar that follows the fluid paths.

1.7 Turbulence properties and length scales

Perhaps one of the greatest challenges of investigating turbulence is that the size and range of the length scales are typically orders of magnitude apart. The dynamic spatial range (DSR), the ratio of the smallest to the largest resolvable or measurable scales, is a typical measure that experimentalists must consider when designing experiments (Adrian, 1997;

Adrian and Westerweel, 2011). The ratio of the largest to smallest length scales in a turbulent flow is proportional to $\mathrm{Re}^{3/4}$ (Lesieur, 2008), so an increase in Re results in a larger DSR. This contributes to the difficulty in resolving environmental flows due to their large Re.

Spectral analysis of turbulent flows shows that turbulent energy is produced at the large scales, which is generally dictated by the length scale of the geometry of the system L. Section 1.6, demonstrated that the large structures break down or cascade into smaller and smaller eddies until viscosity dampens them out and transfers their energy into internal energy. This process and the nomenclature for the length scales are shown schematically in Figure 1.1.

L is typically a characteristic geometric length that produces the vortices, such as a diameter of an object in the free stream. The length scales generated at boundaries are detailed separately following the definitions from Figure 1.1. The length l_0 is the integral length scale, calculated from the autocorrelation function of the velocity measurements:

$$l_0 = \frac{1}{\langle u'^2 \rangle} \int_0^\infty Q(x)\mathrm{d}x \tag{1.21}$$

where $Q(x)$ is the autocorrelation function of the velocity signal. l_0 indicates the scale or size of vortex structures associated with the largest distribution of energy in the flow. λ is the Taylor microscale. λ can be estimated from where the parabola that osculates with the normalised autocorrelation signal $Q(x)/\langle u_i'^2 \rangle$ intersects the abscissa (Pope, 2000). λ indicates the inertial region of the flow, and it is important particularly in isotropic turbulence studies, as the energy dissipation ε can be derived from it. Finally, η is the Kolmogorov microscale, where $\eta = (\nu^3/\varepsilon)^{1/4}$. To properly resolve a turbulent flow, it is generally required that η is also resolved (Tanaka and Eaton, 2007). Not shown in Figure 1.1 are the corresponding dissipative time $\tau_\eta = (\nu/\bar{\varepsilon})^{1/2}$ and velocity $u_\eta = (\nu\bar{\varepsilon})^{1/4}$ scales.

1.8 Turbulence kinetic energy and its rate of dissipation

The turbulence kinetic energy (TKE) is the mean kinetic energy associated with turbulent vortices, described in the previous section. The average fluctuating kinetic energy per unit

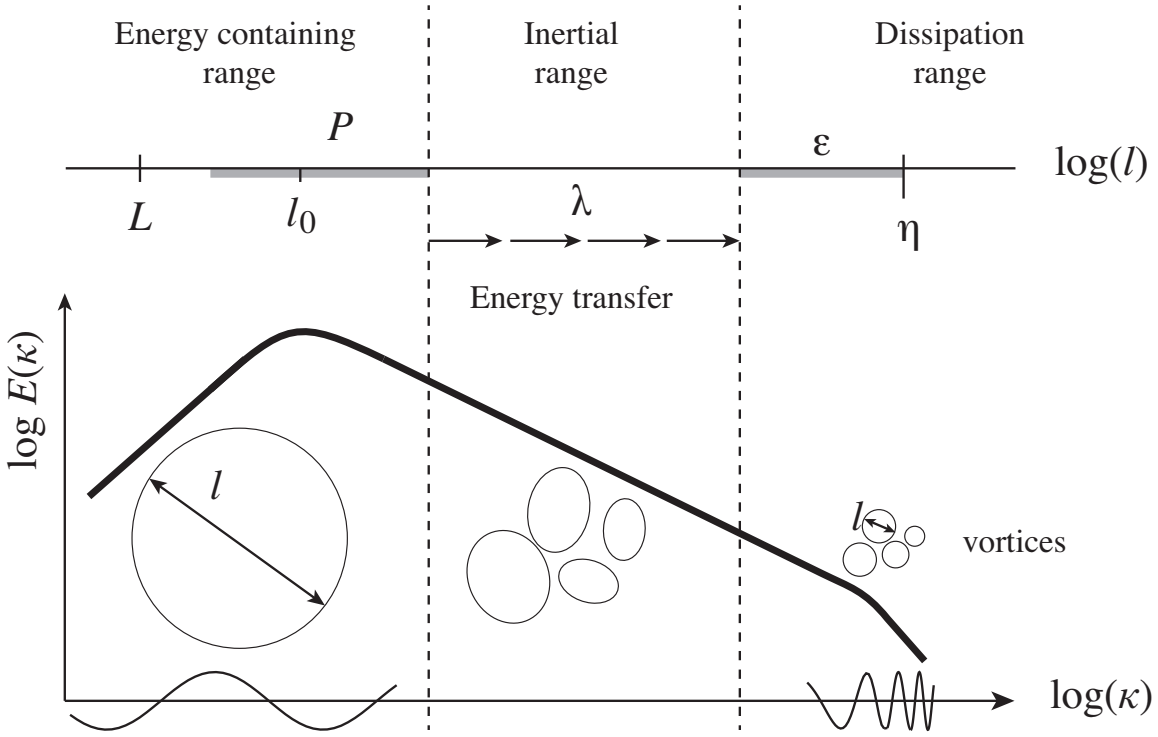

Figure 1.1: Relative sizes of turbulence in the energy cascade. To the left, the largest vortices are created and are in the so called production range P of the flow. The vortices at this scale contain the largest distribution of energy E. In the inertial range, there is lossless transfer of energy from the large to smaller scales until the dissipation range. The dissipation range are the smallest scales of turbulence in the flow η, where the vorticity dissipates into internal energy. κ is the wavenumber, $\kappa = 2\pi/l$. Adapted from Bakker (2006)

mass k is defined as:

$$k = \frac{1}{2}\langle u_i' u_i' \rangle \tag{1.22}$$

which is half the trace of the Reynolds stress tensor $\langle u_i' u_j' \rangle$. As k contains only the stresses normal to the fluid element, the transfer of k throughout the fluid is lossless in terms of energy. Analysis of the separate components can give and indication of whether or not a flow is anisotropic. This type of analysis can give an indication of the dominant turbulence direction. The rate of decay of k along x, along the dominant flow direction, and in the absence of turbulence production, can lead to an estimation of the dissipation of energy and hence the smallest length scales in the flow.

To obtain the energy dissipation contribution from the decay of turbulent kinetic energy, the Reynolds stress equation (Eq. 1.12) has its free indices contracted, is divided by 2 and the definition of k (Eq. 1.22) inserted. Thus, the average energy dissipation $\langle \varepsilon \rangle$, where the angled brackets denote ensemble averaging, derived from the modified Reynolds stress equation (Eq. 1.12) is:

$$\begin{aligned}
\langle \varepsilon \rangle \;=\; & \nu \left\{ 2\Big(\Big\langle \frac{\partial u}{\partial y}\frac{\partial v}{\partial x} \Big\rangle + \Big\langle \frac{\partial u}{\partial z}\frac{\partial w}{\partial x} \Big\rangle + \Big\langle \frac{\partial v}{\partial z}\frac{\partial w}{\partial y} \Big\rangle \Big) \right. \\
& + \Big\langle \Big(\frac{\partial u}{\partial y}\Big)^2 \Big\rangle + \Big\langle \Big(\frac{\partial v}{\partial x}\Big)^2 \Big\rangle + \Big\langle \Big(\frac{\partial u}{\partial z}\Big)^2 \Big\rangle \\
& + \Big\langle \Big(\frac{\partial w}{\partial x}\Big)^2 \Big\rangle + \Big\langle \Big(\frac{\partial v}{\partial z}\Big)^2 \Big\rangle + \Big\langle \Big(\frac{\partial w}{\partial y}\Big)^2 \Big\rangle \\
& \left. + 2\left(\Big\langle \Big(\frac{\partial u}{\partial x}\Big)^2 \Big\rangle + \Big\langle \Big(\frac{\partial v}{\partial y}\Big)^2 \Big\rangle + \Big\langle \Big(\frac{\partial w}{\partial z}\Big)^2 \Big\rangle \right) \right\}
\end{aligned} \tag{1.23}$$

Here, the full expansion of the stress terms is provided to again highlight that to obtain the energy dissipation, an important quantity in the Reynolds stress equations, requires the retrieval of all nine velocity gradients from A_{ij}.

1.9 Identification of vortices

Turbulent flows are dominated by coherent fluctuating motion, where the fluctuating motion is organised into vortices. In order to study turbulence, it is imperative that a universal and objective scheme be employed to identify and analyse vortices. Lugt (1983) defines vortices as the rotation of many particles about a common centre. To identify these regions, the velocity gradient tensor A_{ij} is typically used as it is Galilean invariant – that is, the gradients are independent of inertial frames of reference. Specifically, the Q-criterion (Hunt, 1988), which is the second invariant of A_{ij} has been a popular choice of vortex identification:

$$Q = \frac{1}{2}(\Omega_{ij}^2 - S_{ij}^2) \tag{1.24}$$

Positive values of the Q-criterion indicate regions where the rate-of-rotation is greater than the rate-of-strain, and hence the location of a vortex. Dubief and Delcayre (2000) and Chakraborty et al (2005) show that the Q-criterion performs well, although the choice of threshold can be subjective. There have been other notable works that have explored the use of the Q-criterion coupled with other vortex identification techniques. Kolár (2007) suggested a regime that considers the residual of vorticity in a triple decomposition of motion technique that reduces the ambiguity in vortex identification. Kitzhofer et al (2011) provided a wide range of methods in the context of experimental data to establish vortices as well as other flow phenomena. This work will mainly identify vortices by the Q-criterion as it has been shown to perform well and has become somewhat a standard tool for volumetric flow measurements.

1.10 Topology of the invariants of the velocity gradient tensor

The velocity gradient tensor A_{ij} (or rate of deformation tensor) can be further analysed by its utilisation to identify the complex patterns, in all flows. A_{ij} is split into its symmetric and antisymmetric components (as per Section 1.6):

$$A_{ij} = \frac{\partial u_i}{\partial x_j} = S_{ij} + \Omega_{ij} \tag{1.25}$$

The definition for the symmetric and antisymmetric components are provided in Eq. 1.17a and Eq. 1.17b, respectively. The properties and patterns of vortices in all flows can be decomposed in this way and analysed by the eigenvalues and eigenvectors of A_{ij} (Chong et al, 1989). This type of decomposition is a critical point analysis, which enables the features of a complex 3D flow field to be concisely presented by the characteristics of the vortices (Soria et al, 1994). The eigenvalue characteristic equation is:

$$\lambda^3 + P\lambda^2 + Q\lambda + R = 0 \tag{1.26}$$

where,

$$P = -S_{ii} \tag{1.27a}$$

$$Q = \frac{1}{2}(P^2 - S_{ij}S_{ji} - \Omega_{ij}\Omega_{ji}) \tag{1.27b}$$

$$R = \frac{1}{2}(-P^3 - 3PQ - S_{ij}S_{jk}S_{ki} - 3W_{ij}W_{jk}S_{ki}) \tag{1.27c}$$

P is the divergence (Eq. 1.1), and it follows that for incompressible flows, $P = 0$. Q then reduces to Eq. 1.24. Soria et al (1994) and Ooi et al (1999) show the various types of vortices present in an incompressible flow by plotting distribution of Q vs R. An important line on in the Q - R plane is that of where the discriminant $D = 0$. Martin and Dopazo (1998) take a further look at the dynamics of the invariants, and provide further discussion on the implications of various vortex types. These techniques have been mainly confined to direct numerical simulations (DNS) due to the 3D data at fine scales (for example da Silva and Pereira, 2008). With the advent of 3D measurement techniques, these types of analysis have been employed on volumetric experimental data (Khashehchi et al, 2010).

1.10.1 Canonical turbulent flows

The aim of this section is to provide some of the theoretical background for the types of turbulent flows investigated in this work. In Chapter 3, an open channel flow with grid generated turbulence is investigated. Grid generated turbulence has been vital to the study of homogenous isotropic turbulence, and allows a way to compare experimental data with theoretical models. Chapter 4 deals with wall-bounded turbulence, that is, flow along a solid boundary. These types of flows are vital for bluff body drag, heat transfer and turbulent vortex generation. Finally, Chapter 5 investigates a fountain flow, which is a jet flow with a different density to the ambient fluid (or non-zero buoyancy).

1.10.2 Grid generated turbulence

The main aim of grid generated turbulence experiments is to generate homogeneous turbulence and to study its decay. The pioneering work was performed by Taylor (1935); Batchelor and Townsend (1948b,a); Comte-Bellot and Corrsin (1966, 1971). These experiments are particularly important in forming the theories of turbulence decay as they provide a way to reduce the influence of boundary conditions and enabled a turbulence field that could be well controlled.

It was grid generated turbulence and the idea of homogeneous isotropic turbulence at large numbers that arose to Kolmogorov's theory of the decay of energy dispersion (Kolmogorov, 1991)[2]. His results were based largely on the experimental work of Taylor (Taylor, 1935). His key assumptions were of homogeneity and local isotropy (that is in a small region with respect to the geometry of the flow). From there, Kolmogorov proposed a hypothesis of similarity: At sufficiently high Re, the smallest scales of turbulence have statistics determined uniquely by ν and ε. This lead to the length scale of the dissipation of turbulent energy η, defined as

$$\eta = (\nu^3/\varepsilon_B)^{1/4} \tag{1.28}$$

Further to this, a second hypothesis states that for these high Re flows there is an in-

[2]English translation of his original work: Kolmogorov, A. N. (1941) Doll. Aka. Sauk SSSR: 30(4)

termittent length scale range where viscosity is negligible and thus the statistics of the turbulence can be determined uniquely by ε. This is known as the inertial range, shown in Figure 1.1. Performing a dimensional analysis on the energy of the flow and the energy dissipation as functions of the wave number (length scale of vortices), the '-5/3' power law can be derived.

As mentioned in previous sections, these results have been somewhat of a cornerstone in turbulence theory. However there is increasing evidence of turbulence decay that does not follow this power law, but an exponential law (for example Seoud and Vassilicos, 2007). This implies that there is a large influence on the production of the turbulence (by grids, for example), and thus the idea of universality of the turbulence decay has been challenged.

This section is related to the work in this thesis from a theoretical standpoint and also as the flow measured in Chapter 3 may be considered to be generated turbulence. However, unlike classical grid turbulence investigation, this is a 'special' case, most notably by the use of multiple grids. Additionally, the flow is in a flume where boundary effects cannot be ignored (a requirement of kolmogorov's first hypothesis) and it flow field is shown to be non-homogenous, another condition of the power law decay.

1.10.3 Wall-bounded flows

The vast majority of flows of importance to the field of engineering are wall-bounded flows. As the name suggests, these are the flows that result when a fluid flow interacts with a solid surface, or vice versa. At the solid-fluid interface the flow transitions from the velocity of the solid surface to that of the fluid flow and it is within this transition where the flow generates the so-called boundary layer. The study of boundary layers originated in Göttingen in the early 20th century with the pioneering work of Prandtl (Chapter 7, Darrigol, 2005). The boundary layer is critical in the fields of aeronautics, heat transfers, sediment transport and the drag forces experienced by objects immersed in a flow, to name but a few. This section intends to show a brief summary of how the relevant length scales in boundary layers are defined.

The two essential conditions of wall bounded flows are the kinematic boundary condition and the no-slip condition, that must be applied to the Navier-Stokes equations (Eq. 1.5).

Together, they state that the velocity of the fluid at the surface must be equal to the velocity of the surface. With respect to the frame of reference of the solid, both the normal and tangential components of velocity are zero.

In the boundary layer the viscous forces are important. The boundary layer height is denoted $\delta(x) = \delta$, where x denotes the distance downstream in the flow direction (Figure 1.2). The boundary layer is defined as the region where the mean streamwise component of velocity U is 99% of the free stream velocity U_∞ (or U_0). As shown in Figure 1.2, within the boundary layer there are several important regions, and new scaling variables y^+ and δ^+.

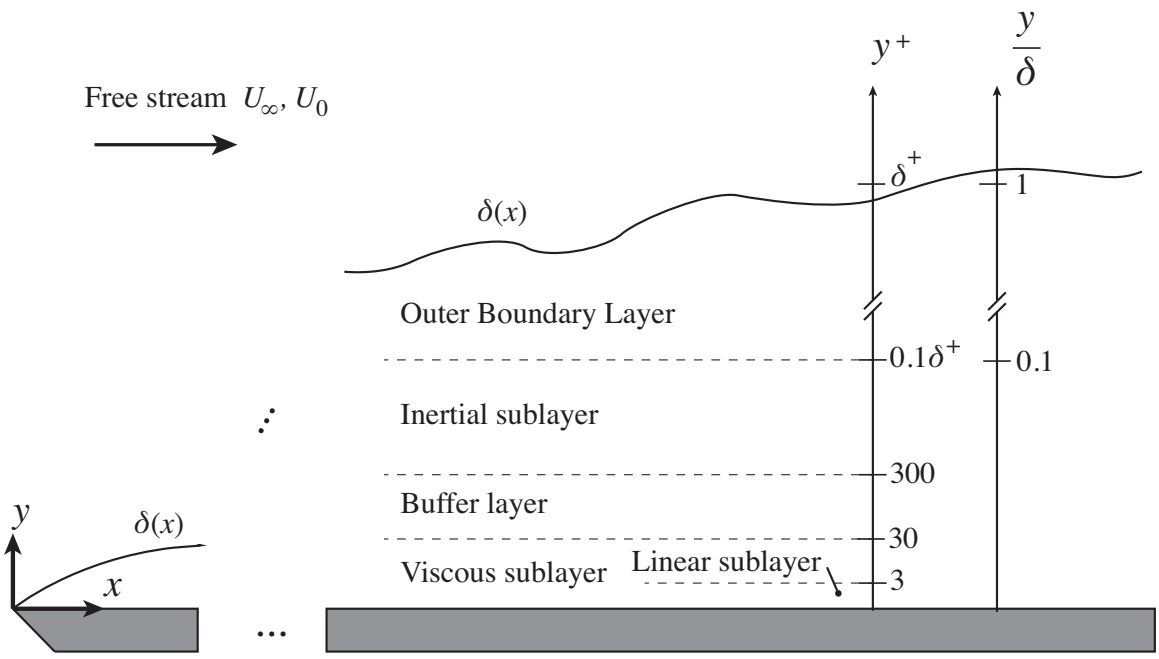

Figure 1.2: Schematic showing the length scales in a turbulent boundary layer (adapted from (George, 2013, Figure 7.2). To the left, the free stream interacts with the beginning of the plate, forming the boundary layer δ. The wall normal y^+ (Eq. 1.29) is shown indicating the distances from the wall of the different regions.

The wall normal y^+ is the dimensionless distance normal to the wall (along the y-axis). The wall normal is commonly used to easily compare the location in the boundary layer and expected regions such as the viscous or linear sublayer, defined as

$$y^+ = \frac{y}{\eta} = \frac{yU_*}{\nu} \tag{1.29}$$

where U_* is the local velocity scaling parameter, or the friction velocity:

$$U_* = \frac{\tau_w}{\rho} = -\langle u_i v_j \rangle + \nu \frac{\partial u}{\partial y} \tag{1.30}$$

where the shear stress at the wall $\tau_w = \mu \partial u / \partial y$. It is the wall shear stress that ultimately dictates important properties for hydraulic and environmental engineers such as sediment transport, and as will be seen in preceding sections is notoriously difficult to measure accurately in experiments. The friction velocity is the local scaling parameter used in boundary layer flows, including the local Reynolds number (Eq. 1.31)

$$\delta^+ = \frac{\delta U_*}{\nu} \tag{1.31}$$

The 'Outer' region (considered to be $y^+ > 30$) is where Reynolds stress terms are important, whereas in the 'inner' region ($y^+ < 0.1\delta^+$) the viscous are important. Note that there is an overlap region where the 'outer' or 'inner' scaling can be be applied. Finally, it should be noted that the magnitude of U_* and δ^+, and thus the flow conditions in the boundary layer) are dependant on the free stream conditions, not the other way around (George, 2013).

1.10.4 Fountain flows

A jet is typically a pipe or conduit type flow being suddenly ejected into a surrounding, larger domain, usually through an orifice or nozzle. A fountain flow is a special case of jet flow where the buoyancy force of the jet fluid opposes its momentum. Chapter 5 presents experimental measurements on the case of fountain flow, where a dense saline solution is injected vertically upwards into an ambient solution of ethanol and water. As the saline solution has higher density than the ambient fluid, it has a negative buoyancy; the fountain fluid wants to sink after it loses its upwards momentum.

In terms of turbulence theory, jets and fountains fall into the category of free shear flows. As the name suggests, free shear implies the shearing of flows in the absence of

solid boundaries. The full turbulence theory behind this large field of turbulence research, and the interested reader should consult Pope (2000); Lesieur (2008) for more details and references on the subject. As mentioned in the Introduction to this work, fountain flows are very important engineering flows. Carazzo et al (2008) lists several specific issues that the study of fountain type flows hopes to address, a few of which include the transport of toxic gases by oil or forest fires, ventilation systems in buildings and climatic impacts of volcanic plumes.

The aims of this thesis is to provide the experimental framework to study these flows in 3D with TPIV, whilst using the valuable experimental data to characterise the turbulence in the flow. Of interest to the field is the fountain start-up (or initialisation), the maximum height the fountains reach and the entrainment and mixing of the fluid.

1.11 Summary of turbulent flows

This section emphasised that turbulence is the fluctuating parcels of vorticity, or vortices, that transport thermal energy, angular momentum and kinetic energy in a flow. From the deterministic equations of motion, the Navier-Stokes equation (or conservation of momentum for a fluid element), were derived. Despite these equations being derived from fundamental principles (that is, the accelerations on a fluid element equated into force divided by mass), proof of the existence and smoothness have not yet been demonstrated.

The contribution of the Reynolds stress to the mean flow equations was analysed, and it was seen that this fluctuating turbulence term could modify the mean flow equations. Although the Reynolds stresses behave as though they were *stresses* (at least from the mean flow perspective), they are properties of the flow. A derivation of the fluctuating part of the Navier-Stokes equations yielded the Reynolds stress equations. This equation showed how various velocity terms were involved in the transport, production and dissipation of the turbulent energy. The mechanism as to how the mean flow provides energy to the fluctuations was also shown.

An overview on the origins of turbulence was presented that showed how the non-linear terms of the Navier-Stokes equations could intensify perturbations. It was then demon-

strated that the vorticity generation and transfer across length scales was due to the vortex stretching mechanism. The range of length scales in a turbulent flow increases proportionally to Re. In order to standardise discussion, turbulence quantities were defined. Finally, methods to locate and characterise vortices in a turbulent flow were shown to be based on the velocity gradient tensor, a convenient choice due to its Galilean invariance.

This thesis will focus on an experimental technique that can retrieve the instantaneous velocity gradient tensor A_{ij} in turbulence flows. With an appropriate number of statistically independent realisations of the flow, the mean and fluctuating velocity gradients can also be computed. This chapter has presented some of the fundamental properties of turbulence that will be of interest to better understand the environmental flows.

Chapter 2

Particle Image Velocimetry (PIV)

2.1 Introduction

Before the advent of whole field measurement techniques, quantitative measurements of flow velocity were conducted by probes such as hot wires or with laser diagnostics approaches, such as laser Doppler velocimetry (Adrian and Westerweel, 2011). The advantages of these point measurements is that they are generally accurate and have a high frequency response that can record the smallest important timescales in turbulence (Sect. 1.7). Point measurements unfortunately cannot give any information about instantaneous flow structures or spatial derivatives (from a single probe), that have been shown to be vital in understanding the dissipation of turbulent energy.

Particle Image Velocimetry (Dudderar and Simpkins, 1977; Adrian, 1984; Willert and Gharib, 1991) (PIV) is a mature and popular technique for measuring a vast range of fluid flows in lieu of point measurements. The imaged motions of tracers dispersed in the fluid yield a field of instantaneous velocity vectors. The emergence of PIV as to its widespread use is in part due to the increase and improvements in technology and introduction of digital cameras, illumination sources and computers (Raffel et al, 2007). This section aims to highlight the key PIV technology with relevant technical importance to all 3D PIV techniques. For more technical and historical information the reader is referred to the texts of Adrian and Westerweel (2011), Boutier (2012) and Raffel et al (2007). In the following

sections, only high image density, double frame PIV is considered. That is, PIV that requires statistical methods to determine the displacement of groups of particles, and each time step is recorded on separate images.

2.1.1 Working principle of PIV

PIV is an optical technique that indirectly measures fluid flows by capturing the movement of particles that are travelling within the flow. The particles that are selected must faithfully follow the flow and when illuminated, scatter sufficient light in order that they can be captured on a camera sensor array. Assuming that the added particles do not change the properties of the fluid or the flow being measured, PIV is a non invasive measurement technique that can determine whole field velocity data.

Figure 2.1 is an adaptation from *Dantec* that shows a schematic of a 2D PIV system. The PIV process can thus be summarised in seven key steps:

1. The flow is seeded with small spherical particles, typically 1 – 5 μm in diameter for experiments in air and 10 – 100 μm in water.

2. The particles are illuminated with a light sheet in two short pulses separated by a small amount of time Δt, typically in the order of micro-seconds but dependent on flow speed and the imaged particle displacement.

3. The particle images are synchronously recorded with a digital camera, historically on a CCD[1] for two-pulse measurements or CMOS[2] for time-resolved.

4. The resulting images are pre-processed (filtered) to remove background noise and improve particle images.

5. Corresponding sequential interrogation windows (*IW*s) are cross-correlated to find the location of the highest probability of particle *pattern* displacement, $\Delta\mathbf{x}$.

6. The velocity is calculated at each *IW* location, $\mathbf{u}(x,y) = \Delta\mathbf{x}/\Delta t$

[1] Charge-Coupled Device

[2] Complementary Metal Oxide Semiconductor

7. The velocity fields are post-processed to remove and replace spurious vectors.

2.1.2 Technical and economic considerations

Most flow measurements involve an optimal compromise between available technology (typically cost limited) and the type of measurements to be made. By and large these considerations are transferrable to other PIV techniques. The following lists several driving considerations.

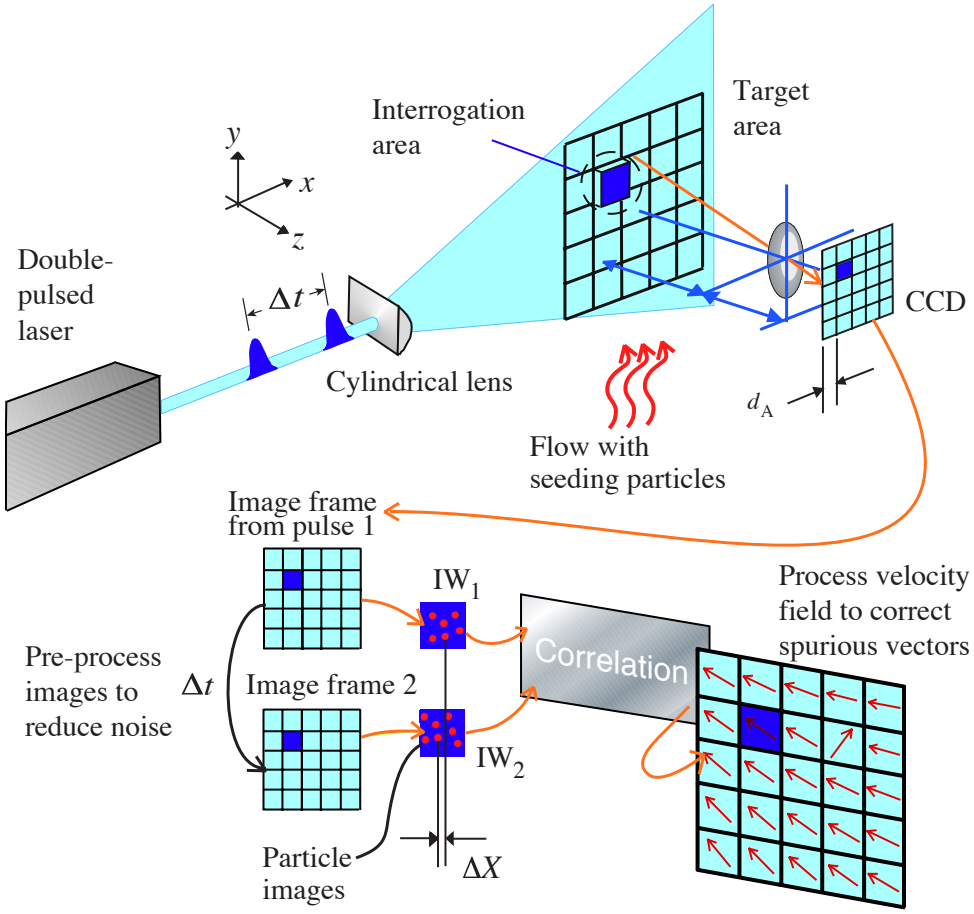

Figure 2.1: PIV process schematic: A light sheet illuminates particles in the flow at two instances. The illuminated particles are imaged onto a digital camera sensor, and by cross-correlation of corresponding interrogation windows (*IW*s), the velocity field is found. Adapted from *Dantec*

- The particles must be small enough to follow the flow faithfully but large enough to be sufficiently illuminated with the available laser power to be captured by the cameras (Boutier, 2012).

- Δt should be selected so that there is sufficient particle displacement to increase accuracy but not too large so that the particles within corresponding *IW*s have diverged from the initial imaged pattern or a portion of them leaving the light sheet introducing random noise (Raffel et al, 2007, p93). Keane and Adrian (1992) proposed that the particle displacement not exceed 25% of the interrogation window size, however if there is a mean flow or iterative/multigrid correlation scheme (described in the following points) this parameter can be relaxed, so long as the quasi-stationary particle motion is not violated.

- The particle images should be a minimum of 3-5 px in diameter to avoid peak locking but too large a diameter can lead to over exposing the particle images and broad correlation peaks (Prasad et al, 1992).

- *IW* size is selected so that the highest resolution as possible is obtained while maintaining at least 5–10 particles in each *IW* to ensure a strong correlation peak (Adrian and Westerweel, 2011).

- Multi-pass algorithms (Soria, 1996) and deforming *IW* (see for example the window displacement iterative multigrid – WIDIM – algorithm by Scarano and Riethmuller, 1999) can improve resolution at the expense of computational effort.

- Appropriate vector processing is required to remove noise and erroneous/spurious vectors, such as an objective median filter (Westerweel et al, 2002), but they are only appropriate to use if there are at least 90% valid vectors.

- The resolution of the measurements can be improved by a post-processing stage known to obtain 'super resolution' data. Two prominent methods to achieve super resolution are as follows.

– Use the PIV vector fields as a basis for tracking the individual particles in a hybrid PIV – particle tracking process (Keane et al, 1995; Stitou and Riethmuller, 2001).

– From the WIDIM approach, Scarano (2004) retrieved non-linear (curved) displacements between IWs from the second order spatial derivatives which improved spatial resolution.

2.2 Towards three component three dimensional (3C3D) PIV

In Section 1.1, the 3D nature of turbulent flow was highlighted. It was therefore natural that experimentalists wanted to retrieve the full three components – three dimensional (3C–3D) velocity data from PIV. More importantly, it is the full velocity gradient tensor which is required to resolve the turbulence equations. As will be seen, determining the position of a particle image in the third dimension has higher uncertainty and is more challenging than the in-plane components. This section gives a brief overview of the prominent methods that have been developed to obtain 3C and 3D velocity data. For more technical information the reader is directed to Maas et al (2009) and Arroyo and Hinsch (2008) and the references therein, along with the works of Adrian and Westerweel (2011) and Raffel et al (2007).

2.2.1 Stereo PIV

Stereo PIV (SPIV) (Arroyo and Greated, 1991; Prasad, 2000) uses the principles of stereo vision to obtain the third, out-of-plane velocity component w in a '2D' plane. The recovery of w is accomplished with the addition of a secondary and unique viewing angle. '2D' in this sense seems oxymoronic, as the technique captures particle movements normal to and within the light sheet. However, the z-coordinate is constant and is typically the centre of the laser sheet. Figure 2.2 compares 2C PIV with Stereo PIV. Both methods show the measurement of an identical particle with coordinates $\mathbf{x}_\mathrm{p} = f(x,y,z,t)$ between two time steps in the laser sheet, of thickness Δz_0. Lower case coordinates refer to the global

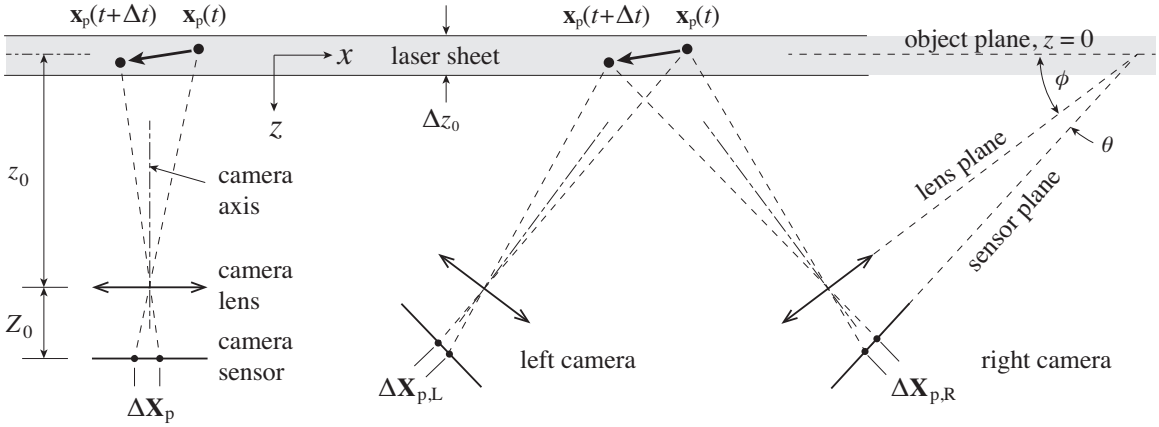

Figure 2.2: Comparison of 2C PIV with normal viewing orientation (left) with Stereo PIV (right). The stereo set-up typically requires an additional camera to obtain a second, unique viewing angle to resolve the out of plane movement.

coordinates and upper case refers to the local camera coordinates. The angle θ between the lens and sensor planes, along with the angle ϕ between the lens and object planes, are chosen to achieve the Scheimpflug condition. The Scheimpflug condition ensures that the focal plane and object plane are coplanar, and hence all particles within the light sheet are in focus.

Figure 2.2 shows that the displacement of $\mathbf{x}_p$ results in a displacement $\mathbf{X}_p$ on the camera sensors. For the 2C PIV setup on the left, the out of plane motion is irrecoverable. However, combining the unique viewing angles of the cameras in SPIV, the out of plane motion can be measured. The cameras must be accurately calibrated in order to correctly perform the out of plane calculation (Calluaud and David, 2004; Wieneke, 2005). The effect and sensitivity of inaccurate camera calibrations were quantified by Scarano et al (2005), who then proposed a correction technique to retrieve an ideal calibration.

There have been many studies where stereo PIV has been used to characterise turbulence. To calculate the energy dissipation, however, an assumption of isotropic turbulence must be made (Calluaud et al, 2011). The isotropic assumption requires that the velocity gradients that cannot be measured are set to the gradients that can be measured. Stereo PIV has also been used to successfully identify coherent structures (Sousa, 2002). The full velocity gradient tensor in a jet flow was measured by Ganapathisubramani et al (2007),

however to obtain the out-of-plane gradients required an assumption of frozen turbulence. Buchmann et al (2011) were able to visualise structures in a turbulent boundary layer by having the laser sheet plane normal to the mean flow direction and, by utilising a stationary turbulence hypothesis, low speed streaks and vortices were captured. These assumptions are valid for homogeneous isotropic turbulence, but for other flow types (open channel flows, shear flows, wall bounded flows, etc.) the limits of the assumption must be validated given expected time and length scales of the turbulence.

2.2.2 Multi-plane PIV

In an effort to increase the data yield from SPIV, Multi-Plane PIV (MP-PIV) (Kahler and Kompenhans, 2000) was developed. The typical MP-PIV set-up is composed of essentially two independent stereo PIV systems (2.3). The two (or multiple) laser sheets are parallel and offset by a small distance s. The technique typically relies on the polarity and collimation of laser light, so that the two laser sheets can be fired simultaneously, but by way of polarisation filters, each imaging system captures only one plane. Kahler and Kompenhans (2000) investigated additional timing regimes optimised for either in-plane or out of plane flows. A similar system was used by Mullin and Dahm (2005) who used a 532 nm (green) and 635 nm (red) laser sheet acquired with two independent SPIV systems enabling the full velocity gradient to be obtained.

The knowledge of the distance s is critical for the calculation of the out of plane gradients. For example, Ganapathisubramani et al (2005) used a laser burn technique to determine that there was an uncertainty of 8% on s. This uncertainty culminated into errors in the out of plane gradients ranging from 9% to 24%.

Liberzon et al (2004) used a 3-plane system termed XPIV. It uses multiple laser planes, such as in Sect. 2.2.2 but also defocusing techniques based on the particle images (explained further in Section 2.2.7). XPIV is limited by the overlap of images, particularly by the larger blurred images in the out-of focus planes. Anther notable and novel use of a multi-plane system was by Foucaut et al (2010), who had the second plane in an orientation normal to the first. In this way, 3D turbulent structures in a wall bounded flow were constructed, assuming that the structures were 'frozen' as they progressed downstream.

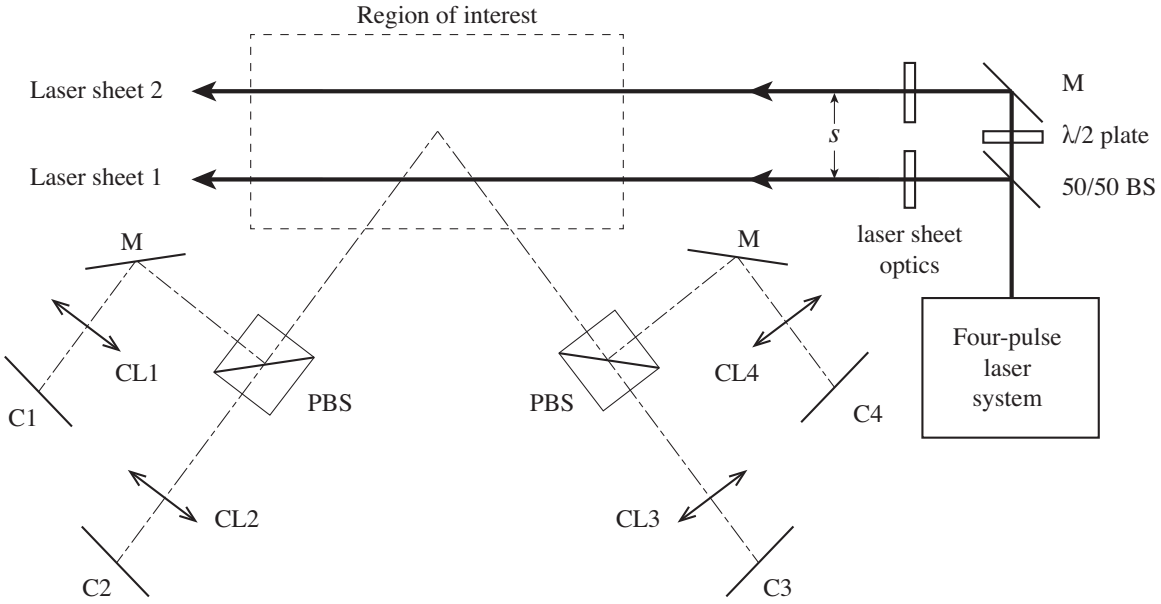

Figure 2.3: Principle of MP-PIV. Laser sheet 2 is translated s normal to laser sheet 1 and has polarisation rotated 90° by the $\lambda/2$ retardation plate. Polarising filters enable the two camera systems (C1 & C4 and C2 & C3) to capture the particle images in each plane. Definitions: C, camera; CL, camera lens; M, Mirror; BS, beam splitter; PBS, polarising beam splitter.

MP-PIV typically requires four cameras and a sophisticated experimental setup compared to stereo PIV, to attain the out-of-plane velocity gradients ($\partial/\partial z$). The limitation is that there can only be one or two planes of this out-of-plane gradient information, which can restrict the analysis of vortices with in-plane axes. As will be seen in Section 2.2.6, a newer, simpler four camera set up (namely, TPIV) can retrieve volumetric velocity fields, and hence the full velocity gradient tensor.

2.2.3 Scanning PIV

Scanning PIV uses a mechanical means to rapidly sweep parallel laser sheets across the measurement volume. Rather than a single plane obtained with PIV, the laser sheet is sequentially translated in its normal direction at a number of discrete locations n_s. Generally,

one velocity field requires two complete scans. For the first sweep, the imaging system acquires an image of the flow at each translated laser sheet position. So long as the time scale of the laser sweep is significantly smaller than that of the flow, a sequence of one complete scan results in a series of *quasi* instantaneous images of the volume. The process is repeated again to obtain the second exposure of PIV images. Considering the modern adaptations where there is one laser pulse per image, Scanning-PIV has two independent time-scales to account for: the PIV-specific time frame between full sweeps Δt, and the duration of a complete scan to the end that the flow is frozen T_{scan} (Brücker, 1995).

After the acquisition, the post processing treatment of the scanning PIV can be considered in two ways: each image can be treated as a separate PIV, SPIV or 2D particle tracking image (for example Brücker and Althaus, 1992; Brücker, 1997; Hori and Sakakibara, 2004), or images can be used to reconstruct the particle positions in space and then be treated as a volumetric method where cross-correlations occur in 3D interrogation volumes (*IV*s) (David et al, 2011). The latter case is termed scanning tomographic PIV. Tomography is a term that up until recently was mainly associated with medical science and computed tomography (CT). In strict adherence to its etymology, tomography is the reconstruction of an object from multiple sections. In this case, each scan location provides a unique section of the object to be reconstructed.

Scanning PIV has several advantages over other volumetric techniques (discussed in the subsequent sections). As the volume is illuminated by a thin sheet, theoretically higher seeding concentrations are possible. Lower laser power is generally required as the illumination is not distributed into a volume and the technique can also be used with in conjunction with other techniques that rely on planar measurements such as laser induced fluorescence (for example Berchet et al, 2013).

A disadvantage of this technique is its ability to obtain a *quasi* instantaneous reconstructed volume, which becomes increasingly difficult as Re increases. This limitation is compounded in that an increase in flow speed would require a higher repetition rate laser and an imaging system capable of recording at very high frequency. For equivalent Re, a volumetric technique must only abide by the Δt for PIV considerations, where the minimum laser frequency is loosely proportional to $1/(n_s \Delta t)$. Finally, the reconstructed particles can

be elongated in the z-direction as a result of the particles being illuminated and imaged in multiple planes during the sweep (Thomas et al, 2011). This elongation can affect the accurate determination of the out of plane velocity vector.

2.2.4 Holographic PIV

Holography is the technique of producing 3D images, or holograms, of a light field. A hologram is made by capturing both a reference light beam and a light disturbed by the object(s) to be recorded. Figure 2.4 shows the two stages of an off-axis holographic PIV (HPIV) reconstruction procedure (see for example Meng and Hussain, 1995; Pu and Meng, 2000). A collimated light source, such as a laser, is required to create the hologram. An undisturbed reference beam creates a regular interference pattern on a holographic plate. Simultaneously the particles are illuminated and the scattered light from the particles also creates an interference pattern on the plate. By passing the reference beam back through the holographic plate, the hologram of the particles is created: a 3D light field is created where the particle positions are recovered. From these recovered particle intensities, a series of 2D scans (or images) of the volume can be made, and hence the particle locations are digitised. With two sequential volumes of particles separated by a small time Δt, a volumetric cross-correlation can yield full volumetric data and the full velocity gradient tensor.

The data yield in experiments can be extraordinary: For example, 800 000 vectors were calculated in experiments by Zhang et al (1997) using a hybrid HPIV system. HPIV took a leap forward when the holographic images could be stored on CCD arrays directly (Meng et al, 2004), albeit at lower resolution than their wet film counterparts. Adaptions of the wholly digital technique have been reported on by Soria and Atkinson (2008), with their in-line HPIV set-up. The authors were able to digitalise the process and remove uncertainties in the plate normal direction and particle elongation with the addition of multiple cameras at various varying orientations around the region of interest. Additionally, the holographic reconstructions could be performed computationally.

The experimental set-up of holographic PIV is not straight forward or inexpensive. For further reading, see the review article of Hinsch (2002) that draws from over 60 references

on the topic. The most severe limitation to Digital HPIV is the limitation to the size of the region of interest (ROI) and at least for the off-axis method, the experimental set up must be maintained to recover the particle positions.

2.2.5 3D Particle Tracking Velocimetry (PTV)

3D PTV is a technique that aims to locate the positions of particles in space and then calculate their trajectory. 3D PTV is a technique akin to the second super resolution approach to planar PIV discussed in Section 2.1.2. One seminal work (Maas et al, 1993) utilised triangulation from multiple camera viewing directions to determine the 3D location of the particles. Various algorithms were subsequently developed to track their trajectories.

Another early and novel 3D PTV technique is termed Defocusing PTV (Willert and Gharib, 1992): its original experimental arrangement consisted of a single camera with an axis-symmetrical three pin-holed aperture. The effect of the modified aperture was that a particle in focus (i.e on the object plane) was imaged as a single *particle* and those particles that were some distance away from the reference plane (i.e. out of focus) were recorded as an equilateral triplet. This process is represented in a 2D case, where the out of focus particle B forms an image pair as a result of imaging through a two pin-holed aperture in Figure 2.5. If B is on the far side of the focal plane, the imaged particles B_i' again form a

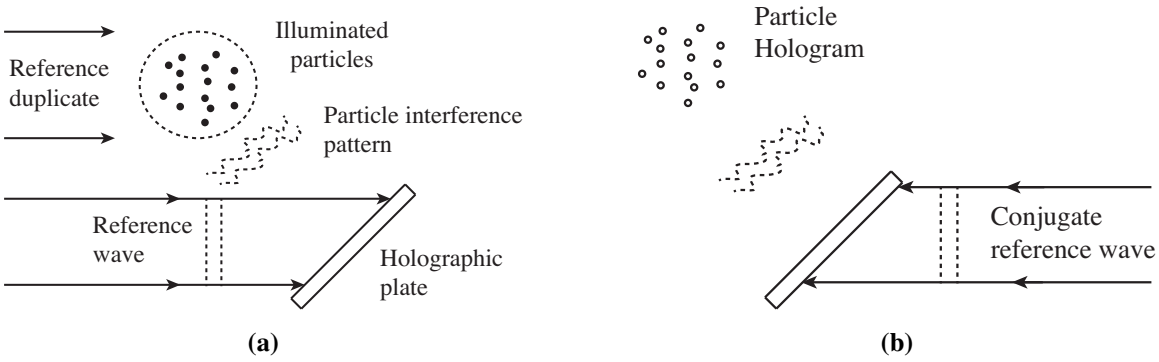

Figure 2.4: Principle of (a) recording and (b) reconstructing particle distributions with off axis holographic PIV. The particle hologram is then typically sampled in translated 2D planes

pair for the 2D case. However, for the real 3D case the triplet would be inverted and hence there is no positional ambiguity for near or far field imaging. The distance between the apexes of the triangles that were identified as a triplet (representing one particle) is thus a function of the particle's out-of-plane position.

Defocusing PTV was further developed by Pereira et al (2000); Pereira and Gharib (2002). Those authors utilised three cameras with parallel axes positioned at the apexes of an equilateral triangle in place of the three holed aperture. This enabled an increase in particle seeding density as there is less particle image overlap. Another improvement to the single camera method was made by Tien et al (2008), who used a colour coded aperture pattern to facilitate simpler particle triplet detection.

Defocusing PTV has been shown to be able to retrieve 3C–3D flow fields, however the great hindrance to its progress is the maximum seeding density that can be used. Over-

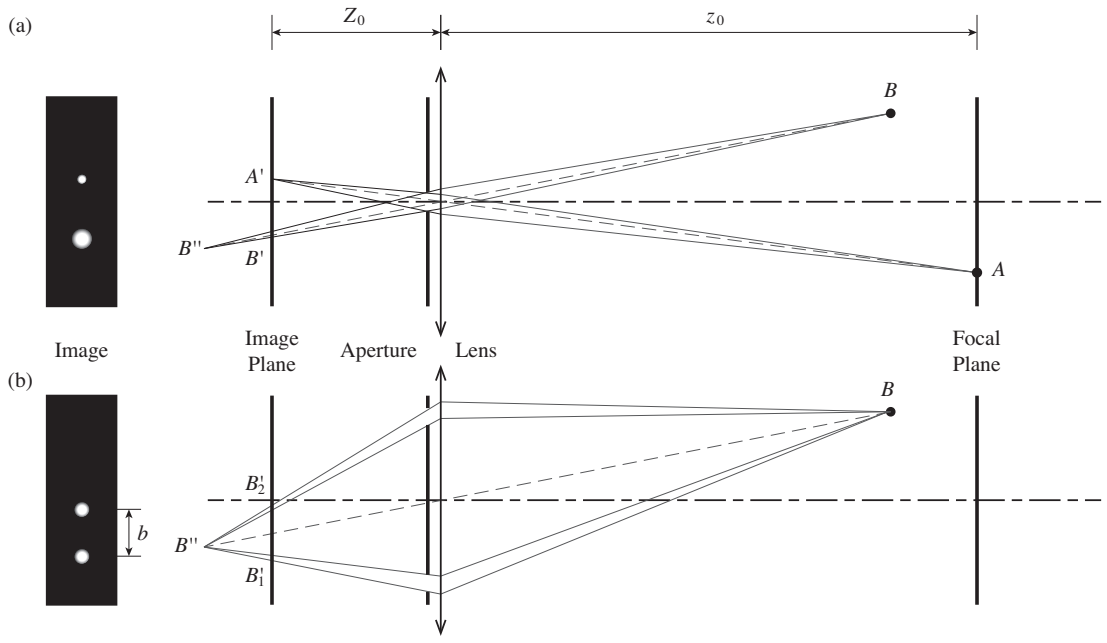

Figure 2.5: Schematic of the working principles of Digital De-focusing PIV. (a) shows how in- and out-of-focus particles are imaged through a single aperture camera. (b) highlights how in a 2-aperture model, a single out of plane particle makes two particle images. The spacing between them b is a function of the z coordinate of the particle. Adapted from Pereira and Gharib (2002)

lapping particle images, proportional to seeding density, are detrimental to locating unique particles, which is integral to the technique. The errors in the out of plane position have been 1.5% of the depth of field compared to 0.15% for the in plane measurements (Tien et al, 2008).

Recently, Wieneke (2013) introduced a novel particle tracking approach termed Iterative Particle Reconstruction (IPR). IPR is a particle tracking method in the sense that particles are represented by their location (x, y, z), intensity and radius. The iterative procedure is based on reducing the residual error between the acquired images and the re-projections of the particles by updating the projected particle locations, intensities and radii incrementally. The IPR method was shown to be robust for particle seeding densities of 0.05 particles per pixel (ppp), with a high accuracy on the particle positions reported and similar computational times compared to TPIV (see Section 2.2.6). Schanz et al (2013b) adapted the IPR method into a time-resolved particle tracking method. The method utilises the calculated particle trajectories from several acquired sequential time-steps of IPR. The trajectories are then used as predictors for particle locations in subsequent time-steps, which are then used as an initialisation step to enable the IPR method to more rapidly converge to the particle distribution. Compared to the 3D PTV methods above, these methods allow a greater seeding density with a high percentage of real particle tracks being reported.

2.2.6 Tomographic PIV

Tomographic PIV (TPIV) aims to reconstruct the volume of particles that have been imaged on multiple camera arrays from unique viewing directions. The reconstruction equations of Herman and Lent (1976), which reconstruct objects from limited viewing angles, were first incorporated into PIV measurements by Elsinga et al (2005b), with a seminal paper the following year (Elsinga et al, 2006b). TPIV reconstructs particles in a 3D volume based on their line-of-sight projections from the digital cameras that recorded them. This is a fundamental difference to scanning tomographic PIV that reconstructs the particle distribution from multiple recorded scans (Section 2.2.3). The 3D velocity field is then obtained similarly to the other volumetric techniques: the volume is divided into IVs and corresponding and sequential IVs are cross-correlated to find the most probable displacement, from which

the velocity vector is calculated.

The simplified TPIV process is presented in Figure 2.6: (from top left) particles in the flow are recorded by multiple cameras related to each other geometrically via accurate calibration; the images are pre-processed to remove noise and enhance the particle images; the volumes of particles are obtained by tomographic reconstruction (see Sect 2.3.1); 3D cross-correlation of the corresponding *IV*s yields the 3C–3D velocity field.

TPIV has the advantage that the experimental set-up is comparatively simple compared to other volumetric techniques such as Holographic PIV, Scanning PIV and MP-PIV – in its simplest form, TPIV requires no moving parts nor accurately aligned polarising filters. Compared to 3D PTV techniques, TPIV offers relatively high particle concentrations, which can lead to an increase in the spatial dynamic range (SDR) through the use of smaller *IV*s. Additionally, the volume of particles is simultaneously illuminated and the region of interest is dependent not on the sensor size but the camera optics.

In comparison to the aforementioned 3D measurement techniques, TPIV emerges as a promising volumetric technique. As such, this method is employed to measure the environmental flows described in this work. The working principles of TPIV will be detailed in Section 2.3.

2.2.7 Other volumetric PIV techniques

This section aims to address some other novel and recent optical techniques that have been developed with the aim of determining 3C-3D velocity fields of fluid motion. For brevity, only the principle of the determination of the third dimension is described. Following this, a 3D correlation or tracking technique is used to extract the velocity fields.

Hain et al (2009) introduced a one camera technique to determine a particle's three dimensional location. Astigmatism in the particle images (the tendency for particles to have ellipsoid shape due to off axis viewing) is utilised to determine each particle's 3D location. The technique showed a reasonably large error in the z component (5.4% of measurement depth). For this reason, the authors concluded that the technique is better suited for experiments with limited optical access or for micro-PIV. A single camera volumetric correlation PIV technique was adopted by Fouras et al (2009) that was also applied to micro-PIV data.

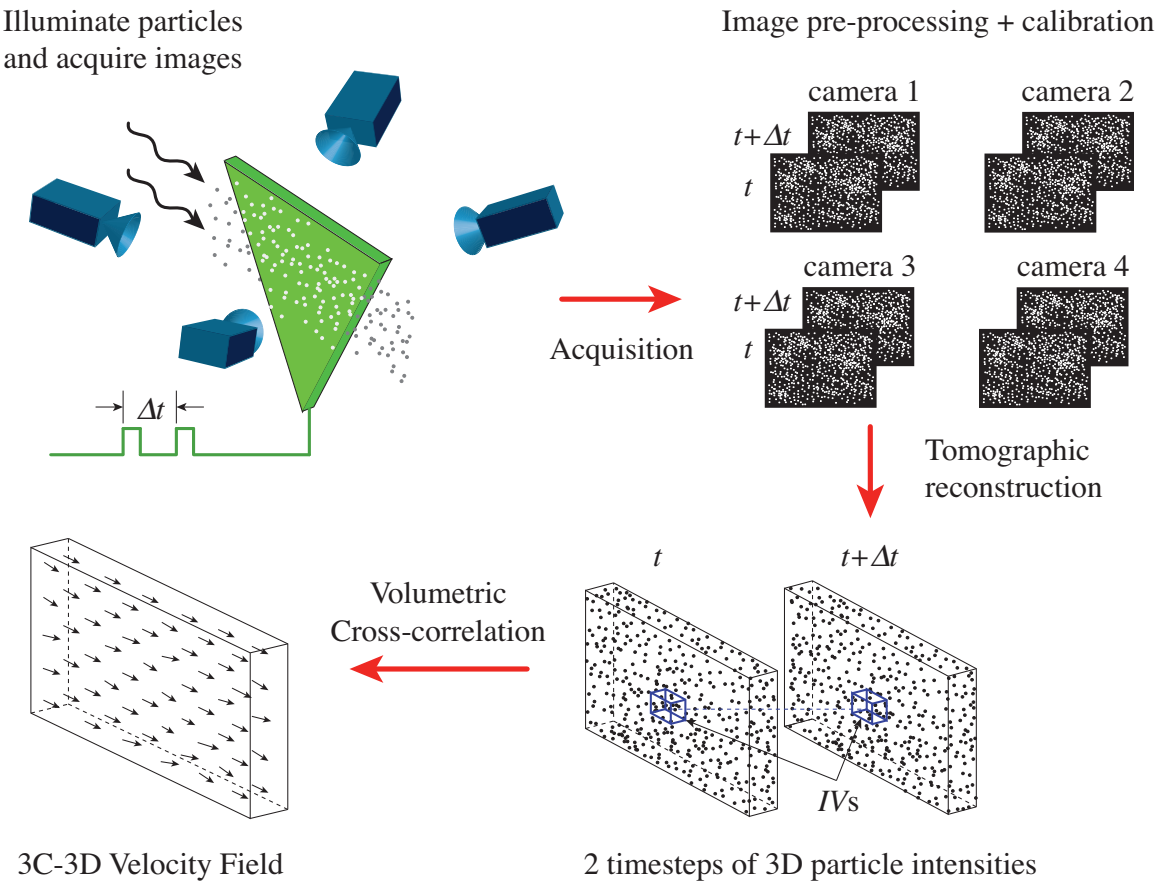

Figure 2.6: Primary features of tomographic PIV (TPIV) process. Adapted from Elsinga et al (2006b)

Belden et al (2010) introduced synthetic aperture PIV (SAPIV). This technique is in an emerging domain of *light field imaging*. SAPIV uses multiple camera arrays (8–25) to image the particles illuminated in a measurement volume. The images are then post-processed to re-focus the particles so that their z location is found. The authors' simulations showed that the technique is able to accurately reconstruct high particle densities (ppp = 0.125 with reconstruction quality of 71%), however experiments were only validated with a ppp of 0.026. At present, it seems difficult to justify the technique over the use of a higher number of cameras in a TPIV experiment, as employed by Schröder et al (2011)

2.2.8 Summary of 3D PIV methods

The push for volumetric measurements has stemmed from the desire to resolve turbulent flows in three dimensions to obtain spatial velocity gradients. Numerous techniques are available that have been described along with some indication of the results that can be obtained and their limitations.

TPIV is perhaps the most versatile of the techniques. It can capture a full volume at high Re simultaneously (as opposed to scanning PIV), it can have a relatively high particle density (compared to PTV techniques), a large region of interest (compared to HPIV), minimal complexity (compared to MP–PIV and multi-camera HPIV) and no inference about frozen turbulence needs to be made (like in time resolved SPIV). Therefore, TPIV has been employed to investigate the experimental environmental flows presented in this work.

2.3 Working Principles of TPIV

This section aims to provide an overview of the working principles of TPIV. Scarano (2013) recently published a thorough review of TPIV with a large reference list that may be of interest for further reading. In addition, the work of Thomas et al (2014) thoroughly investigates a large range of tomographic reconstruction parameters.

2.3.1 Principle of Reconstruction

TPIV yields 3C-3D velocity fields from the reconstruction of particles in space. To aid the description of the reconstruction process, the 2D TPIV acquisition and reconstruction in Figure 2.7 is considered, which is similar to descriptions of the process in Elsinga et al (2006b). A single plane of the 3D volume is presented to simplify the visualisation, without loosing generality. The cameras are considered to be infinitely far from the measurement domain, which implies that the lines-of-sight (LoS) from particle or voxel to pixel are parallel. The cameras have been calibrated (discussed further in Section 2.3.2) so that a 3D point in space of coordinates (x,y,z) can be imaged on a camera sensor $I_c(X,Y)$ by multiplication with the camera matrix.

Figure 2.7a shows the instant that particles in the flow are recorded by the cameras. The light scattered from them by the laser are linear rays to the camera sensor. The particles are imaged as 2D Gaussian spots, but not necessarily axisymmetrically (Schanz et al, 2013a). After the images are acquired, the flow moves the particles onwards, and hence the information about their location is stored on a number of 2D arrays.

Re-projecting the LoSs of the particle images directly back into the flow domain retrieves the particle locations (Figure 2.7b). However, as the LoS of one particle image intersects with multiple LoSs from other cameras, reconstruction artefacts known as *ghost particles* are also recovered. With a simple re-projection such as this, it is impossible to distinguish between the real and ghost particles (more discussion on ghost particles is presented in Section 2.3.6). Figure 2.7(c) shows the discretisation of the volume into regular voxel elements. Voxels have an energy level denoted $E(\mathbf{x}_j)$, where j is an index and N_j is the total number of voxels. Similarly, there are a total of N_i pixels on each camera that have an intensity $I_c(X_i,Y_i)$, with i an index number on each camera number c.

The tomographic reconstruction can be modelled as a set of linear equations of the form $Ax = b$ (Petra et al, 2009). Therefore, from the previous definitions and in conjunction with Figure 2.7, we obtain

$$\sum_{j \in N_i} w_{i,j} E(\mathbf{x}_j) = I(\mathbf{X}_i) \tag{2.1}$$

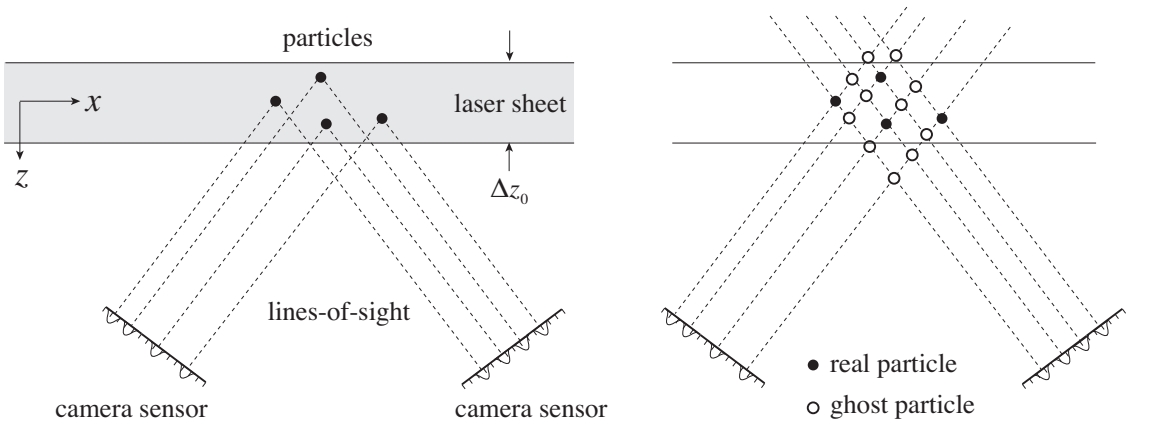

(a) Acquisition

(b) Re-projection

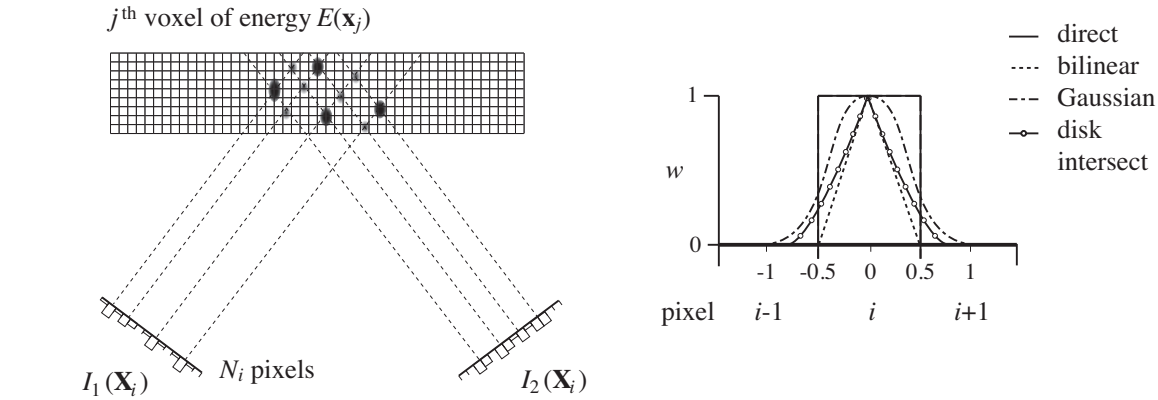

(c) Tomographic Reconstruction

(d) Weighting Functions, $w_{i,j}$

Figure 2.7: Definition of the TPIV reconstruction problem by a simplified 2D model: (a) The images of particles are recorded on two cameras, the position of which determined by their line-of-sights. (b) Re-projecting the particle images along their line-of-sights results locates the particles but also a number of artefacts or ghost particles. (c) Discretisation of the measurement region into voxels, showing that particles occupy a neighbourhood of voxels. After several iterations of a multiplicative algebraic reconstruction algorithm (see Section 2.3.3), the ghost particles tend to have relatively less intensity. (d) Four examples of weighting functions that relate the voxel and pixel energies.

where $w_{i,j}$ is a weight coefficient, and N_i are all of the voxels in the LoS of the ith pixel (see Figure 2.8). As a voxel is projected onto a pixel, $w_{i,j}$ will take a value between 0 and 1 depending on where the LoS intersects the pixel.

Four examples of weighting functions w are shown in Figure 2.7(d). The presented functions have a nominal width of one pixel, however this is a generalisation and not necessarily a requirement. The *direct* method results in 1 if the LoS falls onto the pixel and 0 if not. The *bilinear* method reduces the contribution of a voxel onto a pixel linearly from the pixel centre to its edge. The *Gaussian* method computes w from a Gaussian distribution with a kernel size typically equal to half a pixel length. Atkinson and Soria (2009) used the *disk intersect* method by considering the pixel to be a circle of equal area to the pixel and $w_{i,j}$ calculated as the intersection of a cylinder (3D LoS) through a sphere (Lamarche and Leroy, 1990). The weighting functions can be approximated with a polynomial to reduce computational load.

Early investigations stored a large weighting matrix, but recently calculating w on the fly has shown to give fast reconstructions and importantly it avoids the calculation of a large *weighting matrix*. A weighting matrix is a sparse matrix storing all of the weighting values for each voxel to pixel. Atkinson and Soria (2009) estimated that such a matrix stored in its entirety could require 520 TB, or as a sparse matrix only considering smaller neighbouring subregions, ~ 5 GB. Calculation on the fly further reduces the RAM requirements enabling calculation of multiple reconstructions simultaneously on desktop computers.

Equation 2.1 is ill-posed: I and w are known (the particle images and the geometric relation between camera and voxel space, respectively) but the particle intensity distribution in the voxel space E is not. To this end there are several algorithms that invert the problem in order to find E, discussed in the next two sections.

2.3.2 Camera Calibration

Accurate camera calibration is integral to TPIV: without an accurate camera calibration, the imaged particles' LoSs would not intersect in the volume, and no real particles would be reconstructed. The aim of camera calibration is to map the real world coordinates onto the 2D camera sensor. Experimentally, images are acquired at incremental translations of a

calibration plate through the measurement volume. The result is a series of imaged points (X,Y) corresponding to real world 3D locations (x,y,z). To determine the relationship between them, the 3×4 camera calibration matrix $\mathbf{M}$ is computed from a least squares minimisation or similar approach.

$$\begin{pmatrix} X \\ Y \\ S \end{pmatrix} = \mathbf{M} \begin{pmatrix} x \\ y \\ z \\ 1 \end{pmatrix} \tag{2.2}$$

Once $\mathbf{M}$ is known, any given voxel $E(\mathbf{x}_j)$ can be mapped onto I_c by a simple matrix multiplication. The calculation of $w_{i,j}$ is thus a function of $\mathbf{M}$. The full calibration and calibration correction process is further described in Appendix B.

2.3.3 Reconstruction Algorithms

This section briefly outlines the reconstruction techniques that can be employed by inverting Equation 2.1. Common to all of the following algorithms is the term $\sum_{j \in N_i} w_{i,j} E(\mathbf{x}_j)$, which is shown schematically in Figure 2.8. The term is the weighted contribution of all of the voxels' energy that project onto the *i*th pixel. The algorithms work under the premise that the intensity of a pixel is equal to the sum of the voxels in its LoS. The voxels in this term are shown in shades of grey, representing the weighting coefficient for that voxel (note that the *direct* method would yield uniform grey for the weighting contributions for the nearby particles). In the following algorithm definitions, k represents a number of iterations. One iteration is complete when all of the voxels in E^k are updated to E^{k+1} after considering all pixels from all cameras. In the following, μ is a relaxation factor that can be used to adjust the speed or severity of convergence of the algorithms.

ART The ART (Algebraic Reconstruction Technique) (Gordon et al, 1970) updates E by subtracting the LoS contributions from the measured image intensity and dividing by the sum of the squared weights (Eq 2.3). The algorithm behaves as an OR operator, and hence the voxels in a non-zero pixel's LoS (shaded voxels in figure 2.8 cannot

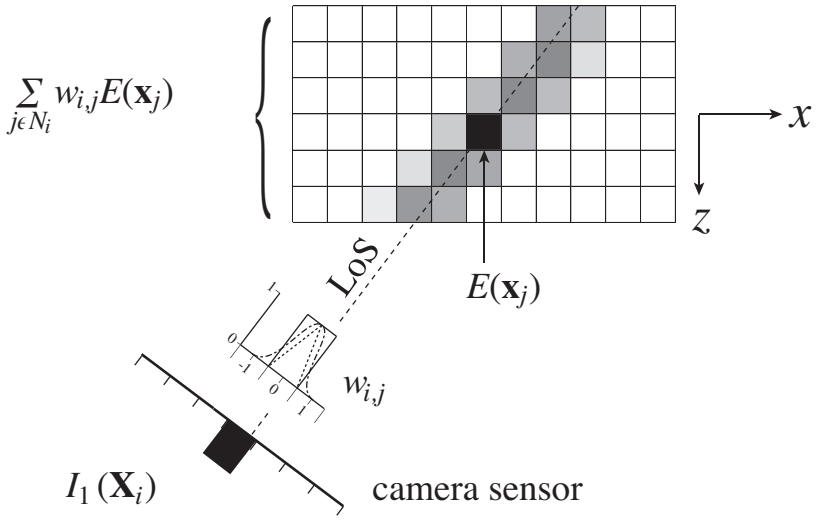

Figure 2.8: TPIV algorithm considerations. The j^{th} voxel of energy E (shown in black) is projected onto the camera and intersects with the i^{th} pixel of intensity I. To update the value of $E(\mathbf{x}_j)$, the sum of the intensity contribution of the other voxels in the pixel's line-of-sight (shaded, $\sum_{j \in N_i} w_{i,j} E(\mathbf{x}_j)$) are considered. This is repeated for each of the c cameras.

be set to zero without any further data manipulation such as volume thresholding). As was shown in Elsinga et al (2006b), reconstruction artefacts along the non-zero pixel LoSs remain in the voxel space and are detrimental to reconstruction quality and subsequent vector calculation.

$$E(\mathbf{x}_j)^{k+1} = E(\mathbf{x}_j)^k + \mu w_{i,j} \left(\frac{I(\mathbf{X}_i) - \sum_{j \in N_i} w_{i,j} E(\mathbf{x}_j)^k}{\sum_{j \in N_i} w_{i,j}^2} \right) \tag{2.3}$$

The simultaneous ART (SART) (Andersen and Kak, 1984) was one improvement to the algorithm, which rather than updating the energy of a voxel from one independent view at a time, the update occurs after all pixel views are calculated for the voxel and the update is the average of all of the weighted views. Another derivation to Eq. 2.3 is the Adaptive ART (AART) (Lu and Yin, 2004) method. Rather than keeping the relaxation parameter μ constant as per previous implementations, the authors increase

μ proportionally to $I(\mathbf{X}_i)$. Despite the improvements in these algorithms, they are additive and therefore more suited to medical imaging which does not tend to deal with sparse data like TPIV.

MART The MART (Multiplicative ART, Eq 2.4) (Herman and Lent, 1976) updates the voxel intensities multiplicatively and behaves as an AND operator. $E(\mathbf{x}_j)$ is updated by considering the ratio of the measured pixel intensity to the LoS contributions of the voxels. As the technique is multiplicative, if a voxel is intersected by the LoS of any zero level pixel, it will also be zero and remain at zero for all proceeding iterations. This removes the noise in the voxels systemic of the ART techniques. The algorithm is applied by considering the pixels of one camera at a time and μ is commonly set to 1. Authors typically apply five iterations of MART based on the synthetic case study of Elsinga et al (2006b).

$$E(\mathbf{x}_j)^{k+1} = E(\mathbf{x}_j)^k \left(\frac{I(\mathbf{X}_i)}{\sum_{j \in N_i} w_{i,j} E(\mathbf{x}_j)^k} \right)^{\mu w_{i,j}} \tag{2.4}$$

SMART The SMART (Simultaneous MART) (Mishra et al, 1999) has a product operator that updates the value of E based on all camera views simultaneously (Eq 2.5). These simultaneous views are contained in the product operator, and represents the weighted product of the ratio of pixel intensities to LoS energy. This process is similar to the SART algorithm described above, however as it is multiplicative, it has the noise reducing benefit of MART. Each iteration of SMART is computationally more efficient than MART, however to achieve equivalent convergence (re-projection quality) of five MART iterations, the algorithm has been shown to require between 10 to 40 iterations (Atkinson and Soria, 2009).

$$E(\mathbf{x}_j)^{k+1} = E(\mathbf{x}_j)^k \prod_{i}^{N_i} \left[\left(\frac{I(\mathbf{X}_i)}{\sum_{j \in N_i} w_{i,j} E(\mathbf{x}_j)^k} \right)^{\mu w_{i,j}} \right]^{1/N_i} \tag{2.5}$$

BiMART The BiMART (Block Iterative MART, Eq 2.6) (Byrne, 2009) is a generalisation of MART and SMART (Thomas et al, 2014). The images are divided into a number of user defined coarse *blocks*, $\mathscr{B}$. This algorithm updates the voxel energy one

camera at a time, however the division of the image into blocks and the subsequent updating of E over a block at a time reduces the computational efficiency.

$$E(\mathbf{x}_j)^{k+1} = E(\mathbf{x}_j)^k \prod_{i \in \mathscr{B}}^{N_i} \left(\frac{I(\mathbf{X}_i)}{\sum_{j \in N_i} w_{i,j} E(\mathbf{x}_j)^k} \right)^{\mu w_{i,j}} \tag{2.6}$$

The object of the BiMART algorithm is to have the computational efficiency of SMART with the convergence speed of MART. The performance of the algorithm is demonstrated in Section 2.3.5.

MENT The maximum entropy (MENT) algorithm was recently introduced for TPIV applications by Bilsky et al (2013). The quoted reduction in complexity is nine times less than SMART and 30 times less than MART per iteration with approximately 5% reduction in reconstruction quality reported. Rather than updating E iteratively, MENT constructs a number c of 2D ridge functions $h(X_i, Y_i)$, equivalent to 2D pseudo images. Ridge functions are also known as pursuit algorithms that aim to reduce dimension, hence the iterations are over the 2D function rather than a 3D volume. The construction of this function is shown in Eq. 2.7, where h has the same dimensions as I. The final reconstruction of E is completed by a single pass product of all of the pseudo function values that view the voxel (Eq. 2.8).

$$h_f(\mathbf{X}_i)^{k+1} = \frac{I_f(\mathbf{X}_i)}{\frac{1}{V} \sum_{l \in L_n} \prod_{g \neq f} h_g^k(\mathbf{X}_l)} \tag{2.7}$$

$$E(\mathbf{x}_j) = \frac{1}{V} \prod_{f(i \in j)} h_f(\mathbf{X}_i) \tag{2.8}$$

In Eq. 2.7, f denotes the current pseudo image being considered and I_f its the corresponding image. V is a normalising factor that the authors took to be the number of voxels along z. L_n is the LoS of the current pixel $(\mathbf{X}_i)$ and $h_g(\mathbf{X}_l)$ correspond to the pixels of the remaining pseudo images that intersect with L_n. The denominator of the equation equates the sum product of the pseudo image pixel intensities that view the voxel.

The MART and SMART algorithms have been used extensively in the literature, while the recent BiMART algorithm has been used by Thomas et al (2014) and the MENT algorithm by Bilsky et al (2013). The algorithm used in this investigation is the BiMART owing to its significant speed up and higher quality. Section 2.3.5 describes as parametric test demonstrating these attributes.

2.3.4 Volume initialisation

All reconstruction methods are iterative and therefore the quality of the initial energy field is key to reduce the number of iterations needed to achieve convergence. The quality of the reconstruction and speed of convergence is thus somewhat dependant on the volume initialisation (Worth and Nickels, 2008). Early TPIV investigations set the initial voxel intensities to unity for the entire volume (Elsinga et al, 2006b). This initialisation is not optimised for two reasons: the volume has a comparatively high energy level in the volume compared to the final reconstructed volume, which is typically sparse (zero intensity), and; as all voxels are non-zero, they must be considered in the first iteration of the reconstruction algorithm, which requires more processing and memory. Reconstructed volumes typically contain $> 95\%$ of zero level voxels and omitting them from the reconstruction process can offer significant computation savings.

The aims of volume initialisation are therefore to rapidly determine which of the voxels will be non-zero, corresponding to where particles are expected to be, and to set the intensities of these non-zero voxels to an equivalent intensity close to what they will be in the final reconstructed volume. Initialisation algorithms are analogous to the re-projection shown in Figure 2.7(b). Computationally, the re-projection is performed by looping through and projecting each voxel onto all pixels that view it Eq. 2.9. This re-projection is achieved by a simple matrix multiplication and is thus computationally inexpensive.

$$E(\mathbf{x}_j) = f(w_{i,j} \cdot I(\mathbf{X}_i)) \quad \text{for } j \in i \tag{2.9}$$

Volume initialisation was first proposed by Worth and Nickels (2008), with an additive and multiplicative first guess (MFG) scheme (Eq. 2.10). The authors found that MFG

performed better, with the voxel intensities determined by the product of the viewing pixels' intensities normalised by raising to the power of $1/N_c$, where N_c is the total number of cameras. The multiplicative LoS (MLOS) initialisation method, proposed by Atkinson and Soria (2009), is the same formulation as MFG with $w_{i,j}$ set to the direct method (Section 2.3.1) and calculated on-the-fly.

$$E(\mathbf{x}_j) = \left(\prod_{j \in i} w_{i,j} \cdot I(\mathbf{X}_i) \right)^{1/N_c} \tag{2.10}$$

The Minimum LoS (MinLOS) was proposed by Putze and Maas (2008) (Eq. 2.11). The MinLOS technique has the lowest complexity – as the name suggests, it takes the minimum value (or intensity) of the pixels that view it, without the additional normalisation step required in multiplicative schemes. In this work the MinLOS algorithm is used owing to this low complexity.

$$E(\mathbf{x}_j) = \min_{j \in i}(w_{i,j} \cdot I(\mathbf{X}_i)) \tag{2.11}$$

Unfortunately, volume initialisation by itself results in insufficient quality for velocity field calculation as ghost particles are indistinguishable from real particles in terms of intensity (Atkinson and Soria, 2009). Therefore reconstruction algorithms are required to reduce the intensity of ghost particles and improve the quality of the reconstructed volumes.

2.3.5 Initialisation and reconstruction performance

In this work, the implemented TPIV process is a combination of initialisation algorithms and reconstruction algorithms. Initialisation is performed with a MinLOS step followed by two iterations of SMART. For the reconstruction process, the BiMART algorithm is used with a block size of 2. To justify the choice of these settings, the following parametric cases were performed on synthetically generated particles and images.

Four cameras viewed the measurement domain in an inverted pyramid configuration – the same configuration used for the three experimental investigations in this work. This has been shown to be an appropriate camera configuration in several synthetic cases (including

DeSilva et al, 2012; Thomas et al, 2014) along with numerous experimental configurations (for example Atkinson et al, 2011; Schröder et al, 2011). The cameras could be considered 'perfect' in that there is no lens distortion, no particle astigmatism or blurring as there is infinite depth of focus and a perfect camera calibration model with no re-projection error. Likewise, no random image noise was added to simulate perfect image processing. A number of particles randomly populated a measurement domain over a range of particles per voxel (ppv) levels. The particle size was set so that the imaged particles matched as closely as possible to the experimental measurements. Figure 2.9 shows the relation between the ppv levels and the resulting image source density N_s and particles per pixel (ppp) level. In the figure, N_s and ppp do not linearly increase with ppv as the particle images are more likely to overlap.

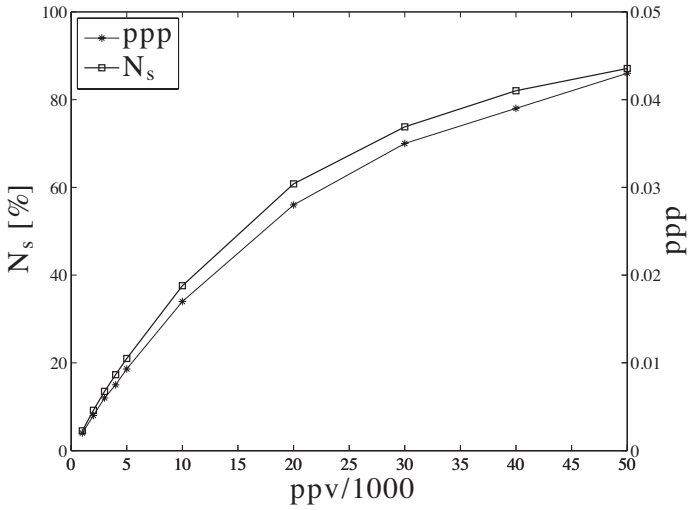

Figure 2.9: The relationship between the predetermined ppv level and resulting source density N_s and particles per pixel, ppp.

In this section, Q is defined to be the correlation coefficient between the initialised volume and the actual particles, rather than the re-projection quality obtained from experimental images (Elsinga et al, 2006b) (for example as shown in Section 5.3.3), this value directly compares the voxel intensity of the generated particles to the intensities produced from the algorithms. This method is a more appropriate comparison tool, as the re-projection quality

can be reduced by a number of factors independent of the algorithms.

Initialisation

Figure 2.10 compares the quality of initialisation of the MinLOS algorithm to the combination of MinLOS with several iterations of a fast implementation of the SMART algorithm over a range of ppv levels. The fast implementation uses a course direct method weighting function, which sacrifices precision for computational speed. The figure shows that the volume initialisation quality is increased with increasing iterations of SMART. Of course, as SMART is a proven reconstruction algorithm, this is not an unexpected result. Most importantly, the figure shows that the increase in quality becomes discernible for two or more iterations of SMART for ppv $\leq 0.02 \equiv N_s = 60\%$. For higher particle concentrations, three or four iterations of SMART become discernible to the increased iterations. The N_s in this work does not exceed 60%, therefore, by combing MinLOS with two iterations of SMART, the initialisation quality can be improved at minimal computational cost.

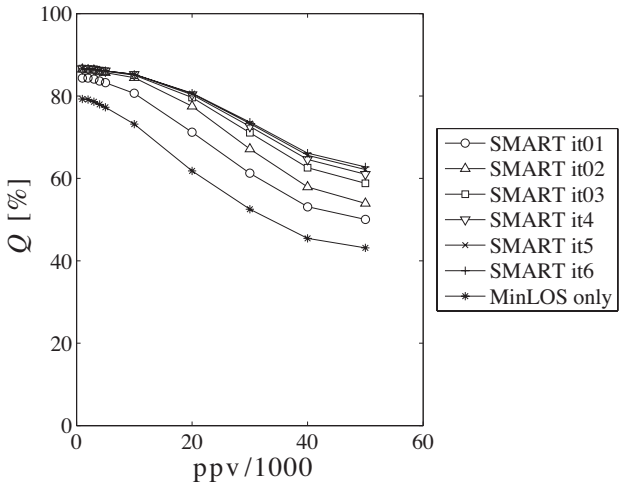

Figure 2.10: Volume quality test for initialisation techniques. MinLOS is combined with SMART at varying iterations to improve initialisation at minimum computational cost.

Reconstruction

The appropriate selection of reconstruction algorithms as well as the optimum number of iterations was investigated. Two important factors to consider in the selection of the algorithms are the reconstruction quality and the reconstruction time. Between these two factors a compromise must be achieved that maximises quality in the least amount of time. In the following analysis, the volumes have been initialised as per the process selected in the Initialisation section discussed previously. The cases investigated in this section are the MART, SMART and two cases of BiMART, with block sizes of 2 and 4 pixels.

Figure 2.11 shows the reconstruction quality compared to iterations. The SMART algorithm is shown to perform increasingly badly for an increase in particle density. MART is consistently the best performing algorithm across all ppv ranges. The BiMART cases are equivalent to MART, with the smaller block size implementation slightly outperforming the larger block size. From these figures, it can be seen that Convergence for the BiMART and MART algorithms occurs after approximately 4 iterations.

Speed of convergence is a significant factor to consider particularly when reconstruction is required on large batches of experimental data. In Figure 2.12(a) & (b), the total time of reconstruction is shown. It should be noted that the timing of these data should be taken as indicative only. Reconstruction was performed on an Intel i7 2.00GHz processor. The total reconstruction time can significantly vary between processor speeds and hardware, however these results highlight the importance of reducing the time, as the TPIV are computationally demanding. In order to give a direct comparison of the speed up ratios, Figure 2.12(c) & (d) have the computational times normalised by the MART time. SMART and BiMART show significant speed ups over MART, with BiMART with block size of 2 out performing the other algorithms.

It is noted that the speed up times for SMART are not the same as those reported in the literature (Atkinson and Soria, 2009). Several reasons for this are that a fast implementation of MART is used that does not carry or perform calculations on zero-voxels, unlike the implementation that was used as comparison. Also, the theoretical reductions in complexity of the algorithms are seldom matched by an equivalent reduction in time owing mainly to the data transfer overhead, algorithm optimisation and hardware limitations.

Therefore, in terms of speed and quality, these synthetic tests have justified the use of a combined reconstruction approach that aims to obtain maximum reconstruction quality in the fastest amount of time. Thus, the MinLOS plus 2 iterations of SMART plus 4 iterations of the BiMART algorithm with block size of 2 pixels is selected for the reconstruction of the particle intensities.

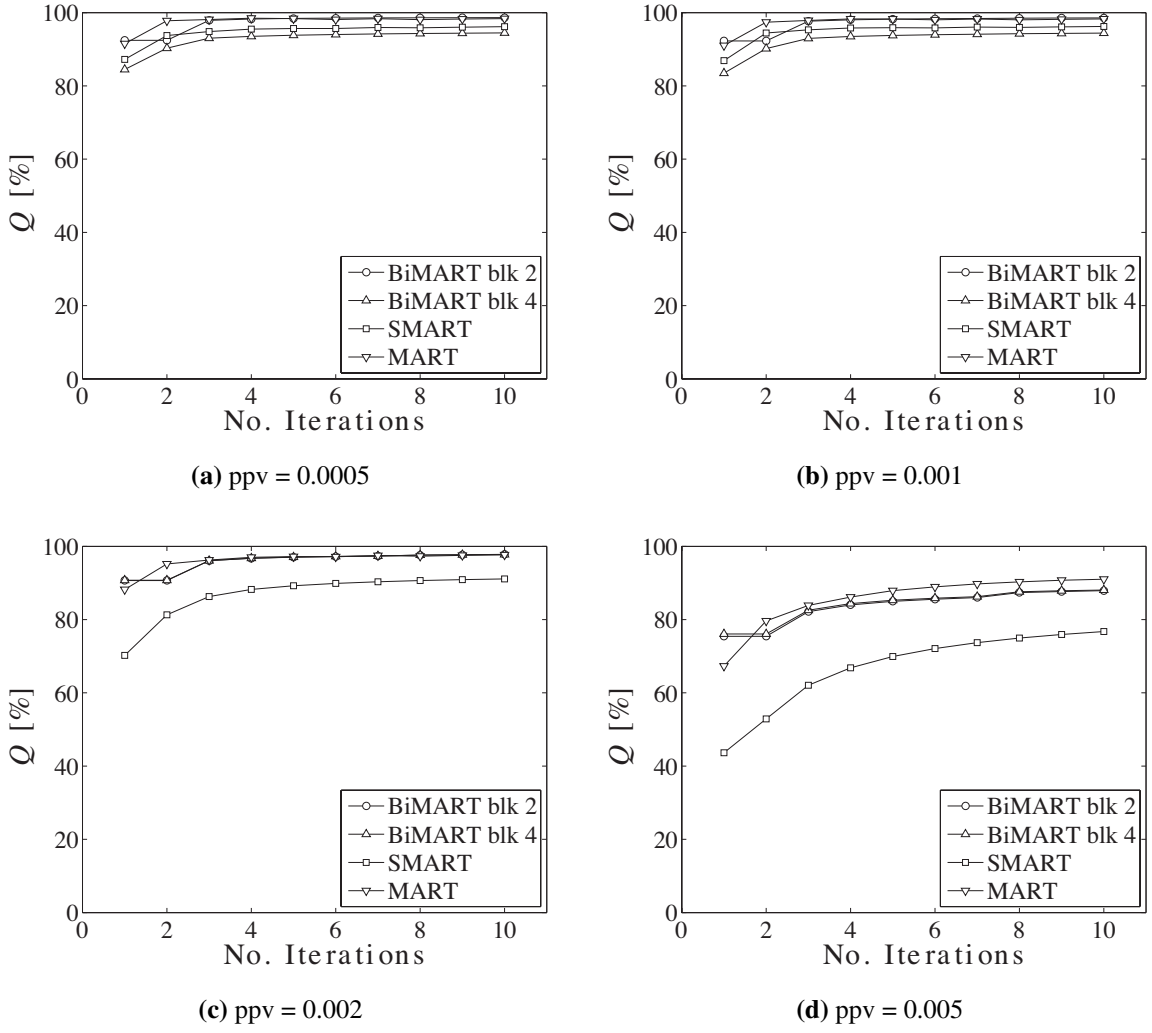

(a) ppv = 0.0005

(b) ppv = 0.001

(c) ppv = 0.002

(d) ppv = 0.005

Figure 2.11: The evolution of the reconstruction quality with iterations over a range of particle densities, ppv for 4 cases of reconstruction algorithm. Convergence after approximately 4 iterations.

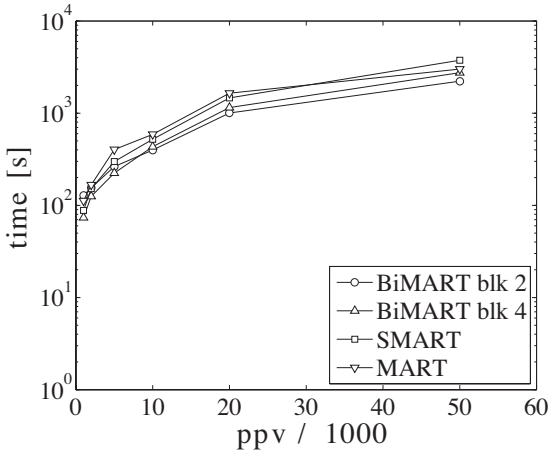

(a) time after 4 iterations

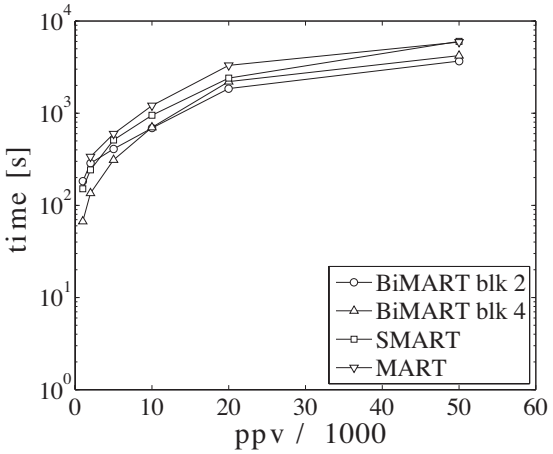

(b) time after 10 iterations

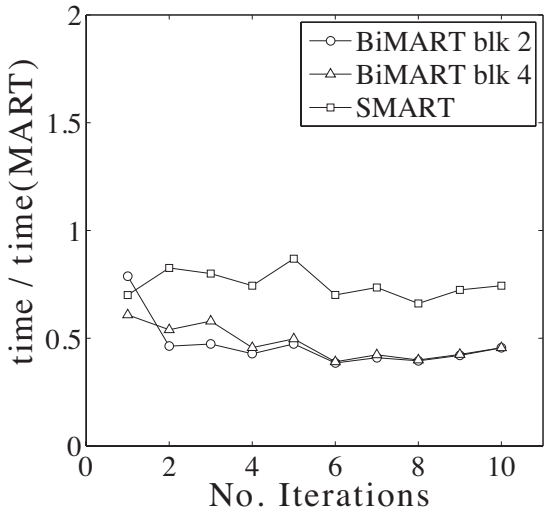

(c) ppv = 0.001

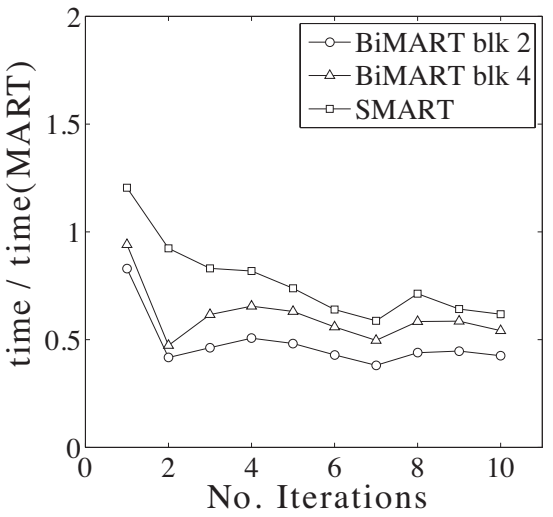

(d) ppv = 0.002

Figure 2.12: Comparative times between the tested algorithms: (a) and (b) compare the total time against the particles per volume (ppv) for 4 iterations and 10 iterations respectively, and; (c) and (d) show the times normalised by the time of the MART algorithm for ppv ranges equivalent to those achieved in the experiments.

2.3.6 Ghost particles

Ghost particles are reconstruction artefacts or intensities that don't correspond to real particles, and are formed by the intersection of LoSs not corresponding to the same particle (see Figure 2.7). Ghost particles have the effect of detrimentally smoothing flows and reducing the magnitudes of flow statistics (Elsinga and Westerweel, 2011b). Ghost particles tend to have the average velocity of the real particles and flatten the correlation peak for correlated data, an effect magnified in flows with strong velocity gradients.

The number of ghost particles that are constructed in a volume is proportional to the number of imaged particles. The number of imaged particles is in turn proportional to the number of particles in the flow and the thickness of the light sheet volume (Novara et al, 2010; Elsinga and Westerweel, 2011b). An increase in seeding density is desirable as it allows smaller IVs and hence higher spatial resolution. For this reason, significant effort has been applied to the reduction or elimination of ghost particles.

After several iterations of a reconstruction algorithm, ghost particles have been reported to have a lower intensity than real particles (Elsinga et al, 2006b). Therefore, volume thresholding to remove lower intensities can be an effective measure in reducing ghost particles (Thomas et al, 2014). As this is an efficient method and easy to implement, volume thresholding is the technique used in this work to remove ghost particles.

There have been other methods to identify and remove ghost particles. DeSilva et al (2013b) developed a spatial filter to remove them – the reasoning is that with good calibration (see section 2.3.2) real particles tend to have a typical shape and also a larger size than the ghost particles. Hence, a spatial filter that matches the shape of a real particle can be passed through the voxel space, and if energy intensities exist that do not match the filter, the intensities are removed. This technique allowed a significant increase in seeding density, and hence higher spatial resolutions.

Novara et al (2010) developed motion tracking-enhanced (MTE) method to remove ghost particles. The process of MTE is as follows: reconstruct two sequential volumes, calculate the velocity field, displace the second velocity field back onto the first from the velocity measurements and then compare the two volumes. As the authors explain, the real particles in both time steps align with each other, and the ghost particles do not. In

this way, the ghost particles can be identified and then removed. Once removed, additional iterations of MART were performed on both time steps and the velocity field determined again, this time without the interaction of ghost particles. They found some flow seeding densities could be increased by a factor of three compared to other studies but at increased computational effort. The same research group found that this technique is optimal in regions of high velocity gradient and only provided a marginal improvement otherwise. Hence, to obtain a balance between computational effort and ghost particle reduction, only regions in the volume with high velocity gradients are considered for MTE.

2.3.7 Volumetric cross-correlation

This section describes the volumetric cross-correlation process and some significant advances to its speed and accuracy. To obtain a volume of velocity vectors, two sequential voxel intensity fields $E_1 = E(t_0)$ and $E_2 = E(t_0 + \Delta t)$ are divided into interrogation volumes, IVs. Each IV in E_1 is then cross-correlated with the corresponding IV in E_2. The spatial correlation of the two reconstructed volumes can be as computationally intensive, or greater than, the reconstruction of the volumes (Discetti and Astarita, 2011). For this reason, new techniques have emerged to try to increase the speed.

For the simplest case of corresponding cubic IVs each of dimension $W \times W \times W$ voxels of E_1 and E_2, denoted IV_1 and IV_2 respectively, the normalised cross correlation coefficient R, with a uniform weighting in the volume, is calculated from (Discetti and Astarita, 2011):

$$R(s_x, s_y, s_z) = \frac{\sum_{ijk}^{W} (IV_1(x_i, y_j, z_k) - \mu_{IV_1})(IV_2(x_i - x_{s_x}, y_j - y_{s_y}, z_k - z_{s_z}) - \mu_{IV_2})}{\sqrt{\sum_{ijk}^{W} (IV_1(x_i, y_j, z_k) - \mu_{IV_1})^2 \cdot (IV_2(x_i - x_{s_x}, y_j - y_{s_y}, z_k - z_{s_z}) - \mu_{IV_2})^2}} \tag{2.12}$$

where (s_x, s_y, s_z) is a displacement measured from the centre of IV_1 and μ_{IV_i} is the average intensity of IV_i. Eq. 2.12 describes the direct correlation procedure, however this calculation can be sped-up by performing the calculation in Fourier space, by considering each IV to be periodic and computing the fast Fourier transform (FFT) of the grey level intensities of the IVs. The cross-correlation method undertaken in this work is based on computing the FFT of the IVs.

The methods employed at reducing computational effort and increasing calculation speed are listed below. Atkinson and Soria (2009) compared the speed of a non-zero direct correlation (that is, direct correlation only considering the non-zero voxels) and FFT correlation and found that only for low seeding densities (or more correctly, non-zero voxel intensities $< 1\%$) was the non-zero direct method faster. A method for analysing 3D IVs as a series of 2D projections of it, the so-called parallel projection correlation, was proposed by Bilsky et al (2011). In their method, IVs are projected onto three orthogonal planes and a 2D correlation is performed with the projections of IV_1 and the corresponding projections from IV_2. The speed-up was up to three times faster for a given cross-correlation iteration, however the technique was found to be sensitive to noise and perhaps could be better suited as a first iteration, followed by a direct correlation in 3D for the second iteration with reduced search radius. Discetti and Astarita (2011) presented several *block* methods and techniques for reducing redundant and repeated calculations that could be tailored to a given flow environment. The authors found that the accuracy of a direct correlation is higher than the FFT implementation (due to periodicity artefacts) when the search radius is in the order of 1 pixel, and thus a direct correlation is recommended as a final iteration of the cross correlation.

Another area of progress is the determination of Lagrangian data from time resolved TPIV (Novara and Scarano, 2013). Lagrangian data enables the calculation of the acceleration (and hence the material derivative of velocity) in the Navier Stokes equations (Eq 1.5). Schmid et al (2012) used time resolved TPIV to study a jet, while Schröder et al (2011) investigated a turbulent boundary layer. Ghaemi et al (2012) were able to obtain the pressure fluctuations from time resolved TPIV measurements.

Finally, and perhaps ultimately, is the push to track individual particles in a fluid flow. PTV techniques have strived to do this, however, typically the particle distributions have been sparse in order to ensure that unique particles are tracked. One exception to this is the relaxation technique proposed by Pereira et al (2006) which was shown to perform well at particle densities equivalent to those found in TPIV. Lei et al (2012) also made headway in developing PTV algorithms and particle identification schemes that improved particle tracking yields for overlapping particle images that are found in high particle density flows.

Schröder et al (2011) were able to track particle locations from TPIV data in a turbulent boundary layer investigation.

2.3.8 Pushing the boundaries of TPIV

TPIV is truly entering an exiting period as new flows are being investigated that were previously deemed to be implausible. The research community is indeed invigorated by this new tool (Scarano, 2013). There have been many documented studies looking into turbulence measurements (for example Worth et al, 2010), boundary layer flows (for example Schröder et al, 2011; Atkinson et al, 2011), flow around bluff bodies (Elsinga et al, 2006b), and jets (Schmid et al, 2012; Khashehchi et al, 2013). Scarano (2013) lists a more comprehensive number of authors for these given categories for the interested reader. The following indicates several interesting and challenging applications of TPIV, in an effort to show the new progress this technique has reached.

The most recent of these at the time of writing is a study by Im et al (2014). They investigated a flow through a silicon nasal cavity, and in order to obtain the velocity fields inside the nose matched the refractive index of the silicon to the water by adding glycerol. Ortiz-Dueñas et al (2010) were able to measure water glycerin drops dropping onto the surface of a silicone oil, a challenging flow to measure owing to the drop interfaces and the need to match the refractive indices of the two fluids. Kühn et al (2012) used TPIV in a large scale application (region of interest size $750 \times 450 \times 165$ mm^3), and used helium bubbles to seed the flow in order that the particle images were large enough. Klinner and Willert (2011) measured the dispersion of a spray of micro sized liquid into air by combining TPIV with a shadowgraphy technique. Elsinga et al (2010a) applied TPIV to a supersonic wall bounded flow revealing flow structures such as arch vortices over low speed tubes. Finally, the energy dissipation was quantified in a Taylor-Couette flow by TPIV and compared to the energy loss measured independently by the motor by Tokgoz et al (2012).

2.3.9 Limitations and accuracy of TPIV

As with all measurement techniques there exist limitations on applicability and accuracy. The formation of reconstruction artefacts, or ghost particles, has shown to be detrimental however several techniques to counteract them have been developed, such as MTE (Novara et al, 2010), ghost particle identification (DeSilva et al, 2013b) or volume thresholding (Thomas et al, 2014). The effect of this noise can effect the resolution of the system

The spatial dynamic range (SDR) is the range of the largest to the smallest resolvable length scales in a PIV measurement. As discussed by Herpin et al (2008), due to the long process-chain of PIV, it is difficult to ascertain the dominant limiting independent parameters that affect SDR. The largest resolvable scales are those bound by the measurement region, and the smallest are defined by the IW size, so that the smallest resolvable scales in PIV are approximately 2.2 times the IW length (Foucaut et al, 2004). As shown by Buchmann et al (2011), the SDR range limitation is particularly pronounced in TPIV measurements. For equivalent camera systems and measurement regions, TPIV will have a lower SDR than planar PIV techniques because the distribution of particles through the volume means that larger IVs compared to the planar IWs are required in order to perform the cross-correlation over 10 particle images.

Worth et al (2010) were able to quantify TPIV errors by comparison with a low Re direct numerical simulation (DNS) of turbulence. At high resolution (in terms of vector spacing to Kolmogorov scale, $\delta x/\eta$), TPIV was able to recover the velocity accurately, however at larger resolutions, the spatial averaging of the *IV*s underestimated the spatial gradients. To counteract this, DeSilva et al (2013a) proposed the divergence filter that corrects velocity fields by maintaining as close as possible the kinetic energy but reduces divergence that is appropriate for high resolution TPIV. Those authors found that gradients and the topology of invariants matched the simulated data more accurately. Recently, Atkinson et al (2014) proposed a filtering regime of TPIV that reduces the noise induced by small scale fluctuations to the end that the experimental measurements approached that of a noiseless system.

2.3.10 SLIP Library

The simple library for image processing (SLIP) has been developed at the University of Poitiers over the past decade (Tremblais et al, 2010). The SLIP library provides a platform for image processing, cross-correlation, and other algorithms, containers, and iterators in the C++ computing language. SLIP is the basis of the TPIV algorithms and cross-correlation programmes used in this work with most of the post-processing and analysis computed with a suite of functions implemented in MATLAB©.

2.4 Summary

PIV and its adaptations have developed into an important tool for measuring turbulent flows. The principles of planar PIV have recently been extended into a variety of volumetric techniques. Volumetric measurements are desirable for experimentalists because the out of plane motions, or more specifically the out of plane velocity gradients, are required in order to characterise turbulent flows. Of these volumetric techniques, TPIV is proving to the most versatile.

The objective of TPIV is to determine the three dimensional position of the tracer particles. This is achieved by projecting the multiple and simultaneous PIV images back into the measurement domain and calculating the most probable intensity distribution that could have made the images. The energy distribution is computed through several iterations of a multiplicative algebraic techniques. Finally, the reconstructed particle field is divided into a number of interrogation volumes (IVs), and through a volumetric cross-correlation between corresponding and sequential IVs, the three-dimensional (3D) velocity field is retrieved. The primary considerations of the TPIV system were described, including camera calibration and ghost particle formation. Some recent studies were listed that push the boundaries of the use of TPIV, and others that focused on the limitations of the technique.

Chapter 3

Evaluation of the energy dissipation by tomographic PIV of an open channel flow behind a series of regular grids

3.1 Introduction

This chapter introduced TPIV measurements to open channel flows. Aside from currents in the ocean, the most common of hydraulic flows on the planet are open channel flows: the flow of water along rivers. Rivers are the lifeblood of the planet, transporting fresh water, aquatic life and nutrients. An investigation into the physics and behaviours of these turbulent flows is crucial to understand the mixing processes and sediment transport in them. The open channel flow investigated in this chapter and the following has several specific uses, the most important being the ability to control the turbulence level at high Reynolds numbers to simulate a flow in a river. The intended application of this flow type is to mimic the turbulence and flow conditions that fish may encounter in rivers or vertical slot fishways. Future investigations will evaluate the swimming capability of various species of fish after the full flow characterisation of the channel.

There are two primary challenges involved with measuring turbulence in open channel flows. Firstly, to ensure that the flow conditions in the apparatus are equivalent to those

typically found in the field, a large experimental rig is required to achieve a high Reynolds number. In addition, to maintain Froude similitude, any scaled model requires proportionally higher flow rates. Thus, the combination of relatively large geometry with high flow rates can cause vibration of the rig and/or measurement equipment. Secondly, the flow is characterised by a highly unsteady free surface that entrains air. This entrainment generates bubbles that can hinder the use of optical techniques. To the author's knowledge, this is the first time Tomographic PIV has been used to measure an open channel flow of this kind, particularly characterised by the highly turbulent free surface.

The flow characteristics that are most significant to the migration of fishes inside open channel flows are large, persistent vortices that occur at the length scale in the order of the species sizes and the turbulent kinetic energy of the flow. Large scale vortices can destabilise fish and excessive turbulent kinetic energy in the flow can induce fatigue in the fish, making upstream progress more difficult (Lacey et al, 2012; Calluaud et al, 2014). It is therefore not a primary objective of these turbulence measurements to resolve the Kolmogorov length scales to fully resolve the flow. In this study, it is of greater importance to measure the larger scale vortices and flow field. Therefore, to completely characterise the vortices and structure of turbulent flow, a three component (3C), three-dimensional (3D) technique where the full velocity gradient tensor is required. The flume used in this investigation was specifically designed to control the mean flow properties, such as bulk velocity, vortex production and energy dissipation. To this end, the inclined open channel flow was divided into sequential pools by a series of trash racks, or regular grids, to simulate the turbulent flow that can be found in rivers (Figure 3.1). This configuration is new, and as such there are no comparable studies in the literature that are appropriate to compare the velocity statistics.

As far as non-invasive techniques are concerned, turbulent flows in water can be characterised by Laser Doppler Velocimetry (LDV). LDV can thus be implemented at very high acquisition rates to obtain the highest frequency velocity fluctuations of the flow. The drawback of LDV is that it is a point measurement, and so it is not possible to obtain the three dimensional (3D) structures nor the full velocity gradient tensor. Particle image velocimetry (PIV) techniques on the other hand can determine spatial gradients over a relatively

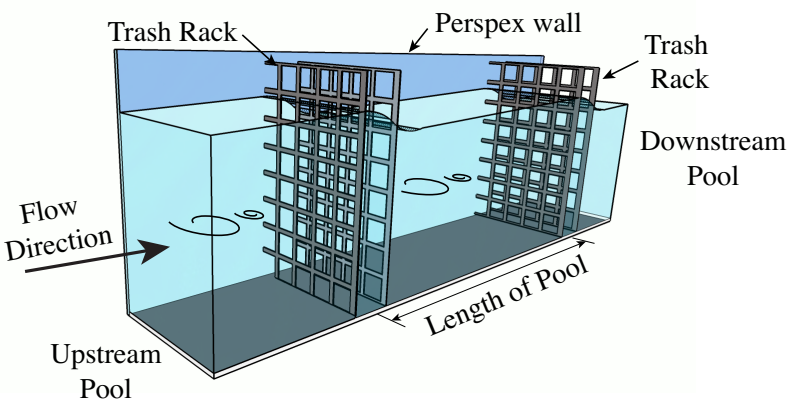

Figure 3.1: Cut-away schematic of one of a series of pools in the flume used in the experiments. The flow conditions are periodic across the pools: the flow is reset at each trash rack, highlighted by the idealised evolution of the vortices. Note that the fine wire meshes upstream of the trash racks are not shown here for greater clarity.

large field of view (See Adrian (1991) and Westerweel (1997) for examples of early PIV studies).

Tomographic PIV (TPIV), first introduced by Elsinga et al (2006b), is used to measure the flow. TPIV has had increasing interest since its inception, particularly in the field of turbulence, as the full velocity gradient can be determined from the measurements. The other advantages of this technique were discussed in greater detail in Section 2.2. Further, a comprehensive review of TPIV studies is given by Scarano (2013).

A recent stereo PIV and TPIV study of grid generated turbulence by Buchmann et al (2010) investigated and compared the performance of the two methods and it was demonstrated that the TPIV technique could retrieve the main turbulence and dissipation characteristics. Worth et al (2010) have investigated the resolution effects of TPIV measurements from synthetic flow fields created from DNS homogeneous isotropic turbulence data. Their results showed that for the calculation of the dissipation required a minimum TPIV resolution of three times the Kolmogorov length scale and that velocity field smoothing is recommended to help control the inherent noise levels. Similar to this study, Cardesa et al (2012) have investigated turbulence in an open channel flow, using 'stitched' 2D PIV extending downstream from grid location.

Other notable studies of turbulence with PIV techniques are those generated by fractal grids (Valente and Vassilicos, 2011; Discetti et al, 2013). In these cases, the turbulence is created with a different input generation to the regular grid. The main implications of these study findings is that the underlying hypothesis of the Kolmogorov type dissipation, that is, turbulence is isotropic at the smaller scales (independent of initial conditions) with a rate of decay governed by a 5/3 power law, has been challenged.

There is a significant difference between the current investigation and what has been reported in the literature, namely that the current investigation is carried out in a turbulent, inclined open channel flow. In the current study, the free surface has a turbulent hydraulic jump or bore. The implications are that the measurement conditions are less ideal than those typically quoted in literature.

In this study, an inclined open channel flow where, in order to prevent the flow accelerating down the slope, a series of trash racks is used to convert potential energy into turbulent kinetic energy and then dissipated along the channel, is investigated. The global power and dissipation characteristics of the flow across each pool were determined, explained further herein. TPIV measurements were taken to see the local energy dissipation behaviour and compare the global findings between the two configurations.

3.2 Experimental Set-up

Experiments were conducted in an open channel (Figure 3.2) at Institut Pprime at the University of Poitiers, France. The inclined channel was rectangular in cross section with dimensions 500 $\times$ 304 mm (height, H $\times$ width, W) and had 30 mm thick perspex walls and base to allow full optical access. The channel was divided into 4 identical pools that were separated by trash rack assemblies (Section 3.2.1). The water was pumped from the lower reservoir into the upper reservoir, and propagated down the channel by gravity. The inclination of the channel for both cases was 5%, or $\theta \approx 2.9^{\circ}$. The weir gate height was adjusted so that there was a regular head loss, ΔH (see Figure 3.6), across each trash rack with a constant flow rate of $Q = 34$ L/s for both configurations.

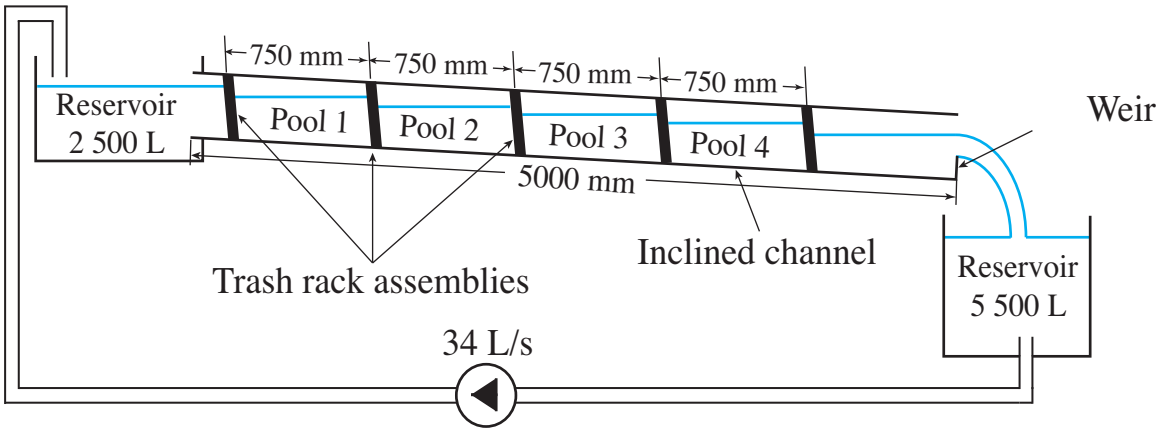

Figure 3.2: Schematic of inclined open channel, divided into 4 identical pools by 5 trash rack assemblies.

3.2.1 Trash Rack and Grid Details

Each pool was separated by a vertical trash rack assembly (Figure 3.3). The trash racks were comprised of, from upstream to downstream, a fine wire mesh and a pair of regular grids that were fabricated from 2 mm thick stainless steel plates. The fine wire mesh ensured that any large eddies from the previous pool were broken up before entering the next pool, resetting the flow. The grid pairs used were G1G2 and G3G4, with square opening geometries as shown in Figure 3.4. Note that for each grid pair, the different mesh sizes produced corresponding solidity ratios σ. The solidity ratios, defined by $\sigma = (D/M)(2 - D/M)$, are given in Figure 3.4, where D is the width of each bar and M is the centre-to-centre bar spacing of the grid. Stream-wise spacing between the grids in the trash rack was 90 mm. There was a fine wire mesh upstream of the grids to break up any large vortex structures and reset the flow. The trash racks housings wrapped around the flume walls and protruded 15 mm into the flow on the sides and base. The upstream edges of the housings were chamfered at 45°.

Despite the geometric similarities in the scaling between the grid pairs, there is difference in the total perimeter length of the openings L_P per unit area, which is proportional to the amount of shear applied to the flow. The number of square openings per unit area N_{sq} can be calculated from $N_{sq} = 1/M^2$. It follows that $L_P = N_{sq} \cdot 4(M - D)$, which is the num-

ber of square openings multiplied by the perimeter length. These values are also detailed in Figure 3.4. The characteristics of the G2 and G4 grids are used for the dimensionless analysis.

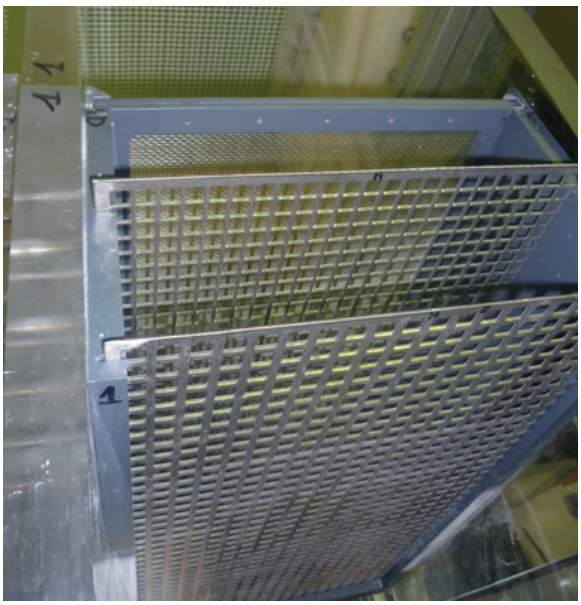

Figure 3.3: Photo of the track assembly with the G1G2 grid geometries installed. Flow is from the top of the image.

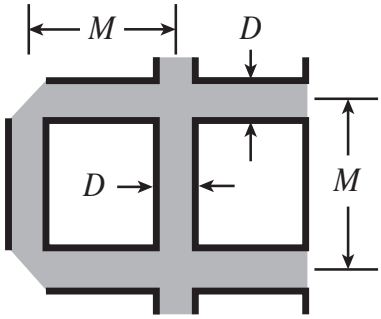

GRADES

Grid	M [mm]	D [mm]	σ	L_P [m]
G1	12	2	0.31	278
G2	14	4	0.49	204
G3	30	5	0.31	111
G4	35	10	0.49	82

Figure 3.4: Grid geometries used in pairs to form the trash racks that divided the channel into pools.

3.2.2 Flow properties

The water temperature was 15.4±0.5 °C with associated kinematic viscosity $\nu = 1.5 \cdot 10^{-6}$ m^2/s. The hydraulic diameter, $D_H = h_c W/(2h_c + W)$, for this channel was in the order of 0.1 m for both grid combinations, where h_c is the flow depth at the centre of the pool, measured from median of 2D PIV images taken of the same flow (see Appendix A.4). The bulk mean velocity of the flow through each pool, $U_0 = Q/(h_c W)$, was 0.36 m/s and 0.34 m/s, corresponding to Reynolds numbers, Re_{D_H} of 30 400 and 28 000 for the G1G2 and G3G4 configurations respectively. Both flows were subcritical, each with a Froude Number $\mathrm{Fr} = U_0/\sqrt{gh_c} \approx 0.2$. The respective Re_M, with respect to grid geometry were 4300 and 9600, which are in the higher ranges of recent PIV studies of grid generated turbulence by Cardesa et al (2012).

3.2.3 Volumetric Dissipated Power and Energy

The flow down the channel is steady on average, and therefore the energy losses are the same for each pool. By applying Bernoulli's (Eq 3.1) between the centre points of two successive pools, it is possible to approximate the bulk head loss ΔH_B. ΔH_B is a measure of the losses generated from the creation of vortices that lead to the dissipation of turbulent kinetic energy, by a combination of the grids (related directly to ΔH) and the skin friction along the channel boundaries, so that

$$\frac{p_0}{\rho g} + \frac{U_0^2}{2g} + y_1 = \frac{p_0}{\rho g} + \frac{U_0^2}{2g} + y_2 + \Delta H_\mathrm{B} \tag{3.1}$$

where the pressure p_0 and velocity U_0 are equal in successive pools. ρ is the water density and g gravity. Therefore, the energy losses are a balance of the change in elevation only, $y_1 - y_2 = \Delta H_B$ = 37.5 mm. The global volumetric dissipated power P_G in a pool, per unit volume, can be estimated by computing the ratio of the work done to the water volume:

$$P_G = \frac{\rho g Q \Delta H_\mathrm{B}}{LWh_c} = \varepsilon_B \rho \tag{3.2}$$

where L is the distance between sequential trash racks. The bulk dissipated energy ε_B can be approximated from Eq 3.2. Table 3.1 summarises the results of this analysis, where it can be seen that there is a greater ΔH in the G1G2 case and a lower h_c, contributing to a higher ε_B than for G3G4. The higher ε_B for G1G2 can be attributed to the higher L_{P}.

The Kolmogorov microscales, that are the length $\eta = (\nu^3/\varepsilon_B)^{1/4}$ (Eq. 1.28), time $\tau_\eta = (\nu/\varepsilon_B)^{1/2}$ and velocity $u_\eta = (\nu\varepsilon_B)^{1/4}$ are introduced in Table 3.1. The microscales define the smallest scales in a turbulent flow where viscous effects dominate and convert turbulence kinetic energy into heat through dissipation.

Table 3.1: Salient properties of the flow for each grid combination

Case	G1G2	G3G4
h_c	310 mm	325 mm
ΔH	45 mm	39 mm
P_G	177 $\mathrm{kg\,m^{-1}s^{-3}}$	168 $\mathrm{kg\,m^{-1}s^{-3}}$
ε_B	0.178 $\mathrm{m^2s^{-3}}$	0.169 $\mathrm{m^2s^{-3}}$
η	0.054 mm	0.055 mm
τ_η	2.96×10^{-3} s	3.11×10^{-3} s
u_η	0.023 $\mathrm{ms^{-1}}$	0.022 $\mathrm{ms^{-1}}$

3.2.4 2D PIV

To gain a greater insight into the global flow, a two component, two-dimensional (2C-2D) PIV study of the flow in pool 3 (the same pool that the TPIV measurements were taken, Section 3.3.1) was conducted. For the purposes of this article, this 2D PIV analysis serves to show the mean flow field which in the central, lengthwise plane of the pool. Further details of the 2D PIV measurements are in Appendix A.4)

Figure 3.5 shows the contour map of mean streamwise component of velocity U normalised by U_0, realised from an average of 500 fields, with bulk flow direction from left to right. One out of every 100 velocity vectors is displayed to aid visualisation of the flow

field. The blue box in the figure indicates the location of the TPIV measurements. Contour lines of $U - U_0$ between -0.010 and 0.025 ms^{-1} were added for $x > 100$ mm to highlight the flow pattern in the centre of pool. In particular, a stronger undercurrent at $y = 50$ mm for $x < 400$ mm persists into the TPIV measurement region. This field also shows a high velocity region near the free surface caused by its plunging action after passing through the trash rack assembly. The flow can be seen to accelerate towards the end of the pool owing the contraction in the channel cross-section by the trash rack housing. The dark blue region propagating from the origin is a recirculation zone, resulting from the bottom of the trash rack housing ending (akin to a flow over a backward facing step). Finally, the jetting of the flow through the grids can also be observed at the entrance to the pool.

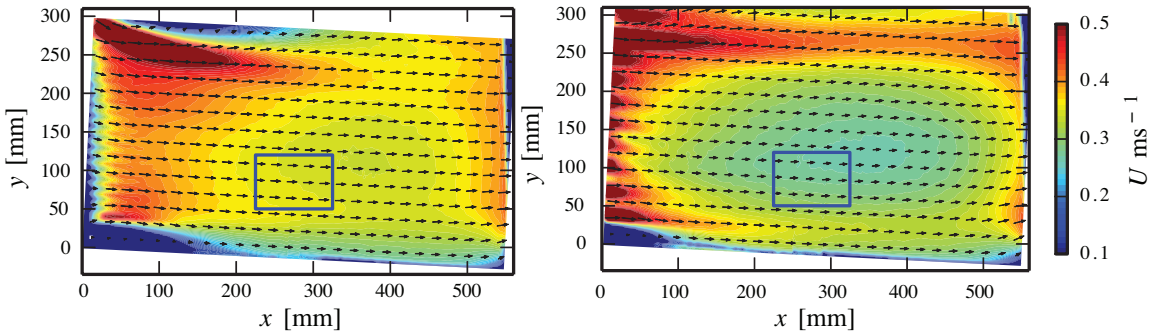

Figure 3.5: Mean 2D PIV flow field, averaged over 500 velocity fields for (a) G1G2 and (b) G3G4. U is the mean component of velocity in the stream wise direction. Only every 100th vector is plotted. The TPIV region (Section 3.3) is indicated by the blue boxes.

3.3 TPIV Set-up

TPIV follows a procedure which involves camera calibration, image acquisition, image processing, reconstruction of particle intensities in a computational volume and calculation of volumetric velocity fields (Elsinga et al, 2006b). At each step, the relevant parameters must be optimised to obtain the utmost quality of results. This section describes the

rationale behind the selection of some of the TPIV parameters used in this study.

3.3.1 TPIV System

TPIV measurements were taken in pool 3 to ensure a fully developed flow (Figure 3.6). The TPIV system was comprised of four 1600 $\times$ 1200 px 8 bit cameras (CV-M2 JAI). The cameras were positioned symmetrically in an inverted pyramid configuration, with declination and inward angles of approximately 20°. The positioning results in a camera angle subtended from the normal of the side walls of $\sim$ 30°. The camera orientation was a balance between approaching the optimum camera subtended angles for TPIV shown to be between 30 – 45° for synthetic images (Thomas et al, 2010; DeSilva et al, 2012), and reducing the aberrations of the particle images due to the high refractive index change at the interface of the air and the channel. Water prisms can be used to negate the optical aberrations by ensuring the air-perspex interface is perpendicular to the camera lens axes, however they were not used in this study. This was due to the need to have unobstructed optical access in the whole pool, and the complexity of the design and placement of the prisms owing to the two 20° in each plane.

All cameras were fitted with 50 mm lenses, 532 nm pass optical filters (corresponding to the laser frequency) and 2-axis lens mounted Scheimpflug adapters, adjusted so that the camera focal planes were coincident with the laser sheet. Additionally, the apertures were set at $f_\# = 22$ during acquisition for superior depth of field. Neutrally buoyant, spherical, polyamide particles (VESTOSINT 2157) of mean diameter $d_{50} \approx 56$ μm and density $\rho_\mathrm{p} = 1.02$ g/cm^3 were seeded in the flow. The average imaged particle diameter was $d_\tau \approx 4.5$ px.

A 15 mm thick laser sheet (corresponding to $1.07M$ and $2.5M$ for G1G2 and G3G4, respectively) was made to illuminate the measurement volume, realised with a double head Nd:YAG laser with 120 mJ per pulse. The laser and laser optics were positioned under the channel, independent from the channel structure. This permitted the identical configuration of the four cameras to view the forward scattering of the seeding particles. The measurement volume in the centre of the pool was 100 $\times$ 70 $\times$ 15 mm^3 ($X \times Y \times Z$, where X is the dimension in the x-direction, and likewise for the other components) and aligned with the flow direction. The laser sheet thickness Δz_0 was regulated with parallel plates spaced

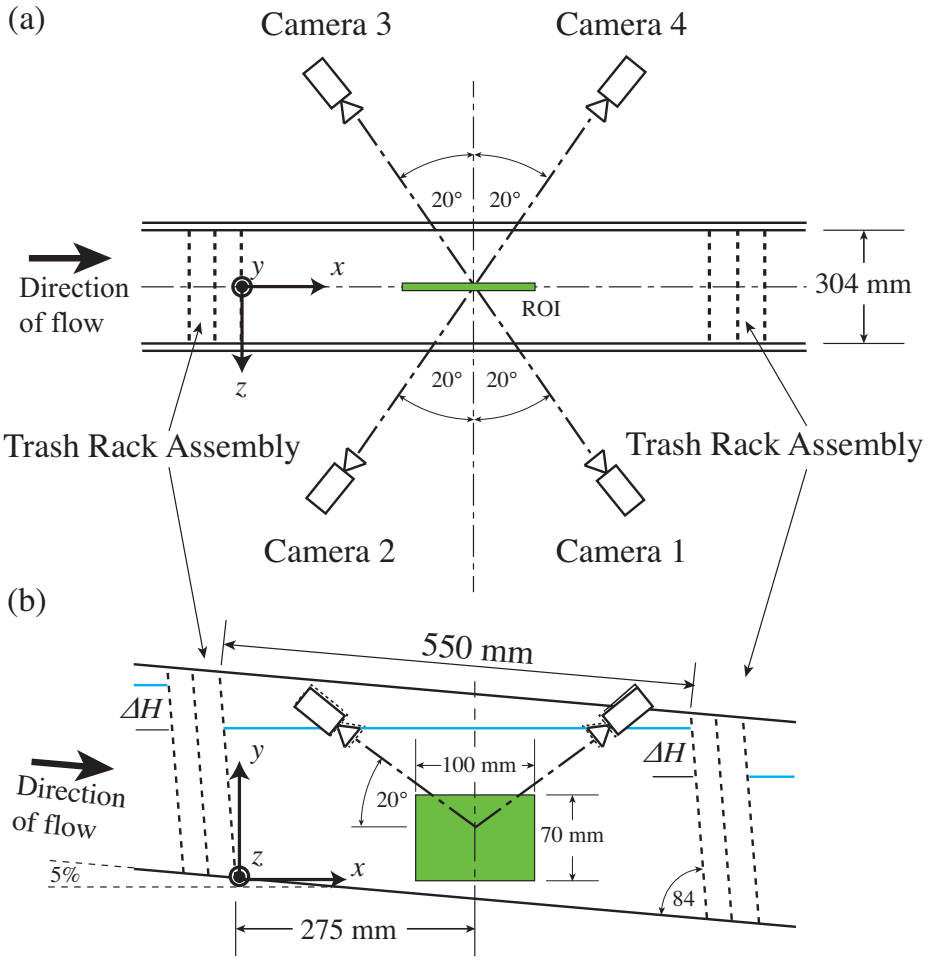

Figure 3.6: Schematic of Pool 3 showing measurement volume or region of interest (ROI) in (a) plan and (b) elevation. The origin and axis orientation along with inverted pyramid configuration of the cameras are shown.

at 15 mm, corresponding to $1.07M$ for G1G2 and $0.43M$ for G3G4. The time between corresponding images, Δt, was 2 ms, chosen to achieve mean particle displacements of $\sim$8 px for each camera. These image double-quadruplicates (8 of which make a velocity field) were acquired at 5 Hz to ensure statistically independent measurements.

3.3.2 Image Processing

For each camera and for corresponding laser pulses, the median image from 50 sequential images was subtracted to remove the background noise. This method was shown to be more effective than local window filters, due to the nature of the background noise. The effect of image filtering is shown in Figure 3.7. The processed images to be reconstructed had a homogeneous particle per pixel of $ppp \approx 0.03$, or an image source density $N_s \approx 0.7$ (Scarano, 2013), for all cameras at both time-steps. A gaussian filtering kernel was then applied to smooth particle images.

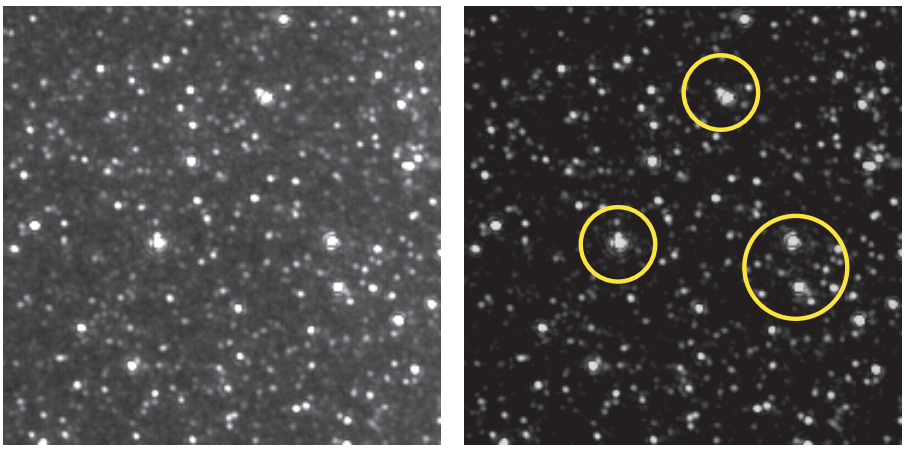

(a) **(b)**

Figure 3.7: 200×200 px sample of (a) raw image and (b) after the median image subtraction. The yellow circles highlight large over exposed 'particle' images caused by small bubble entrainment.

Small bubble entrainment in the water due to the free surface and subsequent turbulent mixing through the trash rack assembly was evident and detracted from the quality of the reconstruction (Figure 3.7). The bubbles had two main effects: primarily, they created image 'particles' larger than the mean when in the illuminated volume that were at times large enough to cause over exposure and an Airy disk effect on the images. The second problem, which was more specific to the G3G4 case was that the bubbles in the foreground, that is, between the illuminated volume and the camera (i.e. not illuminated directly by the

laser sheet) perturbed the line-of-sight of the particles and left regions in the images where there appeared to be no particles. No standard image treatment was able to rectify these effects, therefore if the reconstruction quality deteriorated below a threshold of 75%, the image sets were disregarded.

3.3.3 Volume Reconstruction

The tomographic reconstructions and correlations were made using the SLIP library developed at the University of Poitiers (Tremblais et al, 2010). A pinhole model was used to calibrate the cameras, improved with a volumetric self calibration technique analogous to Wieneke (2008). Reconstruction was split into a volume initialisation and volume reconstruction phase, with the aim of optimising the available reconstruction algorithms.

The volume initialisation step was performed by a MinLOS (Putze and Maas, 2008; Worth and Nickels, 2008) that was proceeded by 2 iterations of SMART (Atkinson and Soria, 2009). The SMART algorithm has been shown to perform faster than MART for reconstruction, however it also requires more iterations to obtain similar reconstructed volumes. SMART is therefore used to improve the quality of volume initialisation at minimum computational cost, and to speed up convergence of the subsequent reconstruction algorithm. The volume reconstruction was computed with 4 iterations of the BiMART algorithm (Byrne, 2009; Thomas et al, 2014). The BiMART algorithm (Eq. 3.3) performs similarly to the MART algorithm but the division of the images into *blocks* permits greater computational efficiency. The images $I(X_i)$are divided into a number of coarse *blocks*, $\mathscr{B}$. The division into blocks enables parallel processing at MART quality reconstructions of the voxel intensity.

$$E(\mathbf{x}_j)^{k+1} = E(\mathbf{x}_j)^k \prod_{i \in \mathscr{B}}^{N_i} \left(\frac{I(\mathbf{X}_i)}{\sum_{j \in N_i} w_{i,j} E(\mathbf{x}_j)^k} \right)^{\mu w_{i,j}} \tag{3.3}$$

where μ is a relaxation parameter which was set dynamically (Thomas et al, 2014), $E(\mathbf{x}_j)$ is the energy of the voxels, and $w_{i,j}$ is the weighting coefficients. A 2D gaussian filter was passed through each x–y voxel plane in the first 2 iterations and a volume thresholding was applied (Discetti and Astarita, 2011). This increases the correlation quality for a synthetic

case and could have the effect of reducing ghost particles (Thomas et al, 2014).

Ghost particles have been investigated thoroughly (Novara et al, 2010; Elsinga and Westerweel, 2011b) and have been shown to smooth velocity gradients and hence turbulence statistics. DeSilva et al (2013a) has shown a technique to identify ghost particles with a template matching filter, with the assumption that reconstructed particles are spherical and ghost particles are non-spherical and fragmented. Ghost particles are shown to have lower intensity than real particles (Elsinga et al, 2006b), and hence a gaussian filtering and volume thresholding is believed to aid ghost particle reduction.

The reconstructed volumes were 20% larger in the z direction. This is to ensure that the ghost particles are distributed over a larger volume and to increase the signal to noise ratio. This measure also prevents high intensities at the volume edges resulting from lines-of-sight that pass through less of the volume, and hence effecting the correlation. The volume is then trimmed to a size within the laser sheet so that only the particles reconstructed within the laser sheet are correlated.

The reconstruction programmes developed from the SLIP suite run on multiple processors. For a reconstructed domain of $1074 \times 710 \times 237$ voxels, the complete reconstruction of each volume is in the order of 6 minutes running on 4-cores of an Intel i7 2.6GHz processor. As the weighting coefficients are calculated on the fly, and only non-zero voxel elements carried, the RAM required per volume is in the order of 2GB, enabling analysis on desktop computers.

3.3.4 Vibration Correction with Self-Calibration

The camera calibration mapping function M, which maps real-world coordinates to the camera image, is required to be accurate to within a fraction of a pixel (ideally 0.1 px or less) for a successful tomographic particle reconstruction (Wieneke, 2008). During the experiments, the flume and camera rig vibrated unavoidably due to the energy of the flow which invalidated the camera mapping obtained from the camera calibration. This was despite the experimental rig being a solid construction of 80×80 mm^2 cross section extruded aluminium framing. All of the cameras were on a common rack that was securely fastened to the main frame of the flume. The two camera pairs were each on a section

that cantilevered out from either side of the rig to allow optical access through the side walls of the flume. The laser and laser sheet optics were independent of these, positioned on the solid concrete floor beneath the flume. Single-image vibration correction was first proposed by Michaelis and Wolf (2011), utilising the volume self-calibration technique introduced by Wieneke (2008). The volume self-calibration technique performs a calibration on the particles themselves, in order to update M until the required mapping accuracy for TPIV is achieved. For these measurements, each acquisition had its calibration updated by a individual volume correction (IVC) scheme (Earl et al, 2015, , Appendix C) to correct this.

3.3.5 Velocity field calculation

A two pass $64 \times 64 \times 64$ voxel correlation volume with 75% overlap was used to find the most probable displacement of particles across the two reconstructed volumes. This resulted in 20992 vectors per acquisition at a spatial resolution of $\delta x = 1.5$ mm. A median vector replacement regime was implemented as per Westerweel and Scarano (2005), with the number of spurious vectors found to be between 2–4% per volume. As tomographic reconstruction had been shown to be particularly susceptible to noise (Worth et al, 2010), a bilateral filter (Tomasi and Manduchi, 1998) was used to filter the velocity fields, which was preferred over a gaussian filter as it preserves edges.

To rationalise the filtering technique, Figure 3.8 shows an unfiltered u-component of velocity compared with the same signal filtered with a Gaussian kernel and bilateral filtering. The Gaussian and bilateral filters both had $3 \times 3 \times 3$ kernels with standard deviation equal to 1 vx. Figure 3.8a shows the raw velocity signal taken along one single row along the x-axis of a velocity field. A superficial examination of the plot verifies that the bilateral filter maintains edges in the data, whilst smoothing smaller scale fluctuations, whereas the Gaussian smooths the curve indiscriminately. Figure 3.8b shows the same curves in the frequency domain, plotted against the wave number $k = 2\pi/\delta x$, normalised by the Kolmogorov length scale η. These curves were generated by averaging all of the available rows along the x-axis for one velocity field. This graph shows how the larger scales contain the most energy, as shown in Figure 1.1. The bilateral filter maintains the longer wave length

energy and reduces the shorter wavelengths, whereas the Gaussian increases some of the mid range energy and then has a large 'peel off', at smaller wavelengths, an effect widely reported in the literature (for example, Worth et al, 2010). This can be a desirable effect at higher resolution measurements where noise can artificially augment the smaller scales, however, as the raw data does not display this behaviour, the bilateral filter is preferred.

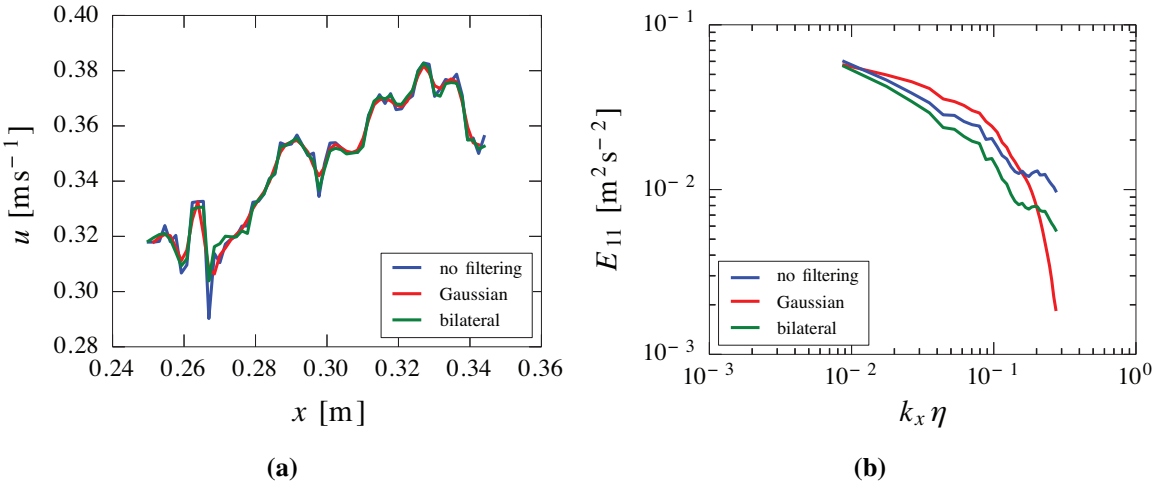

Figure 3.8: Effect of Gaussian and bilateral filtering on the u component of velocity. (a) Shows a single row along the x-axis of the velocity signal and (b) the energy spectrum, calculated over all similar rows in a single velocity field.

3.3.6 TPIV Resolution

The field of view size and resolution is a compromise between capturing global flow features, such as structures, and resolution. It was known *a priori* that these PIV measurements would not capture the Kolmogorov scale η resolution, as presented in Table 3.1. The vector spacing of this study is in the order of 22η. To capture the Kolmogorov scale, the optimum vector spacing must have been $\eta/10 < \delta x < \eta/2$ (Tanaka and Eaton, 2007).

The correlation volume size is selected to ensure that they capture at least 10 reconstructed particles, therefore, the more particles that are seeded in the flow, the smaller the interrogation volumes can be used. This in turn reduces the centre-to-centre vector spac-

ing, δx. However, seeding density also increases the effect of ghost particles (Elsinga and Westerweel, 2011a), which has the effect of broadening the cross-correlation peak with ramifications for the statistics of the computed velocity. A regime to reduce ghost particles such as that proposed by Novara et al (2011) is not appropriate for a flow dominated by a relatively uniform distributed velocity. In addition, it was found that the addition of more particles in the flow had the effect of detrimentally increasing the turbidity of the water, reducing the signal to noise ratio of the experiments. This highlights some of the challenges and compromises of selecting or designing the TPIV and cross-correlation resolution. The resolution effects of the TPIV analysis is the subject of future work, where higher resolution TPIV, LDV and 2D PIV measurements will compliment the current study.

3.4 Results

In total, 2000 volumes were reconstructed resulting in 1000 velocity fields for each trash rack configuration. All statistical calculations incorporated the full complement of data. The lower case u, v, and w refer to the instantaneous velocities in the x, y and x directions respectively (Figure 3.6). An over-bar denotes temporal averaging, angled brackets denote ensemble averaging. All velocity gradients were calculated from a central differencing scheme except along the volume edges a forward or backward differencing scheme was employed. For calculations involving the velocity gradients, the gradients at the volume edges were omitted. For the instantaneous velocity plots in the following section, the edge gradients were used.

3.4.1 Instantaneous Velocity Fields

The TPIV analysis gives fully volumetric 3 component and 3 dimensional velocity fields. The vorticity fields ω were calculated to observe and compare the vorticity structures present in each configuration (Figure 3.9). In this figure, the vorticity iso-surfaces showing ω_x are plotted with every third velocity vector with the mean velocity subtracted. The presence and size of vorticity is greater, as expected, in the G3G4 case compared to the G1G2 case. It is noted that G3G4 has larger grid sizes in the trash rack and, in a dimensionless

sense, it is nearer to the back of the trash rack. To further highlight this, the Q-criterion is plotted in Figure 3.10 overlaid with the fluctuating velocity. The Q-criterion is a method commonly used to isolate vortex centres, so the structures in this figure indicate the presence and size of the structures in the flow.

3.4.2 Mean Velocity Fields

Figure 3.11 shows contours of the average velocity U averaged over each x-plane and for each velocity field. The figure shows that the two configurations generate different flow regimes that are not homogenous in the y direction. In the G1G2 case, there is a strong under flow in the measured region. This is contrary to the G3G4 case, which tends to have a lower velocity at the bottom of the measurement volume. For both cases, the range of velocity does not exceed 10%.

The measured values of U for both cases correspond well with the 2D PIV measurements bulk flow velocity U_0 estimated from the flow rate. For both configurations, the contours indicate that the flow is decelerating in the stream-wise direction; this is explained by the increase in flow depth along x. The contour plots also show that more velocity fields are required to form the mean field, owing to the variability in the contour lines.

The plots of the average turbulence intensity $TI = u_i'/U$ (Figure 3.12) show another aspect to these flow fields. In the G1G2 configuration (Figure 3.12a) there is an approximately uniformly distributed, or *homogenous*, TI throughout the majority of the volume that decreases in the stream wise direction from $TI \approx 6\%$ to $TI \approx 5.5\%$. However, the volume also catches the top of the fluctuating boundary layer from the channel bottom, which is indicated by the locally high region of TI at the bottom of the figure. For the G3G4 case (Figure 3.12b), there is a steeper reduction in TI from about 11% to 9%, though it is not uniformly distributed y; there is a high TI in the lower, upstream side of the volume.

3.4.3 Spectral Analysis

The Taylor micro scales λ can be computed from the autocorrelation $Q(x)$ of the spatial velocity signal. For every streamwise row of velocity vectors along the x-axis, the auto-

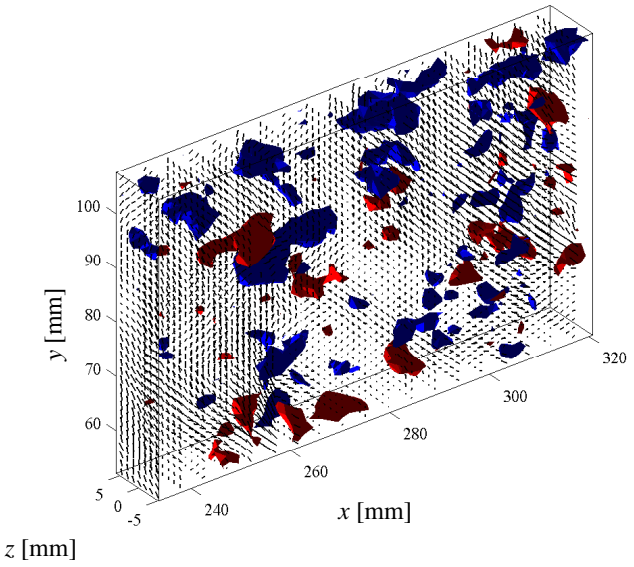

(a)

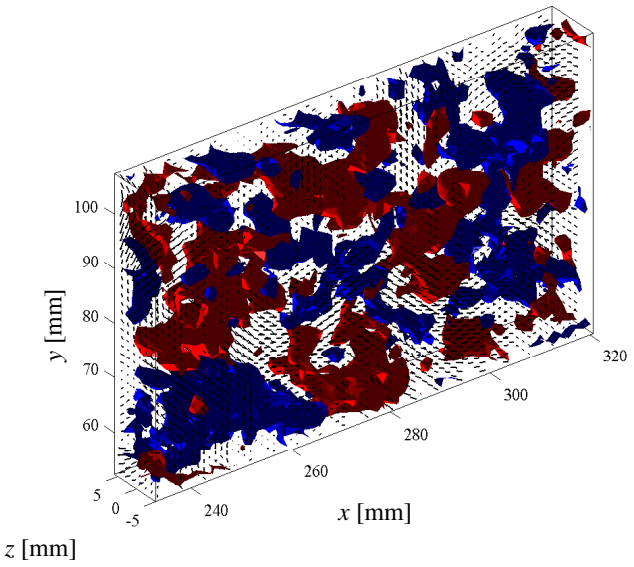

(b)

Figure 3.9: ω_x iso-contours at 0.008 s^{-1} (red) and -0.008 s^{-1} (blue) for configuration (a) G1G2 and (b) G3G4 with velocity vectors (1/6th plotted for clarity). Smaller structures and a lower vorticity level created by the smaller M can be visualised from the 3D instantaneous plots. Flow direction is from left to right.

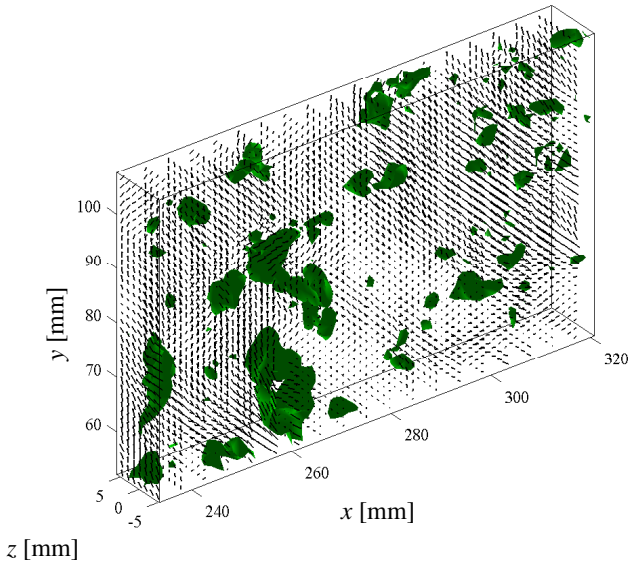

(a)

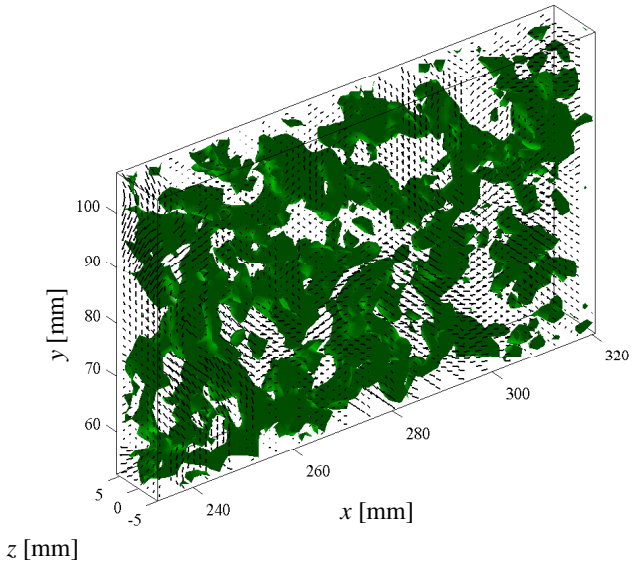

(b)

Figure 3.10: Q iso-contours at 0.040 s^{-2} for configuration (a) G1G2 and (b) G3G4 with fluctuating velocity vectors (1/6th plotted for clarity). Smaller structures and a lower vorticity level created by the smaller M can be visualised from the 3D instantaneous plots. Flow direction is left to right.

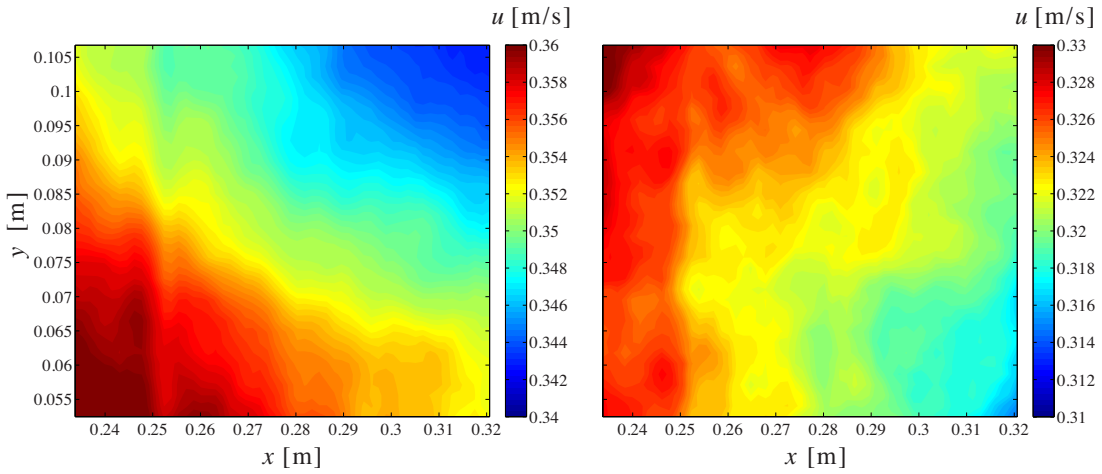

(a) (b)

Figure 3.11: Contour plots of the mean streamwise velocity component U for (a) G1G2 and (b) G3G4 show two different flow regimes. Flow direction is from left to right. Note that the contour scales have changed between (a) and (b) in order to show appropriate colour contrast of velocity.

correlation is calculated. λ can then be estimated from where the parabola that osculates with the normalised autocorrelation signal $Q(x)/\langle u_i'^2 \rangle$ intersects the abscissa (Pope, 2000). Each velocity component was normalised by its corresponding variance. A parabola of form $p(x) = 1 - x^2/\lambda^2$ was fitted to the central three points of the $Q(x)/\langle uv'^2 \rangle$, and from this, λ was found.

The Taylor micro scales for each component are presented in Table 3.2. The microscales show that the streamwise component of velocity u has the largest Taylor microscale for both cases, implying that there are larger vortices in the inertial range of the energy cascade in the streamwise direction. This is in line with the theory that the turbulence is distributed across the components from the mean flow direction. This result is also in line with the anisotropic behaviour reported in Figure 3.14b, however the largest length scales do not correspond in the G1G2 case. The Kolmogorov scales calculated in Section 3.2.3 correspond well with the Taylor microscales being approximately the same independent of the grid size. With respect to grid size (also presented in Table 3.2), there is a significant relative difference, with the normalised Taylor scales of G3G4 being half of

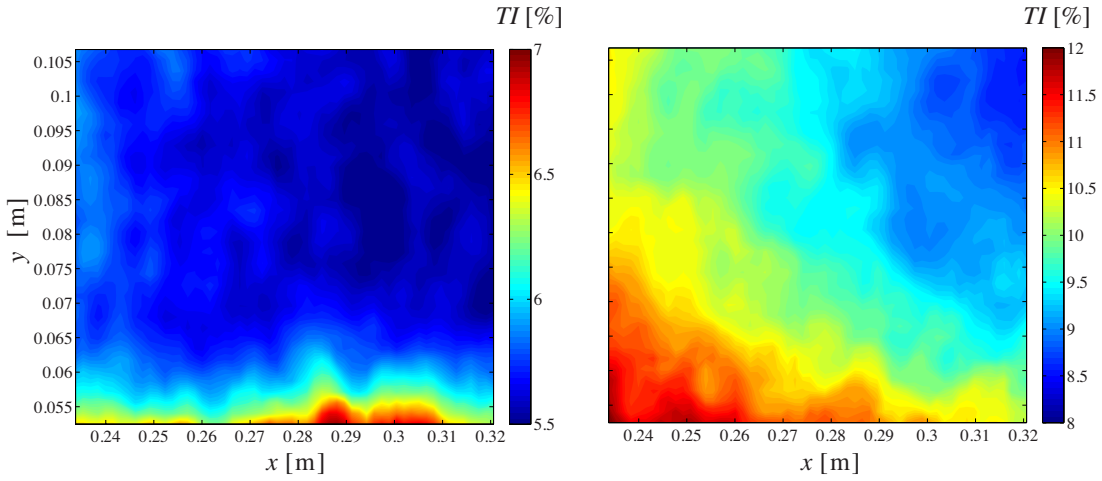

(a) (b)

Figure 3.12: Contour plots of the turbulence intensity ($TI = u_i'/U$) for (a) G1G2 and (b) G3G4. For G1G2, the water column and effect of the bottom of the channel is evident by the sharp increase in TI there; G3G4 does not have such discernible features. Flow direction is from left to right. Note that the contour scales have changed between (a) and (b) in order to show appropriate colour contrast of TI

those in G1G2. This shows that the size of vortices where viscosity becomes important is approximately independent of the grid size and closely related to the pool geometry.

The autocorrelation function $Q(x)$ can also be used to compute the integral length scale l_0 (Eq 3.4). The integral length scales characterise the largest eddies in the flow (Pope, 2000). $Q(x)$ was computed for the streamwise u, v and w components and presented in Figure 3.13.

$$l_0 = \frac{1}{\langle u'^2 \rangle} \int_0^\infty Q(x) \mathrm{d}x \tag{3.4}$$

Here, only the positive $Q(x)$ was considered for the l_0 calculations, which were conducted for each velocity component. The results of this analysis are presented in Table 3.2. Despite the large difference of M for both configurations, interestingly the largest eddy sizes are relatively similar between the trash racks. l_0 is seen to be largest for the stream wise component. This result seems anti-intuitive, as one would expect larger vortices pro-

Table 3.2: Turbulent length scales calculated from the autocorrelation function of velocity propagating down the streamwise direction, in both absolute terms and with respect to the grid size M

length scale	G1G2		G3G4	
	[mm]	[–]	[mm]	[–]
λ_u	5.23	$0.34M$	5.34	$0.15M$
λ_v	4.86	$0.31M$	4.92	$0.14M$
λ_w	4.01	$0.27M$	4.70	$0.13M$
$l_{0,u}$	8.60	$0.57M$	9.01	$0.25M$
$l_{0,v}$	7.08	$0.47M$	7.02	$0.20M$
$l_{0,w}$	5.72	$0.38M$	6.79	$0.19M$

duced by the larger grid. This is no doubt the case, however the results indicate that by the time the flow reaches midway down the pool, the larger vortices generated by the G3G4 grid have already largely cascaded into smaller vortices, only marginally larger than those produced by a grid under half its size. Thus, the vortices highlighted by the Q-criterion in Figure 3.10, that identified many more vortices in the G3G4 case with the Q-criterion, is misleading in terms of determining the size of the vortices.

3.4.4 Turbulence Kinetic Energy

The full turbulence kinetic energy k can be obtained from the three fluctuating components of velocity that were obtained. The definition of k is presented in Equation 3.5 and evolution of $k(x)$ is plotted in Figure 3.14.

$$k = \frac{1}{2}\Big(\langle u'u'\rangle + \langle v'v'\rangle + \langle w'w'\rangle\Big) \tag{3.5}$$

From Figure 3.14a it is observed that the decay of turbulence kinetic energy can be described by a power law. This confirms the trends of the decay of TI, which is essen-

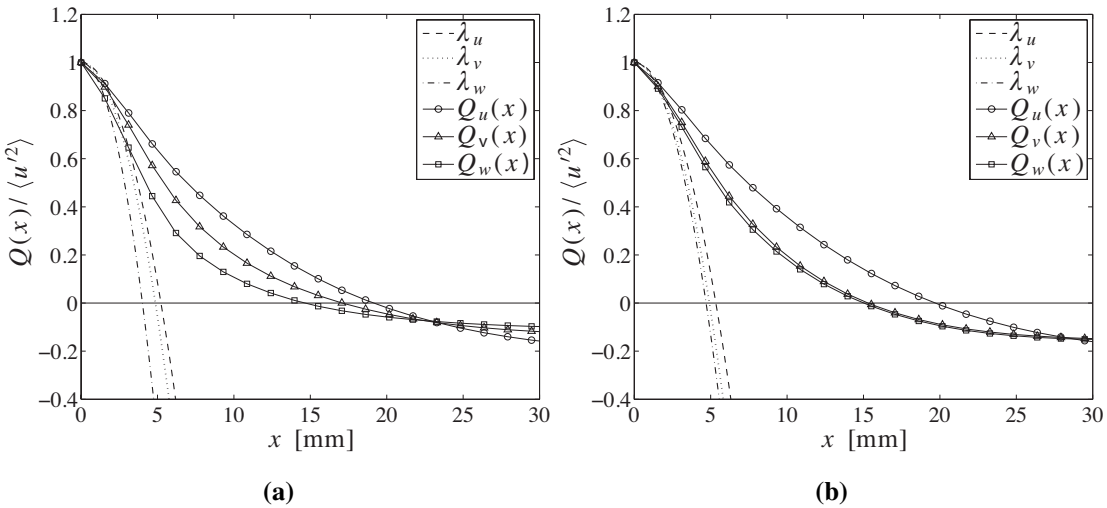

Figure 3.13: The autocorrelation of velocity components and Taylor microscale calculations for (a) G1G2 and (b) G3G4. u has the largest Taylor microscale for both cases, implying that there are larger energy carrying vortices in that direction.

tially the normalised square root of k. Thus, normalisation of the streamwise distance by M shows that the turbulence generated from the two different sized grids are related. This result bodes well with classical grid generated turbulence measurements (for example Lavoie et al, 2007), and with the theory presented in Section 1.10.1. However, note that for both cases, k does not exactly follow the power law, particularly at the streamwise limits. This shows that although related, there is still a significant difference between the flow fields. Figure 3.14b shows the components of the k, namely the variance of the fluctuating components $\langle u_i' u_i' \rangle$. For both grid configurations there are large disparities between the components, indicating an anisotropic flow. In the G3G4 case, the contributions of the streamwise and lateral components are approximately equal and are stronger than the vertical component. However this is not the case for the G1G2 configuration, where the lateral component is twice as strong as the stream wise and vertical components of velocity. This effect confirms the previous observation: the global flow conditions for each grid combination are not simply scaled versions of one another.

From the 2D PIV velocity fields presented in Figure 3.5, it can be seen that increasing M does not just augment the turbulence level, as it might in a classical grid generated

turbulence experiment, it also creates new global flow field. Aside from the free surface effects of the G1G2 case, the velocity decreases relatively constantly along the y the further downstream from the grid it is. On the other hand, the free surface jet is much more prominent in the G3G4 case, and there is also a strong under flow with a smaller flow reverse region towards the channel bottom (also visible in Figure 3.11). Therefore, the anisotropy, or more specifically, the modification of the anisotropic components can be explained by the change in global flow parameters.

It should be noted that TPIV reconstruction can induce a bias in the direction of the thickness of the laser sheet through the reconstruction of elongated particles (Scarano, 2013). This bias tends to increase the random noise in the correlation, which in turn increases the variance of w. Although this effect is not discounted from these results, it does not appear to be the case in the G3G4 configuration where the vertical fluctuating component is equally high, leading toward the conclusion that it is a flow feature. The influence of the boundary layer, as can be seen in Figure 3.12, is the reason that $\langle w'w' \rangle \langle u'u' \rangle$ for the G1G2 case.

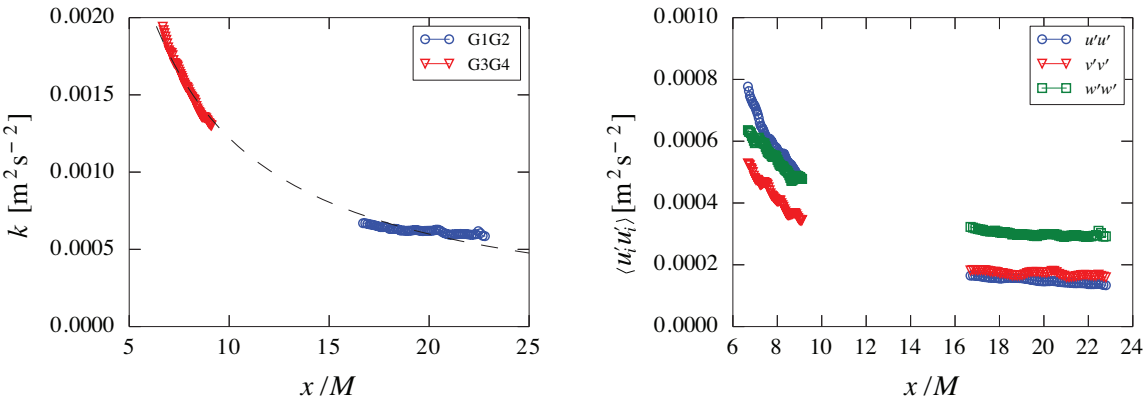

Figure 3.14: Evolution of (a) k and (b) the three components of k. The streamwise direction x is normalised by the respective grid spacing M, showing the decay of energy. The dashed line in (a) shows the power low of the form $A \cdot (x/M)^b$, where $A = 0.013$ and $b = -1.028$

3.4.5 Dissipation of turbulence energy

This section uses several techniques to calculate the energy dissipation in the pool. The results computed in the following sections are presented in Table 3.3. To compare the bulk energy dissipation ε_B with the energy dissipation measured in the pools, ε_B is multiplied by the ratio of the measurement volume to the volume of the pool, so that

$$\varepsilon_{B,\mathrm{V}} = \varepsilon_B \frac{XYZ}{LWh_c} \tag{3.6}$$

where the subscript V indicates averaging over the volume. The discussion of this method with those that follow is presented in Section 3.4.6.

Energy dissipation in measurement volume by Bernoulli analysis

A direct comparison of the bulk dissipation at the channel scale cannot be compared efficiently with the dissipation measured by TPIV. However, the TPIV results could be compared to a Bernoulli analysis of the flow in the measurement volume by considering the time average velocity statistics. In Section 3.2.3, the analysis of Eq. 3.1 from the global pool reduced to $y_1 - y_2 = \Delta H_B$. To analyse the measurement volume however, the measured flow conditions such as k and U can replace the bulk flow rate, and the change in elevation can be modified to consider the vertical component of velocity, so that the Bernoulli's equation becomes

$$\frac{1}{\rho g}(p_1 - p_2) + \frac{1}{2g}(k_1 - k_2) + \frac{1}{2g}(U_1^2 - U_2^2) + \int_1^2 \frac{V(x)}{U(x)}\mathrm{dx} = \Delta H_{\text{pool,1-2}} \tag{3.7}$$

where the 1 and 2 subscripts indicate the upstream and downstream positions of the measurement volume $x = 0.225$ and $x = 0325$ m, respectively, and $\Delta H_{\text{pool,1-2}}$ are the losses for the whole depth of the pool between points 1 and 2 in x. The integral term containing $V(x)/U(x)$ computes the elevation change of the flow, extracted from the mean velocity fields. Note that the mean flow is assumed to be 2D in the volume, $W \approx 0$. The pressure terms are calculated by calculating the water depth at 1 and 2 from the raw 2D PIV images (Appendix A.4). An assumption of statistical stationarity has also been applied. The

calculation of these terms is presented in Appendix A.3. Finally, to calculate the ensemble averaged energy dissipation in the volume $\langle\varepsilon\rangle_{\mathrm{V}}$, Eq. 3.2 is modified to

$$\frac{gQ_{\mathrm{V}}\Delta H_{\text{pool,1-2}}}{XYZ}\cdot\frac{Y}{h_c}\cdot\frac{Z}{W}=\langle\varepsilon\rangle_{\mathrm{V}} \tag{3.8}$$

to reflect analysis in the measurement volume. In Eq. 3.8, Q_{V} is the flow rate through the volume, computed directly from $\langle U\rangle$ and the fractions Y/h_c and Y/h_c have been introduced as the losses contained in $H_{\text{pool,1-2}}$ are for the full depth and width of the pool, respectively, and thus must be reduced over the measurement volume. The results of this analysis are presented in Table 3.3 and are discussed further in Section 3.4.6.

Calculation of energy dissipation from decay of turbulent kinetic energy

The decay of $k(x)$ (Figure 3.14a) can also be used as an estimator for the dissipation rate $\langle\varepsilon\rangle_k$, as defined in Equation 3.9 (Buchmann et al, 2010). In order to determine the gradient, a power law was fitted to both cases, and the derivative taken in the middle of the volume ($x=0.275$) (See Appendix A.3 for the fitting data). These results are presented in Table 3.3 and compared with the other turbulence statistics.

$$\langle\varepsilon\rangle_k=-\frac{1}{2}\langle U\rangle\frac{\mathrm{d}\langle k\rangle}{\mathrm{d}x} \tag{3.9}$$

Direct calculation of energy dissipation

Finally, the energy dissipation $\langle\varepsilon\rangle$ was obtained directly from Equation 3.10 (George and Hussein, 1991) from the TPIV measurements. As can be seen, the equation requires the full velocity gradient tensor, which TPIV is able to yield.

$$
\begin{aligned}
\langle \varepsilon \rangle \;=\; \nu \Bigg\{ & 2\Big(\Big\langle \frac{\partial u}{\partial y}\frac{\partial v}{\partial x} \Big\rangle + \Big\langle \frac{\partial u}{\partial z}\frac{\partial w}{\partial x} \Big\rangle + \Big\langle \frac{\partial v}{\partial z}\frac{\partial w}{\partial y} \Big\rangle \Big) \\
& + \Big\langle \Big(\frac{\partial u}{\partial y}\Big)^2 \Big\rangle + \Big\langle \Big(\frac{\partial v}{\partial x}\Big)^2 \Big\rangle + \Big\langle \Big(\frac{\partial u}{\partial z}\Big)^2 \Big\rangle \\
& + \Big\langle \Big(\frac{\partial w}{\partial x}\Big)^2 \Big\rangle + \Big\langle \Big(\frac{\partial v}{\partial z}\Big)^2 \Big\rangle + \Big\langle \Big(\frac{\partial w}{\partial y}\Big)^2 \Big\rangle \\
& + 2\Bigg(\Big\langle \Big(\frac{\partial u}{\partial x}\Big)^2 \Big\rangle + \Big\langle \Big(\frac{\partial v}{\partial y}\Big)^2 \Big\rangle + \Big\langle \Big(\frac{\partial w}{\partial z}\Big)^2 \Big\rangle \Bigg) \Bigg\}
\end{aligned}
\tag{3.10}
$$

To use the ensemble average, the flow must be statistically stationary, $\partial\varepsilon/\partial t = 0$. Figure 3.15a shows the plot of the magnitude of the spatially averaged $\langle\varepsilon\rangle$ for each independent velocity field. From this figure the steady state condition can be confirmed, as there is no evolution with time. Figure 3.15a also shows that the variance of $\langle\varepsilon\rangle$ is high, the standard deviation divided by the $\langle\varepsilon\rangle$ for G1G2 is 24% while for G3G4 it is 17%. The mean and standard deviation of $\langle\varepsilon\rangle$ are presented in Table 3.3. Note that this metric does not consider the spatial variation and that this is the variance of data that is already *spatially averaged*. The standard deviation of *each* dissipation point in the volumes was also calculated, and the equivalent metrics are 360% for G1G2 and 460% for G3G4. These metrics show the importance of acquiring a significant amount of data so that the mean values are not overly contaminated by the variance.

Figure 3.15b shows the cumulative mean of $\langle\varepsilon\rangle$ and it can be observed that the mean converges after approximately 300 velocity fields. Considering the high standard deviation, as discussed earlier, this again confirms that the flow was statistically stationary over time. The Kolmogorov microscale η_ε is computed by substituting Eq. 3.10 into $\eta_\varepsilon = (\nu^3/\varepsilon)^{1/4}$, also presented in Table 3.3.

In Figure 3.15c, $\langle\varepsilon\rangle$, spatially averaged in y- z-planes, is plotted as a function of x/M. From this figure it can be seen that the dissipation decreases rapidly along x/M for the G3G4 case while it remains approximately constant for the G1G2 case further 'downstream'. This finding is consistent with the turbulence theory presented in Section 1.10.1.

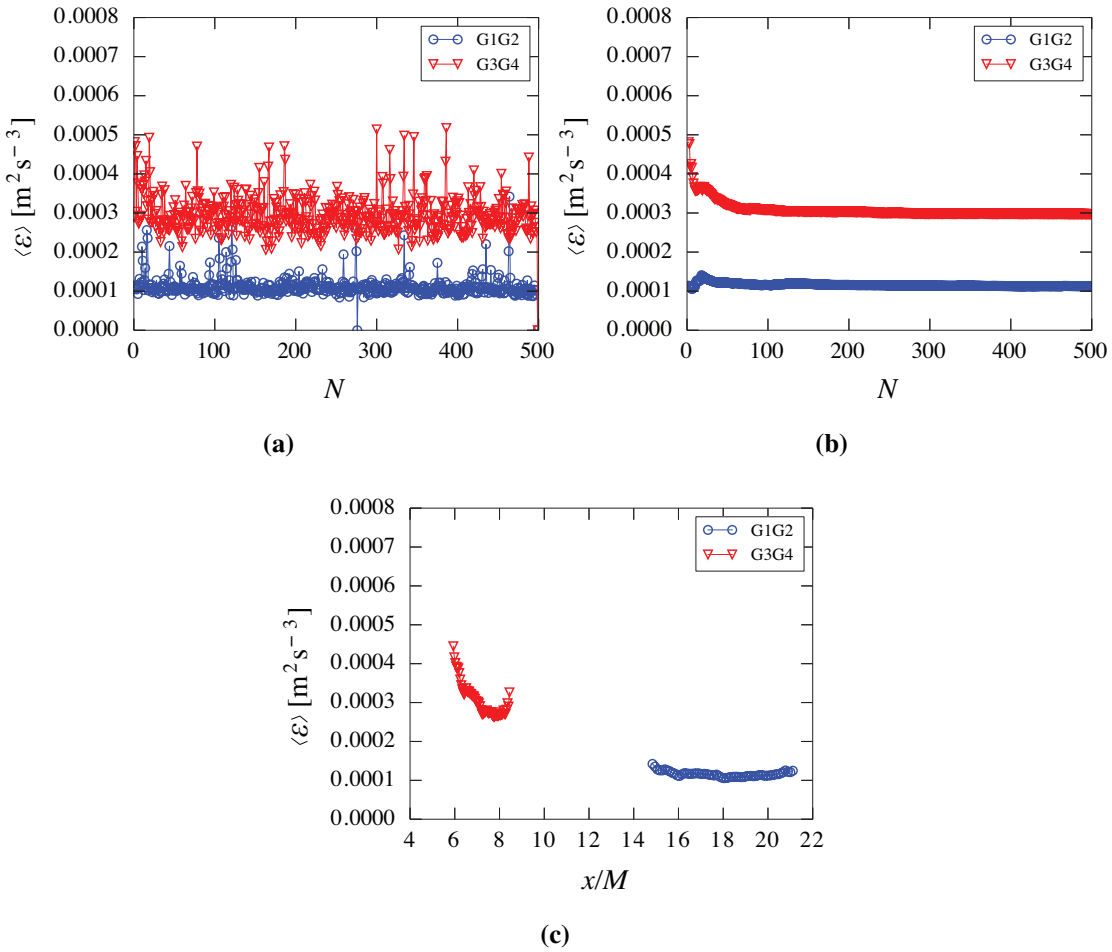

Figure 3.15: Evolution of the energy dissipation $\langle \varepsilon \rangle$ against (a) sample number N, (b) the cumulative average, and, (c) against the streamwise distance x normalised by grid size M.

Vorticity analysis

Figure 3.16 shows the root mean square (RMS) of each vorticity component where anisotropy can be observed. The RMS is appropriate in this case as the mean of the vorticity components was found to be zero. The vorticity in Figure 3.16 has a slightly stronger ω_z component than the ω_x and ω_y components in the G3G4 configuration, corresponding to vortices that *roll* down the flow. For the G1G2 case, no such observation can be drawn, with essentially isotropic vorticity components. The spatial and temporal average of enstrophy $\langle \omega^2 \rangle$ is another turbulent characterisation of the vorticity energy presented in Table 3.3. From

a superficial interpretation of Figure 3.9, these results bode well as the G3G4 case shows much more vorticity at the iso-surface threshold than its G1G2 counterpart.

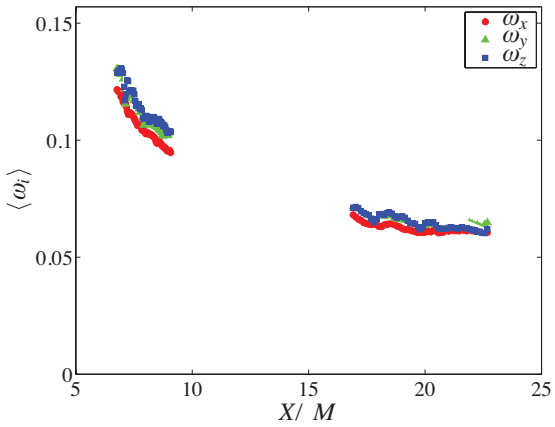

Figure 3.16: Dissipation of vorticity ω in the direction of flow for G1G2 and G3G4 configurations.

3.4.6 Comparison of energy dissipation methods

This section compares the computation of $\langle\varepsilon\rangle_{\mathrm{V}}$, $\langle\varepsilon\rangle_k$ and $\langle\varepsilon\rangle$ from the TPIV results to the bulk energy dissipation $\varepsilon_{B,\mathrm{V}}$, computed from the global flow conditions. These results are presented in Table 3.3. Recall that $\varepsilon_{B,\mathrm{V}}$ is a global approximation of the pools' dissipation by considering two corresponding points in consecutive pools and computing the losses with the Bernoulli equation; $\langle\varepsilon\rangle_{\mathrm{V}}$ integrates the Bernoulli equation onto the measurement volume; $\langle\varepsilon\rangle_k$ is calculated from the decay of k, and; $\langle\varepsilon\rangle$ is calculated from the gradients in the measurement volume.

The bulk calculation characterises the global flow, therefore in comparison with the locally derived metrics, this measure should yield the most approximate results. Unlike $\langle\varepsilon\rangle_k$ and $\langle\varepsilon\rangle$, $\varepsilon_{B,\mathrm{V}}$ is higher for G1G2, which is explained by the higher head drop ΔH across the trash racks. The higher ΔH results in a reduced h_c, and hence higher $\varepsilon_{B,\mathrm{V}}$ (from Eq 3.2). This can be physically explained due to the greater amount of shear created by the smaller grids, related to its greater L_{P} (Figure 3.4). Combining this observation with

Table 3.3: Summary of spatially and temporally averaged turbulence statistics. Bracketed terms indicate the corresponding standard deviation values. This table includes the bulk calculation of dissipation to aid comparison.

Statistic		G1G2	G3G4
TI	[–]	5.67 %	9.92 %
TKE ($\times 10^4$)			
$\langle k \rangle$	[m^{2}s^{-2}]	6.21	15.6
$\langle u'u' \rangle$	[m^{2}s^{-2}]	2.95	11.9
$\langle v'v' \rangle$	[m^{2}s^{-2}]	3.42	8.45
$\langle w'w' \rangle$	[m^{2}s^{-2}]	6.02	10.82
Dissipation ($\times 10^3$)			
$\varepsilon_{B,\mathrm{V}}$ (Eq. 3.6)	[m^{2}s^{-3}]	0.167	0.150
$\langle \varepsilon \rangle_{\mathrm{V}}$ (Eq. 3.8)	[m^{2}s^{-3}]	1.57	0.47
$\langle \varepsilon \rangle_k$ (Eq. 3.9)	[m^{2}s^{-3}]	0.14	1.17
$\langle \varepsilon \rangle$ (Eq. 3.10)	[m^{2}s^{-3}]	0.11 (0.03)	0.30 (0.05)
Vorticity			
$\langle \omega \rangle$	[s^{-1}]	0.129 (0.005)	0.222 (0.012)
$\langle \omega_i \rangle$	[s^{-1}]	0.062 (0.004)	0.106 (0.008)
$\langle \omega_j \rangle$	[s^{-1}]	0.066 (0.004)	0.113 (0.009)
$\langle \omega_k \rangle$	[s^{-1}]	0.065	0.114
Enstrophy			
$\langle \omega^2 \rangle$	[s^{-2}]	0.017	0.049
Length scales			
$l_{0,u}$	[mm]	8.60	9.01
λ_u	[mm]	5.23	5.34
η_ε	[mm]	0.34	0.27

Table 3.4: Contribution of terms in Equation 3.7 for the calculation of ΔH_{pool}

Case	$\frac{1}{\rho g}(p_1 - p_2)$	$\frac{1}{2g}(k_1 - k_2)$	$\frac{1}{2g}(U_1^2 - U_2^2)$	$\int_1^2 \frac{V(x)}{U(x)}\mathrm{dx}$
G1G2	8.7%	0.0%	0.0%	91.2%
G3G4	25.6%	2.2%	0.0%	72.2%

the locally calculated ε leads to the conclusion that there is a higher dissipation of energy immediately behind the trash racks for G1G2: the higher vorticity created upstream has largely dissipated by the time the flow reaches the centre of the channel where the measurements are made. This means that the smaller G1G2 grids generate more vortices which dissipate more flow energy and hence $\varepsilon_{B,\text{V,G1G2}} > \varepsilon_{B,\text{V,G3G4}}$. On the other hand, the larger vortices generated by the G3G4 case persist further downstream and have a strong level of dissipation by the time they reach the measurement region.

The Bernoulli analysis integrated over the volume provides the most comprehensive estimation for ε, as it considers both local and global features of the flow in the pool. As per the bulk calculation, $\langle\varepsilon\rangle_{\text{V,G1G2}} > \langle\varepsilon\rangle_{\text{V,G3G4}}$, however the difference is threefold. To investigate this further, the proportional contribution of total energy of each term in Eq. 3.7 was calculated (Table 3.4), as the $\Delta H_{\text{pool,1-2}}$ is directly proportional to $\langle\varepsilon\rangle_{\text{V}}$. Interestingly, the kinetic energy and mean flow drop contribute a negligible amount to $\Delta H_{\text{pool,1-2}}$: the majority of the energy is owed to the change in flow elevation. The energy from the pressure head term also plays a significant role. This analysis shows that the application of the Bernoulli equation considers the global properties more than the local, and is as not dependent on measurement resolution as the larger scale vortices are those that contain the most energy. Comparing the results to $\varepsilon_{B,\text{V}}$, this analysis implies that the energy dissipation at the centre of the pool is greater than the bulk mean. This can be explained by considering that the flow still has a significant portion of the pool to flow down, and as the flow profile is not uniform, there are likely to be regions in the flow where the dissipation is lower. The $\langle\varepsilon\rangle_{\text{V,G1G2}}$ was found to be an order of magnitude greater than the other three methods for the same grid. This seems to imply that greater dissipation is occurring at the boundary of free surface. With respect to $\langle\varepsilon\rangle_{\text{V,G3G4}}$, it is three times greater than $\varepsilon_{B,\text{V,G3G4}}$

As previously mentioned, both $\langle\varepsilon\rangle_k$ and $\langle\varepsilon\rangle$ yield greater dissipation for the G3G4 case than for G1G2. This appears to be inline with the other turbulence metrics, such as greater vorticity and k for the G3G4 case. $\langle\varepsilon\rangle_k$ only considers dk/dx and $\langle U\rangle$ in its formulation. It was shown in Section 1.8 that k represents a lossless transfer of energy from the large to small scales. Recall that the larger scales contain the greatest proportion of k (Figure 3.8 and Figure 1.1). The results of $\langle\varepsilon\rangle_k$ presented in Table 3.3 were taken at the centre of the volume, so considering the x limits of the volume, $0.116\cdot10^3 < \langle\varepsilon\rangle_{k,\mathrm{G1G2}} < 0.184\cdot10^3$ and $1.85\cdot10^3 < \langle\varepsilon\rangle_{k,\mathrm{G3G4}} < 0.850\cdot10^3$ m^{2}s^{-3}. Regarding $\langle\varepsilon\rangle_{k,\mathrm{G1G2}}$, its value is well aligned with all but $\langle\varepsilon\rangle_{\mathrm{V,G1G2}}$. For $\langle\varepsilon\rangle_{k,\mathrm{G3G4}}$, it is an order of magnitude greater than $\varepsilon_{B,\mathrm{V,G3G4}}$, and several times greater than the remaining methods.

The last method for calculating the energy dissipation, $\langle\varepsilon\rangle$, is calculated on the gradients of the flow. Six of the nine gradients are shearing type gradients, that work against the viscosity of the fluid. As has been previously discussed, it is the smallest scale vortices that dissipate kinetic energy into internal energy. As the vector spacing of the gradients used to calculate $\langle\varepsilon\rangle$ were not at small enough, it is expected that this result would underestimate the dissipation (Tokgoz et al, 2012). This is indeed the case, where $\langle\varepsilon\rangle_{\mathrm{G1G2}}$ is approximately 30% less than $\langle\varepsilon\rangle_{k,\mathrm{G1G2}}$ and 50% less than $\varepsilon_{B,\mathrm{V,G1G2}}$. It is seen that $\langle\varepsilon\rangle_{\mathrm{G3G4}}$ is three times greater than $\langle\varepsilon\rangle_{\mathrm{G1G2}}$.

In summary, this section shows the difficulties an experimentalist may have in computing the energy dissipation in an open channel flow. With relative certainty it can be stated that $\langle\varepsilon\rangle$ would tend to underestimate the dissipation. One might hypothesise that ε_B would obtain approximately the correct magnitude. However it could not distinguish between the local flow conditions, which from an analysis of $\langle k\rangle$, $\langle\omega\rangle$ and the instantaneous plots indicate a greater turbulence and vorticity level, implying greater dissipation there. The same could be said for the calculation of $\langle\varepsilon\rangle_{\mathrm{V}}$, where one might make the hypothesis that a close approximation to be found, but the same problem arises where the G1G2 dissipation was found to be the highest.

In order to investigate these findings further, an analysis of the flow along the bed of the flume has been undertaken and is presented in Chapter 4. One of the aims is to conduct similar analyses in another measurement region, to enhance the understanding of how the

flow energy is dissipated into internal energy. It should be noted that a high frequency point measurement technique such as LDV could indeed be employed to obtain the full energy spectrum and hence give a better indication of the required resolution of the TPIV system. In this way, the limitations and accuracy of each calculation of the dissipation could be correctly validated. This is the subject of future work. The following section computes the errors of the TPIV measurements, confirming that the measurements are high quality with minimal uncertainties.

3.5 Error analysis

Finally, an uncertainty analysis method proposed by Moffat (1988) and utilised by Atkinson et al (2011) was used to determine the random velocity error $\delta(u)$. $\delta(u)$ can be determined from the error in the fluctuating divergence $\delta(\nabla \cdot u_i')$, which is approximated by the RMS of the fluctuating divergence, by

$$\delta(\nabla \cdot u_i') = \sqrt{\frac{3}{2(\delta x)^2}}\delta(u) \tag{3.11}$$

if the assumption is made that the $\delta(u)$ is uniform in all directions. To obtain units of px/px (:= m/m), the gradients are multiplied by Δt; Table 3.5 presents the results. $\delta(u)$ was found to be less than or equivalent to other recent studies ranging from Scarano et al (2006) with $\delta(u) \approx 0.2$ px, Atkinson et al (2011) with $\delta(u) \approx 0.5$ px, and Buchmann et al (2011) with $\delta(u) = 0.2$ px. The velocity errors of this study correspond to relative errors in the order of $1 - 2\%$. This relatively low level of uncertainty indicates good quality results.

3.5.1 Divergence Tests

The analysis of the velocity gradients $V_{ij} = \partial u_i / \partial x_j$ can give an indication of the accuracy of the results (Ganapathisubramani et al, 2007; Khashehchi et al, 2010; Mullin and Dahm, 2006). For incompressible flows, it follows that for every point in the flow, $\nabla \cdot \mathbf{u} = 0$ in order to conserve mass. The infinitesimal gradients in experimental data are approximated from

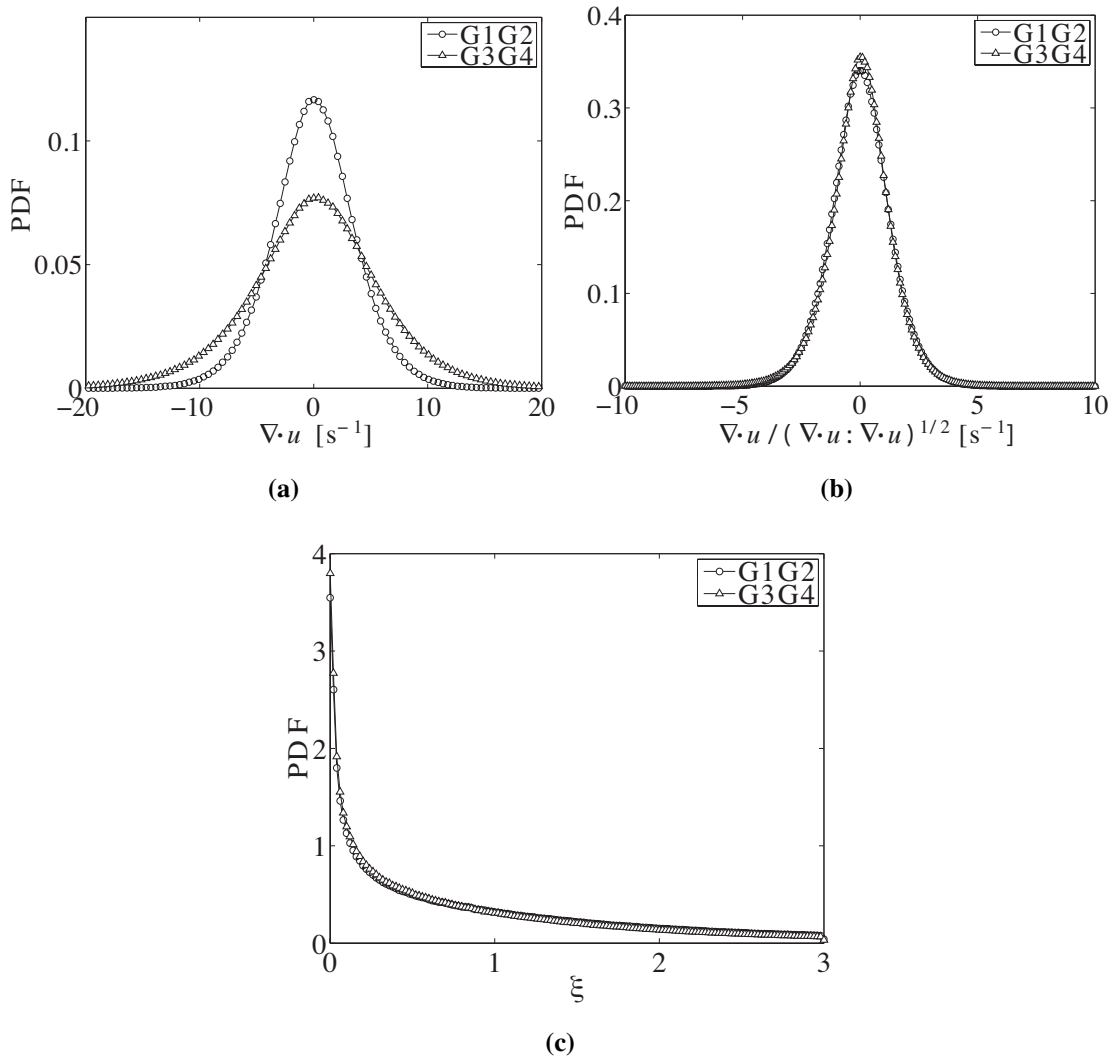

Figure 3.17: Probability density functions of (a) $\nabla \cdot \mathbf{u}$ (b) $\nabla \cdot \mathbf{u}/(\nabla \cdot \mathbf{u} : \nabla \cdot \mathbf{u})^{1/2}$ for the G1G2 and G3G4 configuration. (c) shows the evolution of ξ for both configurations

the discretised velocity vectors and their coordinates by a second order central differencing scheme, for example:

$$\frac{\partial u}{\partial x} \approx \frac{\Delta u_i}{\delta x_i} = \frac{u_{i-1} - u_{i+1}}{2\delta x} \tag{3.12}$$

where in this case the subscript i refers to the index of the vector location. The deviation from zero divergence can be related to random errors in the measurement, but there is also

a contribution of the resolution of the data. The larger δx is, the less the infinitesimal assumption holds true. In Figure 3.17 the probability density functions (PDFs) for $\nabla \cdot \mathbf{u}$ and the $\nabla \cdot \mathbf{u}$ normalised by the norm of the global divergence $|\nabla \cdot \mathbf{u}|$ are shown. From Figure 3.17a, G3G4 is observed to have a greater divergence error than the G1G2 case. This is apparently owing to the greater level of fluctuations in the larger grid case and higher Re_M, but with a lower Re_{D_H}. The rms of the normalised divergence is in the order of three times greater than studies from Worth et al (2010) and Buchmann et al (2011), however the finest resolution of those studies were approximately seven times finer than in this work. Thus the higher rms of the divergence can be explained by the departure from the resolution of an infinitesimal fluid element (Section 1.2).

The result in Figure 3.17a highlights the difficulty in conducting turbulence measurements experimentally. In both configurations, all experimental parameters were constant: the seeding density, camera orientation, reconstruction and correlation parameters, Δt between images and flow rate. A change to a courser grid geometry resulted in a slower flow with higher turbulence intensity. It is unclear whether or not the higher divergence error in the G3G4 case is due to higher uncertainty (relative error) in the interrogation volume displacement or the flatter correlation peak due to the higher fluctuations.

DeSilva et al (2013b) have recently implemented a divergence correction scheme that has shown to reduce the divergence of TPIV measurements and could be a promising remedy to reduce the divergence. However, the effects of applying such a scheme on multiple resolutions has yet to be rigorously investigated, particularly on the resolutions found in this study.

Normalising the divergence by its norm (Figure 3.17b) collapses both curves on top of each other. As stipulated by Atkinson et al (2011), this is due to the norm containing the errors of the divergence within. Figure 3.18 shows the joint PDFs of the divergence gradients in order to investigate these errors further. As per Ganapathisubramani et al (2007), the joint PDF of ∂u_x against $-(\partial v_y + \partial w_z)$ is shown along with the other two permutations of rearranging the $\nabla \cdot \mathbf{u}$ equation. The diagonal through these plots indicate the divergence free line, and the spread around this line characterise the divergence error. The figures reveal similar patterns when comparing corresponding gradients between the

two configurations. The contour lines for the G1G2 case differ to those of the G3G4 due to the higher overall divergence error shown in Figure 3.17a. From this analysis, the $\partial u/\partial x$ gradients have the greatest tendency to zero, while the $\partial v/\partial y$ gradients have the least. Interestingly, these are not the out-of-plane gradients, where it may be expected that due to particle elongation and higher variance might lead to higher contribution to the divergence error.

To further investigate the quality of the results, ξ, a stringent divergence test proposed by (Zhang et al (1997)) and defined as

$$\xi = \frac{\left(\frac{\partial u}{\partial x} + \frac{\partial v}{\partial y} + \frac{\partial w}{\partial z}\right)^2}{\left(\frac{\partial u}{\partial x}\right)^2 + \left(\frac{\partial v}{\partial y}\right)^2 + \left(\frac{\partial w}{\partial z}\right)^2} \tag{3.13}$$

was calculated. This equation expresses the ratio of the divergence squared divided by the sum of the squared linear deformation gradients that form the divergence. Hence, ξ can quantify the magnitude of divergence errors, where the lower the value of ξ, the better quality are the results. The evolution of ξ for both the G1G2 and G3G4 configurations are presented in Figure 3.17c and the means presented in Table 3.5. It can be seen that both grid combinations have equivalent evolution of ξ, and the mean values of ~ 0.74 – 0.8 is in the range found in the DNS study of Zhang et al (1997) and before additional filtering by Ganapathisubramani et al (2007).

The results obtained in the previous section are presented in Table 3.3. It is evident that from the various methods of analysing the divergence error (normalising by $|\overline{\nabla \cdot \mathbf{u}}|$, ξ) or from the anticipated error on the velocity measurements (Equation 3.11) gives varying indications on the accuracy and confidence level of these measurements. Compared to Ganapathisubramani et al (2007) and Worth et al (2010), the joint PDFs (Figure 3.18) do not follow the divergence free line with the same level of correlation, but are similar to those found in Buchmann et al (2011). The mean of ξ was found to be in the same level as Zhang et al (1997) who analysed a DNS study. It was found that comparing $\delta(u)$ to other TPIV measurements gives equivalent or better uncertainty results.

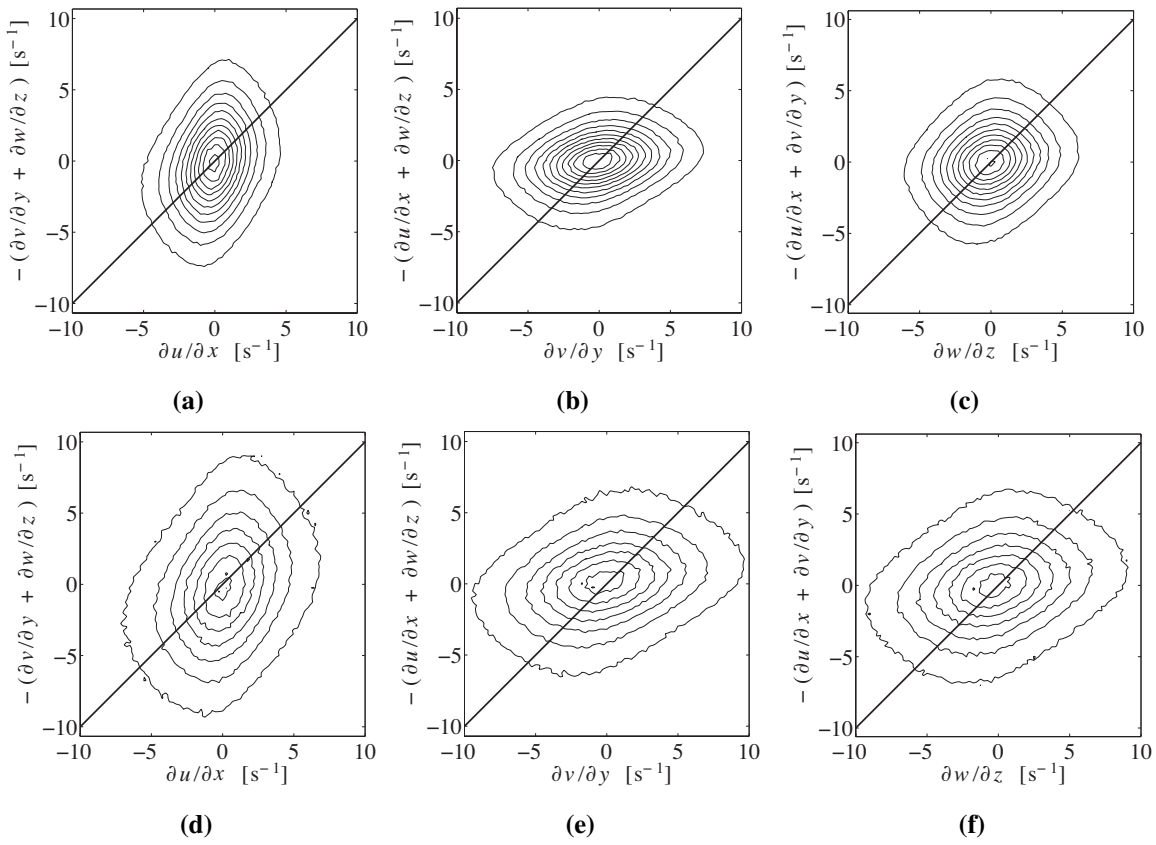

Figure 3.18: Joint PDF of the divergence gradients for (a – c) G1G2 and (d – e) G3G4. The contours start at a minimum of 6.25×10^{-4} s^{-1} and increase in increments of 6.25×10^{-4} s^{-1}.

Table 3.5: Velocity gradient statistics of the flow for each grid combination

Statistic		G1G2	G3G4
$\overline{\nabla \cdot \mathbf{u}}$	[s^{-1}]	0.021	0.031
$var(\nabla \cdot \mathbf{u})$	[s^{-1}]	14.54	37.28
std$(\nabla \cdot \mathbf{u})$	[s^{-1}]	3.81	6.11
$\nabla \cdot \mathbf{u}/\lvert\overline{\nabla \cdot \mathbf{u}}\rvert$	[–]	0.007	0.007
$var(\nabla \cdot \mathbf{u}/\lvert\overline{\nabla \cdot \mathbf{u}}\rvert)$	[–]	1.68	1.75
std$(\nabla \cdot \mathbf{u}/\lvert\overline{\nabla \cdot \mathbf{u}}\rvert)$	[–]	1.30	1.32
$\overline{\xi}$	[–]	0.795	0.745
$\delta(\partial u_i/\partial x_i)$	[px/px]	0.0076	0.0122
$\delta(u)$	[px]	0.10	0.15

3.6 Closing remarks

This chapter measured the flow in the centre of a pool in an open channel flow with TPIV. The 2D PIV results showed that the grids, despite having the same solidity ratio and geometry, generated different global flow fields in the pool. This is supported by the results of the turbulent analysis, which showed the anisotropy of the turbulent kinetic energy components. The size and prominence of three dimensional structures was visualised and quantified (Figures 3.9 & 3.10). It is important to recall that the vorticity and Q-criterion all required the full velocity gradient tensor to calculate.

The mean velocity and turbulence profiles showed two very different flow regimes for both cases. The small G1G2 configuration showed TI that appeared to be homogeneous in the water column with strong influences from the boundary layer and higher local velocity toward the channel bottom. For the G3G4 case, although there is also a tendency of higher TI towards the channel bottom, the mean velocity profile showed that the higher amplitudes tended to be higher off the bottom. Therefore the flows that were investigated were not Re_M independent.

Despite the lack of Re_M dependence, the decay of k along the normalised streamwise

direction (Figure 3.14) showed that a single power law could indeed link the two cases. It can also be seen that the flow is highly anisotropic in terms of the components of k, however in terms of the components of vorticity, there is a much less pronounced anisotropy. Turbulence statistics such as the λ and l_0 were determined. From this analysis, it was seen that the dominate sizes of the vortices in the flows were similar. This is a rather counter intuitive result as one might expect larger vortices in the G3G4 case owing to the larger M. This shows that although the vorticity and enstrophy showed higher levels in G3G4, the length scales indicate that the largest vortices of size l_0 are equivalent. The Taylor microscales, indicating the length scales when viscous effects become important, are also equivalent, as Re for each configuration is similar.

Finally, the difficulty of calculating the energy dissipation has been highlighted. An analysis of four methods was conducted, comparing global properties to local. To investigate this further, two regions along the channel bed were investigated in Chapter 4, enabling these differences to be decomposed further.

The aim of this chapter was to characterise the turbulence in an open channel. To this end, several important turbulence parameters were found, showing the decay of turbulence energy, the decay of vorticity and the decay of energy dissipation. The largest sizes of vortices were determined, and the 3D flow features were visualised. These measurements were made possible by the implementation of a vibration correction scheme. An analysis such as this has important implications in hydraulic engineering. By changing the grids in the channel, different turbulent flow fields were generated. These results can be used to study the turbulent mixing in rivers and to link the effects of turbulent parameters on the swimming performance of fish.

Chapter 4

Analysis of Turbulent Boundary Layer with TPIV

4.1 Introduction

Studying turbulence in open channel flows is an important endeavour to predict the transport of turbulent energy and momentum, and the processes of mixing and vortex structures. The aim of this chapter is to continue the investigation of the turbulence in an open channel flow to gain an insight into its energy dissipation, generation, and anisotropy. In the flow considered in this work, the turbulence is generated at the wall and through a series of trash racks. An objective is to investigate the influence of the turbulence generated at the grid compared to the generation at the wall, and hence measurements are conducted near the channel bottom. In this work, tomographic particle image velocimetry (TPIV) was used to capture full three dimensional velocity fields in an open channel flow at the wall.

Open channel flows can be divided into three main regions as a function of the depth of the flow h in the wall normal direction y (Nezu and Nakagawa, 1993): (1) the wall region $(y/h \lesssim 0.15)$, where the 'inner' boundary layer treatments are applicable; (2) the free surface region $(y/h \gtrsim 0.6)$, where the global flow properties such as h and the bulk velocity define turbulent structures. This is also where the free surface acts to dampen out turbulent fluctuations normal to its surface, and; (3) the intermediate region $(0.15 \lesssim y/h \lesssim 0.6)$,

which is not strongly influenced by the wall nor the free surface (Figure 4.1). The TPIV measurement regions in this paper are $0 < y/h < 0.12$, and therefore in the wall region.

A prominent feature of wall bounded shear flows is the presence of coherent vortex structures that occur at a range of scales as a function of the distance from the wall. These features include streaks, omega vortices, hairpin structures, ejections and sweeps that travel together in packets (Ganapathisubramani et al, 2003; Hurther et al, 2007). These structures have been shown to propagate from the 'inner' to the 'outer' boundary layer (Adrian et al, 2000). The outer boundary layer is outside of the inertial sublayer, from the definition of boundary layer theory, within the wall region of an open channel flow (Section 1.10.1). A schematic of the division of the wall region flow into the boundary layer regions and their respective heights is presented in Figure 4.2.

Sweeps, or Q4 regions, occur when $v' < 0, u' > 0$, and ejections, or Q2 regions, occur when $v' > 0, u' < 0$, where the primes indicate the velocity fluctuation from the mean field

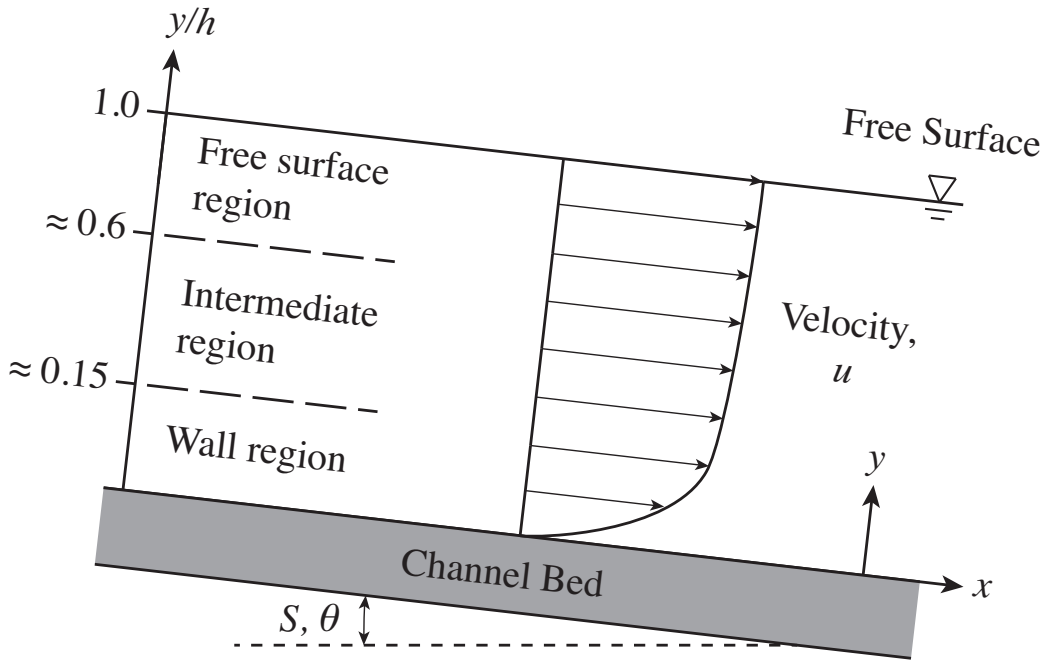

Figure 4.1: Schematic of an open channel flow showing the coordinate system and the three main regions according to depth in the flow. S is the slope (also represented as angle θ) and h is the depth of the flow measured along the y-axis.

(Adrian et al, 2000). Sweeps and ejections are coherent packets of flow that are correlated with the wall generated vortex structures. The ejections are low momentum flow events, and vortices tend to wrap around these regions into hairpin or cane like structures. The direction and relative magnitude of these turbulence structures are indicated in Figure 4.2.

A resurgence of turbulence measurements in open channel flows was observed in the 1980s with the increased feasibility of Laser Doppler Anemometry (LDA) (Nezu and Nakagawa, 1993). These measurement replaced probe measurements such as hot film anemometry, which are sensitive to low velocities, water impurities, temperature changes and entrained air bubbles in the flow. As previously argued, the ability of point measurements to resolve the finer scales of turbulence at the smallest timescales, they are unable to resolve turbulent structures without the assumption of frozen turbulence and isotropy of the gradients.

Using 2D PIV, Adrian et al (2000) were able to capture these regions, and significant

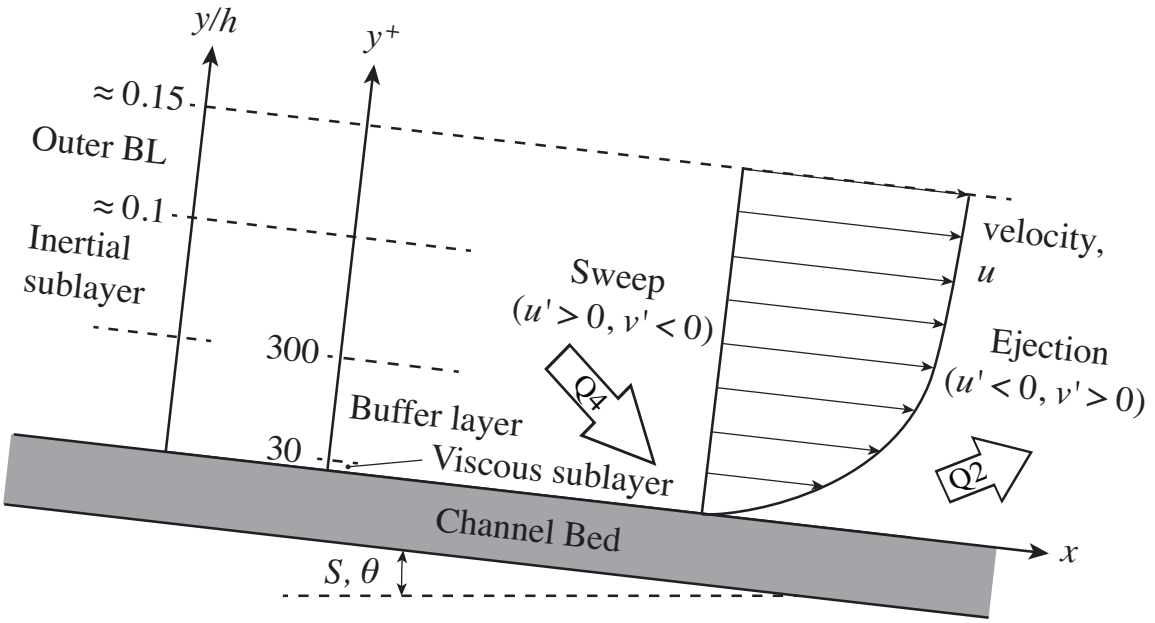

Figure 4.2: Schematic of the boundary layer. y^+ is the dimensionless wall unit (see Section 4.2.2), BL is shorthand for boundary layer. Sweep and ejection phenomena (Q4 and Q2 regions, respectively) are shown.

contributions to the identification and analysis of these regions were made by Stanislas et al (2008) with stereo PIV. Hurther et al (2007) linked the concept of outer boundary layer flow structures with the turbulent kinetic energy and momentum using an acoustic Doppler velocimetry profiler. Ganapathisubramani et al (2003) used stereo PIV measurement planes parallel to the wall to identify turbulence phenomena and their intensity at different heights. Dennis and Nickels (2011) combined stereo PIV measurements with Taylor's hypothesis of frozen turbulence to reconstruct the three-dimensional turbulent structures that propagate down stream. These authors were able to perform conditional averaging on high and low speed streaks, and the hairpin vortices that straddle them.

Regarding analysis of the classical boundary layers over flat plates and the structures in them, TPIV has been employed to investigate turbulent boundary layers in the buffer and inertial boundary layer regions, equivalent to this chapter. To take one example, Schröder et al (2011) used time resolved TPIV along a flat plate that enabled the visualisation of turbulent boundary layer phenomena such as low speed velocity streaks and hairpin vortices, as well as turbulence characteristics. The authors made spatial correlations of the events to form averages of their structures to give an insight into their behaviours. At the resolution of their system (that did not resolve the viscous length scales), they found that their measurements captured approximately 85% of the turbulent kinetic energy. Atkinson et al (2011) recently analysed the errors associated with boundary layer measurements with TPIV.

Unlike classic boundary layer investigations, the flume used in this study is divided by a series of trash racks. Trash racks are commonly used in spillways and fish passageways to transfer the mean flow energy into turbulence energy. In this sense, the study is quite unique and as such is difficult to find quantitative data in the literature to compare the findings. The goals of this study are to characterise the turbulence, turbulence structures, the boundary layer and the energy dissipation and generation in a pool of a flume. This work is a follow up of the earlier investigation presented in Chapter 3 that studied the evolution of the energy dissipation in the intermediate region, in the same channel. In this study, a higher resolution TPIV setup is employed to characterise the turbulence at the wall.

4.2 Experimental Setup

The experiments were conducted under the same flume and identical conditions as those presented in Section 3.2. A notable difference is that for this chapter, only the flow with the G1G2 combination of grids is investigated (see Figure 3.4 for trash rack details). Figure 4.3 presents the equivalent G1G2 velocity field as shown in Figure 3.5, this time with the two TPIV measurement regions shown by the red boxes (details of the 2D PIV measurements are in Appendix A.4). The two regions will have the following names: midway down the pool, the region of interest is denoted R_1, while the second region of interest approaching the downstream trash rack is labelled R_2. These two regions are both located in the central xy-plane of the flume.

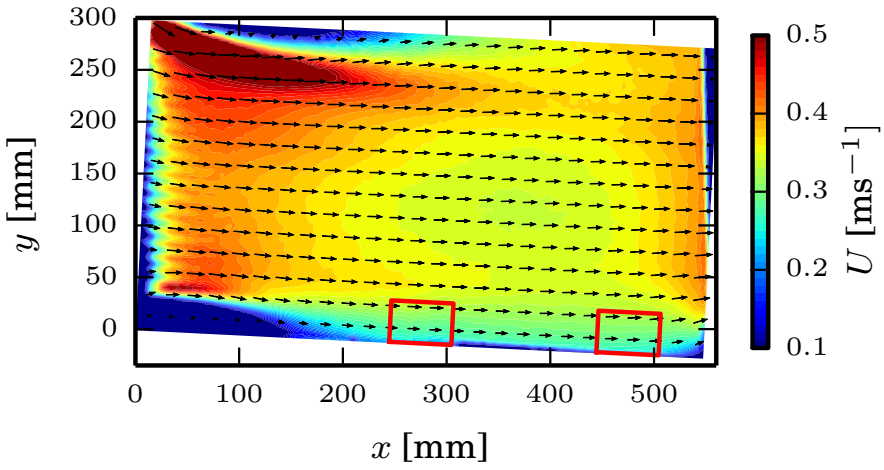

Figure 4.3: Mean 2D PIV flow field, averaged over 500 velocity fields for G1G2. U is the mean component of velocity in the stream wise direction. Only every 100th vector is plotted. The TPIV regions (Section 4.2.3) are indicated by the red boxes.

4.2.1 Flow properties

The water temperature was 15.4±0.5 °C with associated kinematic viscosity $\nu = 1.15 \cdot 10^{-6}$ m^2/s. A table containing the key parameters for this flow is presented in Table 4.1. The hydraulic radius is defined as $R_h = h_c W/(2h_c + W)$, where h_c is the flow depth at the centre of the pool, measured normal to the bottom. The bulk mean velocity of the flow through each pool is $U_0 = Q/(h_c W)$. The Froude Number is defined as $\mathrm{Fr} = U_0/\sqrt{g h_c}$. The Reynolds number with respect to hydraulic radius is denoted Re_{R_h}, and with respect to the grid mesh size as Re_M. TPIV measurements were conducted in pool 3, discussed further in Section 4.2.3.

Table 4.1: Global flow properties in the pool for the G1G2 grid combination

Parameter	Value
ΔH [m]	0.06
h_c [m]	0.31
U_0 [m/s]	0.360
R_h [m]	0.10
Re_{R_h} [–]	31 300
Re_M [–]	4 300
Fr [–]	0.20

4.2.2 Wall region scaling parameters

To enable direct comparison with other turbulent boundary layer studies, the scaling described in the following and in Section 1.10.1 was used. The friction velocity U_* is computed by fitting a log law (Eq. 4.1) to the measured velocity profile $U(y)$ from the TPIV measurements (Section 4.2.3),

$$\frac{U}{U_*} = \frac{1}{\kappa}\ln\frac{yU_*}{\nu} + B + w\left(\Pi, \frac{y}{h}\right) \tag{4.1}$$

where κ is the von Kármán's constant (set to 0.4), B is the additive constant (typically assumed to be approximately 5.0), w represents the wake function and Π is Coles parameter (Coles, 1956). As discussed in Nezu and Rodi (1986), the wake function goes to zero in the near wall region ($y/h \leq 0.15$). Thus, as the measurements presented in this study are inside the near wall region, the wake function is taken to be zero. Only the lower quarter of the measurement region is used to fit the profile. Figure 4.4 shows the fit of Eq. 4.1 for both the R_1 and R_2 regions. For each region, the data is presented on a linear axis (against y and y/h_c) and a semiology axis. The log plots amplify the deviation of the data from the curve in the lower region. As can be observed, the log laws fit the data well across the range shown.

There has been considerable debate about the universality of the κ and B 'constants' (as noted in Marusic et al, 2010; George, 2007, both of these 'constants' appear to have Reynolds and flow condition dependancy). For the R_2 region, $B = 5$ was an appropriate value to use, however for R_1, using the same value for B had significant deviations from the measured data. The least-squares approach for fitting Equation 4.1 to the experimental data yielded $B = 18$, a significant departure from results reported in the literature. The explanation for this is based on the difference between the data in the literature and these experiments; this value is typically calculated based on a fully developed boundary layer. However, Figure 4.3 shows clearly that the measurement region is just behind a return flow region, and hence the boundary layer is still evolving or transitioning in the stream wise direction. By the time the flow reaches R_2, it appears that the boundary layer flow closely resembles a fully developed boundary layer.

The scaling variables are thus listed in Table 4.2. The wall unit $y^* = \nu/U_*$ is used here to normalise the wall normal distance and is equal to the viscous length. The wall unit also indicates how well the flow has been resolved (Section 4.2.6). From this point on, all results are plotted against the dimensionless wall distance $y^+ = y/y^*$. Table 4.2 also presents the boundary layer thickness δ and boundary layer Reynolds number (Eq. 4.2).

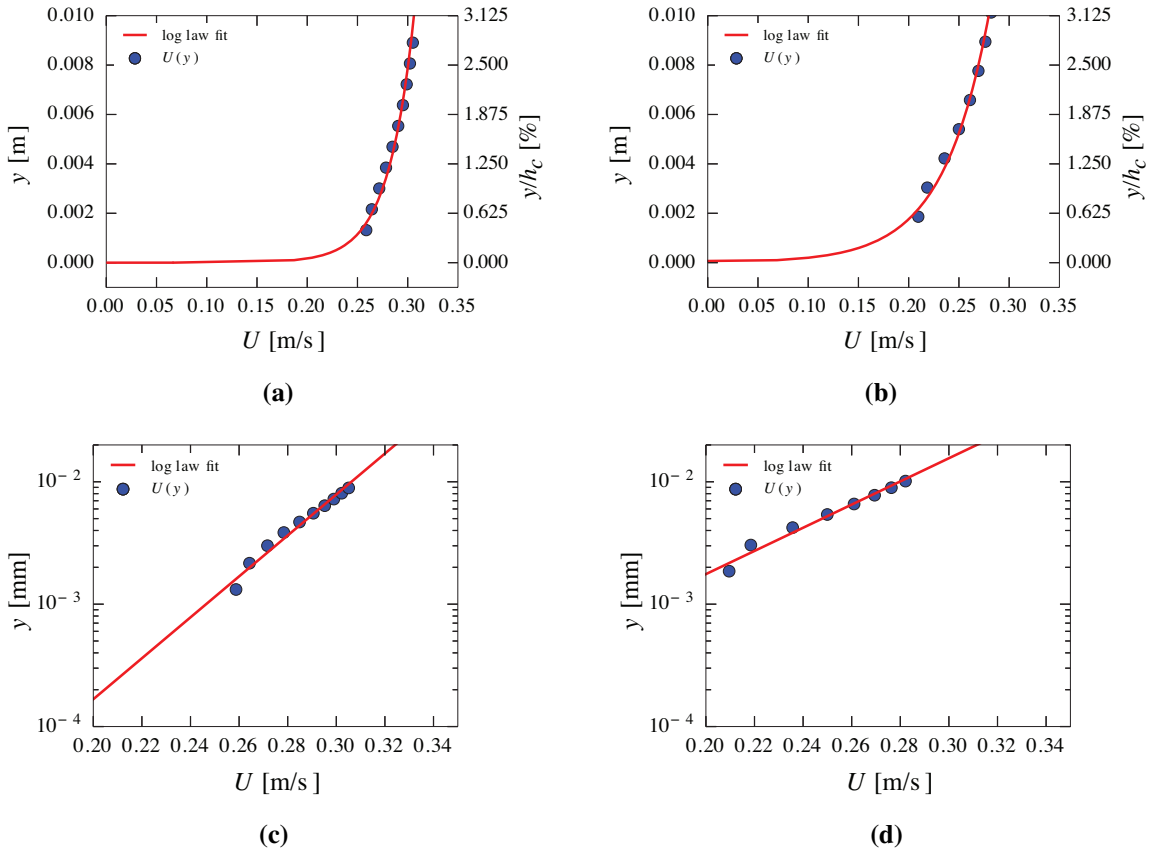

Figure 4.4: Log law fit (from Eq. 4.1) to the mean velocity profile $U(y)$ of (a & c) region R_1, (b & d) region R_2. The experimental data can be well described by a log-law, however the additive constant B was modified to 18 for the R_1 region.

$$\mathrm{Re}_\tau = \delta^+ = \frac{\delta U_*}{\nu} \tag{4.2}$$

It should be noted that for pipe flow, $\delta = D/2$ (where D is the diameter of the pipe) and for classical boundary layer studies over a flat plate with uniform free-stream, $\delta = \delta_{99\%}$ (where $\delta_{99\%} = y(U = 0.99U_0)$. As the TPIV measurement regions do not cover the full boundary layer thickness, δ was calculated from the 2D PIV data (Figure 4.3).

Table 4.2: Summary of wall region inner boundary flow variables

Variable		R_1	R_2
U_*	[m/s]	0.019	0.016
$y^* = \nu/U_*$	[mm]	0.079	0.094
δ	[m]	0.05	0.06
δ^+		826	835

4.2.3 TPIV measurements

The TPIV system was comprised of four 1600 $\times$ 1200 px 8 bit cameras. For R_1, the cameras were positioned symmetrically in an inverted pyramid configuration, with declination and inward angles of approximately 20° as per the experiments in Chapter 3 (Figure 4.5a). For R_2 the downstream cameras were required to be positioned centrally above the measurement region in the y-direction, as the trash rack housing obstructed optical access (Figure 4.5b).

All cameras were fitted with 105 mm lenses, 532 nm pass optical filters (corresponding to the laser frequency) and 2-axis lens mounted adapters to ensure the Scheimpflug condition. The apertures were set at $f_\# = 16$ during acquisition. Neutrally buoyant, spherical, polyamide particles of mean diameter $d_{50} \approx 20\ \mu$m and density $\rho_\mathrm{p} = 1.02$ g/cm^3 were used to seed the flow. The particle density, size and quantity were carefully selected to achieve a

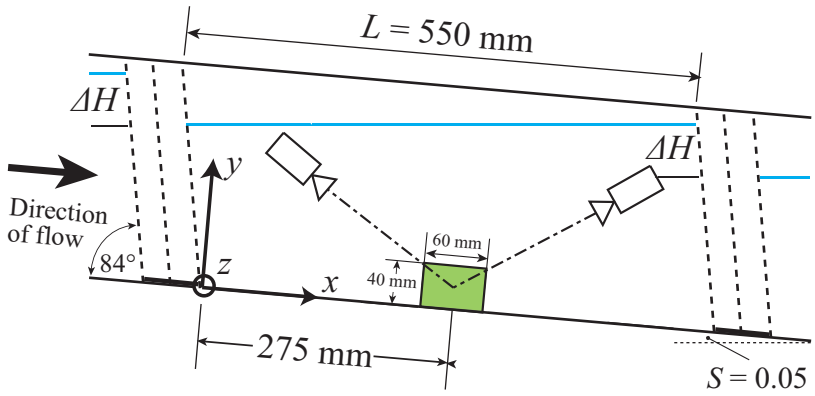

(a) R_1: Centrally located region of interest

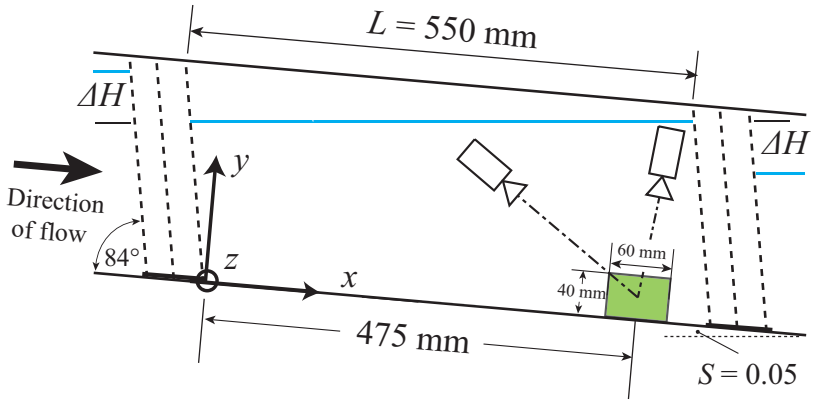

(b) R_2: Downstream region of interest

Figure 4.5: Schematic of Tomographic PIV locations along the boundary in pool 3 of the (a) region of interest R_1 in the centre of the pool, and, (b) R_2 with centre of region 75 mm from the trash rack. The camera positions were adjusted for R_2 due to the optical impediment of the trash rack. Only the cameras in the foreground are shown, however there were four in total, with the omitted cameras symmetrically opposite on the other side of the flume.

compromise between signal to noise ratio, resolution, and particle image size. Particularly in the study of turbulence calculations, it is imperative that the particles follow the flow truthfully.

A 10 mm thick laser sheet was made to illuminate the measurement volume, realised with a double head Nd:YAG laser with 120 mJ per pulse. The laser and laser optics were positioned under the channel, independent from the channel structure. Both R_1 and R_2 were $50 \times 60 \times 10$ mm^3 ($x \times y \times z$). The laser sheet thickness Δz_0 was regulated with parallel plates spaced at 10 mm. The time between corresponding images, Δt, was 0.8 ms, chosen to achieve maximum particle displacements of $\sim$8 px for each camera. These image double-quadruplicates (8 of which make a velocity field) were acquired at 2.5 Hz.

4.2.4 Image Processing

For each camera and for corresponding laser pulses, the median image from 50 sequential images was subtracted to remove the background noise. This method was shown to be more effective than local window filters, due to the nature of the background noise, which included laser light dispersion on the channel bottom. The processed images to be reconstructed had a homogeneous particle per pixel of $ppp \approx 0.03$, or an image source density $N_s \approx 0.7$ (Scarano, 2013), for all cameras at both time-steps. A gaussian filtering kernel was then applied to smooth the particle images.

An example of the image filtering from one of the cameras is shown in Figure 4.6. One of the challenges of measuring the boundary layer with TPIV is that to be sure the reconstructed velocity field contains the full velocity field all the way to the channel floor, as shown in Figure 4.6a. As the measurement volume is determined by the union of the cameras' field of view, it is necessary to capture an area below the channel bottom. The temporal median filtering stage (Figure 4.6b) can help remove the reflection on the channel bottom, however with a significant side-effect. The particles that are in the line of sight of the cameras that pass through the reflected area are lost, or severely reduced. In Figure 4.6c, looking to where the reflection used to be, it is possible to see a local reduction in ppp. The result is that fewer particles are reconstructed near the near wall.

(a) **(b)** **(c)**

Figure 4.6: The filtering of a PIV image acquired from one of the cameras. (a) shows the raw image, (b) is the median of 50 images, where the laser light reflection on the channel bottom is visible. (c) Shows the filtered image. Particle images have been depleted in the reflection region.

4.2.5 Volume Reconstruction and Vibration Correction

The tomographic reconstruction steps were performed with the same algorithms and method as discussed in Section 3.3.3. The final reconstructed volume size was $1089 \times 851 \times 202$ voxels. The complete reconstruction of each volume was in the order of 15 minutes running on 4-cores of an Intel i7 2.93GHz processor. Additionally, the same vibration treatment (namely, the IVC scheme, Section 3.3.4 and Appendix C) was imperative for these measurements.

4.2.6 Velocity field calculation

A two pass $64 \times 64 \times 64$ voxel correlation volume with 75% overlap was used to find the most probable displacement of particles across the two reconstructed volumes. This resulted in 20 992 vectors per acquisition at a spatial resolution of $\delta x = 0.84$ mm or $\approx 11y^*$ for R_1 and $\approx 9y^*$ for R_2. Although this resolution is not sufficient to measure the dissipative scales, similar to the investigation of Dennis and Nickels (2011), the large scale turbulent fluctuations and turbulence structures are of greater importance. The effect is that the velocity field calculated by the TPIV is a low-pass filtered version of the original.

A median vector replacement regime was implemented as per Westerweel and Scarano

(2005), with the number of spurious vectors found to be approximately 8% per volume. This level of spurious vectors is high, however as discussed in Section 4.2.4, there is a lack of particles in the near wall region. Further analysis showed that the spurious vectors were indeed concentrated in the low region of the reconstructed volume where the laser reflection was filtered. Thus, these vectors were removed so as to not affect the velocity statistics, but as a consequence very-near wall regions do not have data. In short, due to the reflection of the laser light on the bottom of the channel and subsequent image filtering, there is no data available in the lower 2 mm of the flow ($y^+ < 25$). A bilateral filter was used to filter the velocity fields, which was preferred over a gaussian filter as it preserves edges (Section 3.3.5). Spatial velocity gradients have been calculated with a second order central difference scheme.

4.3 Results

Recall that u, v, and w are the instantaneous components of velocity and primes denote the root mean square of the fluctuations from the means U, V, and W, in the x, y and z directions respectively. 350 statistically separated flow fields for each region are considered.

4.3.1 Mean velocity fields

To highlight the type of velocity fields being measured, a 2D field of U/U_0 (Figure 4.7a & 4.7b) and V/U_0 (Figure 4.7c) are shown. Comparing the downstream region R_2 with R_1, the influence of the trash rack screen and housing can be seen particularly by the upwelling observed. The global reduction in the U/U_0 levels at R_2 is attributed to the increase in depth in the pool along x. The reduction can also be attributed to the boundary layer development, as discussed in Section 4.2.2 and Section 4.3.2, where the change in frequency, spatial arrangement and probability of the turbulent structures modifies the mean profile (as per the mechanism outlined in Eq. 1.12).

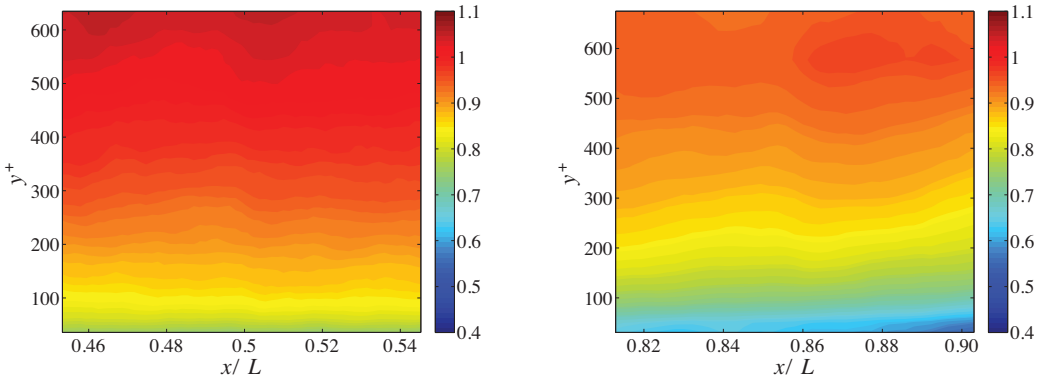

(a) R_1, U/U_0

(b) R_2, U/U_0

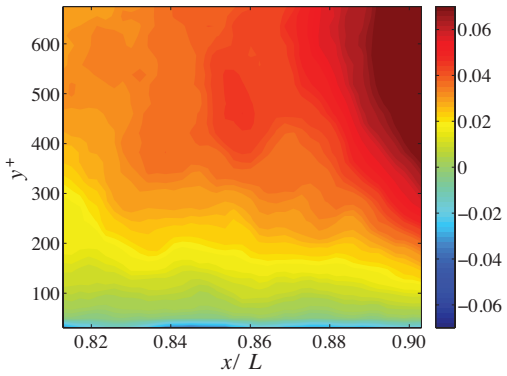

(c) R_2, V/U_0

Figure 4.7: For the G1G2 grid configuration, contour maps of the streamwise component of velocity U/U_0 for (a) R_1 and (b) R_2 are shown. (c) Shows the contour maps of the wall normal component of velocity V/U_0 for R_2. Flow is from left to right. Note that the contour scale in (c) has changed from (a) and (b) to reveal the flow features.

4.3.2 Instantaneous velocity fields

The velocity vectors presented in this section are from the perspective of an inertial frame of reference moving at $0.8U_0$ in the x-direction. For clarity, only a quarter of the vectors in the xy-plane are plotted in Figure 4.8. The instantaneous fields are analysed to show the vortex structures and velocity fields that are extracted.

Figure 4.8a & 4.8b show instantaneous velocity fields in the R_1 region where the Q2 and

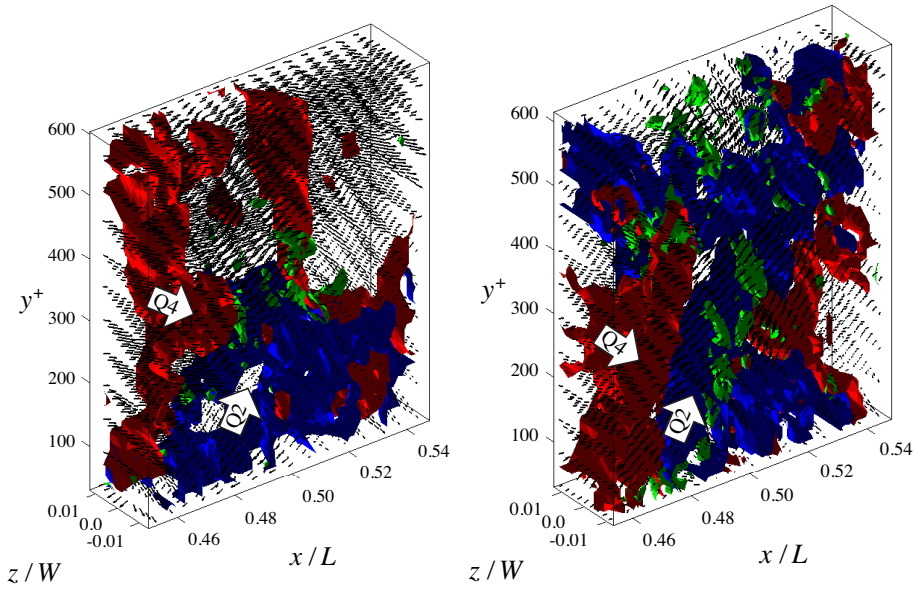

(a) R_1

(b) R_1

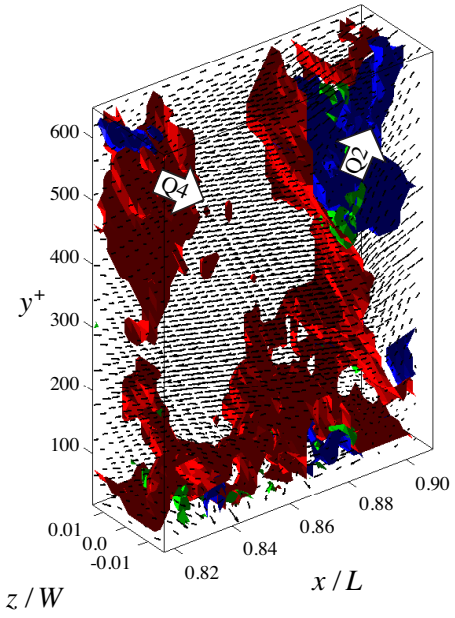

(c) R_2

Figure 4.8: Instantaneous velocity field at a moving frame of reference at $0.8U_0$. Flow is from left to right, with only a quarter of the vectors in the xy-plane plotted. The blue surfaces bound Q2 while the red surfaces bound regions of Q4. The green levels are iso-surfaces of the Q-criterion indicating vortex locations.

Q4 regions can be identified. The blue surfaces bound ejections (Q2) while the red surfaces bound sweeps (Q4). In Figure 4.8a, at a position $x/L = 0.47$, $y^+ = 60$, a classic formation of the ejection and sweep interaction can be seen that extends vertically upward towards the downstream at approximately 45°. The green regions are vortices, highlighted by the Q-criterion (Hunt, 1988). Although the vortices identified in Figure 4.8a don't have a hairpin or cane like vortex shape, it can be seen that small vortex packets populate the region between the two zones. In Figure 4.8b on the other hand, a coherent and large ejection can be seen, also orientated at approximately 45°, where fingers of vorticity wrap around the low speed region. This low momentum region is bounded by two sweep regions, a flow event described in Perry et al (1986); Adrian et al (2000) and shown in other experimental studies (for example Dennis and Nickels, 2011; Atkinson et al, 2011; Schröder et al, 2011; Gao et al, 2013).

Figure 4.8c presents the same fields for the R_2 measurement region. Further downstream, the large Q2 and Q4 events observed in R_1 appear to be larger, and the accompanying vortices are less frequent. The larger scale structures also appear more often in the buffer and inertial sublayers and occupy the upper regions of the measurement domain ($y^+ > 300$). The figure also shows evidence of smaller vortices and Q2 and Q4 events in the lower buffer layer, which have been generated at the wall.

4.3.3 Velocity field probability density functions

The organisation of the sweep and ejection phenomena observed in Figure 4.8 can be analysed further by considering the histograms of the velocity components. Figure 4.9a shows the probability density functions (PDFs) of the normalised streamwise component for R_1 and R_2. Both regions contain several distinct peaks, where the peaks $u/U_0 > 1$ correspond to high momentum, Q4 flow events. The next peak lower corresponds to Q2, low momentum flow events, as indicated in the figure. The peaks at lower velocities are due to the slower turbulent flow events next to the wall. Figure 4.9b shows the normalised v component PDFs. There is a skewness, or shouldering, towards $v/U_0 < 0$, equivalent to $-v'$ events for R_1 (Q4) and a peak in of positive v' for R_2 (Q2).

As noted by Hurther et al (2007), PDFs such as these are essentially composed by the

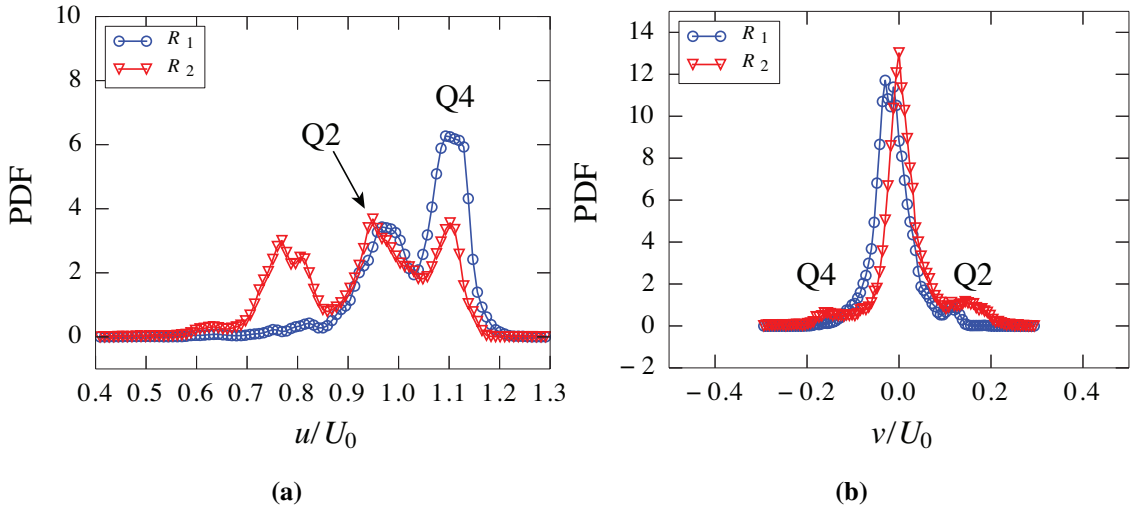

Figure 4.9: Probability density function (PDFs) of (a) the streamwise component of velocity u/U_0 and (b) v/U_0, show high and low momentum flow events.

superposition of normal distributions about a signature velocity of the turbulent structures. For example, by observation the Q4 events for R_1 and R_2 regions appear to have a mean or signature velocity at approximately $1.1U_0$. For a more robust approach to this analysis, a curve fitting procedure was undertaken to decompose the curves into their turbulent events. Thus, a curve of the form $f(u/U_0) = f_{Q2} + f_{Q4}$, where f_{Q2} and f_{Q4} are normal distributions of the form

$$f = A \cdot e^{\frac{\mu - u/U_0}{2\sigma^2}} \tag{4.3}$$

where μ is the mean of the curve, σ its standard deviation and A expresses the height of the function. To isolate the Q2 and Q4 regions for the u component PDFs, only $u/U_0 > 0.82$ was considered. The results of this analysis are shown in Figure 4.10. As can be seen in Figure 4.10b, the PDF is dominated by the velocity with $v \approx 0$, and the least squares algorithm was not able to find the Q2 and Q4 peaks on the shoulder regions of the curve, unlike for the well defined peaks in the u component plot (Figure 4.10a). To solve this, it was necessary to fit a single Gaussian curve to the data and then subtract it; the result of which shown in Figure 4.10c. After the subtraction, the Q2 and Q4 peaks are clearly

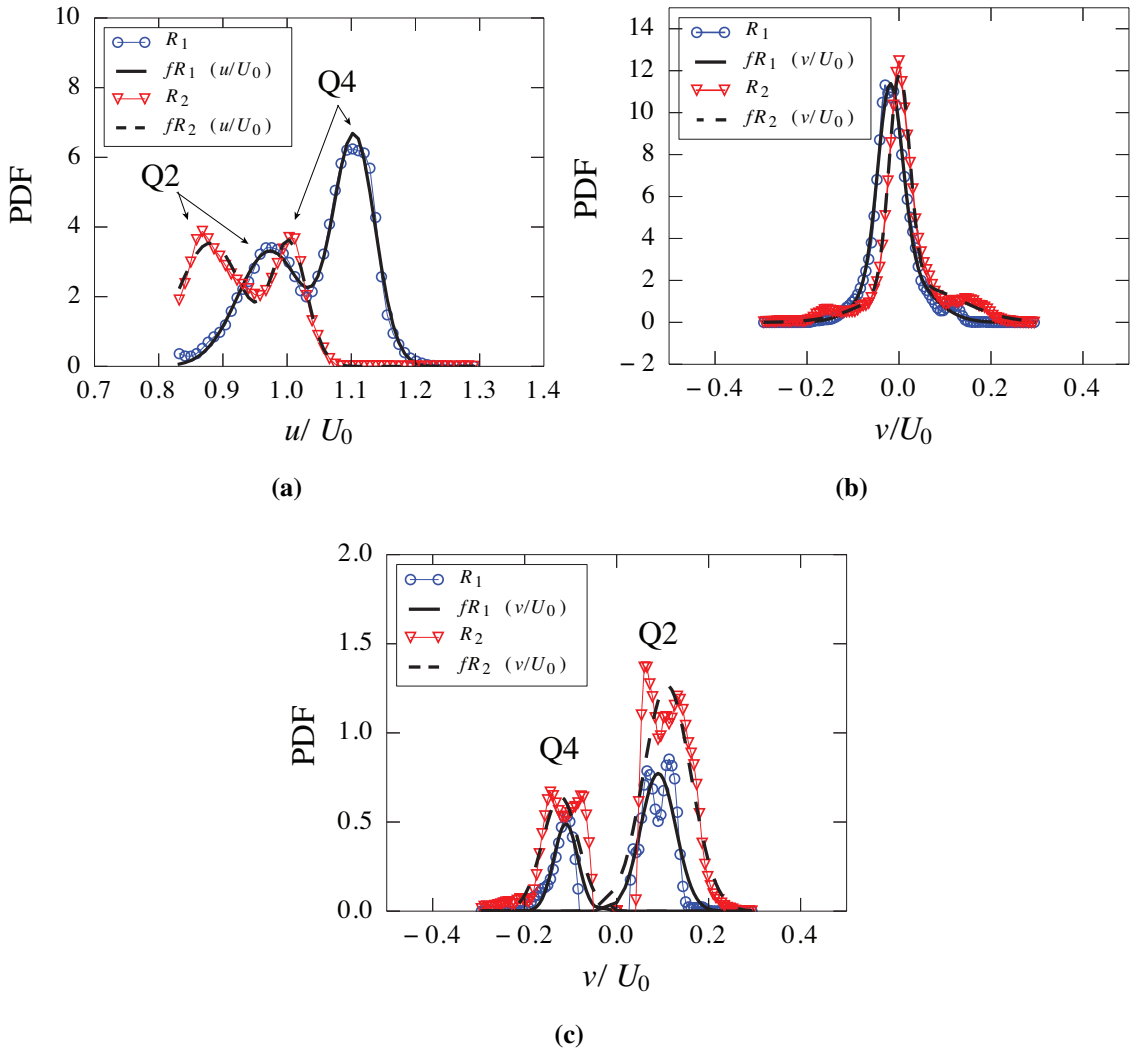

Figure 4.10: Probability density function (PDFs) with superimposed normal distributions for analysis of turbulent structures, (a) u and (b and c) v components of velocity. Figure (c) has had the central velocity distribution removed to highlight the less prominent features.

visible and were able to be decomposed into the Q2 and Q4 events.

The coefficients of Eq. 4.3 shown in Table 4.3. Along with the coefficients, a relative probability P was computed by comparing the areas under the Gaussian fits. From Table 4.3, several observations can be made. Firstly, regarding the u analyses, the occurrence of a high momentum sweep event has drastically reduced, from 56.2 – 34.2%. Rather than

slender and tall distribution, the turbulent events have higher variance, and with respect to U_0, less momentum. Analysing the v components, in both R_1 and R_2 regions, as previously noted, the velocity detonated by $v = 0$ dominates ($> 75\%$ flow for both regions). This is explained by the wall suppressing wall normal velocity via the kinematic boundary condition. The relative probability of the occurrence of a Q2 and Q4 event has approximately doubled from R_1 to R_2, contrary to the u component behaviour. Both Q2 and Q4 events in both regions as identified by the v component have peaks at $\pm 0.1 U_0$.

Table 4.3: Analysis of Q2 and Q4 turbulence events, where column indicate parameters found by least squares analysis of Eq. 4.3 with raw data. P is the relative probability of the event.

Function	A	μ	σ	P [%]
$f_{u,\mathrm{Q2}}$ (R_1)	3.32	0.97	0.05	43.80
$f_{u,\mathrm{Q4}}$ (R_1)	6.58	1.10	0.03	56.20
$f_{u,\mathrm{Q2}}$ (R_2)	3.54	0.88	0.05	65.82
$f_{u,\mathrm{Q4}}$ (R_2)	3.45	1.00	0.03	34.18
$f_{v=0}$ (R_1)	10.87	-0.02	0.03	89.64
$f_{v,\mathrm{Q4}}$ (R_1)	0.49	-0.11	0.03	3.12
$f_{v,\mathrm{Q2}}$ (R_1)	0.77	0.09	0.04	7.24
$f_{v=0}$ (R_2)	12.17	0.00	0.03	77.76
$f_{v,\mathrm{Q4}}$ (R_2)	0.64	-0.12	0.04	6.16
$f_{v,\mathrm{Q2}}$ (R_2)	1.27	0.11	0.05	16.08

4.3.4 Velocity field joint probability density functions

To further the investigation on the arrangement of the turbulent structures in the measurement region, the joint probability functions (JPDFs) of u and v are plotted in Figure 4.11. The figures are then divided into quadrants from the normalised zero velocity axes, which correspond to the ejection and sweep events, labelled Q2 and Q4, respectively (see Figure 4.2). Figure 4.11 shows two types of normalisation: in the top row, the velocity components have had the local means subtracted. The resulting distribution is what would be achieved from an array of probe measurements. The peaks observed in Figure 4.9 have been effectively removed from the data, leaving a skewed distribution of velocity fluctuations. The bottom row of figures, however, have had the streamwise component of velocity normalised by the bulk velocity. Subtraction of the bulk velocity (or a fraction of it) is equivalent to applying a constant velocity to the frame of reference of the observations, that is, it is a Galilean invariant normalisation. As a result, in the bottom row of figures, the turbulent flow features are preserved. This indicates that they indeed travel as coherent parcels with a signature velocity and velocity distribution. This demonstrates a key advantage of spatial measurements over point measurements; the ability to directly measure the coherent turbulent phenomena.

It is also noted that in the bottom row of figures in Figure 4.11, normalisation by U_0 is rather arbitrary for dividing the probabilities into quadrants, as any fraction of U_0 could be chosen as a normalisation, artificially modifying the expected probability of any particular event (for example Adrian et al, 2000, used $0.8U_0$ for their observations, as was the case in Figure 4.8). Thus, these JPDFs are best interpreted as an ensemble, where normalisation by the local mean gives a more appropriate distribution of sweeps and ejections, and thus the bulk velocity normalisation can provides more information on the shape and relative probability of the events. In both regions, the Q2 ejection events tend to be more disperse with a larger variance, whereas the contrary is true for the sweeps. Another way of posing this, is that the sweep events tend to be of a particular velocity, whereas ejection events are more varied in their behaviour. Coupling this hypothesis with the bottom row of figures, it can indeed be seen that there are multiple peaks in the ejection quadrant, all corresponding to approximately the same wall normal velocity v, but at several steps of streamwise velocity

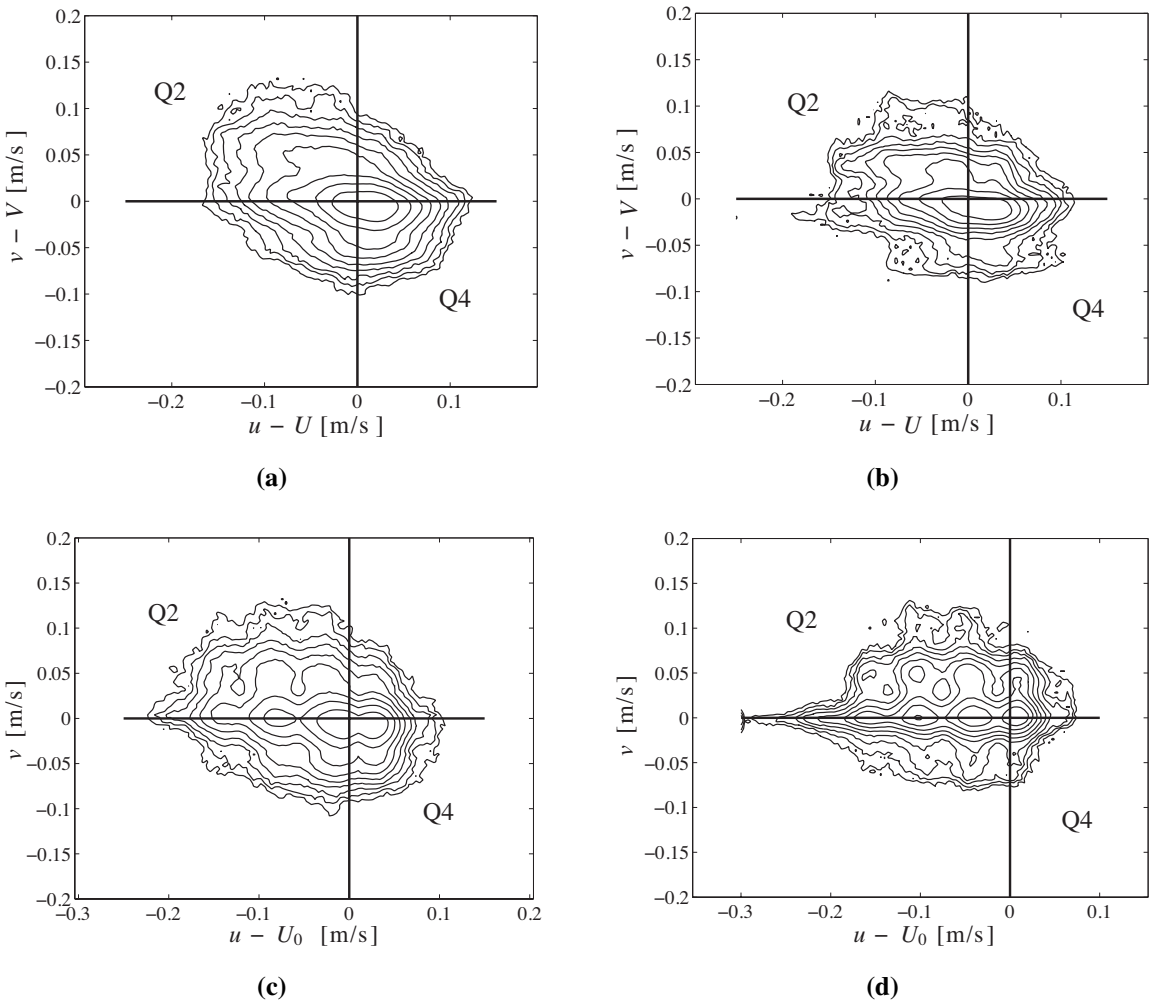

Figure 4.11: Joint probability density functions (JPDFs) of the streamwise u and wall normal v components of velocity for (a & c) R_1 and (b & d) R_2. The top row of figures have been normalised by the corresponding component of local mean, whilst the bottom row have had the streamwise component normalised by the bulk velocity.

u. Finally, comparing the regions to each other, it can be seen that further downstream in R_2, the turbulence events have become much more clearly defined with the JPDF showing much clearer probability peaks, particularly in the Q2 region. This observation can also be seen directly in Figure 4.9. The higher variance of the R_1 region events point to the influence of the turbulence from the trash rack.

4.3.5 Reynolds stresses

From the 3 components of velocity, it is possible to retrieve the full Reynolds stress tensor $\langle u_i' v_j' \rangle$. Figure 4.12 shows the 6 unique Reynolds stress terms normalised by U_0^2 and the evolution with height from the boundary. In Figure 4.12a, which considers R_1, this analysis shows that the turbulence energy is anisotropic, with the stream wise component $\langle u'^2 \rangle$ containing the most energy. Further downstream in R_2 (Figure 4.12b), there is greater tendency for isotropy. The 2D PIV image of the mean velocity in the pool (Figure 4.3) can aid the interpretation of this result. Immediately upstream of R_1, there is a recirculation region, where the water column flow reattaches to the channel bottom. At these stage, the boundary layer flow is not fully developed. Additionally, the turbulence by the trash rack is much more prevalent at this location than it is further downstream. Thus, by the time the flow reaches R_2, the turbulence has reduced and, as can be seen in the figure, has become isotropic.

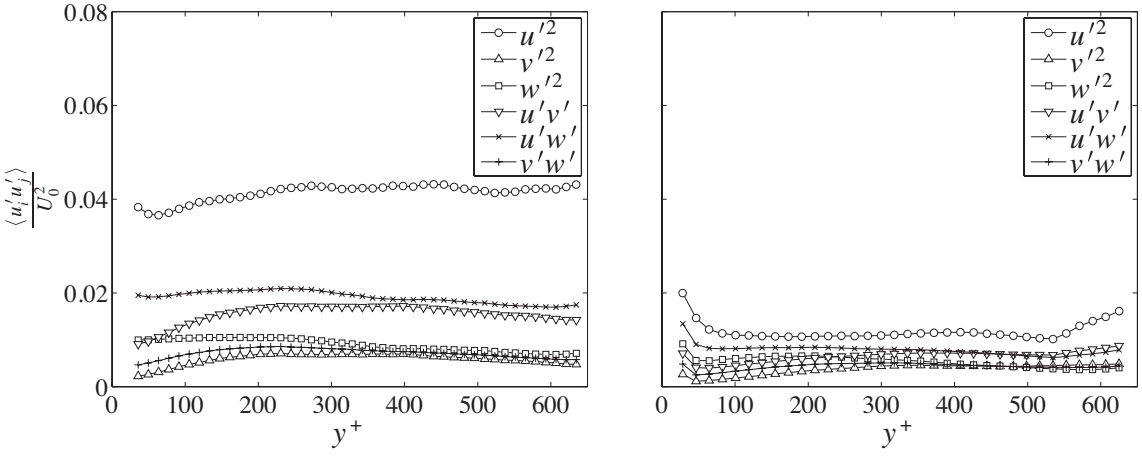

(a) R_1 **(b)** R_2

Figure 4.12: Reynolds stresses and their distribution along the wall normal y^+ direction for (a) R_1 and (b) R_2. These plots have the same ordinate scales.

Figure 4.12 shows the influence of the trash rack on the flow field. In this case, the Reynolds stresses are completely dominated by the grid generated turbulence. In most

boundary layer studies, the free stream turbulence is kept to a minimum, and the turbulence is generated only at the wall, which then propagates up through the fluid through turbulent diffusion. In those cases, the Reynolds stresses are highest near the wall and decay in the wall normal direction. For the measurements in this flume, the turbulence generated at the trash racks dominates, particularly at R_1, where there is a slight tendency for the stresses to *reduce* closer to the wall compared to the turbulence generated by the grids. Further downstream in R_2 however, the grid generated turbulence has decayed. In this region, the turbulence generation at the wall ($y^+ < 80$) tends to be higher than further away from the wall.

Despite the departure of this experiment from classic DNS boundary layers (which are typically in pipes or over flat plates in channels), a common observation is the increase in Reynolds stresses very close to the wall (see the review of Marusic et al, 2010, and references therein). Although the measurements were only able to obtain two velocity vectors in the region $y^+ < 80$, the data presented here show evidence of the same phenomena. In region R_1 however, it can be seen that the Reynolds stresses are as high near the wall as they are away from the wall. Again, this shows the influence of the turbulence in the water column generated by the trash racks.

Turbuence kinetic energy

Related to the Reynolds stresses is the turbulence kinetic energy, k, where $k = \mathbf{tr}(u_i' u_j')$, or the trace of the Reynolds stress tensor. In Figure 4.13a, k for both regions are plotted against the x-axis, to visualise the reduction in turbulence energy as the flow passes further downstream. Similar to the results found in the centre of the pool (Figure 3.14a), k tends to decay following a power law, although in this case, particularly for R_1, the curve deviates from the data rather significantly in the x bounds. In Figure 4.13b, the three components of k are plotted. The $\langle u'u' \rangle$ dominates in both regions, indicating the presence of large streamwise fluctuations. Both cases also show that, owing to the kinematic boundary condition of the flume bed, the $\langle v'v' \rangle$ components are suppressed. In the R_2 region, the kinetic energy appears to increase, following an initial decay. This is explained by the trash rack housing downstream causing a change in the flow pattern in R_2, resulting in higher energy

dissipation (for example, see Figure 4.7c, which shows a sudden increase in V/U_0 from $x/L > 0.88$ and $y^+ > 300$). The ensemble averaged turbulence kinetic energy $\langle k \rangle$ and its three components are displayed in Table 4.4

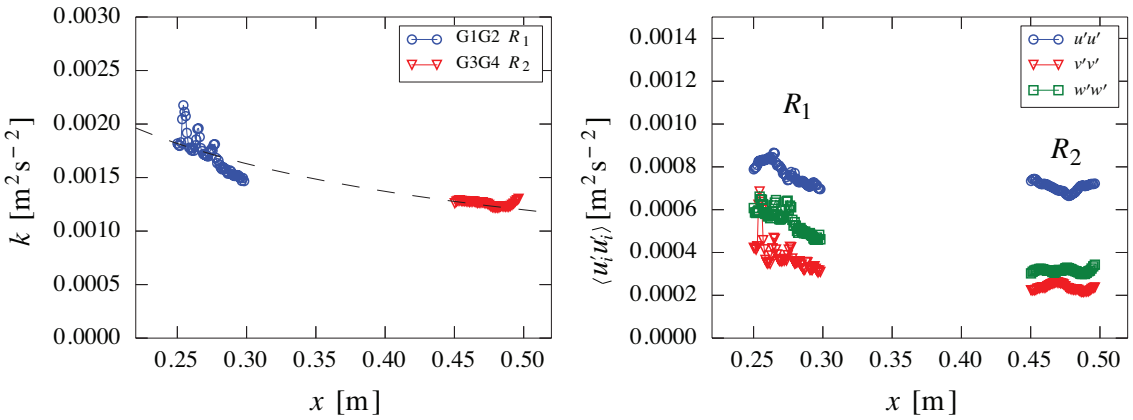

(a) **(b)**

Figure 4.13: (a) Decay of k along streamwise direction x for both measurement regions. The dashed line is a power law fit of the form $A \cdot x^b$ with coefficients $A = 7.90 \cdot 10^{-4}$ and $b = -0.601$. (b) Decomposition of k into its three components $u_i' u_i'$

4.3.6 Dissipation of turbulence energy

Analogous to Section 3.4.5 of the previous chapter, the energy dissipation in the regions are investigated with several methods. This will enable a comparison between the two regions R_1 and R_2 and between the wall-bounded flow and the measurements made in the centre of the pool. The global dissipation, ε_B is calculated from Eq. 3.6, using the corresponding dimension sizes of the regions.

Energy Dissipation in measurement volume by Bernoulli analysis

This section carries out the same analysis as that presented in Section 3.4.5. The Bernoulli equation of Chapter 3 (Eq. 3.7) is identically used to analyse each region, displayed again

for ease of reference.

$$\frac{1}{\rho g}(p_1 - p_2) + \frac{1}{2g}(k_1 - k_2) + \frac{1}{2g}(U_1^2 - U_2^2) + \int_1^2 \frac{V(x)}{U(x)}\mathrm{dx} = \Delta H_{\text{pool,1-2}} \tag{4.4}$$

As per Chapter 3, the pressure terms are found by calculating the water depth at 1 and 2 from the raw 2D PIV images. The assumption of statistical stationarity has been identically applied. Finally, to calculate the ensemble averaged energy dissipation in the volume $\langle\varepsilon\rangle_{\mathrm{V}}$, Eq. 3.8 is utilised, with the appropriate volume dimensions utilised in the denominator. The results of this analysis are presented in Table 4.4 and are discussed further in Section 4.4.

Calculation of energy dissipation from decay of turbulent kinetic energy

The decay of k along x (Figure 4.13) can also be used as an estimator for the dissipation rate $\langle\varepsilon\rangle_k$, as defined in Equation 3.9 (Buchmann et al, 2010). In order to determine the gradient, a power law was fitted to both regions separately, and the derivatives taken in the centre of the corresponding volume (See Appendix A.3 for the fitting data). These results are presented in Table 4.4 and compared with the other turbulence statistics.

Direct calculation of energy dissipation

The energy dissipation averaged over all of the available velocity fields $\langle\varepsilon\rangle$ is considered. The energy dissipation acts to reduce the turbulent energy fluctuations that are associated with the energy of the vortices, at the smallest scales y^*. To calculate $\langle\varepsilon\rangle$ requires the full velocity gradient tensor:

$$\langle\varepsilon\rangle = 2\nu\langle s_{ij}s_{ij}\rangle \tag{4.5}$$

where $s_{ij} = (\partial u_j/\partial x_i + \partial u_i/\partial x_j)$ is the instantaneous rate-of-rotation tensor. Note that Eq. 4.5 is equivalent to Eq. 3.10. Figure 4.14a shows the evolution of $\langle\varepsilon\rangle(y^+)$ for R_1 and R_2. It can be seen that the energy dissipation is globally higher for R_1 than R_2. For both regions, there is a tendency for the energy dissipation to reduce as y^+ increases. This finding is consistent with results presented in the literature (for example Park et al, 2012). The wall thus has the effect of dissipating energy, and it can also be seen that further

downstream, the energy dissipation is less. Note that the edge data points were calculated with first differences, explaining the small peaks at the plot limits. Figure 4.14b shows the evolution of $\langle\varepsilon\rangle(x)$. As per the results presented in Chapter 3 (see Section 3.4.5), the level of energy dissipation reduces as a function of distance downstream of the trash racks. On close inspection of the R_2 $\langle\varepsilon\rangle(x)$, the dissipation increases slightly from $x > 0.48$ m. This is consistent with the $k(x)$ curve of R_2 (Section 4.3.5) and the mean images (Figure 4.7c). The mean values of the energy dissipation are presented in Table 4.4.

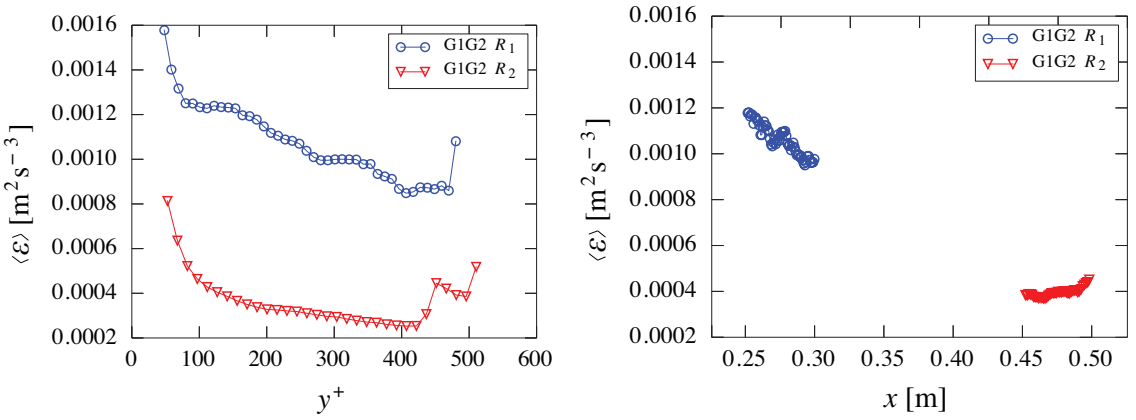

Figure 4.14: Energy dissipation distribution (a) with respect to the wall normal direction and (b) the streamwise direction.

4.4 Comparison of energy dissipation methods

4.4.1 Boundary layer regions R_1 and R_2

Four methods have been implemented to measure the energy dissipation in two regions along the channel bottom. Based on many experiments of grid generated turbulence and the theory presented in Section 1.10.1, it is well documented that k and ε decay along x. All of the methods, except $\varepsilon_{B,\mathrm{V}}$ confirmed this, returning $\varepsilon_{R_1} > \varepsilon_{R_2}$. In terms of magnitude, the global measure $\varepsilon_{B,\mathrm{V}}$ returned the lowest values by an order of magnitude. As was the case

Table 4.4: Energy dissipation and turbulence kinetic energy statistics.

Statistic		R_1	R_2
TKE ($\times 10^4$)			
$\langle k \rangle$	[m^2s^{-2}]	17.2	12.6
$\langle u'u' \rangle$	[m^2s^{-2}]	15.3	14.1
$\langle v'v' \rangle$	[m^2s^{-2}]	7.98	4.75
$\langle w'w' \rangle$	[m^2s^{-2}]	11.3	6.46
Dissipation ($\times 10^3$)			
$\varepsilon_{B,\mathrm{V}}$ (Eq. 3.6)	[m^2s^{-3}]	0.037	0.037
$\langle \varepsilon \rangle_\mathrm{V}$ (Eq 4.4 & Eq 3.8)	[m^2s^{-3}]	0.65	0.45
$\langle \varepsilon \rangle_k$ (Eq. 3.9)	[m^2s^{-3}]	1.69	1.33
$\langle \varepsilon \rangle$ (Eq 4.5)	[m^2s^{-3}]	1.07 (0.53)	0.36 (0.2)

for the centre pool case presented in Chapter 3, this stems from the averaging of dissipation over the whole pool, which is unable to deal with the energy dissipation close to the wall, nor the streamwise position in the pool.

The Bernoulli equation integrated over the measurement volume, that yields $\langle \varepsilon \rangle_\mathrm{V}$, was decomposed to analyse the contribution of each term in the equation. This decomposition shows that the contributions of the terms are similar to those found in the centre pool case (Table 3.4); the metric is dominated by the flow elevation. As the V component of the flow is parallel to the channel bed, the flow elevation is approximately equal to the channel elevation ($y_1 - y_2$). As the measurement volumes are in the order of 50 mm in length, the difference between p_1 and p_2 contributes less to the overall magnitude.

The $\langle \varepsilon \rangle_k$ method yielded the highest values for both regions. It is noted that there are too few velocity fields for full convergence (as can be seen by the $k(x)$ data in Figure 4.13). This may have an effect on the final curve fit of $k(x)$ and hence the value, however as the curves are found by a fitting of a least squares algorithm and thus finds the central

Table 4.5: Contribution of terms in Equation 4.4 for the calculation of ΔH_{pool}

Case	$\frac{1}{\rho g}(p_1 - p_2)$	$\frac{1}{2g}(k_1 - k_2)$	$\frac{1}{2g}(U_1^2 - U_2^2)$	$\int_1^2 \frac{V(x)}{U(x)}\text{dx}$
R_1	13.0%	1.6%	0.0%	85.4%
R_2	15.0%	0.3%	0.0%	84.7%

path through the data, the effect of this should be minimal. The lack of convergence does effect the gradients, and as a consequence the calculation of $\langle\varepsilon\rangle$. Despite the relatively few velocity fields used to calculate the gradients, Figure 4.14 shows $\langle\varepsilon\rangle_k(y^+)$ to be a smooth curve and thus convergence has been achieved.

4.4.2 Comparison of R_1 and R_2 and centre pool regions

This section directly compares the turbulence results of Chapter 3 with the current. The measurements are directly linked as they were conducted in the same flume. Notable differences are of course the different measurement locations but also the measurement resolution, with the TPIV measurement volumes in R_1 and R_2 approximately half the size in all dimensions. Particular focus will be on the analysis of k and ε. As only the G1G2 grids were investigated in this chapter, the comparison will only be made with the G1G2 case from Chapter 3. In this section, it will be referred to as simply G1G2. To facilitate the discussion, the relevant results are compiled in Table 4.6 and Table 4.7

The TKE results shows several interesting features of the turbulence in the pool. Firstly, k is more than double the magnitude in the two boundary layer regions than in the centre of the pool. The boundary layer generates vortices due to the Q2 and Q4 events, and these vortices draw energy from the mean flow. As mentioned previously, the $\langle v'v'\rangle$ components for R_1 and R_2 are suppressed by the wall. For G1G2, $\langle v'v'\rangle$ is also relatively weak compared to the other components. This is due to the to the dampening effect of the free surface. For the boundary layer cases, the streamwise component $\langle u'u'\rangle$ is equivalent to the total energy of k. Compared with G1G2, the streamwise component is less significant, and it is the lateral component with the most energy. This analysis shows not only how k is distributed in the channel, but all of its components $\langle u_i'u_i'\rangle$. The influence of the wall can be

Table 4.6: Compilation of k turbulence statistics from Table 3.3 and Table 4.4.

Statistic $[m^2s^{-2}]$	G1G2	R_1	R_2
TKE ($\times 10^4$)			
$\langle k \rangle$	6.21	17.2	12.6
$\langle u'u' \rangle$	2.95	15.3	14.1
$\langle v'v' \rangle$	3.42	7.99	4.75
$\langle w'w' \rangle$	6.02	11.3	6.46

seen to augment the streamwise components while suppressing the lateral and wall normal components, while in the centre of the pool, it is the lateral component that dominates.

Concerning the energy dissipation methods, the global method $\varepsilon_{B,\mathrm{V}}$ has already been shown to be ineffective to obtain the local dissipation, so no further discussion of it is given. The integration of the Bernoulli equation over the volumes indicates that the energy dissipation in G1G2 is greater than at the flume bed. The decomposition of terms in Eq. 3.7 and Eq. 4.4 showed that it was the flow elevation that contributed most to the head losses for the three cases. Recall that the final value of $\langle \varepsilon \rangle_\mathrm{V}$ is dependent on the head losses ΔH_V, the size of the volume with respect to the pool, and the volumetric flux, Q_V/YZ (from Eq. 3.8). This leads to a reduction of ΔH_V for R_1 and R_2 owing to the smaller measurement volumes. Compounded with this, U is less at the flume wall compared to the centre of the flow, owing to the boundary layer. This results in a Q_V/YZ term of 0.92 and 0.76 times the G1G2 case for R_1 and R_2, respectively.

With respect to $\langle \varepsilon \rangle$, calculated from the gradients of the flow, R_1 and R_2 are respectively ten times and three times greater than G1G2. Some of this difference must be attributed to the difference in resolution. As the boundary layer regions had interrogation volumes that were physically smaller, the averaging of the smaller scales in the flow are less. Unfortunately, there is currently no data that can quantify this effect. All methods produce a different ε, and thus the Kolmogorov length scale η is also uncertain. Calculating η from the minimum and maximum ε for all cases gives a range of $0.173 < \eta < 0.34$ mm. The

Table 4.7: Compilation of ε values from Table 3.3 and Table 4.4.

Statistic [m^2s^{-3}]	G1G2	R_1	R_2
Dissipation ($\times 10^3$)			
$\varepsilon_{B,V}$	0.167	0.037	0.037
$\langle\varepsilon\rangle_V$	1.57	0.65	0.45
$\langle\varepsilon\rangle_k$	0.14	1.69	1.33
$\langle\varepsilon\rangle$	0.11	1.07	0.36

calculation of $\langle\varepsilon\rangle_k$ however is less dependent on resolution, as the k is contained in the larger scales. Further, the method of computing the gradients from a power law fitted with a least squares method can work to reduce the effect of variance. The R_1 and R_2 show to dissipate an order of magnitude more turbulent kinetic energy than G1G2.

4.5 Concluding remarks

TPIV measurements enable a whole field insight into turbulence flows. Open channel flows tend to be difficult to measure with optical techniques owing to the scattering of the undulating free surface, vibration of the rig, laser reflections on the channel bed and air entrainment. For these measurements, the vibration correction scheme was critical for extracting results from TPIV results.

Despite these challenges, TPIV revealed the turbulent structures such as sweeps and ejections. Within these events, vortex structures that appeared to wrap around the low momentum events were revealed, findings consistent to those in the literature. The two measurement regions show that the boundary layers in them are at different stages of development. R_1, just downstream of a return flow, due to the wake of the trash racks, was not fully developed. It was found that the additive constant B in Eq. 4.1, normally taken to be 5, was not applicable for R_1 as it was for R_2. Analysing the results further with velocity PDFs and JPDFs, this difference was quantified. Fitting normal distributions over the turbulent

events enabled a probabilistic analysis, where the signature velocity and variance of the Q2 and Q4 events could be extracted.

The Reynolds stresses showed the anisotropy of the turbulence energy. The anisotropy was found to be higher upstream owing to the turbulence generated by the trash racks. Downstream, lower turbulence energy and a more isotropic flow were observed. Downstream, the generation of turbulence was greater at the near wall region. The evolution of $k(x)$, as well as $\varepsilon(y^+)$ and $\varepsilon(x)$ were investigated. The components of k were seen to be highly anisotropic, with the wall normal component suppressed by the wall, and the stream wise component contributing the greatest amount of energy. The energy dissipation ε was calculated with several methods, and these were compared with the results from the G1G2 case from Chapter 3. These measurements have allowed the characterisation of the turbulence in the pool, tying together boundary layer theory, grid generated turbulence and turbulent open channel flows. One potential application of these measurements is to see how the turbulence effects the swimming capabilities of fish.

Chapter 5

Tomographic PIV measurements of a turbulent fountain with refraction index matching

5.1 Introduction

5.1.1 Fountain Flow

Fountain flows occur when the resultant buoyant forces of a jet flow oppose its momentum. Fountain flows are also called negatively buoyant jets, referring to the action of the buoyant forces. The fountain flows investigated in this work are composed of dense fluids injected vertically upwards into lighter fluids. If there is insufficient upward momentum flux, the jet reaches a finite height and then collapses on itself as a plunging plume (Srinarayana et al, 2009). The collapsed source fluid then spreads radially from the jet along the bottom boundary (Friedman et al, 2007). The fountain of this type can be broken into 3 main parts (Cresswell and Szczepura, 1993): the jet flow region, that dominates near the exit nozzle; the cap region, where the large-scale upwards motion stagnates and spreads laterally, and the annular reverse flow region, where the dense fluid has opposing velocity to the jet direction (Figure 5.1). Otherwise, if there is sufficient upward momentum flux, the jet will continue until impinging on an upper boundary or diffusing into the ambient fluid.

Fountains are prominent in both the natural and industrial environment and exist in a large range of scales. Explosive volcanic eruptions, for example, are large scale fountain flows, where the ejection fluid is a mixture of hot and dense material injected into the density stratified atmosphere (Kaminski et al, 2005). The density changes at the top of a cumulus cloud, and the exhaust from industrial chimneys are other examples of fountain flows in the environment (Woods and Caulfield, 1992; Turner, 1966). A more recent environmental consideration arises from the highly saline water discharged from a desalination plant into the ocean (Bleninger and Jirka, 2008). Studying these flows is important to understand the physics behind them and to help predict dispersion, entrainment and eventually concentration of expelled pollutants.

Fountains are characterised by the Reynolds number for the ratio of inertial versus viscous effects, and two dependent variables, namely the Froude number for penetration height

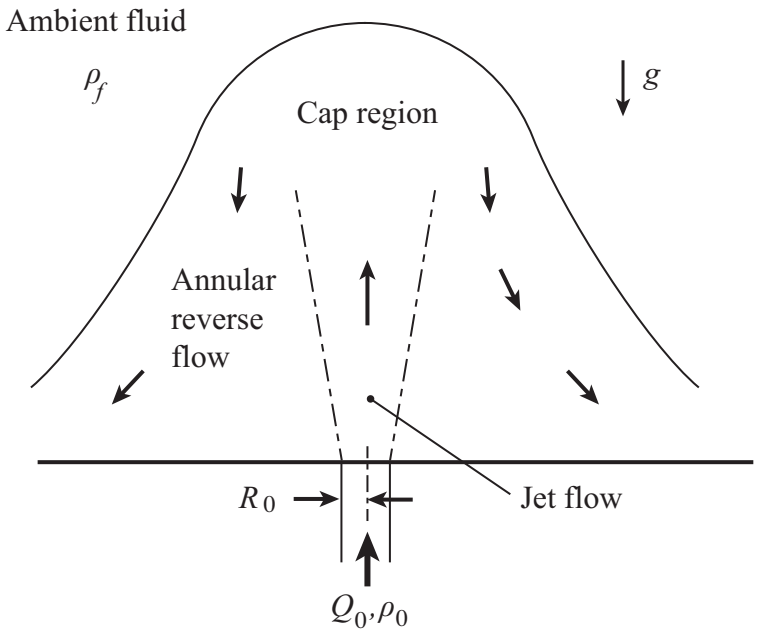

Figure 5.1: Schematic of an upward pointing fountain flow. The fountain can be divided into three main regions: the central jet flow, the annular reverse flow, and the 'cap' region where large scale reversal occurs. Adapted with permission from Cresswell and Szczepura (1993)

and Richardson number for the negative buoyancy to inertia stabilising effect, defined by

$$\mathrm{Fr} = \frac{U_0}{\sqrt{R_0 \sigma}}, \qquad \mathrm{Re} = \frac{U_0 R_0}{\nu_0}, \qquad \mathrm{Ri} = \frac{R_0 \sigma}{U_0^2} = \frac{1}{\mathrm{Fr}^2} \tag{5.1}$$

respectively. Given that the subscript 0 refers to a property at the jet source, R_0 is the radius of the exit nozzle, V_0 is the characteristic velocity calculated from the flow rate Q_0 by $V_0 = Q_0/\pi R_0^2$, and ν_0 is the viscosity of the jet. σ is the reduced gravity between the density of the fountain fluid ρ_0 and ambient fluid ρ_f, defined as $\sigma = g(\rho_0 - \rho_f)/\rho_f = g(\Delta\rho/\rho)$, where g is acceleration due to gravity (Figure 5.1). For negatively buoyant jets, the entrainment and mixing rates are less than for positively buoyant jets, the case where buoyancy acts in the direction of the jet (Baines et al, 1993).

The fountain flows examined in this work are of the type which are referred to as *forced* by Kaye and Hunt (2006), that is when $\mathrm{Fr} \geq 3$. A forced fountain flow with two fluids of different density from a circular exit is the idealised type of environmental flows described above. It should be noted, however, that there have been numerous studies of various other fountain configurations. These include investigations of planar fountains, fountains impinging on a solid surface, density gradients in the ambient fluid (Baines et al, 1993; Daviero et al, 2001), source fluids that change density difference sign depending on entrainment (by using a mixture of methanol and ethylene glycol that increases density as it mixes with water Kaminski et al, 2005) and fountains penetrating an interface (see for example the historical review of plume theory of List, 1982).

5.1.2 Experimental measurements of fountain flows

Williamson et al (2008) have recently conducted flow visualisation tests to characterise fountain behaviour over a large range of low Reynolds numbers with varying Froude number. Although this work largely focuses on laminar to transitional fountains, their results also included several forced turbulent fountains, which are unsteady and highly axisymmetric. Flow visualisation techniques have been used to characterise these types of fountain, such as injecting dye into the fountain source, a method employed by Pantzlaff and Lueptow (1999) and Philippe et al (2005). Flow visualisation has given very interesting insight

into fountain height, transition to turbulence entrainment and fountain width (Kaminski et al, 2005; Carazzo et al, 2010). However, particularly for turbulent flows, flow visualisation can give misleading results as swirls of tracking dye may remain as a coherent structure even though there is no longer vorticity at its centre (Adrian and Westerweel, 2011).

The measurement of buoyant jets differs to that of standard jets, as the properties of the source fluid are not the same as those of the ambient fluid. It is often the change in the refractive indices of the fluids that is exploited to make experimental measurements by techniques such as shadowgraphy (Baines et al, 1993). However, it is this difference in refractive indices that hinders the use of optical measurement techniques like particle image velocimetry (PIV) (see for example Hama, 1962; Gursul et al, 1990; ONeill et al, 2004), which rely on unperturbed lines-of-sight, for measuring these categories of flow. For optical techniques such as PIV to work in fountain flows with acceptable errors, it is required that the refractive indices of the fountain source and ambient fluid are the same.

Point wise measurements of a positively buoyant jet have been investigated with two hot wires to obtain the velocity and temperature correlations (George et al, 1977). Cresswell and Szczepura (1993) measured a fully developed fountain of different temperatures by Laser Doppler Velocimetry (LDV). With the use of a specially designed probe, the errors caused by laser beam bending due to the refractive index changes of the hot and cold water were quantified.

Friedman et al (2007) used PIV to measure and characterise a large range of negatively buoyant flows. The authors were able to extract the centreline velocities of the fountains (when permitted), which enabled the retrieval of the fountain centreline velocity and verification of their proposed corrected Ri. Gono et al (2012) used time resolved scanning stereo PIV of a laminar, low Froude number positively buoyant jet. The limitations of this technique are that the scanning sweep must be significantly faster than the maximum flow velocity to 'freeze' the flow field. Table 5.1 provides a sample of some experimental investigations of fountain and jet flows, in addition to the key parameters of the fountains and measurement techniques. The table highlights a lack of volumetric velocimetry techniques to analyse these flows.

Table 5.1: Sample of Experimental investigations on fountain flow. † indicates inferred data

Author	Details	Re	Fr	$\Delta\rho/\rho$	R_0 [mm]	Q_0 [L/s]
Baines et al (1993)	Vertical up fountain, Shadowgraphy	10 500	54.5	0.11†	0.65	0.011
Cresswell and Szczepura (1993)	Vertical down fountain, hot water jet into cool ambient, LDV	5 000	3.1	−0.024	7.5	0.023
Pantzlaff and Lueptow (1999)	Vertical up jet, flow visualisation. and PIV	2500 – 21 000	5.7	0.98 & 1.04	5.08	0.0095 – 0.08
Kaminski et al (2005)	Vertically down, positive and negative buoyant fountains, flow visualisation.	365 – 3 798	3.06 – 22.4	−0.0296 – 0.0337†	2.00 – 6.05	$7.3{\cdot}10^{-4}$ – 0.023
Friedman et al (2007)	Vertical up fountain, index-matched PIV, PLIF	158.6 – 11 650	0.82 – 1.15	0.11 – 0.55	9.4 – 18.8	0.0001 – 0.003†

Table 5.1: Sample of Experimental investigations on fountain flow. † indicates inferred data (continued)

Author	Details	Re	Fr	$\Delta\rho/\rho$	R_0 [mm]	Q_0 [L/s]
Williamson et al (2008)	Vertical up fountain, flow visualisation	15 – 1 900	0.7 – 100	0.004 – 0.16	0.54 – 4.80	$6{\cdot}10^{-5}$ – 0.02
Shao and Law (2009)	Horizontal dense jet, PIV and PLIF	5 000 – 10 500	7.7 – 16.2	0.02	6.48	0.051– 0.107
Burridge and Hunt (2012)	Vertical up fountain, flow visualisation	924 – 4 022	0.4 – 45	0.015 – 0.15†	5.1 – 11	0.015– 0.065
Gono et al (2012)	Vertical up, positive buoyant jet, time resolved scanning PIV	200	0.3	0.003	10 (sq.)	0.0032
Present Study	Vertical up fountain, TPIV	496 – 992	4.4 – 12.2	0.004 – 0.01	4.5	0.0067 – 0.013

5.1.3 Tomographic Particle Image Velocimetry

Although TPIV is becoming increasingly widespread, a brief explanation on how the refractive index changes the performance is presented. The technique is reliant on an accurate camera calibration to precisely find the particles in space through re-projection. The camera system is calibrated by traversing a calibration plate through the volume to be measured. A camera calibration matrix can then be determined which describes the coordinates that a pixel's line-of-sight passes through (Zhang, 1999).

This technique automatically accounts for optical aberrations and fixed perturbations of the lines-of-sight such as through air-perspex-water interfaces. This case is demonstrated in Figure 5.2, where Camera A, typical of experiments measuring a homogenous fluid, has lines-of-sight perturbed by several interfaces, but they remain constant in time. The injection of a fluid with a different refractive index leads to a perturbation of the line of sight, as shown by Camera B in Figure 5.2, which cannot be resolved from the camera calibration made in the homogenous fluid. As such, the tomographic reconstruction would not be able to ascertain the locations of particles in the flow.

Elsinga et al (2005a) proposed a technique that utilises background orientated Schlieren measurements to correct for optical distortions induced by density changes in airflows for planar PIV. Although significant improvements were made to the measurement accuracy with this technique, they were not sufficient for a TPIV reconstruction. Recently, Ortiz-Dueñas et al (2010) used refraction index matching of two immiscible fluids to measure the coalescence of drops using TPIV, and Lecordier et al (2012); Weinkauff et al (2013) measured a flame that had varying refractive indices in space and time, corrected by a volume calibration. Im et al (2014) achieved measurements inside a model of the human nasal cavity by matching the fluids refractive indices to the housing material. The versatility of TPIV to measure a vast array of challenging flow fields is an exciting direction for volumetric experimental measurements. The aim of this chapter is to show the applicability of TPIV in measuring flows where refractive indices must be considered and to obtain previously unknown flow physics of turbulent fountains.

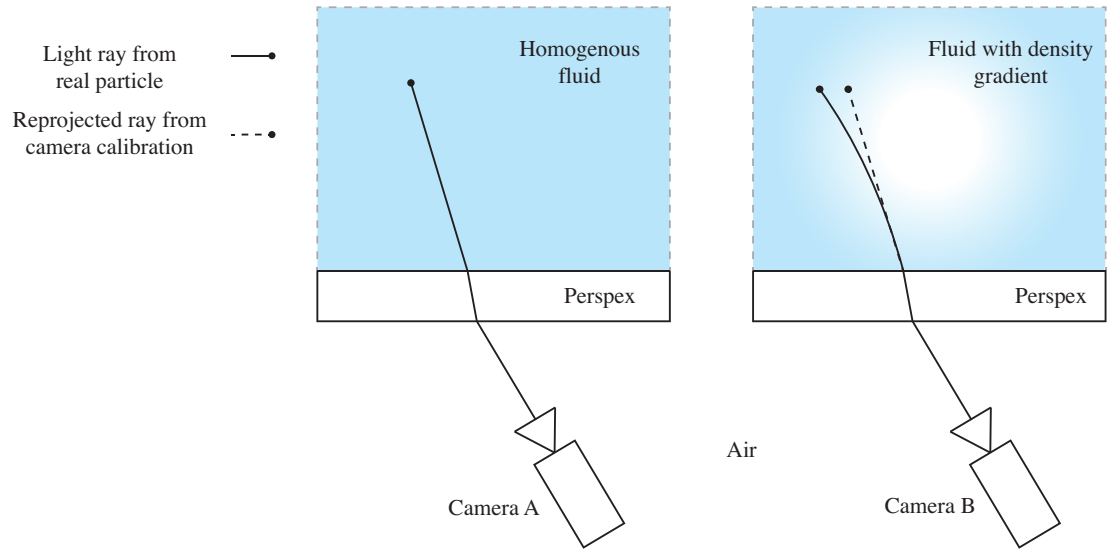

Figure 5.2: The effects of unsteady perturbations of refractive indices for particle imaging. Unlike for camera A where both rays are coincident, the unsteady density gradient on the right hand side results in an actual and re-projection anomaly of the particle position.

5.2 Experimental Set-up

The experiments were conducted at the University of Sydney in the experimental rig shown schematically in Figure 5.3. The tank was 25 cm deep with 34×34 cm^2 base. The nozzle from the header tank was centrally located and flush with the tank bottom with $R_0 = 4.75$ mm. The control valve was used to set the flow rate, and the experiment was initiated and stopped with a quick action on/off valve. The flow rate was known to within $\pm$ 4 mL/min. An experiment involves injecting saline water from a sudden start and at a constant flow rate into the bottom of a tank filled with a solution of fresh water and methylated spirits (0.95 mL/mL ethanol), after the refraction indices of both fluids have been matched. Matching the refractive indices of fluids with ethanol and salt water for stratified flows was first explored by Hannoun (1985). Some of the advantages of using these solutions are that they are readily available, affordable and don't suffer from double diffusion effects.

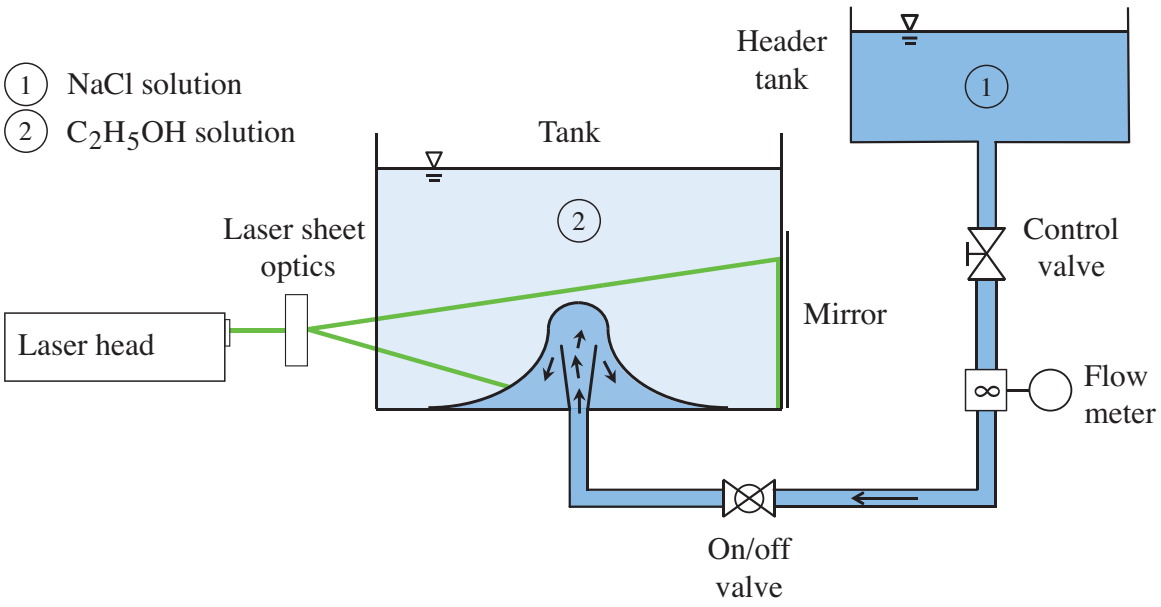

Figure 5.3: Schematic of experimental set-up up of fountain flow. The saline fountain fluid was injected into the lower tank of ethanol in water solution. A laser volume illuminated the central region of the lower tank for TPIV.

5.2.1 Experimental regime

Table 5.2 lists the range of flow rates and densities and resulting Re, Fr and Ri numbers. As described in section 5.2.2, a change in salinity results in a change in the refraction index of the fluid, and this needed to be matched with the methylated spirits concentration in the lower tank. In Table 5.2 the three density differences are labelled as shorthand cases for easy reference: $\rho 05$, $\rho 07$, and $\rho 10$ corresponding to the value of $\Delta\rho/\rho$ of the experiments. The concentrations of NaCl used were in the order of 0.02-0.06 mol/L, and thus the dynamic viscosity ν_0 of the brine source would have varied by no more than 1% (Kestin et al, 1981). Thus, the viscosity was considered to be constant across the range of flows in these experiments.

5.2.2 Refraction-Index Matching

In these experiments, controlling the refractive indices of the fluids took precedence over setting the densities. It is possible to calculate *a priori* the concentrations of salt and alcohol-solution water, normally from an empirically derived table Daviero et al (2001). However, it was found that it was necessary to experimentally modify the alcohol concentration further, until matched. As indicated by Hannoun (1985), when ethanol and water are combined to form a solution, the temperature of the solution increases. For this reason, the solutions were allowed to rest before refractive index matching and then testing in an effort to ensure that refractive indices were matched at the same temperatures. However, the lab where the experiments were conducted was not temperature controlled and temperature variations were recorded during the tests.

Figure 5.4 shows the small apparatus used to measure and verify the refractive indices of the inlet fluid and reservoir fluid were matched. A low-energy laser beam with the same wavelength as that used in the TPIV acquisition (section 5.3) was fired through a small cubic receptacle filled with the fluid to be tested. The refracted laser beam was then shone onto a target approximately 2 metres away. The fluid in the receptacle was replaced with a sample from the alcohol solution directly from the tank. As different refractive indices lead to a different lateral position of the laser beam on the target, the solution of the

Table 5.2: Experimental parameters that were investigated in this study

case	$\rho 05$	$\rho 07$	$\rho 10$
$\Delta\rho/\rho$	0.534%	0.747%	1.050%
Q_0 [L/min]	0.4	0.4	0.4
U_0 [m/s]	0.094	0.094	0.094
Re	496	496	496
Fr	6.123	5.179	4.368
Ri	0.027	0.037	0.052
Q_0 [L/min]	0.6	0.6	0.6
U_0 [m/s]	0.141	0.141	0.141
Re	745	745	745
Fr	9.185	7.768	6.552
Ri	0.012	0.017	0.023
Q_0 [L/min]	0.8	0.8	0.8
U_0 [m/s]	0.188	0.188	0.188
Re	993	993	993
Fr	12.247	10.358	8.736
Ri	0.007	0.009	0.013

alcohol was adjusted until the laser beam was coincident with the spot on the gauge from the corresponding saline solution. When adjusting the concentrations of both the salt and alcohol, care was taken to thoroughly stir the tanks to ensure that homogenous solutions were obtained.

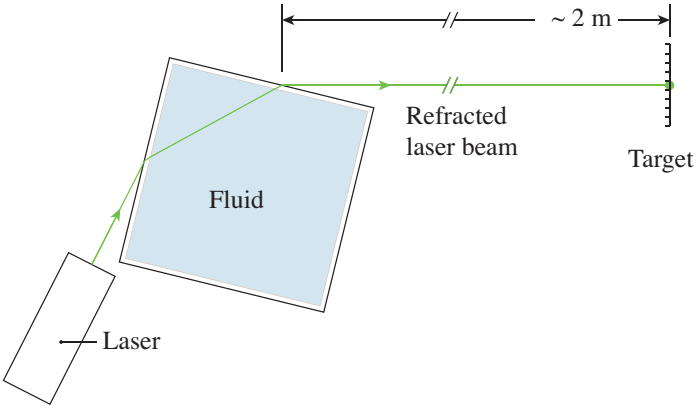

Figure 5.4: Apparatus to verify refraction index matching. The laser beam refracts through the liquid to be tested onto the target. The concentration of the second liquid is adjusted until the laser beam hits the same mark on the target as it does when shone through the first liquid.

5.3 TPIV set-up

5.3.1 Laser and optical details

TPIV measurements were taken in the lower section of the tank to capture the fountain flow (Figure 5.5). The TPIV system was designed as built at the University of Sydney. The TPIV system was comprised of four 1280 $\times$ 1024 px 8 bit Mikrotron cameras positioned in an inverted pyramid configuration, all cameras subtending an angle with the normal of the laser sheet of approximately 27°. All cameras were fitted with lens mounted two-axis tilt adapters, adjusted to achieve the Scheimpflug condition.

A laser sheet volume of thickness $\Delta Z = 11$ mm, was used to illuminate the measurement

volume, realised with a single head YAG laser with 10 mJ per pulse. A mirror on the back side of the tank was used to increase the illumination of the volume, which had the added benefit of creating forward scatter of the particles for all cameras (Figure 5.5). The particles were 10 μm silver coated hollow spherical glass beads. The measurement volume in the centre of the tank was $60 \times 50 \times 11$ mm^3 $(x \times y \times z)$. The acquisition frequency was 110 Hz, chosen to ensure maximum particle displacements of $\sim$8 px for the largest flow rate case. The tomographic reconstructions and correlations were made using the SLIP library developed at the University of Poitiers (Tremblais et al, 2010).

Table 5.3 presents a summary of the cameras settings used in the experiment: the focal length of the lenses Z_0, the aperture f-stop settings, magnification factor M_0 positions and theoretical focal depth δz of the cameras in the TPIV experiment.

Table 5.3: Camera settings (Figure 5.5). δz is the focal depth for theoretically well focussed particle images.

	Z_0 [mm]	f-stop	M_0 [mm]	δz [mm]
Camera 1	85 mm	5.6	0.11	1.8
Camera 2	85 mm	4	0.11	1.6
Camera 3	105 mm	5.6	0.11	2.6
Camera 4	105 mm	4	0.12	2.9

Cameras 1 and 2 were positioned closer to the measurement volume to ensure that M_0 for all cameras were equivalent and adjusted so the subtended angles of the camera axes with the laser plane at $z = 0$ were alike. The lens apertures had to be open as wide as possible (low f-stop) due to the low energy intensity of the laser. These reduced aperture settings meant that the focal depth δz was less than the laser sheet thickness $\Delta z_0 = 11$ mm. Due to the viewing angles of the camera combined with the less than ideal depth of focus, particle astigmatism on the imaged particles was observed. There is more discussion on this point in Section 5.3.3.

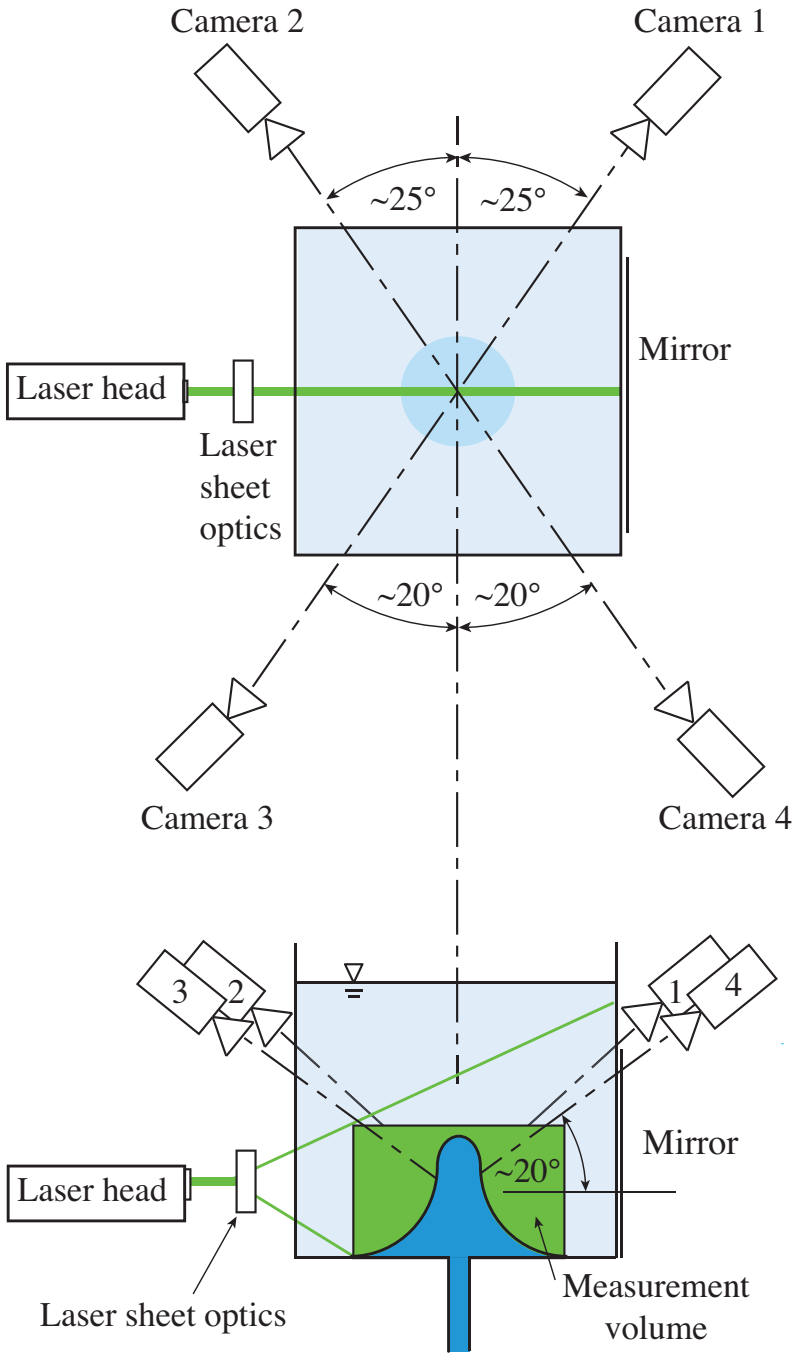

Figure 5.5: Schematic of TPIV system in experimental set-up. 4 cameras were located in an inverted pyramid configuration around the measurement region.

5.3.2 Reconstruction

To remove the background noise from the images, such as bright spots or reflections from the apparatus, a temporal – spatial median filter was applied. The median of 200 images was calculated and then subtracted from the images. A gaussian filter was then applied to enhance the particle images. The processed images to be reconstructed had a homogeneous particle per pixel of $ppp \approx 0.025$, or an image source density $N_s \approx 0.4$. The cameras were calibrated with a pinhole model, improved with a volumetric self calibration technique analogous to Wieneke (2008) that was calculated from 20 sequential images. The reconstruction process was split into a volume initialisation and volume reconstruction phase, with the aim of optimising the reconstruction. These steps were performed with the same algorithms as method as discussed in Section 3.3.3. The resolution of the TPIV system was 8.5 voxel width/mm.

5.3.3 Reconstruction quality assessment

The reconstructed volumes were 15% larger than the laser volume thickness to distribute the ghost particles energy inside a bigger volume and to improve the signal-to-noise ratio. This measure also prevents high intensities at the volume edges resulting from lines-of-sight that pass through less of the volume, and hence effecting the correlation. The volume is then trimmed to a size within the laser sheet so that only the particles reconstructed within the laser sheet are correlated. An averaged, normalised, reconstructed energy profile $E_{xy}(z)/\hat{E}$ is presented in Figure 5.6, where $\hat{E}$ is the maximum of $E_{xy}(z)$ and the xy subscript denotes spatial averaging over each xy plane. From this figure the reconstructed laser sheet profile is clearly visible. The aforementioned edge effects are visible, but do not affect the correlation, as the volume was trimmed for $-5.5 < z < 5.5$ mm.

The laser sheet profile does not display the usual top hat profile used in most TPIV measurements. The particle astigmatism (Section 5.3.1) is believed to be the primary reason for this, a shortcoming of the apertures of the cameras required to be open in order to image the particles. Despite this, there is a good signal-to-noise ratio, taken to be the ratio of the highest to the lowest reconstructed intensity, approximately equal to 5 (Scarano, 2013).

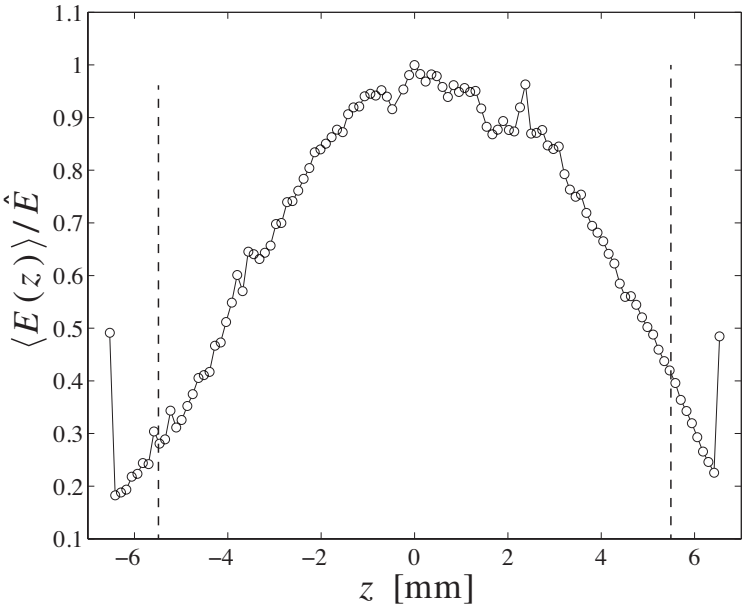

Figure 5.6: Normalised laser sheet profile of a reconstructed volume. The reconstructed signal-to-noise is approximately 5, estimated from the lowest to highest $\langle E(z)\rangle$. The dashed lines indicate the locations of the applied trim.

The reconstruction quality, denoted by the correlation coefficient Q_I (Equation 5.2) as proposed by Elsinga et al (2006b), is one indicator of the quality of the reconstruction. Q_I is a measure of the difference between the intensity of the pixels (i, j) of the filtered images I and the intensity of the corresponding pixel locations, I_r, by projecting the reconstructed volume intensity. In these experiments, the average Q_I was found to be 82%, which is above the widely accepted 75% lower threshold.

$$Q_f = \frac{\sum I(i,j) \cdot \sum I_r(i,j)}{\sqrt{\sum I^2(i,j) \cdot \sum I_r^2(i,j)}} \tag{5.2}$$

As an index refraction matching regime was implemented for these experiments, the correlation coefficient was spatially verified to ensure that there was no bias in Q_I due to differences in refractive indices of the source and ambient fluid. If there were, it would be expected that there would be a local region of high or Q_I corresponding to the fountain location. Therefore, for an example case of $\rho 07$, $Q_0 = 0.4$ L/min, a 32×32 pixel, non-overlapping sliding window was passed through 10 images pairs to calculate an average local correlation coefficient, the result of which is shown in Figure 5.7. For the case considered here, the fountain height is approximately half way up the domain. However, the figure shows that Q_I is close to uniformly distributed across the image. The exception to this is the low Q_I (blue) regions on the sides, which correspond with areas of image masking.

5.3.4 Velocity Field Calculation

A two pass $40 \times 40 \times 40$ voxels interrogation volume with 75% overlap was used to calculate the cross-correlation and hence velocity fields. For the highest flow rate cases, it was found that a preliminary pass of an $80 \times 80 \times 80$ voxels correlation window was required to capture the jet region of the fountain correctly. The final velocity fields were 30 600 vectors at a spatial resolution of $\delta x_i = 1.19$ mm. A median vector replacement regime was implemented as per Westerweel and Scarano (2005), with the number of spurious vectors found to be between 2–4% per volume. As tomographic reconstruction had been shown to be particularly susceptible to noise (Worth et al, 2010), a $3 \times 3 \times 3$ bilateral filter was used

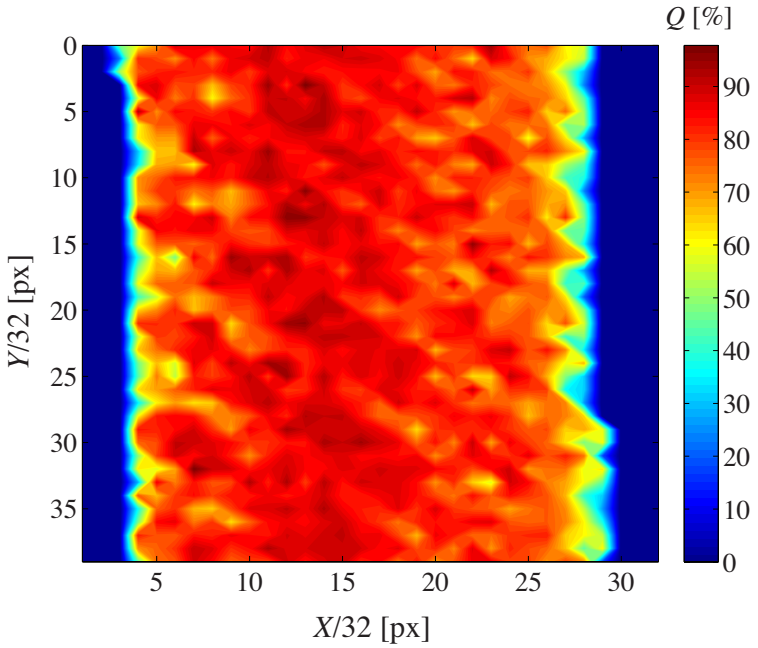

Figure 5.7: The local reconstruction quality coefficient Q_f, averaged over 10 images in 32×32 non-overlapping sliding window. X and Y are the image coordinates. The blue edges are where the images were masked so that only the union of all images are considered. This image shows a close to uniform distribution of $Q_f \approx 80\%$ and hence no bias according to the fluid refractive indices.

to filter the velocity fields spatially, preferred over a gaussian as it is edge preserving.

5.3.5 Computational Time

The reconstruction programmes developed from the SLIP suite run on multiple processors. The reconstruction of a particle volume, each containing $7.5 \cdot 10^7$ voxels needed in the order of 8 minutes running on 8 cores of an Intel i7 3.4GHz processor. The correlation algorithms required approximately 12 minutes on the same machine.

5.4 Results

The results are divided into three main sections: firstly, a time series of the start-up of the fountain flows are presented; secondly, analysis of the instantaneous fountains once they had reached a fully developed state, and; lastly, the averaged properties of the fountains at the fully developed state. Due to high reflection of the laser light in the jet orifice the data in a region immediately above the jet is not available.

5.4.1 Fountain initialisation velocity fields

The initialisation of the fountain was captured, and the results show some characteristics of the flow entrainment and mixing. Figure 5.8 shows eight chronological images from just after the moment of initialisation $t = 0.045$ s until $t = 4.545$ s for the $\rho 07$, $Q_0 = 0.4$ L/min case. In the images, the red iso-surfaces represent the jet region of the flow by linking areas of $v = 0.01$ m/s and similarly the blue regions by $v = -0.01$ m/s. This definition of the jet ensures that it can be distinguished from the stationary ambient fluid. The contour plane represents the instantaneous magnitude of lateral velocity u, ranging from blue $u = -0.02$ m/s to red $u = 0.02$ m/s. An explanation of the flow features of each frame of Figure 5.8 are listed as follows.

(a) Moments after initialisation, the fountain fluid is introduced into the tank by a rapid start. At this point, the fluid just above the jet nozzle is displaced radially outwards,

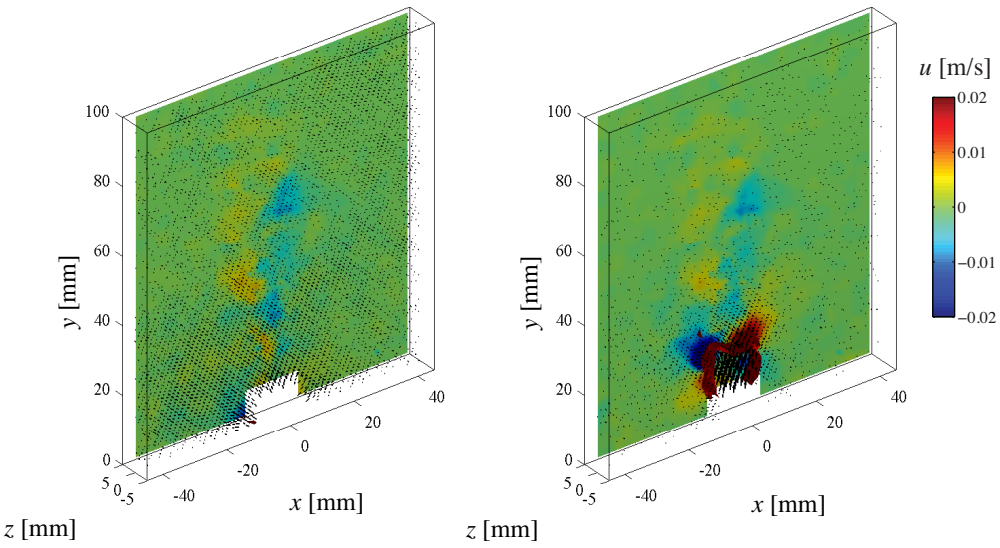

(a) $t = 0.045$ s

(b) $t = 0.455$ s

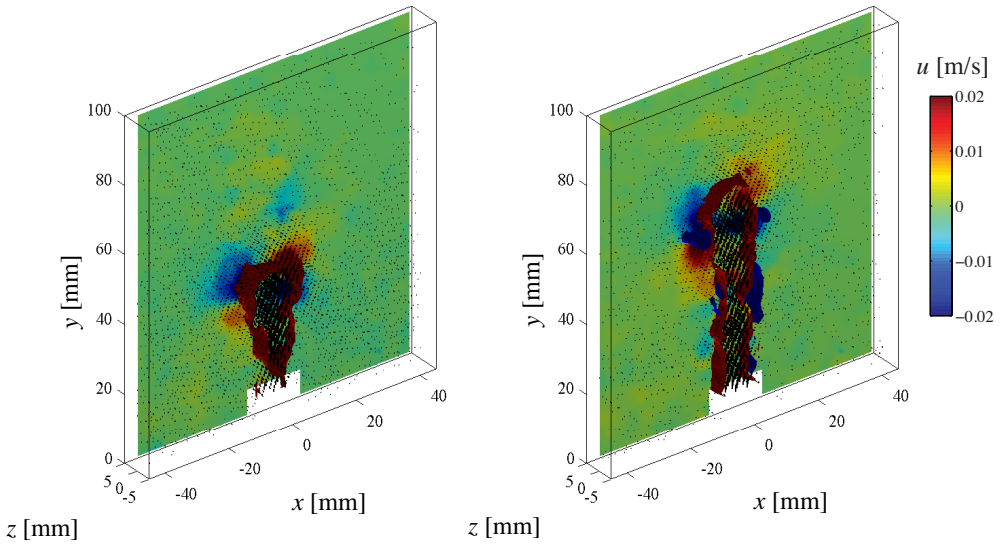

(c) $t = 0.909$ s

(d) $t = 1.364$ s

Figure 5.8: Initialisation of fountain $\rho 07$ $Q_0 = 0.4$ L/min. The plane at the rear indicates lateral velocity component, and the red and blue regions link regions of $v = 0.01$ m/s and $v = -0.01$ m/s respectively. Description of the fountain events provided in text.

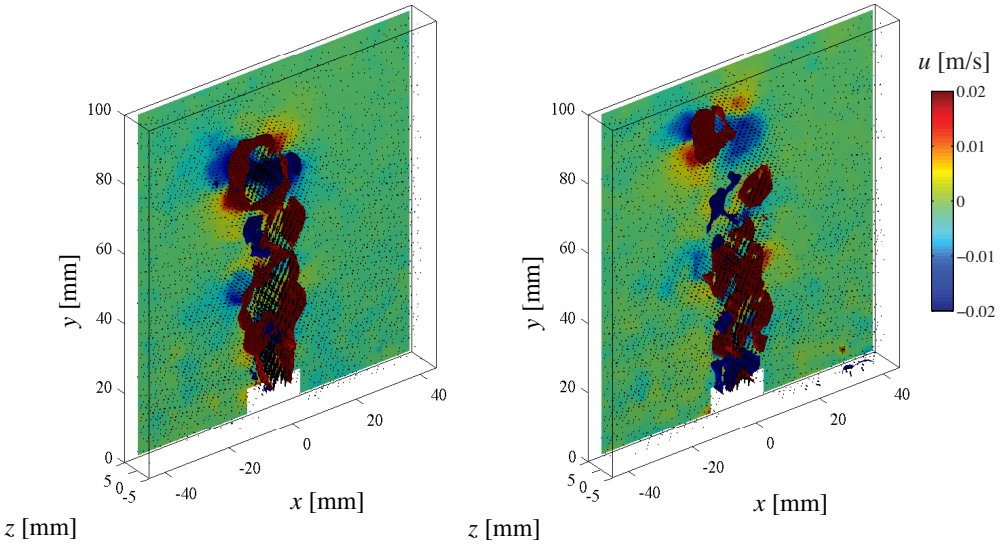

(e) $t = 1.818$ s **(f)** $t = 2.273$ s

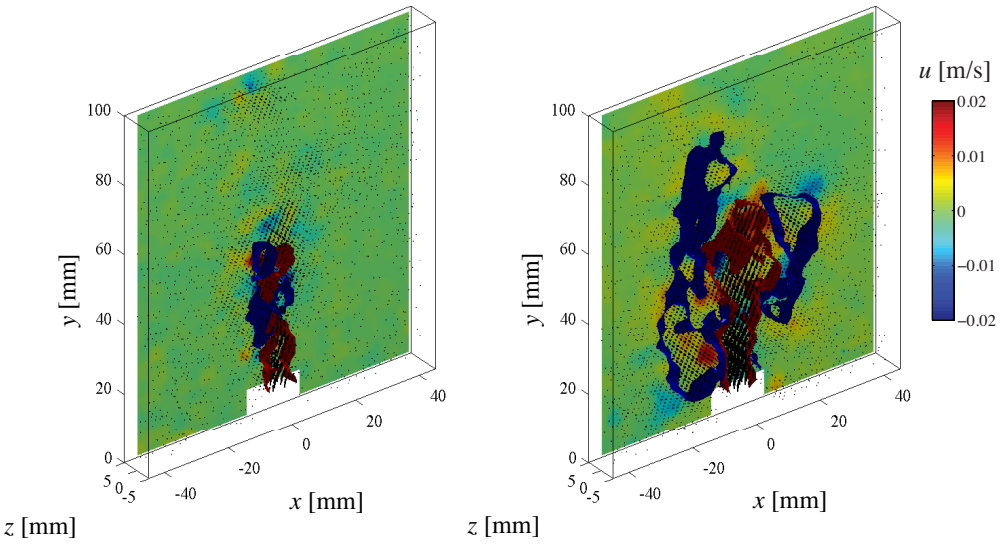

(g) $t = 2.818$ s **(h)** $t = 4.545$ s

Figure 5.8: Initialisation of fountain $\rho 07$ $Q_0 = 0.4$ L/min (continued).

highlighted by the small red and blue lateral components on the contour surface just to the sides of the nozzle region.

(b) At $t = 0.455$ s, the stage of the jet region displays a dip at the centreline. This is the effect of the ring vortex that is ejected at the moment of initialisation. This vortex ring is highlighted by the outward lateral velocity at the top couple with inward lateral velocity just beneath.

(c) The cap region is dominated by the vortex ring and rises to approximately 90% of the fully developed fountain height (see Figure 5.11). The jet region is initially stable.

(d) At t=1.364 s, the cap region exceeds the fully developed fountain height. To the sides of the jet region, small volumes of fluid with negative velocity (bounded by the blue iso-surfaces) are observed. These regions have separated from the upward momentum of the jet due to the shear action at the interface of the jet into the ambient fluid.

(e) & (f) These images show the detachment of the vortex ring in the cap region from the jet, also observed by Williamson et al (2011); Burridge and Hunt (2012). Large instabilities in the jet region are observed as the fountain becomes increasingly unstable. The lateral velocity components are alternating seemingly periodically up the length of the jet.

(g) The jet and fountain region have appeared to stagnate as the negative buoyant forces at this moment are large owing to the high quantity of salt water that is now directly above the jet region.

(h) Finally, the jet fluid that was initially ejected collapses over the jet column forming the annular reverse regions that become more stable as the fountain becomes fully developed. The angular reverse regions highlighted by the blue iso-surfaces are asymmetrical, highlighting the high level of turbulence and the importance of investigating these flows with volumetric techniques.

5.4.2 Fully developed fountain: instantaneous velocity fields

Figure 5.9 shows corresponding instantaneous velocity fields of $\rho 05$ (a), $\rho 07$ (b) and $\rho 10$ (c) at a flow rate of $Q_0 = 0.4$ L/min. These images show how the 3D jet region fluctuates and contain structures of downward velocity. These packets are associated with high vorticity events at the interface of the jet and the annular reverse flow region, which for this region of Re is also highly transitional. The figures indicate that these structures with net $-v$ component of velocity act to increase the unsteadiness of jet region as they interact with it. These structures reveal some of the interesting physics of the fountain flows, and the mechanism in which the jet region transitions to the cap region.

The surface contours in Figure 5.9 also reveal similar sized structures of lateral velocity. These structures are more pronounced as Fr increases. At these instantaneous fields, the lateral velocity packets do not correlate with the structures highlighted by the iso-surfaces. This indicates that in the annular reverse region there is lateral mixing due to shearing action as opposed to strong vortex mixing.

Figure 5.10 shows instantaneous velocity fields of $\rho 05$ (a), $\rho 07$ (b) and $\rho 10$ (c) at a flow rate of $Q_0 = 0.6$ L/min. In this figure, the iso-surfaces of the Q-criterion are used to highlight the vortices. For all cases, the corkscrew-like swirl is rotating as a positive R_y. Figure 5.10(a) shows that small vortex regions are present at the interface of the jet and the annular reverse region of the fountain. The collapsing fluid is notably more steady in the annular reverse region, and the vorticity in those regions are significantly less than in the jet regions, which is particularly noticeable in the $\rho 07$ and $\rho 10$ cases. Figure 5.10(b) show a strong mixing event where at $\sim y = 70$ mm there is a strong downward flow region at the jet interface. In the $\rho 10$ case (Figure 5.10c), the cap region of the fountain contains two dominant vortex structures ($\sim y = 60$ mm). These structures reveal some of the interesting physics of the fountain flows, and the mechanism in which the jet region transitions to the cap region.

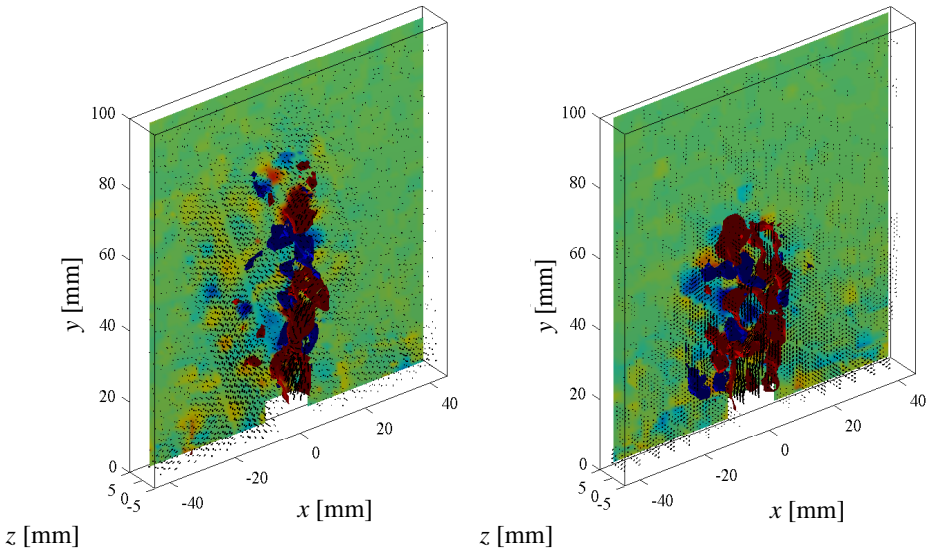

(a) $\rho 05$, Fr = 6.1 **(b)** $\rho 07$, Fr = 5.2

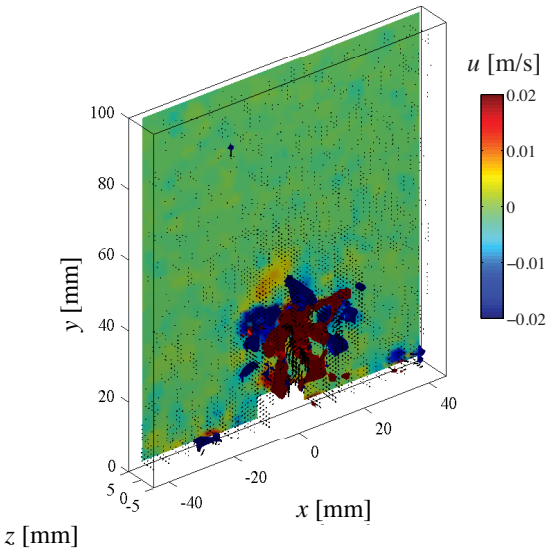

(c) $\rho 10$, Fr = 4.4

Figure 5.9: 3D instantaneous velocity fields of the $Q_0 = 0.4$ L/min flow rate fountains for (a)$\rho 05$; (b) $\rho 07$, and; (c) $\rho 10$. In the top row, the vector colours are proportional to the axial component of velocity v, where red is positive up and blue is the downward flow in the annular reverse flow region.

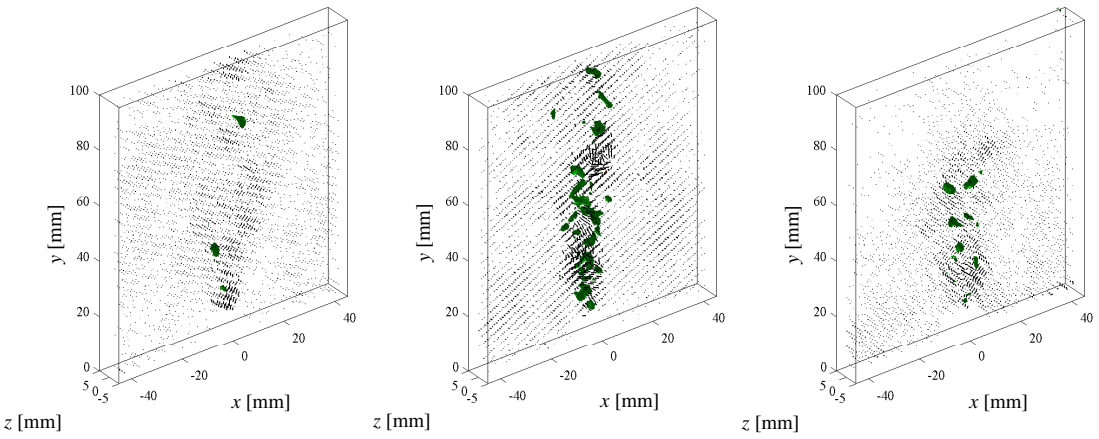

(a) $\rho 05$, Fr = 6.1 **(b)** $\rho 07$, Fr = 5.2 **(c)** $\rho 10$, Fr = 4.4

Figure 5.10: 3D instantaneous velocity fields of the $Q_0 = 0.6L/min$ flow rate fountains for (a) $\rho 05$; (b) $\rho 07$, and; (c) $\rho 10$. Iso-surfaces of the Q-criterion are shown to highlight the vortices.

5.4.3 Fully developed fountain: mean velocity fields

In this section the full range of fountains that were investigated are presented. The averaged quantities for the fully developed fountains were realised over 250 sequential velocity fields. Figure 5.11 shows all 9 permutations of flow rate and density differences. The red iso-surfaces capture the jet region of the fountain and join regions of the velocity fields where $v = 0.01$ m/s. The blue iso-surfaces show the annular reverse flow region and connect velocities of $v = -0.01$ m/s. These regions help visualise the height and breadth of the fountain region.

The xy plane at $z = -4$ mm of the plots in Figure 5.11 shows contours of the mean radial velocity component u, where red indicates maximum positive 0.05 m/s and blue -0.05 m/s with respect to the x-direction. These lateral velocity components, when considered in conjunction with the iso-surfaces, can indicate the average level of mass transport between the fountain regions. All figures contain the cap region of the fountain (maximum extent of the jet region). The outward, radial flow along the bottom of the tank can be observed in all figures. All of the fountains show varying patterns of radial components between the jet and

annular regions. For example, for the $\rho 05$ case, the annular region is on average being re-entrained into the jet region. It was observed that the averaged fountains were symmetrical, however a notable exception is the $\rho 05$ case where only one side of the annular reverse flow region appears to be present. This highlights the sensitivity to the fountain start-up conditions and limited time for averaging.

Generally the averaged fountains are symmetrical, however a notable exception is the $\rho 05$, $Q_0 = 0.4$ L/min case (Figure 5.11a) where only one side of the annular reverse flow region appears to be present. This highlights the sensitivity to the fountain start-up conditions and limited time for averaging. The mean images in the high Re fountains have a higher measurement noise level than the other cases. This is due to a temperature induced refractive index change, as discussed in Section 5.2.2.

The low Re figures show a steadier averaged fountain – an expected result, as Re is important only for the turbulence level of the fountains (Friedman et al, 2007). The convergence of the averaging is notably less for the higher Re-Fr fountain cases, such as Figure 5.11c. Another reason for these asymmetries is because it was not possible to take longer averages without filling up the tank with too much brine, as discussed further in Section 5.4.7.

The averaged, fully developed fountains enable analysis of the dependence of the mean penetration height z_m as a function of Fr. Turner (1966) and Baines et al (1990) found that, for the range of Fr of these experiments, the fountain penetration height z_m scales according to

$$z_m = C' \mathrm{Fr} R_0 \tag{5.3}$$

where C' is an experimentally calculated constant. The steady state fountain height z_m was determined as the position where $v = 0$ in the vertically upward projected area of the jet orifice. Figure 5.12 shows the plot of $z_m(\mathrm{Fr}) = C' \mathrm{Fr} R_0$, where C' was found to be 2.71. For the fountain cases where $\mathrm{Fr} > 8.7$, z_m was inferred by linearly extrapolating v from $h = 80$ mm. The data for the extrapolated values are therefore indicative only and were not used in the calculation of C', and are shown as unfilled markers. A regression analysis for the data for $\mathrm{Fr} < 8.7$ yielded an $R^2 > 0.95$ and thus that the steady state fountain height is directly proportional to Fr, as widely reported in the literature. The solid line in Figure 5.12

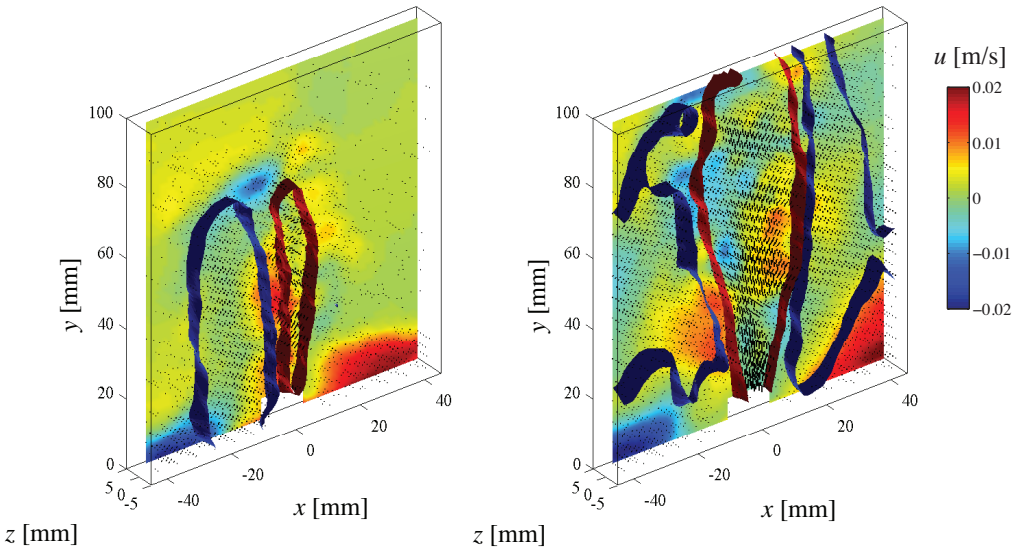

(a) p05, $Q = 0.4$ L/min,
Fr = 6.1, Re = 496

(b) p05, $Q = 0.6$ L/min,
Fr = 9.2, Re = 745

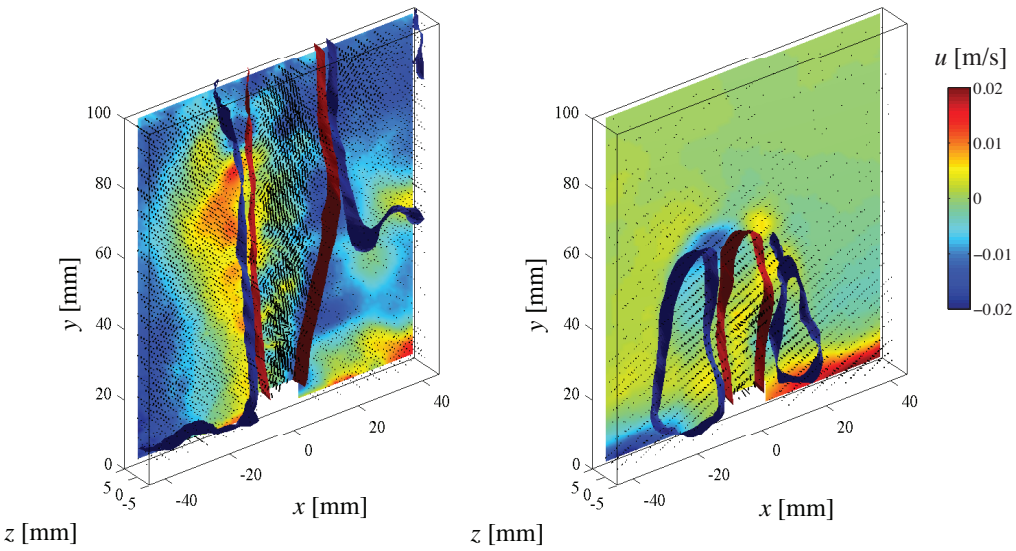

(c) p05, $Q = 0.8$ L/min,
Fr = 12.2, Re = 993

(d) p07, $Q = 0.4$ L/min,
Fr = 5.2, Re = 496

Figure 5.11: 3D mean velocity fields for all fountain cases and flow rates. The red and blue iso-surfaces separate the fountain into the jet and annular reverse regions by joining velocities of $v = 0.01$ m/s and $v = -0.01$ m/s respectively.

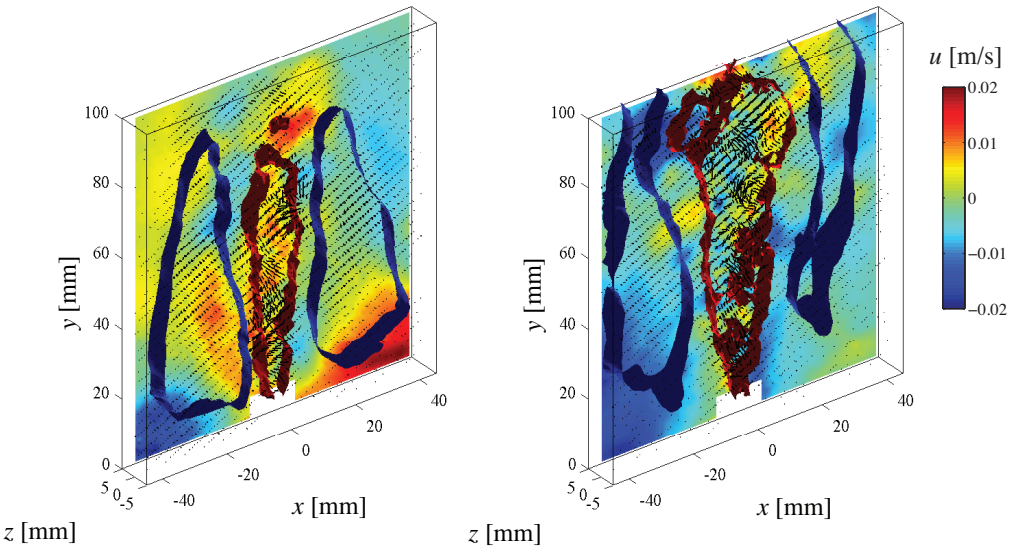

(e) p07, $Q = 0.6$ L/min, Fr = 7.8, Re = 745

(f) p07, $Q = 0.8$ L/min, Fr = 10.4, Re = 993

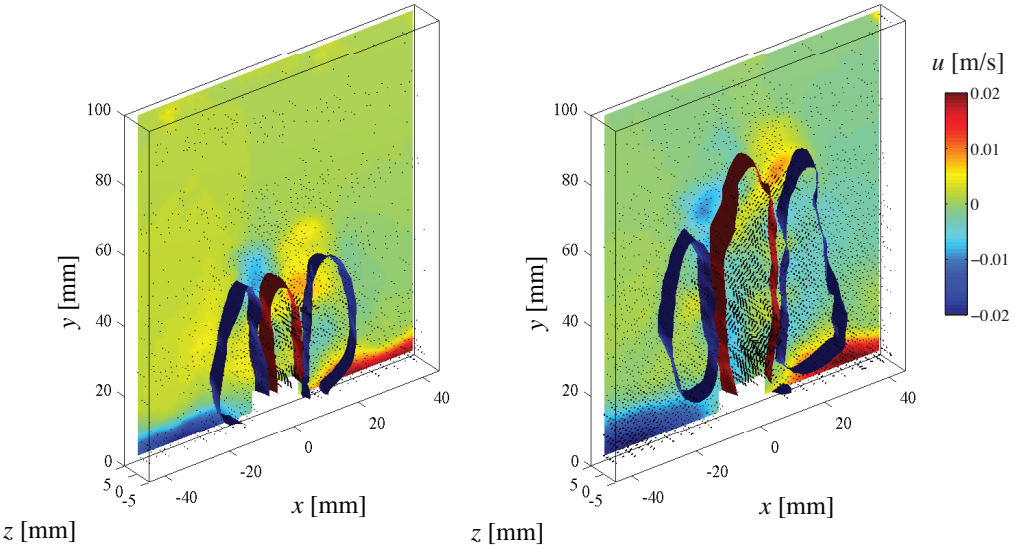

(g) p10, $Q = 0.4$ L/min, Fr = 4.4, Re = 496

(h) p10, $Q = 0.6$ L/min, Fr = 6.6, Re = 745

Figure 5.11: 3D mean velocity fields for all fountain cases and flow rates (continued).

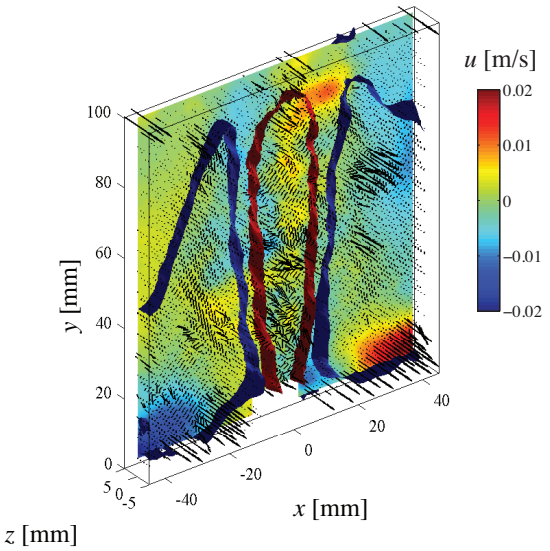

(i) p10, $Q = 0.8$ L/min,
Fr = 8.7, Re = 993

Figure 5.11: 3D mean velocity fields for all fountain cases and flow rates (continued).

shows the steady state height curve with coefficient of $C' = 2.46$ as determined by Burridge and Hunt (2012). The data presented here also compare well with the value determined by Carazzo et al (2010), who found $C' = 2.68$ from their laboratory measurements.

The calculation of this C' coefficient has been explored in more detail by Carazzo et al (2010). C' is sensitive to entrainment rate and start-up conditions. The sensitivity of the entrainment rate is also a function the jet flow quality (that is, whether or not it is fully developed). The restricted length of the inlet conditions in these experiments is likely to be a major source of the variability present in this data. Friedman (2006) showed that turbulent fountain heights can fluctuate by up to 60% for this particular range of Ri, and therefore with a relatively short statistic average to draw from, this effect could also help explain the variability.

Figure 5.13 shows an example of the centreline velocity v_c normalised by U_0. This plot is a good check to ensure that the velocities in the jet correspond to the bulk velocity. Extrapolating $v(h)/U_0$ to zero yields approximately $v = U_0$.

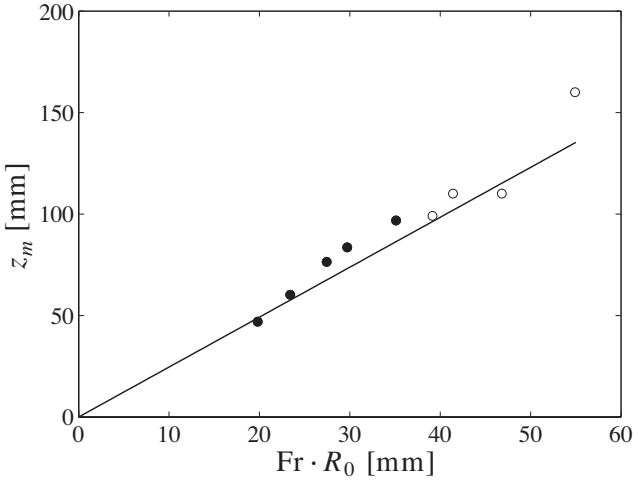

Figure 5.12: Linear dependence of the fountain heights $z_m = C'\mathrm{Fr}R_0$, where the constant of proportionality $C' = 2.71$. The unfilled markers indicate extrapolated data, the solid line represents the fitting curve from Burridge and Hunt (2012)

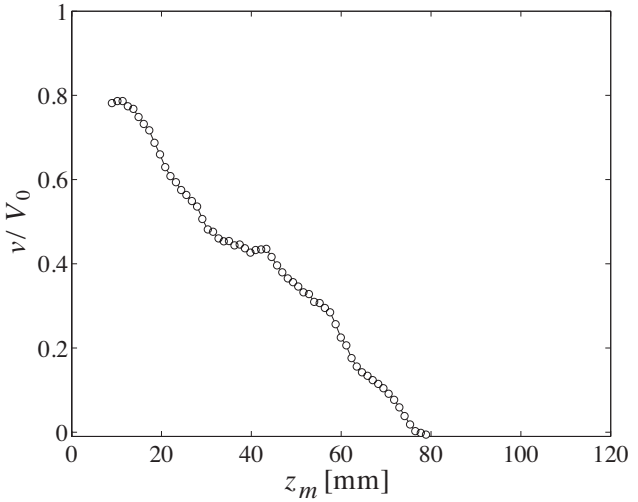

Figure 5.13: An example of the centreline velocity v_c normalised by the bulk velocity U_0. This is the case of $\rho 10$, $Q_0 = 0.6$ L/min (Fr $= 6.6$). z_m, the maximum height of the fountain is calculated where $v = 0$, and for this fountain is $z_m = 82.1$ mm.

5.4.4 Turbulence properties

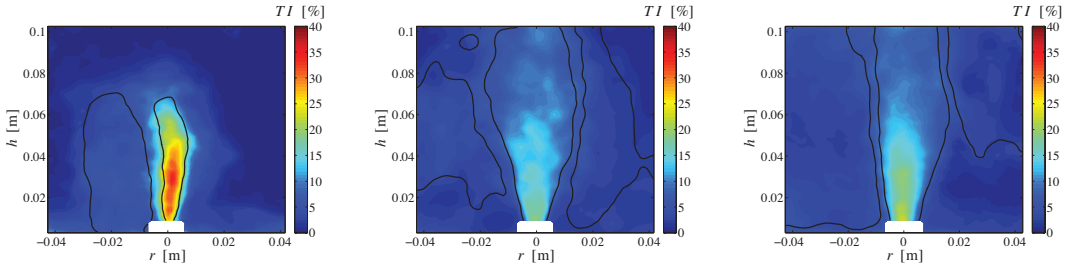

(a) p05, $Q = 0.4$ L/min, Fr = 6.1, Re = 496

(b) p05, $Q = 0.6$ L/min, Fr = 9.2, Re = 745

(c) p05, $Q = 0.8$ L/min, Fr = 12.2, Re = 993

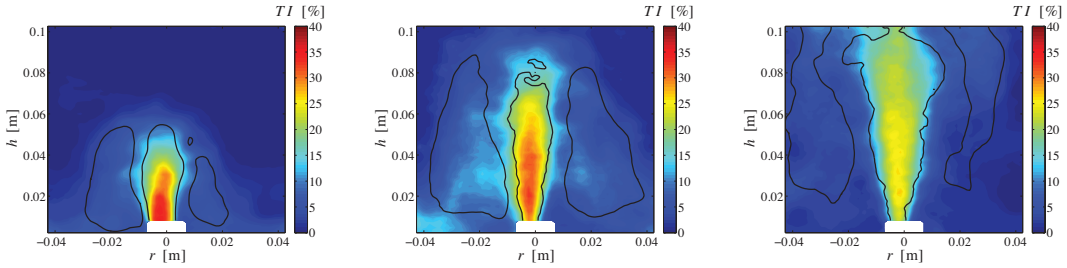

(d) p07, $Q = 0.4$ L/min, Fr = 5.2, Re = 496

(e) p07, $Q = 0.6$ L/min, Fr = 7.8, Re = 745

(f) p07, $Q = 0.8$ L/min, Fr = 10.4, Re = 993

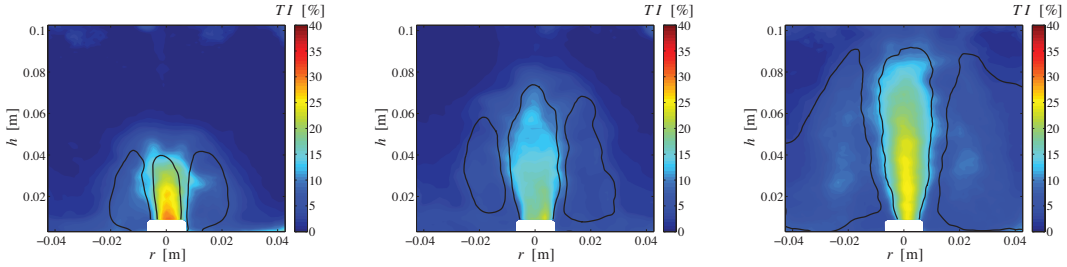

(g) p10, $Q = 0.4$ L/min, Fr = 4.4, Re = 496

(h) p10, $Q = 0.6$ L/min, Fr = 6.6, Re = 745

(i) p10, $Q = 0.8$ L/min, Fr = 8.7, Re = 993

Figure 5.14: Contour map showing the average turbulence intensity TI over 250 sequential velocity fields. The figures highlight the high turbulent fluctuations in the jet regions. The black contour lines define the mean boundaries of the jet and annular reverse flow regions.

An indication of the relative level of turbulence is the turbulence intensity, defined as

$$TI = u'/U_0 \tag{5.4}$$

where

$$u' = \sqrt{\frac{1}{3}(u'u' + v'v' + w'w')} \tag{5.5}$$

Figure 5.14 shows contour plots of the temporally and spatially (over the depth of the volume) averaged levels of TI for the fully developed fountains over 250 sequential velocity fields. The figure shows all 9 permutations of flow rate and density differences, where Re is constant for each column of figures, increasing from left to right, and the density difference increases by row. It is noted that the turbulence statistics, after so few sequential velocity fields, has not fully converged, which is confirmed by the unsteady contour interfaces in the figure. The black contour lines define the mean boundaries of the jet and annular reverse flow regions.

Figure 5.14 shows where the turbulent kinetic energy in the flows are concentrated. The figures highlight the increase of the relative turbulent energy in the jet regions compared to the annular reverse regions and indeed the cap region. In addition, the turbulence intensity is greatest along the jet centreline towards the jet exit, and tends to reduce until the steady state height. These results diverge from those of Cresswell and Szczepura (1993) who found the highest turbulence regions at the shear layer interface, and not until approximately $6R_0$ was the turbulent energy highest at the centreline of the jet. This discrepancy is largely due to the ensemble averages being computed over the depth of the reconstructed volume and also due to the lack of spatial resolution of the measurements in those regions.

The influence of Re and Fr on the turbulent fountains can be investigated from Figure 5.14, although it is noted that the range of Re is limited. As each column of images has the same Re, it can be observed that there is a Fr dependence of TI, a finding also shown in Papanicolaou et al (2008) and Carazzo et al (2010). More specifically, in Figure 5.14 a, b and c, the TI is proportional to Fr. There is evidence of this relationship in the middle (Re = 745) and right hand side (Re = 993) columns, however Figure 5.14b and c depart slightly from this proportionality, perhaps due to the lack of statistical convergence.

5.4.5 Characterisation of mixing

In lieu of a system that measures the dispersion of the concentration of the fountain directly, here an analysis of the topology of the invariants of the velocity gradient tensor, A_{ij} (Eq 5.8), is considered to determine the physical actions in which the vorticity can mix. A full discussion of the topology of invariants is described in Chong et al (1989) and Soria et al (1994). A similar analysis of this type was considered by Khashehchi et al (2010) at the turbulent/non-turbulent interface of a neutrally buoyant jet. For completeness, the velocity gradient tensor is defined as:

$$A_{ij} = \frac{\partial u_i}{\partial x_j} = S_{ij} + \Omega_{ij} \tag{5.6}$$

$$S_{ij} = \frac{1}{2}\left(\frac{\partial u_i}{\partial x_j} + \frac{\partial u_j}{\partial x_i}\right) \tag{5.7}$$

$$\Omega_{ij} = \frac{1}{2}\left(\frac{\partial u_i}{\partial x_j} - \frac{\partial u_j}{\partial x_i}\right) \tag{5.8}$$

The properties and patterns of vortices in all flows can be decomposed in this way and analysed by the eigenvalues and eigenvectors of A_{ij} (Chong et al, 1989). This type of decomposition is a critical point analysis, which enables the features of a complex 3D flow field to be concisely presented by the characteristics of the vortices (Soria et al, 1994). The eigenvalue characteristic equation of A_{ij} is:

$$\lambda^3 + P\lambda^2 + Q\lambda + R = 0 \tag{5.9}$$

where,

$$P = -S_{ii} \tag{5.10a}$$

$$Q = \frac{1}{2}(P^2 - S_{ij}S_{ji} - \Omega_{ij}\Omega_{ji}) \tag{5.10b}$$

$$R = \frac{1}{2}(-P^3 - 3PQ - S_{ij}S_{jk}S_{ki} - 3\Omega_{ij}\Omega_{jk}S_{ki}) \tag{5.10c}$$

The first invariant, P, is simply the divergence, so for this analysis is zero. The Q and R invariants can then be split into the invariants of the strain tensor by setting $\Omega_{ij} = 0$ and likewise the rate-of-rotation tensor by setting $S_{ij} = 0$ (Soria et al, 1994). These invariants then take a Ω or S subscript, respectively. From this analysis, the predominant vortex types can be analysed in terms of relative strength of shear and rotation contributions.

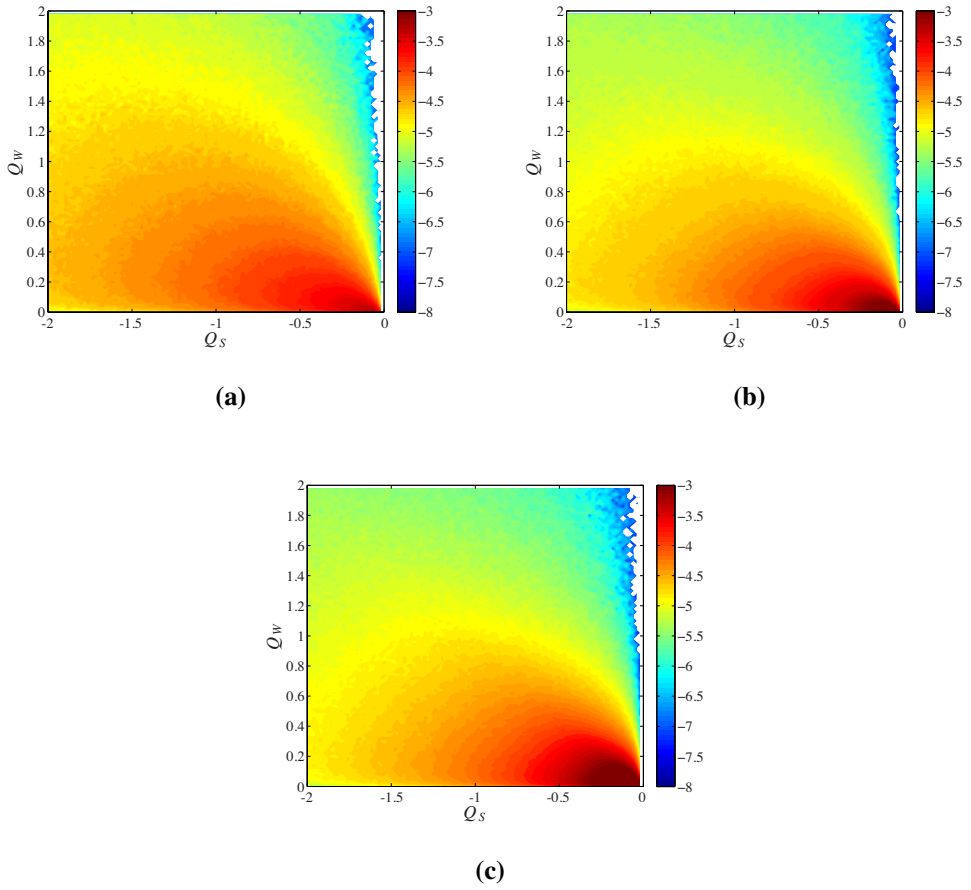

Figure 5.15: Joint probability density functions of the strain Q_S versus rotation Q_Ω dominated vortices. These are for the fountains at flow rate $Q_0 = 0.6$ L/min for (a) $\rho 05$; (b) $\rho 07$, and; (c) $\rho 10$. The colours indicate the normalised probability, and the colour bar level indicate the power-10 index.

Figure 5.15 shows the topology of the invariants of the Q_S-Q_Ω plane for all three cases for $Q_0 = 0.6$ L/min. The plots are formed by creating joint pdfs of the Q_S and Q_Ω invariants. As the ambient fluid of the fountains contribute negligible energy to the vorticity and strain in the flow, the entire measurement volume can be considered and the resulting topology map is indicative of the physics of the fountain only.

In Figure 5.15, it can be seen that there is a tendency for a greater shear contribution as the density difference increase (or as Fr decreases). Conversely, the rotation component of the $\rho 05$ case is observed to be higher. The $\rho 05$ case has the highest mean fountain height and thus a larger interface between the jet and annular reverse region of the flow. The higher average centreline velocity of this case compared to the higher density cases induces greater shear at the jet–annular reverse interface. This in turn induces greater Kelvin-Helmholtz type-instabilities in that region that have a tendency to form vortices and thus an increased rotation component. Therefore, it can be seen that the topology of invariant analysis has the ability to succinctly characterise the vortices in the fountains, revealing the dominant actions in the flow.

5.4.6 Error analysis

This section investigates whether there was an influence in the $\Delta\rho$ and Q_0 on the accuracy of the results. One of the most commonly used gauges of measurement quality stems from analysing the divergence of the velocity field, $\nabla \cdot u_i$, which for an incompressible flow such as these fountains is equal to zero. Following from this, an uncertainty analysis method proposed by Moffat (1988) and utilised by Atkinson et al (2011) is used to determine the random velocity error $\delta(u_i)$. $\delta(u_i)$ can be determined from the error in the fluctuating divergence $\delta(\nabla \cdot u_i')$, which is approximated by the RMS of the fluctuating divergence, by

$$\delta(\nabla \cdot u_i') = \sqrt{\frac{3}{2(\Delta x)^2}}\,\delta(u) \tag{5.11}$$

The results of Eq. 5.11 are presented in Table 5.4 for each case. From this table the divergence has no correlation with the change in density but it is proportional to Re. With higher Re, it is expected that the flow has a higher turbulence energy, characterised

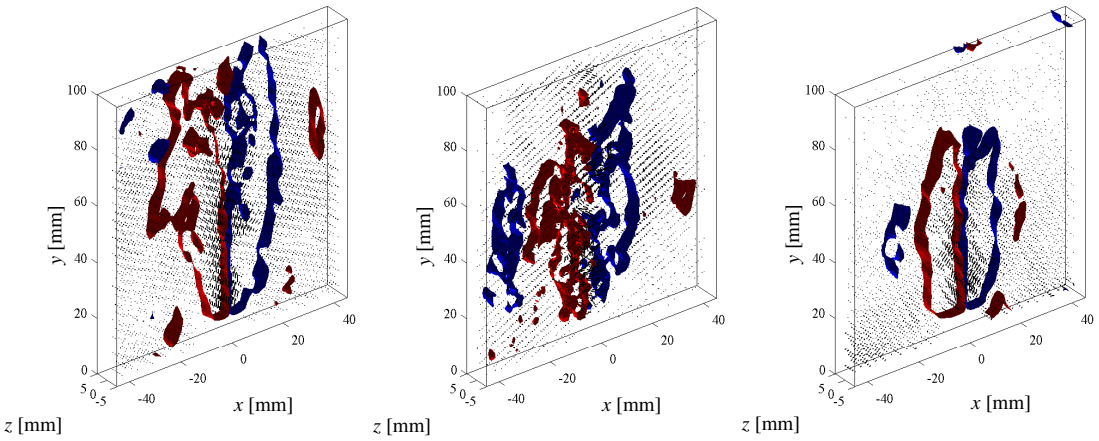

Figure 5.16: so-surfaces of regions in the fountain that have divergence > 1 s^{-1} (red) and < -1 s^{-1} (blue) at flow rate $Q_0 = 0.6$ L/min for (a) $\rho 05$, (b) $\rho 07$, and (c) $\rho 10$. This indicates that the divergence is not randomly distributed throughout the measurement volume, but in a region occupied by the fountain flow.

by higher fluctuations, and also the smallest scales of the flow decrease. As the cross-correlation interrogation volumes and the Δt of the acquisition rate were identical across all Re, it is expected that the random error is also higher due to the departure from the resolution of an infinitesimal fluid element. The higher divergence errors in those cases is explained by the lack of adequate temperature control (Section 5.2.2). The values presented in Table 5.4 are inline with other TPIV studies in the literature (Atkinson et al, 2011, for example).

Table 5.4: Normalised random velocity error for each fountain case, in units of [px/px] from Eq. 5.11

case	$\rho 05$	$\rho 07$	$\rho 10$
Re = 496	0.032	0.021	0.021
Re = 745	0.021	0.070	0.025
Re = 993	0.063	0.090	0.077

Figure 5.16 shows iso-surfaces of regions in the fountain that have $\nabla \cdot u_i > 1$ s^{-1} (red) and $\nabla \cdot u_i < -1$ s^{-1} (blue) to ascertain whether the errors are random or correlated spatially in the flow field. Here it can be seen that the divergence is highly correlated with the interfaces of the jet and annular divergence flow of the fountain. These are the regions of the flow where the shear stresses and small scale vorticity are highest. For the experimental configuration in this work, the resolution could not capture the smallest scales of vorticity, so it is reasonable to assume that the experimentally measured divergence in this region is also highest.

5.4.7 Limitations

Particle astigmatism was present due to the focal depth δz (Table 5.3) being less than the laser sheet thickness Δz_0 (Figure 5.6). A non uniform optical transfer function utilised by Schanz et al (2013a) could be used to improve the results of experimental images such as these. Additionally, a system similar to that employed by Schröder et al (2008), which

utilised a system of mirrors to generate a light sheet from a multi-pass laser beam, could be one method to improve the illumination of the particles. With higher illumination, it would be possible to close the lens apertures to reduce astigmatism. Water prisms (Prasad and Jensen, 1995) or an octagonal shaped tank (as employed by Fujisawa et al, 2011) could also mitigate against the astigmatism by reducing the angle the camera axis made with the glass tank sides.

Despite best efforts, the illuminations of the exit nozzle resulted in the flow field directly exiting the nozzle was not resolved. This problem is persistent in PIV studies and makes the near wall regions difficult to measure. The relatively small size of the tank meant that care had to be taken in order to reduce the effects of its finite size. The averaged flow fields are not statistically independent and affect the intermittency (Cresswell and Szczepura, 1993).

5.5 Discussion

This study aimed to investigate the global features of a turbulent fountain with a volumetric measurement system in order to resolve the turbulent structures. The results presented in this chapter highlight some interesting features of forced fountains. The possibility of using TPIV in multi-fluid flows such as fountains has been explored. Combining TPIV with refractive index matching techniques opens a wealth of possibilities of measuring multiphase flows in full 3D.

Additionally, the unsteady 3D interfaces of the fountains, bounding the jet, cap and annular reverse region were located. The sequential TPIV system enabled the observation of the jet initialisation and then transitional phases of the fountain until a fully developed fountain regime was established. The mean fountain velocity field showed the fountain height dependence on Fr. All of the instantaneous fields enabled the visualisation of velocity structures in the jet region, and it could be seen that the interaction of the jet with small structures of downward moving velocity worked to disrupt the jet flow.

This investigation aimed to investigate the global features of a turbulent fountain with a volumetric measurement system in order to resolve the turbulent structures and obtain a global. As with all experimental measurements, the dynamic spatial range of the acquisi-

tion system is a compromise between the global features of a flow to the smallest turbulent scales. The TPIV employed here was designed to capture the global features of the flow, and as a consequence, the resolution of the system was not fine enough to resolve the Kolmogorov scales. In order to measure those scales, a higher resolution camera could be employed or a smaller field of view with larger optics to zoom in to the area. The effect of filtering has been shown to reduce divergence error, however rather indiscriminately. Recently, Atkinson et al (2014) have investigated appropriate filters that could help mitigate this.

As discussed by Hannoun (1985); Daviero et al (2001), adding ethanol to water increases the entropy of the solution and as a result increases its temperature. This is a result of the hydrogen bonds between the ethanol molecules breaking in order to form new bonds with the water molecules as the solution is made. Due to the confinement of the lab and lack of temperature control, the temperature of the fluids could not be properly regulated, and as a result, the data quality of the higher density difference cases was not as high as those for the lower density difference. As the quality of the data was shown to be high quality however, the temperature change effects in this study could be considered insignificant. Thus, the advantages of using this combination of fluids for refraction index matching for measuring fountain flows has been demonstrated.

Chapter 6

Conclusions

The previous chapters have described investigations into the nature of turbulence in environmental flows. The theory presented showed how turbulence effects the mean flow field and transports energy from the large to small scales through vortex stretching and finally dissipation into internal energy. As the vortices in turbulent flows are three dimensional phenomena, in order to fully characterise and understand them, a measurement technique that can resolve the full 3C–3D velocity field is required. TPIV is such a technique, and it was utilised and optimised to increase our understanding of these flows.

The optimisation involved investigating a new tomographic reconstruction algorithm, called BiMART (Byrne, 2009; Thomas et al, 2014), which was shown to achieve high quality reconstructed fields with reduced computational time. When analysing large sets of experimental data (often approaching terabytes), necessary to decompose the turbulence statistics with reduced uncertainty, speed of calculation without compromising quality is vital for making such investigations feasible.

In the first experiment, TPIV was used to measure the flow in a pool of an inclined open channel behind a trash rack. Open channel flows in the lab are designed to generate flows equivalent to the flows found in rivers or flows in vertical slot fishways. Two trash rack assembly configurations of different sized grids with equivalent solidity ratios were compared. Analysis of the bulk energy dissipation through the pools was compared with the energy dissipation measured directly from the 3D velocity field data and by integrating Bernoulli's equation over the measurement region. Although it was estimated from

the bulk analysis *a priori* that the resolution of the TPIV system would not capture the dissipative scales ($\delta x > \eta$), some very interesting results were obtained. Analysis of the vorticity and energy dissipation shows qualitative and quantitative agreement of the decay of turbulent kinetic energy for classical grid generated turbulence, despite the flow fields generated by the trash racks being globally different. The anisotropy in the turbulent kinetic energy was found that was contrary to the vorticity components which appeared to be essentially isotropic. Finally, a thorough analysis of the errors showed that the results were high quality.

In the second experiment, two regions in the same flume were investigated at the channel bed, at $x/L = 0.5$ (R_1) and $x/L = 0.85$ (R_2). These measurements were at higher resolution than the measurements made in the intermediate region of the channel. Ejection (Q2) and sweep (Q4) regions were identified in the 3D velocity field, and the location of coherent vortices marked by high values of the Q-criterion in both regions. The vortices captured were concentrated between the sweep and ejections, and were observed to wrap around the low momentum ejection regions. An analysis of the probability and joint probability functions enabled the extraction of quantitative statistics on the different turbulent flow phenomena observed. Additionally, statistical analysis of the Reynolds stress distribution through the boundary layer was undertaken, showing that R_1 was still a transitional boundary layer, while R_2 was fully developed. The turbulence in the flow generated by the grids was found to dominate the energy in the flow, even very close to the wall in R_1. However, near the end of the pool in R_2, most of this energy had dissipated and an increase in the turbulent contribution due to the wall bounded turbulence was observed. The Reynolds stresses also revealed that the turbulence had become largely isotropic in the R_2 region. The turbulence properties of the flow were found to be characterised by the streamwise location in the pool and by the turbulence produced by the grids.

Open channel flows were shown to be very challenging to measure. The high flow rate required to achieve high Re results in a turbulent, undulating free surface, and also resulted in vibration of the rig. This vibration was almost undetectable, corresponding to a number of voxels of misalignments of the cameras' LoSs. In fact, results that at first glance seem reasonable, are contaminated with additional reconstruction noise that particularly effects

the calculation of velocity gradients. A major contribution of this work was to develop a vibration correction scheme and to quantify the effects of using a number of differing schemes compared to nothing at all. This ensured that the experiments conducted in the open channel were of the highest quality.

Finally, a regime of turbulent fountains from a circular exit were investigated. The TPIV system was designed and built in-house. In order to employ TPIV, a stringent refraction index matching test and verification was developed. This included a local correlation map of the re-projection quality of the images to verify that there were no reconstruction errors due to mismatched refraction indices. TPIV revealed qualitative and quantitative features of the large scale structures in the fountains during initialisation and also after they had reached a fully developed state. The initialisation showed the various stages of a fountain's life, with an initial burst that detaches from the jet region of the fountain observed, followed by the stagnation, and then collapse of the fountain. For the fully developed fountains, the jet and annular reverse regions were captured, and the turbulence intensity revealed that for this regime of fountains they were not Re independent.

Analysis of the topology of the invariants of the velocity gradient tensor revealed the shearing and rotating contributions of the fountain flows, providing insight into the mixing and entrainment that are typically observed in such flows. A major contribution to the field of engineering is that a rigorous treatment of TPIV was shown to be able to measure complex 3D flows with differing densities, such as pyroclastic eruptions, wastewater pumped into the ocean or the heavy brine water waste from desalination plants.

The aims of these investigations were to understand the fundamental properties of environmental flows by characterising the turbulence in a 3D measurement domain. To this end, it has been demonstrated that TPIV has enabled the objectives of this work to be achieved and in the process, an increased understanding about these environmental flows was gained. The anisotropy of the open channel flow highlighted the need to recover the full velocity gradient tensor so that the energy dissipation could be obtained without any assumptions of the out of plane gradients. Other open channel flows, in the context of fluvial studies for example, could benefit from TPIV measurements, particularly near the bed where the physics of sediment transport are of interest. Additionally, the development of vibration

correction schemes will enable future measurements to be of the highest quality. In the case of the fountain flow, a new way to measure fountains has been developed with positive implications for future measurements, whether it be testing a larger range of Fr and Re, or for specific engineering applications, to study the 3D turbulence and mixing phenomena.

Bibliography

Adrian RJ (1984) Scattering particle characteristics and their effect on pulsed laser measurements of fluid flow: speckle velocimetry vs particle image velocimetry. Applied optics 23(11):1690–1691

Adrian RJ (1991) Particle-imaging techniques for experimental fluid mechanics. Annu Rev Fluid Mech 23:261–304

Adrian RJ (1997) Dynamic ranges of velocity and spatial resolution of particle image velocimetry. Measurement Science and Technology 8:1393–1398

Adrian RJ, Westerweel J (2011) Particle Image Velocimetry. Cambridge University Press

Adrian RJ, Meinhart CD, Tomkins CD (2000) Vortex organization in the outer region of the turbulent boundary layer. Journal of Fluid Mechanics 422:1–54

Andersen AH, Kak AC (1984) Simultaneous Algebraic Reconstruction technique (SART): A superior implementation of the ART algorithm. Ultrasonic Imaging 6:81–94

Arroyo MP, Greated CA (1991) Stereoscopic Particle Image Velocimetry. Measurement Science and Technology 2:1181–1186

Arroyo MP, Hinsch KD (2008) Recent Developments of PIV towards 3D Measurements. Appl Physics 112:127–154

Atkinson C, Soria J (2009) An efficient simultaneous reconstruction technique for tomographic particle image velocimetry. Experiments in Fluids 47(4-5):553–568

Atkinson C, Stanislas M, Soria J (2011) Two and three-dimensional geometry of low speed streaks in wall-bounded turbulence using tomographic PIV. In: 9TH International Symposium on Particle Image Velocimetry - PIV11 Kobe, Japan, July 21-23, 2011

Atkinson C, Buchmann Na, Amili O, Soria J (2014) On the appropriate filtering of PIV measurements of turbulent shear flows. Experiments in Fluids 55(1):1654

Bailly C, Comte-Bellot G (2003) Turbulence, (in french) edn. CNRS Editions, Paris

Baines WD, Turner JS, Campbell IH (1990) Turbulent fountains in an open chamber. Journal of Fluid Mechanics 212(-1):557

Baines WD, Corriveau AF, Reedman TJ (1993) Turbulent fountains in a closed chamber. Journal of Fluid Mechanics 255:621–646

Bakker A (2006) Lecture slides from Dartmouth College - Lecture 9, Kolmogorov's Theory. URL www.bakker.org/dartmouth06/engs150/

Batchelor GK, Townsend AA (1948a) Decay of Isotropic Turbulence in the Initial Period. Proceedings of the Royal Society A: Mathematical, Physical and Engineering Sciences 193(1035):539–558

Batchelor GK, Townsend AA (1948b) Decay of Turbulence in the Final Period. Proceedings of the Royal Society A: Mathematical, Physical and Engineering Sciences 194(1039):527–543

Belden J, Truscott TT, Axiak MC, Techet AH (2010) Three-dimensional synthetic aperture particle image velocimetry. Measurement Science and Technology 21(12):125,403

Berchet A, Thomas L, Braud P, David L (2013) Instantaneous volumic concentration and velocity measurements of a jet in crossflow for the evaluation of the entrainment. Experiments in Fluids 54(12):1608

Bilsky AV, Dulin VM, Lozhkin VA, Markovich DM, Tokarev MP (2011) Two-dimensional Correlation Algorithms for Tomographic PIV. In: 9TH International Symposium on Particle Image Velocimetry - PIV11 Kobe, Japan, July 21-23, 2011, pp 1–4

Bilsky AV, Lozhkin VA, Markovich DM, Tokarev MP (2013) A maximum entropy reconstruction technique for tomographic particle image velocimetry. Measurement Science and Technology 24(4):045,301

Bleninger T, Jirka GH (2008) Modelling and environmentally sound management of brine discharges from desalination plants. Desalination 221(1-3):585–597

Boutier A (2012) Laser Velocimetry in Fluid Mechanics. John Willey & Sons, Inc.

Brücker C (1995) Digital-Particle-lmage-Velocimetry (DPIV) in a scanning light-sheet : 3D starting flow around a short cylinder. Experiments in Fluids 19:255–263

Brücker C (1997) 3D scanning PIV applied to an air flow in a motored engine using digital high-speed video. Measurement Science and Technology 8:1480–1492

Brücker C, Althaus W (1992) Study of vortex breakdown by particle tracking velocimetry (PTV). Experiments in Fluids 13(5):339–349

Buchmann NA, Atkinson C, Soria J (2010) Tomographic and Stereoscopic PIV measurements of Grid- generated Homogeneous Turbulence. In: 15th Int Symp on Applications of Laser Techniques to Fluid Mechanics Lisbon, Portugal, 05-08 July, 2010

Buchmann NA, Willert C, Soria J (2011) Tomographic Particle Image Velocimetry using Pulsed , High Power LED Volume Illumination. In: 9TH International Symposium on Particle Image Velocimetry - PIV11 Kobe, Japan, July 21-23, 2011, vol Ill

Burridge HC, Hunt GR (2012) The rise heights of low- and high-Froude-number turbulent axisymmetric fountains. Journal of Fluid Mechanics 691:392–416

Byrne C (2009) Block-iterative algorithms. International Transactions in Operational Research 16:427–463

Calluaud D, David L (2004) Stereoscopic particle image velocimetry measurements of the flow around a surface-mounted block. Experiments in Fluids 36(1):53–61

Calluaud D, David L, Pineau G, Texier A, Larinier M (2011) Turbulence kinetic energy dissipation rate estimation from PIV velocity fields : Application to the study of the flow in vertical slot fishways . In: 34th IAHR World Congress - Balance and Uncertainty, 33rd Hydrology & Water Resources Symposium, 10th Hydraulics Conference. 26 June - 1 July 2011, Brisbane, Australia, July, pp 2768–2775

Calluaud D, Pineau G, Texier A, David L (2014) Modification of vertical slot fishway flow with a supplementary cylinder. Journal of Hydraulic Research 52(5):614–629

Carazzo G, Kaminski E, Tait S (2008) On the rise of turbulent plumes: Quantitative effects of variable entrainment for submarine hydrothermal vents, terrestrial and extra terrestrial explosive volcanism. Journal of Geophysical Research 113(B09201):1–19

Carazzo G, Kaminski E, Tait S (2010) The rise and fall of turbulent fountains: a new model for improved quantitative predictions. Journal of Fluid Mechanics 657:265–284

Cardesa JI, Nickels TB, Dawson JR (2012) 2D PIV measurements in the near field of grid turbulence using stitched fields from multiple cameras. Experiments in Fluids 52(6):1611–1627

Chakraborty P, Balachandar S, Adrian RJ (2005) On the relationships between local vortex identification schemes. Journal of Fluid Mechanics 535:189–214

Chong MS, Perry AE, Cantwell BJ (1989) A General Classification of Three-dimensional Flow Fields. In: Topological Fluid Mechanics: proceedings of the IUTAM Symposium, Cambridge UK, 13-19 August 1989, pp 408 – 420

Coles D (1956) The law of the wake in the turbulent boundary layer. Journal of Fluid Mechanics 1(2):191–226

Comte-Bellot G, Corrsin S (1966) The use of a contraction to improve the isotropy of grid-generated turbulence. Journal of Fluid Mechanics 25:657–682

Comte-Bellot G, Corrsin S (1971) Simple Eulerian time correlation of full-and narrow-band velocity signals in grid-generated, isotropic turbulence. Journal of Fluid Mechanics 48:273

Cresswell RW, Szczepura RT (1993) Experimental investigation into a turbulent jet with negative buoyancy. Physics of Fluids A: Fluid Dynamics 5(11):2865

Darrigol O (2005) Worlds of Flow: A history of hydrodynamics from the Bernoullis to Prandtl. Oxford University Press

David L, Jardin T, Braud P, Farcy A (2011) Time-resolved scanning tomography PIV measurements around a flapping wing. Experiments in Fluids 52(4):857–864

Daviero GJ, Roberts PJW, Maile K (2001) Refractive index matching in large-scale stratified experiments. Experiments in Fluids 31(2):119–126

Dennis DJC, Nickels TB (2011) Experimental measurement of large-scale three-dimensional structures in a turbulent boundary layer. Part 1. Vortex packets. Journal of Fluid Mechanics 673:180–217

DeSilva CM, Baidya R, Khashehchi M, Marusic I (2012) Assessment of tomographic PIV in wall-bounded turbulence using direct numerical simulation data. Experiments in Fluids 52(2):425–440

DeSilva CM, Baidya R, Marusic I (2013a) Enhancing Tomo-PIV reconstruction quality by reducing ghost particles. Measurement Science and Technology 24(2):024,010

DeSilva CM, Philip J, Marusic I (2013b) Minimization of divergence error in volumetric velocity measurements and implications for turbulence statistics. Experiments in Fluids 54(7):1557

Discetti S, Astarita T (2011) A fast multi-resolution approach to tomographic PIV. Experiments in Fluids 52(3):765–777

Discetti S, Ziskin IB, Astarita T, Adrian RJ, Prestridge KP (2013) PIV measurements of anisotropy and inhomogeneity in decaying fractal generated turbulence. Fluid Dynamics Research 45(6):061,401

Dubief Y, Delcayre F (2000) On coherent-vortex identification in turbulence. Journal of Turbulence 1(December 2013):N11

Dudderar TD, Simpkins PG (1977) Laser speckle photography in a fluid medium. Nature 270:45–47

Earl TA, Paetzold J, Cochard S (2013) Tomographic Piv Measurements of Turbulent Fountains With Refraction Index Matching. Journal of Flow Visualization and Image Processing 20(3):179–208

Earl TA, Cochard S, Thomas L, David L (2014) Investigation of the turbulent boundary layer and associated energy dissipation in an open channel flow behind a series of regular grids. In: Riverflow 2014, International Conference on Fluvial Hydraulics. 3-5 September, Lausanne, Switzerland, pp 1–8

Earl TA, Cochard S, Thomas L, Tremblais B, David L (2015) Implementation of vibration correction schemes to the evaluation of a turbulent flow in an open channel by tomographic particle image velocimetry. Measurement Science and Technology 26(1):015,303

Ecke R (2004) The Turbulence Problem An Experimentalists Perspective. Los Alamos Science 29:124–141

Elsinga GE, Westerweel J (2011a) The point-spread-function and the spatial resolution of PIV cross- correlation methods. In: 9TH International Symposium on Particle Image Velocimetry - PIV11 Kobe, Japan, July 21-23, 2011

Elsinga GE, Westerweel J (2011b) Tomographic-PIV measurement of the flow around a zigzag boundary layer trip. Experiments in Fluids 52(4):865–876

Elsinga GE, Oudheusden BW, Scarano F (2005a) Evaluation of aero-optical distortion effects in PIV. Experiments in Fluids 39(2):246–256

Elsinga GE, Wieneke B, Scarano F, Oudheusden BWV (2005b) Assessment of Tomo-PIV for three-dimensional flows. In: 6th International Symposium on Particle Image Velocimetry Pasadena, California, USA, September 21-23, 2005, pp 1–10

Elsinga GE, Oudheusden BWV, Scarano F (2006a) Experimental assessment of Tomographic-PIV accuracy. In: 13th Int Symp on Applications of Laser Techniques to Fluid Mechanics

Elsinga GE, Scarano F, Wieneke B, Oudheusden BW (2006b) Tomographic particle image velocimetry. Experiments in Fluids 41(6):933–947

Elsinga GE, Adrian RJ, Van Oudheusden BW, Scarano F (2010a) Three-dimensional vortex organization in a high-Reynolds-number supersonic turbulent boundary layer. Journal of Fluid Mechanics 644:35

Elsinga GE, Westerweel J, Scarano F, Novara M (2010b) On the velocity of ghost particles and the bias errors in Tomographic-PIV. Experiments in Fluids

Foucaut JM, Carlier J, Stanislas M (2004) PIV optimization for the study of turbulent flow using spectral analysis. Measurement Science and Technology 15(6):1046–1058

Foucaut JM, Coudert S, Stanislas M, Delville J (2010) Full 3D correlation tensor computed from double field stereoscopic PIV in a high Reynolds number turbulent boundary layer. Experiments in Fluids

Fouras A, Lo Jacono D, Nguyen CV, Hourigan K (2009) Volumetric correlation PIV: a new technique for 3D velocity vector field measurement. Experiments in Fluids 47(4-5):569–577

Friedman PD, Vadakoot VD, Meyer WJ, Carey S (2007) Instability threshold of a negatively buoyant fountain. Experiments in Fluids 42(5):751–759

Fujisawa N, Gono T, Yamagata T, Maeda A (2011) Simultaneous volume mapping of concentration and velocity fields by time-resolved scanning LIF and stereo PIV. In: Forum on recent developments in Volume Reconstruction Techniques applied to 3D fluid and solid mechanics, vol m, pp 1–4

Ganapathisubramani B, Longmire EK, Marusic I (2003) Characteristics of vortex packets in turbulent boundary layers. Journal of Fluid Mechanics 478:35–46

Ganapathisubramani B, Longmire EK, Marusic I, Pothos S (2005) Dual-plane PIV technique to determine the complete velocity gradient tensor in a turbulent boundary layer. Experiments in Fluids 39(2):222–231

Ganapathisubramani B, Lakshminarasimhan K, Clemens NT (2007) Determination of complete velocity gradient tensor by using cinematographic stereoscopic PIV in a turbulent jet. Experiments in Fluids 42(6):923–939

Gao Q, Ortiz-Dueñas C, Longmire E (2013) Evolution of coherent structures in turbulent boundary layers based on moving tomographic PIV. Experiments in Fluids 54(12):1625

George W, Hussein H (1991) Locally axisymmetric turbulence. Journal of Fluid Mechanics 223:1–23

George WK (2007) Is there a universal log law for turbulent wall-bounded flows? Philosophical transactions Series A, Mathematical, physical, and engineering sciences 365(1852):789–806

George WK (2013) Lectures in Turbulence for the 21st Century. January, Available online: www.turbulence-online.com/

George WK, Alpert RL, Tamanini F (1977) Turbulence measurements in an axisymmetric buoyant plume. International Journal of Heat and Mass Transfer 20:1145–1154

Ghaemi S, Ragni D, Scarano F (2012) PIV-based pressure fluctuations in the turbulent boundary layer. Experiments in Fluids 53(6):1823–1840

Gono T, Syuto T, Yamagata T, Fujisawa N (2012) Time-resolved scanning stereo PIV measurement of three-dimensional velocity field of highly buoyant jet. Journal of Visualization 15(3):231–240

Gordon R, Bender R, Herman GT (1970) Algebraic reconstruction techniques (ART) for three-dimensional electron microscopy and x-ray photography. Journal of theoretical biology 29(3):471–81

Gursul I, Lusseyran D, Rockwell D (1990) On interpretation of flow visualization of unsteady shear flows. Experiments in Fluids 9:257–266

Hain R, Kähler CJ, Radespiel R (2009) Principles of a Volumetric Velocity Measurement Technique Based on Optical Aberrations. Imaging Measurement Methods pp 1–10

Hama FR (1962) Streaklines in a Perturbed Shear Flow. Physics of Fluids 5(6):644

Hannoun IA (1985) Matching the refractive index in density stratified flows. Tech. rep., Technical Memorandum 85-1, W.M. Keck Labarotory of hydraulics and Water Resources, California Institute of Technology

Herman GT, Lent A (1976) Iterative Reconstruction Algorithms. Computational Biology Medicine 6(3):273–294

Herpin S, Wong CY, Stanislas M, Soria J (2008) Stereoscopic PIV measurements of a turbulent boundary layer with a large spatial dynamic range. Experiments in Fluids 45(4):745–763

Hinsch KD (2002) Holographic Particle Image Velocimetry. Measurement Science and Technology 13(4):61–72

Hori T, Sakakibara J (2004) High-speed scanning stereoscopic PIV for 3D vorticity measurement in liquids. Measurement Science and Technology 15(6):1067–1078

Hunt J (1988) Eddies, Streams, and Convergence Zones in Turbulent Flows. Centre for Turbulence Research pp 193–208

Hurther D, Lemmin U, Terray EA (2007) Turbulent transport in the outer region of rough-wall open-channel flows: the contribution of large coherent shear stress structures (LC3S). Journal of Fluid Mechanics 574:465

Im S, Heo GE, Jeon YJ, Sung HJ, Kim SK (2014) Tomographic PIV measurements of flow patterns in a nasal cavity with geometry acquisition. Experiments in Fluids 55(1):1644

Kahler CJ, Kompenhans J (2000) Fundamentals of multiple plane stereo particle image velocimetry. Experiments in Fluids pp 70–77

Kaminski E, Tait S, Carazzo G (2005) Turbulent entrainment in jets with arbitrary buoyancy. Journal of Fluid Mechanics 526:361–376

Kaye NB, Hunt GR (2006) Weak fountains. Journal of Fluid Mechanics 558:319

Keane RD, Adrian RJ (1992) Theory of cross-correlation analysis of PIV images. Applied Scientific Research 49:191–215

Keane RD, Adrian RJ, Zhang Y (1995) Super-resolution particle imaging velocimetry. Measurement Science and Technology 6:754–768

Kestin J, Khalifa E, Correia RJ (1981) Tables of the Dynamic and Kinematic Viscosity of Aqueous NaCL Solutions in the Temperature Range 20-150 C and the Pressure Range 0.1-35 Mpa. J Phys Chem Ref Data 10(1):71–87

Khashehchi M, Elsinga GE, Ooi A, Soria J, Marusic I (2010) Studying invariants of the velocity gradient tensor of a round turbulent jet across the turbulent / nonturbulent interface using Tomo-PIV. In: 15th Int Symp on Applications of Laser Techniques to Fluid Mechanics Lisbon, Portugal, 05-08 July, 2010

Khashehchi M, Ooi A, Soria J, Marusic I (2013) Evolution of the turbulent/non-turbulent interface of an axisymmetric turbulent jet. Experiments in Fluids 54(1):1449

Kitzhofer J, Nonn T, Brücker C (2011) Generation and visualization of volumetric PIV data fields. Experiments in Fluids 51(6):1471–1492

Klinner J, Willert C (2011) On the implementation of tomographic shadowgraphy for spray diagnostics. In: 9TH International Symposium on Particle Image Velocimetry - PIV11 Kobe, Japan, July 21-23, 2011, 3

Kolár V (2007) Vortex identification: New requirements and limitations. International Journal of Heat and Fluid Flow 28(4):638–652

Kolmogorov A (1991) The local structure of turbulence in incompressible viscous fluid for very large Reynolds numbers. Proceedings of the Royal Society of London Series A, Mathematical and Physical Sciences 434:9–13

Kühn M, Ehrenfried K, Bosbach J, Wagner C (2012) Large-scale tomographic PIV in forced and mixed convection using a parallel SMART version. Experiments in Fluids 53(1):91–103

Lacey J, Neary V, Liao J, Enders J, Tritico H (2012) The IPOS framework: linking fish swimming performance in altered flows from laboratory experiments to rivers. River Research and Applications 28(4):429–443

Lamarche F, Leroy C (1990) Evaluation of the volume of intersection of a sphere with a cylinder by elliptic integrals. Computer Physics Communications 59:359–369

Lavoie P, Djenidi L, Antonia RA (2007) Effects of initial conditions in decaying turbulence generated by passive grids. Journal of Fluid Mechanics 585:395

Lecordier B, Demare D, Vervisch LMJ, Reveillon J, Trinite M (2001) Estimation of the accuracy of PIV treatments for turbulent flow studies by direct numerical simulation of multi-phase flow. Measurement Science and Technology 12:1382–1391

Lecordier B, Gobin C, Lacour C, Cessou A, Tremblais B, Thomas L, David L (2012) Tomographic PIV study of lifted flames in turbulent Axisymmetric jets of methane . In: Int Symp on Applications of Laser Techniques to Fluid Mechanics, Lisbon Portugal, 09-12 July, pp 1–9

Lei YC, Tien WH, Duncan J, Paul M, Ponchaut N, Mouton C, Dabiri D, Rösgen T, Hove J (2012) A vision-based hybrid particle tracking velocimetry (PTV) technique using a modified cascade correlation peak-finding method. Experiments in Fluids 53(5):1251–1268

Lesieur M (2008) Turbulence in Fluids, 4th edn. Springer

Liberzon A, Gurka R, Hetsroni G (2004) XPIV - Multi-plane stereoscopic particle image velocimetry. Experiments in Fluids 36(2):355–362

List EJ (1982) Turbulent Jets and Plumes. Annual Review of Fluid Mechanics 14(1):189–212

Lu W, Yin FF (2004) Adaptive algebraic reconstruction technique. Medical Physics 31(12):3222

Lugt HJ (1983) Vortex Flow in Nature and Technology. John Willey & Sons, Inc.

Maas HG, Gruen A, Papantoniou D (1993) Experiments in Fluids Particle tracking velocimetry in three-dimensional flows. Experiments in Fluids 15:133–146

Maas HG, Putze T, Westfeld P (2009) Recent Developments in 3D-PTV and Tomo-PIV. Imaging Measurement Methods pp 53–62

Martin J, Dopazo C (1998) Dynamics of velocity gradient invariants in turbulence: Restricted Euler and linear diffusion models. Physics of Fluids 10(8):2012–2025

Marusic I, McKeon BJ, Monkewitz Pa, Nagib HM, Smits aJ, Sreenivasan KR (2010) Wall-bounded turbulent flows at high Reynolds numbers: Recent advances and key issues. Physics of Fluids 22(6):065,103

Meng H, Hussain F (1995) In-line recording and off-axis viewing technique for holographic particle velocimetry. Applied optics 34(11):1827–40

Meng H, Pan G, Pu Y, Woodward SH (2004) Holographic particle image velocimetry: from film to digital recording. Measurement Science and Technology 15(4):673–685

Michaelis D, Wolf CC (2011) Vibration Compensation for Tomographic PIV using Single Image Volume Self Calibration. In: 9TH International Symposium on Particle Image Velocimetry - PIV11 Kobe, Japan, July 21-23, 2011, vol 2

Mishra D, Muralidhar K, Munshi P (1999) a Robust MART Algorithm for Tomographic Applications. Numerical Heat Transfer: Part B: Fundamentals 35(4):485–506

Moffat RJ (1988) Describing the Uncertainties in Experimental Results. Experimental Thermal and Fluid Science pp 3–17

Mullin JA, Dahm WJA (2005) Dual-plane stereo particle image velocimetry (DSPIV) for measuring velocity gradient fields at intermediate and small scales of turbulent flows. Experiments in Fluids 38:185–196

Mullin JA, Dahm WJA (2006) Dual-plane stereo particle image velocimetry measurements of velocity gradient tensor fields in turbulent shear flow. II. Experimental results. Physics of Fluids 18(3):035,102

Nezu I, Nakagawa H (1993) Turbulence in Open Channel Flows, iahr monograph edn. A. A. Balkema, Rotterdam

Nezu I, Rodi W (1986) Open-channel flow measurements with a laser doppler anemometer. Journal of Hydraulic Engineering 112(5):335–355

Novara M, Scarano F (2013) A particle-tracking approach for accurate material derivative measurements with tomographic PIV. Experiments in Fluids 54(8):1584

Novara M, Batenburg KJ, Scarano F (2010) Motion tracking-enhanced MART for tomographic PIV. Measurement Science and Technology 21(3):1–18

Novara M, Ianiro A, Scarano F (2011) Adaptive interrogation for 3D-PIV. In: 9TH International Symposium on Particle Image Velocimetry - PIV11 Kobe, Japan, July 21-23, 2011, pp 3–6

Ooi A, Martin J, Soria J, Chong MS (1999) A study of the evolution and characteristics of the invariants of the velocity-gradient tensor in isotropic turbulence. Journal of Fluid Mechanics 381:141–174

Ortiz-Dueñas C, Kim J, Longmire EK (2010) Investigation of liquid–liquid drop coalescence using tomographic PIV. Experiments in Fluids 49(1):111–129

ONeill P, Soria J, Honnery D (2004) The stability of low Reynolds number round jets. Experiments in Fluids 36(3):473–483

Pantzlaff L, Lueptow RM (1999) Transient positively and negatively buoyant turbulent round jets. Experiments in Fluids 27(2):117–125

Papanicolaou PN, Papakonstantis IG, Christodoulou GC (2008) On the entrainment coefficient in negatively buoyant jets. Journal of Fluid Mechanics 614:447

Park GI, Wallace JM, Wu X, Moin P (2012) Boundary layer turbulence in transitional and developed states. Physics of Fluids 24(2012)

Pereira F, Gharib M (2002) Defocusing digital particle image velocimetry and the three-dimensional characterization of two-phase flows. Measurement Science and Technology 13:683–694

Pereira F, Gharib M, Dabiri D, Modarress D (2000) Defocusing digital particle image velocimetry : a 3-component 3-dimensional DPIV measurement technique . Application to bubbly flows. Experiments in Fluids pp 78–84

Pereira F, Stüer H, Graff EC, Gharib M (2006) Two-frame 3D particle tracking. Measurement Science and Technology 17(7):1680–1692

Perry AE, Henbest S, Chong MS (1986) A theoretical and experimental study of wall turbulence. Journal of Fluid Mechanics 165:163–199

Petra S, Schroder A, Schnorr C (2009) 3D Tomography from Few Projections in Experimental Fluid Dynamics. Imaging Measurement Methods 106:63–72

Philippe P, Raufaste C, Kurowski P, Petitjeans P (2005) Penetration of a negatively buoyant jet in a miscible liquid. Physics of Fluids 17(5):053,601

Pope SB (2000) Turbulent Flows. Cambridge University Press

Prasad AK (2000) Stereoscopic particle image velocimetry. Experiments in Fluids 29(February):103–116

Prasad aK, Jensen K (1995) Scheimpflug stereocamera for particle image velocimetry in liquid flows. Applied optics 34(30):7092–9

Prasad AK, Adrian RJ, Landreth CC, Offutt PW (1992) Effect of Resolution on the speed and accuracy of particle image velocimetry interrogation. Experiments in Fluids 116:105–116

Pu Y, Meng H (2000) An advanced off-axis holographic particle image velocimetry (HPIV) system. Experiments in Fluids 29:184–197

Putze T, Maas HG (2008) 3D determination of very dense particle velocity fields by tomographic reconstruction from four camera views and voxel space tracking. In: The International Archives of the Photogrammetry, Remote Sensing and Spatial Information Sciences, pp 33–38

Raffel M, Willert CE, Wereley ST, Kompenhans J (2007) Particle Image Velocimetry, A Practical Guide. Springer

Richardson LF (1922) Weather Prediction by Numerical Process. Cambridge University Press

Scarano F (2004) A super-resolution particle image velocimetry interrogation approach by means of velocity second derivatives correlation. Measurement Science and Technology 15(2):475–486

Scarano F (2013) Tomographic PIV: principles and practice. Measurement Science and Technology 24(1):012,001

Scarano F, Riethmuller ML (1999) Iterative multigrid approach in PIV image processing with discrete window offset. Experiments in Fluids 26(6):513–523

Scarano F, David L, Bsibsi M, Calluaud D (2005) S-PIV comparative assessment: image dewarping+misalignment correction and pinhole+geometric back projection. Experiments in Fluids 39(2):257–266

Scarano F, Elsinga GE, Bocci E, Oudheusden BWV (2006) Investigation of 3-D Coherent Structures in the Turbulent Cylinder Wake using. In: 13th Int Symp on Applications of Laser Techniques to Fluid Mechanics, Lisbon, Portugal, 26-29 June, 2006, pp 26–29

Schanz D, Gesemann S, Schröder A, Wieneke B, Novara M (2013a) Non-uniform optical transfer functions in particle imaging: calibration and application to tomographic reconstruction. Measurement Science and Technology 24(024009):1–15

Schanz D, Schröder A, Gesemann S, Michaelis D, Wieneke B (2013b) Shake The Box : A highly efficient and accurate Tomographic Particle Tracking Velocimetry (TOMO-PTV

) method using prediction of particle positions. In: 10th International Symposium on Particle Image Velocimetry - PIV13. Delft, The Netherlands, July 1-3., pp 1–13

Schmid PJ, Violato D, Scarano F (2012) Decomposition of time-resolved tomographic PIV. Experiments in Fluids 52(6):1567–1579

Schröder A, Geisler R, Elsinga GE, Scarano F, Dierksheide U (2008) Investigation of a turbulent spot and a tripped turbulent boundary layer flow using time-resolved tomographic PIV. Experiments in Fluids 44(2):305–316

Schröder A, Geisler R, Staack K, Elsinga GE, Scarano F, Wieneke B, Henning A, Poelma C, Westerweel J (2011) Eulerian and Lagrangian views of a turbulent boundary layer flow using time-resolved tomographic PIV. Experiments in Fluids 50(4):1071–1091

Seoud RE, Vassilicos JC (2007) Dissipation and decay of fractal-generated turbulence. Physics of Fluids 19(10):105,108

Shao D, Law AWK (2009) Turbulent mass and momentum transport of a circular offset dense jet. Journal of Turbulence 10(40):1–24

da Silva CB, Pereira JCF (2008) Invariants of the velocity-gradient, rate-of-strain, and rate-of-rotation tensors across the turbulent/nonturbulent interface in jets. Physics of Fluids 20(5):055,101

Soloff SM, Adrian RJ, Liu ZC (1997) Distortion compensation for generalized stereoscopic particle image velocimetry. Measurement Science and Technology 8(12):1441–1454

Soria J (1996) An investigation of the near wake of a circular cylinder using a video-based digital cross-correlation particle image velocimetry technique. Experimental Thermal and Fluid Science 12(2):221–233

Soria J, Atkinson C (2008) Towards 3C-3D digital holographic fluid velocity vector field measurementtomographic digital holographic PIV (Tomo-HPIV). Measurement Science and Technology 19(7):074,002

Soria J, Sondergaard R, Cantwell BJ, Chong MS, Perry AE (1994) A study of the fine-scale motions of incompressible time-developing mixing layers. Physics of Fluids 6(2):871

Sousa JMM (2002) Turbulent flow around a surface-mounted obstacle using 2D-3C DPIV. Experiments in Fluids 33:854–862

Srinarayana N, Armfield S, Lin W (2009) Impinging plane fountains in a homogeneous fluid. International Journal of Heat and Mass Transfer 52(11-12):2614–2623

Stanislas M, Perret L, Foucaut JM (2008) Vortical structures in the turbulent boundary layer: a possible route to a universal representation. Journal of Fluid Mechanics 602:327–382

Stitou A, Riethmuller ML (2001) Extension of PIV to super resolution using Adel Stitou and M L Riethmuller. Measurement Science and Technology 12:1398–1403

Tanaka T, Eaton JK (2007) A correction method for measuring turbulence kinetic energy dissipation rate by PIV. Experiments in Fluids 42(6):893–902

Taylor GI (1935) Statistical Theory of Turbulence. Proceedings of the Royal Society of London Series A, Mathematical and Physical Sciences 151(873):421–444

Thomas L, Vernet R, Tremblais B, David L (2010) Influence of geometric parameters and image preprocessing on tomo-PIV results. In: 15th Int Symp on Applications of Laser Techniques to Fluid Mechanics Lisbon, Portugal, 05-08 July, 2010

Thomas L, Tremblais B, Braud P, David L (2011) Comparison of Algebraic tomography PIV and scanning PIV for fluid flow. In: Forum on recent developments in Volume Reconstruction Techniques applied to 3D fluid and solid mechanics, vol i, pp 2–5

Thomas L, Tremblais B, David L (2014) Optimization of the volume reconstruction for classical tomo-PIV algorithms (MART , BIMART and SMART): synthetic and experimental studies . Meas Sci Technol in press

Tien WH, Kartes P, Yamasaki T, Dabiri D (2008) A color-coded backlighted defocusing digital particle image velocimetry system. Experiments in Fluids 44(6):1015–1026

Tokgoz S, Elsinga GE, Delfos R, Westerweel J (2012) Spatial resolution and dissipation rate estimation in Taylor Couette flow for tomographic PIV. Experiments in Fluids 53:561–583

Tomasi C, Manduchi R (1998) Bilateral Filtering for Gray and Color Images. In: Sixth International Conference on Computer Vision, pp 839–846

Tremblais B, David L, Arrivault D, Dombre J, Chatellier L, Thomas L (2010) SLIP: Simple Library for Image Processing (version 1.0), http://www.sic.sp2mi.univ-poitiers.fr/slip/

Turner JS (1966) Jets and plumes with negative or reversing buoyancy. Journal of Fluid Mechanics 26:779–792

Valente PC, Vassilicos JC (2011) The decay of turbulence generated by a class of multiscale grids. Journal of Fluid Mechanics 687:300–340

Weinkauff J, Michaelis D, Dreizler a, Böhm B (2013) Tomographic PIV measurements in a turbulent lifted jet flame. Experiments in Fluids 54(12):1624

Westerweel J (1997) Fundamentals of digital particle image velocimetry. Measurement Science and Technology 8:1379–1392

Westerweel J, Scarano F (2005) Universal outlier detection for PIV data. Experiments in Fluids 39(6):1096–1100

Westerweel J, Hofmann T, Fukushima C, Hunt J (2002) The turbulent/non-turbulent interface at the outer boundary of a self-similar turbulent jet. Experiments in Fluids 33(6):873–878

Wieneke B (2005) Stereo-PIV using self-calibration on particle images. Experiments in Fluids 39(2):267–280

Wieneke B (2008) Volume self-calibration for 3D particle image velocimetry. Experiments in Fluids 45:549–556

Wieneke B (2013) Iterative reconstruction of volumetric particle distribution. Measurement Science and Technology 24(2):024,008

Willert CE, Gharib M (1991) Experiments in Fluids Digital particle image velocimetry. Experiments in Fluids 10:181–193

Willert CE, Gharib M (1992) Three-dimensional particle imaging with a single camera. Experiments in Fluids 358:353–358

Williamson N, Srinarayana N, Armfield SW, McBAIN GD, Lin W (2008) Low-Reynolds-number fountain behaviour. Journal of Fluid Mechanics 608(2008)

Williamson N, Armfield SW, Lin W (2011) Forced turbulent fountain flow behaviour. Journal of Fluid Mechanics 671:535–558

Woods AW, Caulfield CP (1992) A Laboratory Sudy of Explosive Volcanic Eruptions. Journal of Geophysical Research 97:6699–6712

Worth NA, Nickels TB (2008) Acceleration of Tomo-PIV by estimating the initial volume intensity distribution. Experiments in Fluids 45(5):847–856

Worth NA, Nickels TB, Swaminathan N (2010) A tomographic PIV resolution study based on homogeneous isotropic turbulence DNS data. Experiments in Fluids 49(3):637–656

Zhang J, Tao B, Katz J (1997) Turbulent flow measurement in a square duct with hybrid holographic PIV. Experiments in Fluids 23:373–381

Zhang Z (1999) Flexible camera calibration by viewing a plane from unknown orientations. In: Proceedings of the Seventh IEEE International Conference on Computer Vision, IEEE, vol 1, pp 666–673, DOI 10.1109/ICCV.1999.791289

Appendix A

Turbulent channel: experimental set-up and supplementary results

For experiments conductedinthePassesdesPoissonsturbulentchannel, from 31 January to 10 February 2012. This appendix contains additional information of the experimental rig, materials used, laser optics setup and particle information. In addition to this, supplementary data are presented that were used in the calculation of the losses by Bernoulli analysis of the volume.

A.1 Materials

The following list contains the primary experimental equipment required to conduct the TPIV experiments.

- 4 CV-M2 JAI cameras, 1600×1200 (H $\times$ V), 50 mm lens, $f\_\#$ 22
- 4 lens mounted two-axis Scheimpflug adapters
- 5 three-axis universal rotation mountings
- 1 LaVision calibration plate, 13×13points, 15 mm spacing, rows of two planes 1.5mm displaced in Z-direction, 12 mm total thickness

- 1 twin pulse Big Sky Laser laser, 120 mJ per pulse
- 3 water reservoirs, 3 300 L and 2 200 L downstream, $\sim$ 2 500 upstream maximum capacity
- 1 flum $305 \times 520 \times 5000$ mm^3 (W $\times$ H $\times$ L)
- 5 pools, 750 mm centre-to-centre down the length of the channel
- 5 trash rack assemblies, total housing length 198 mm with three turbulent grids spaced (upstream to down stream) 90 mm and 85 mm
- 1 acquisition computer, 2 core 2.66 GHz, 2 GB RAM, RAID 0, 1.5 TB HD
- 1 computer for motion control of camera and calibration plate support
- 1 pump with flow meter achieving 34 L/s at 100% power
- 1 electronic inclinometer of accuracy $0^\circ/90^\circ = 0.1^\circ$; 1° –v $89^\circ = 0.2^\circ$

A.2 Additional information of the apparatus

Trash rack housing and flume end

Details of the trash rack housing are presented in Figure A.1a whilst two views of the flume end are presented in Figure A.1b.

Laser Optics

Figure A.2 shows the layout and spacing of the laser sheet optics used to generate the laser sheet volume.

Particle information

The particles used in Chapter 3 were VESTOSINT 2157 natural colour polymide 12 fine powder. Approximately round geometry.

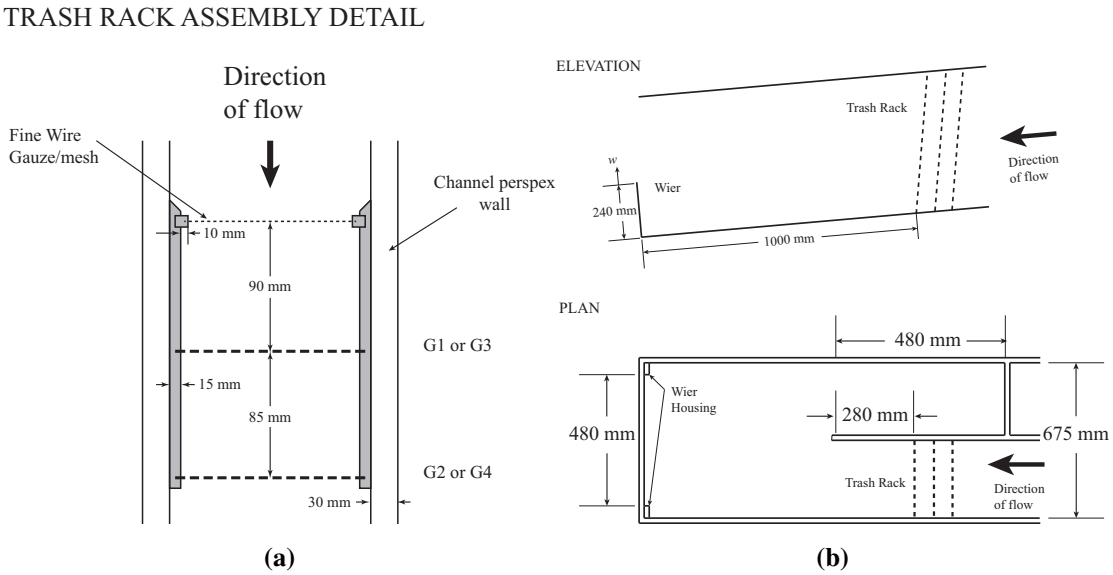

Figure A.1: Schematic of the trashrack housing (a) and flume end (b)

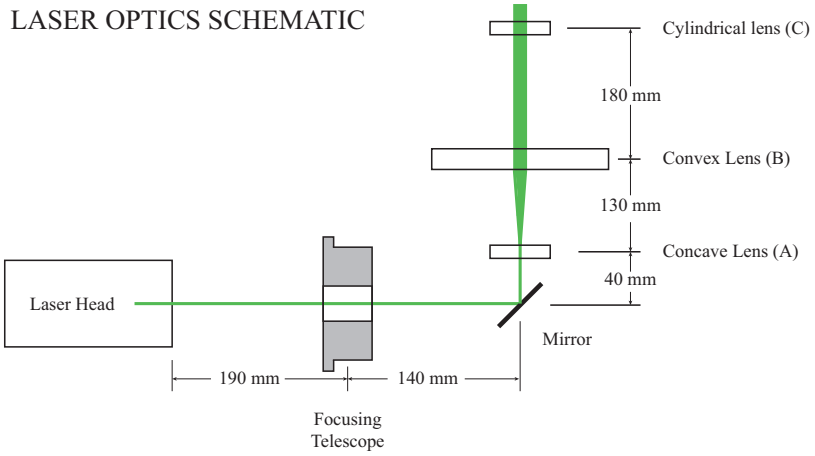

Figure A.2: Schematic of the laser optics details. (A) 50.8 mm Dia. concave $f = -100$ mm, (B) 145 mm Dia. convex $f = 250$ mm, (c) 40 mm Dia, 16×24 mm^3 (H $\times$ L) cylindrical lens $f \approx 10$ mm. The focusing telescope contains tow 25 mm diameter lenses, concave the convex for focusing laser on mirror.

Powder Information

Property		Test method		Unit	VESTOSINT 2157 natural color
		international	national		
App. bulk density		ISO 60	DIN EN ISO 60	g/dm³	≥ 350
Average particle size	d50		Laser diffraction analysis (Malvern Mastersizer)	µm	approx. 56

Density, water absorption, thermal, mechanical and electrical properties

Property		Test method		Unit	VESTOSINT 2157 natural color
		international	national		
Melting point		ISO 3146	DIN EN ISO 3146	°C	184
Density	23 °C	ISO 1183	DIN EN ISO 1183	g/cm³	1.016
Shore hardness D		ISO 868	DIN EN ISO 868		75
Ball indentation hardness	H30	ISO 2039-1	DIN EN ISO 2039-1	N/mm²	90
Tensile test		ISO 527-1	DIN EN ISO 527-1		
Stress at yield		ISO 527-2	DIN EN ISO 527-2	MPa	43
Strain at yield				%	6
Strain at break				%	> 100
Volume resistivity		IEC 60093	DIN IEC 60093	Ω · m	10^{12}
Dielectric breakdown voltage	K20/P50	IEC 60243-1	DIN EN 60243-1	kV/mm	90
Water absorption	100 °C, immersion	ISO 62	DIN EN ISO 62	%	1.9
Moisture absorption		ISO 62	DIN EN ISO 62		
	23 °C, 96 % r. h.			%	1.3
	23 °C, 50 % r. h.			%	0.5
Coef. of linear expansion	23 – 55 °C	ISO 11359	DIN 53752	$10^{-4} \cdot K^{-1}$	1.09
Thermal conductivity			Referring to DIN 52612	W/m · K	0.23 – 0.29
Specific heat			DIN 53765	J/g · K	2.35
Taber abraser		ASTM D 1242	DIN 53754	mg/100 turns	14

Pigmentation may affect values.

Figure A.3: Details of Vestosint particles used in TPIC experiments (Chapter 3)

A.3 Supplementary results and curve fitting

This section contains supplementary data for the calculations presented in Section 3.4.5 and Section 4.3.6. The calculated data are presented in Table A.1, followed by key images from the analysis. Recall that the subscript 1 refers to the upstream position of the volume 2 refers to the downstream position. The images that support the results are Figure A.4 and Figure A.5, which shows the curve fitting for the turbulent kinetic energy k and Figure A.6 and Figure A.7 for the mean flow.

Table A.1: Summary of calculated parameters for Bernoulli analysis of measurement volume, Chapter 3 and Chapter 4 (lower half).

Parameter	Comments	G1G2	G3G4
$y_1 - y_2$	Channel elevation	5 mm	5 mm
$h_1 - h_2$	Water depth	-4.5 mm	-4.5 mm
$\frac{p_1 - p_2}{\rho g}$	Pressure head	0.46 mm	0.46 mm
$k_1 - k_2$	Kinetic energy loss	8 mm^2s^{-2}	781 mm^2s^{-2}
$U_1^2 - U_2^2$	Mean flow loss	7.1 mm/s	6.7 mm/s
$s_1 - s_2 = \int_1^2 \frac{V(x)}{U(x)} \text{dx}$	Elevation change of flow	4.8 mm	1.3 mm
Q_V	Local flow rate	0.278 L/s	0.255 L/s
ΔH_pool	Losses over h_c	5.3 mm	1.8 mm
Parameter	Comments	R_1	R_2
$y_1 - y_2$	Channel elevation	2.7 mm	2.7 mm
$h_1 - h_2$	Water depth	-2.3 mm	-2.3 mm
$\frac{p_1 - p_2}{\rho g}$	Pressure head	0.43 mm	0.43 mm
$k_1 - k_2$	Kinetic energy loss	1065 mm^2s^{-2}	181 mm^2s^{-2}
$U_1^2 - U_2^2$	Mean flow loss	0.7 mm/s	5.4 mm/s
$s_1 - s_2 = \int_1^2 \frac{V(x)}{U(x)} \text{dx}$	Elevation change of flow	2.83 mm	2.43 mm
Q_V	Local flow rate	0.103 L/s	0.085 L/s
ΔH_pool	Losses over h_c	3.3 mm	2.87 mm

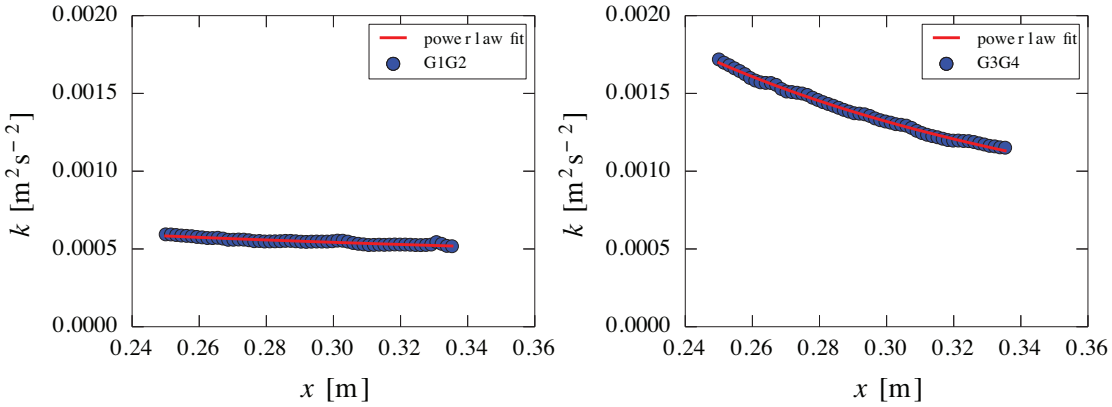

(a) **(b)**

Figure A.4: Fitting of k for calculation of energy dissipation (Section 3.4.5), and calculation of k_1, k_2 parameters in Table A.1. (a) G1G2, (b) G3G4. The fitting curve, $a \cdot x^b$, has coefficients $a = 3.36 \cdot 10^{-4}$, $b = -0.399$ for G1G2, $a = 2.50 \cdot 10^{-4}$, $b = -1.381$ for G3G4

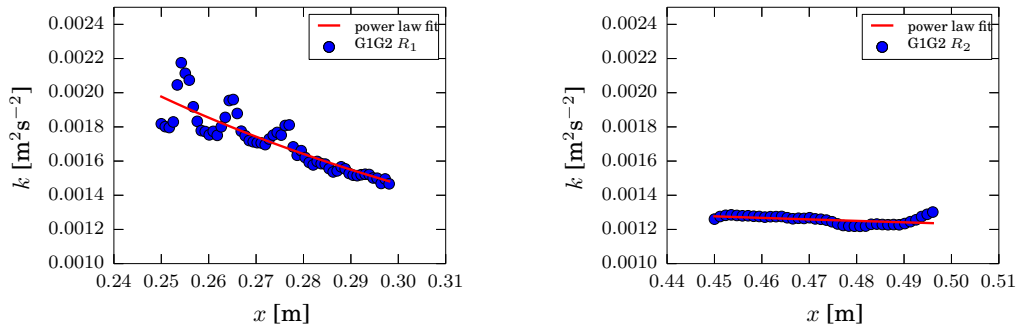

(a) **(b)**

Figure A.5: Fiitting of k for calculation of energy dissipation (Section 3.4.5), and calculation of k_1, k_2 parameters in Table 4.3.6 for G1G2 (a) R_1, (b) R_2. The fitting curve, $a \cdot x^b$, has coefficients $a = 2.03 \cdot 10^{-4}$, $b = -1.641$ for R_1 and $a = 9.83 \cdot 10^{-4}$, $b = -0.326$ for R_2

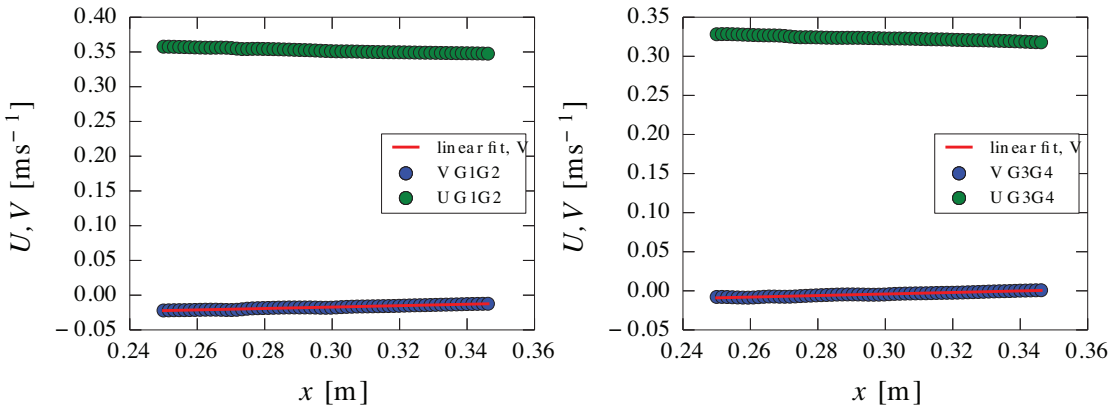

(a) **(b)**

Figure A.6: Plot of $U(x)$ and $V(x)$ for analysis of dissipation in the measurement volume by Bernoulli analysis (Section 3.4.5). (a) G1G2, (b) G3G4. The fitting curve, $a \cdot x + b$, has coefficients $a = 0.102$, $b = -0.0477$ for G1G2 and $a = 0.098$, $b = -0.0334$ for G3G4

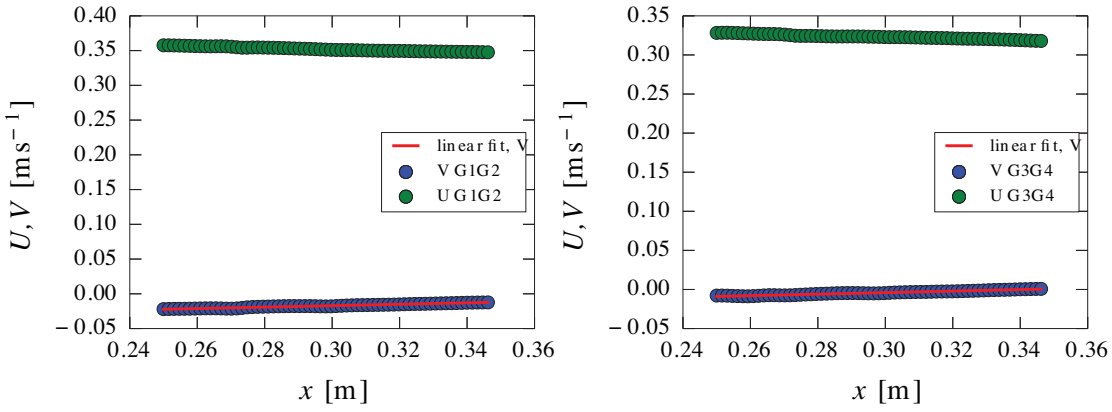

(a) **(b)**

Figure A.7: Plot of $U(x)$ and $V(x)$ for analysis of dissipation in the measurement volume by Bernoulli analysis (Section 3.4.5) for G1G2 (a) R_1, (b) R_2. The fitting curve, $a \cdot x + b$, has coefficients $a = 0.006$, $b = -0.0026$ for R_1 and $a = 0.228$, $b = -0.0963$ for R_2

A.4 Appendix - Technical Details of 2D PIV Measurements

This section provides the technical details of the 2D PIV field of Figure 3.5. Two 1600×1200 px 8 bit CV-M2 JAI cameras were used to acquire the images. Both cameras' lens axes were normal to the laser sheet and each camera recorded half of the pool (with a central overlap of the region in the order of 50 mm). Both cameras were fitted with 50 mm lenses. The particles used were the same as those used for the TPIV measurements, illuminated by the same double head Nd:YAG laser. The time step between image pairs was $\Delta t = 2500$ νs, and velocity fields were required at 7 Hz.

The vector fields were calculated for each camera separately using Davis LaVision software and stitched together in a post-processing step. The vector fields were calculated from a no-deforming, multi-pass implementation, with first interrogation window size 64×64 px to 16×16 px. For the last pass a high accuracy Whittaker algorithm was applied. The vector windows had a 50% overlap between resulting in $\delta x = 2.13$ mm vector spacing and with approximately 50 000 vectors in total for a velocity field of the entire pool.

The field of view of each camera is shown in the median images, for computing the background noise, in Figure A.8. The images overlap in the central region by approximately 50 px.

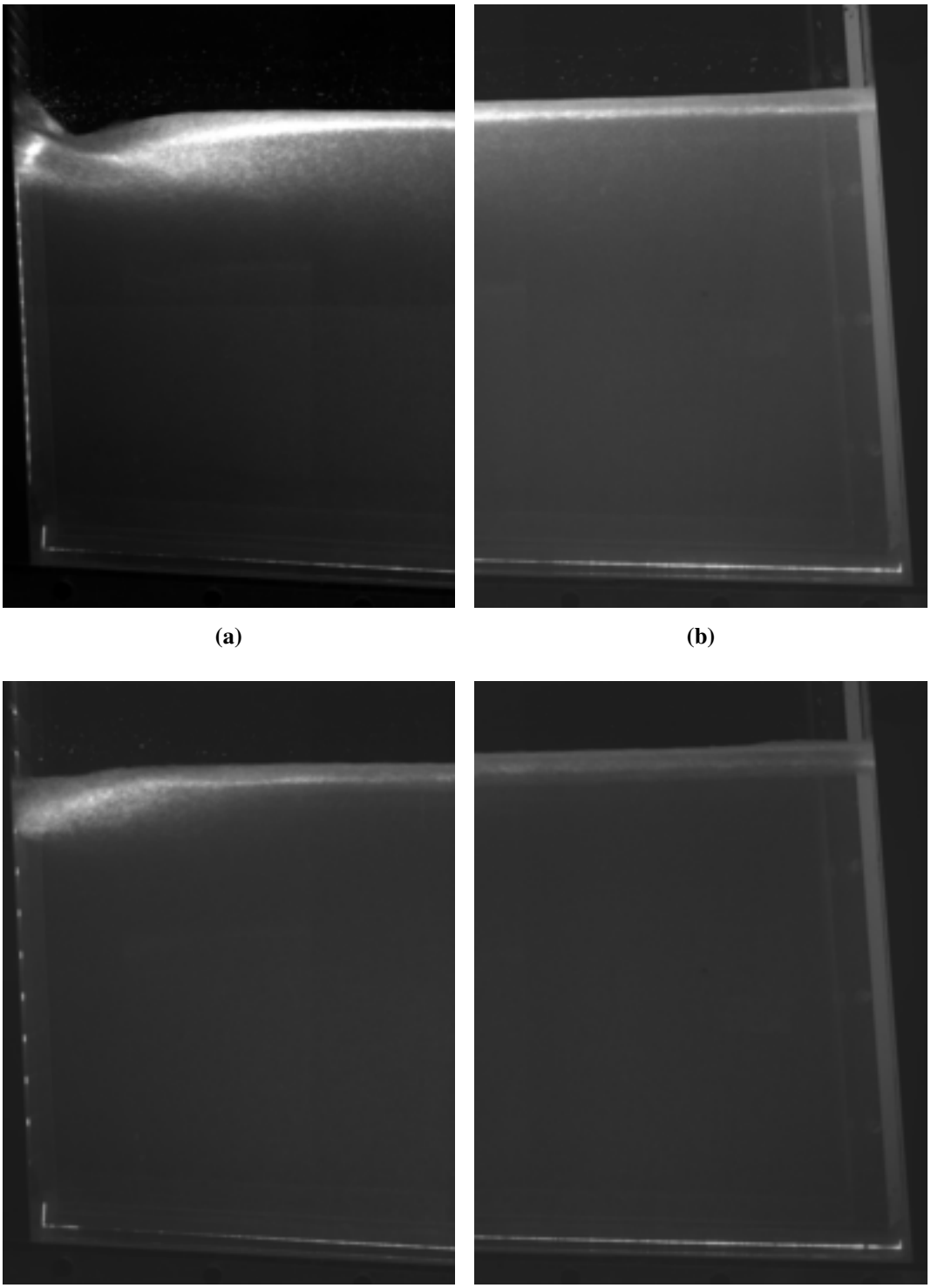

(a) **(b)**

(c) **(d)**

Figure A.8: Median of 50 images of the 2D PIV experiment. (a) upstream G1G2, (b) downstream G1G2, (c) upstream G3G4, (b) downstream G3G4,

Appendix B

Camera Calibration for TPIV

A fundamental process in all PIV measurements is the camera calibration. This section will briefly detail the principles and methods for calibrating the optical setup for TPIV measurements.

B.1 Calibration Targets

Calibration targets are typically flat plates with homogeneous markings or etchings at accurately known grid positions. The most common type of commercially available calibration plate is an anodised aluminium plate with white dots accurately and precisely etched into identically corresponding grid locations on both sides. However, for smaller fields of view and different experimental configurations, other calibration targets may be more appropriate, such as laminating the calibration crosses between perspex (Figure B.1a). For the fountain experiments conducted at the University of Sydney, a calibration plate was manufactured with a water-jet cutter. The grid of markers was also water-jet cut, initially as pilot holes and the post drilling through the thickness of the plate to ensure that corresponding points were identically located on both sides of the plate. The plate was then made black, and white filler was spread into the holes to provide enough contrast (Figure B.1b).

a) b)

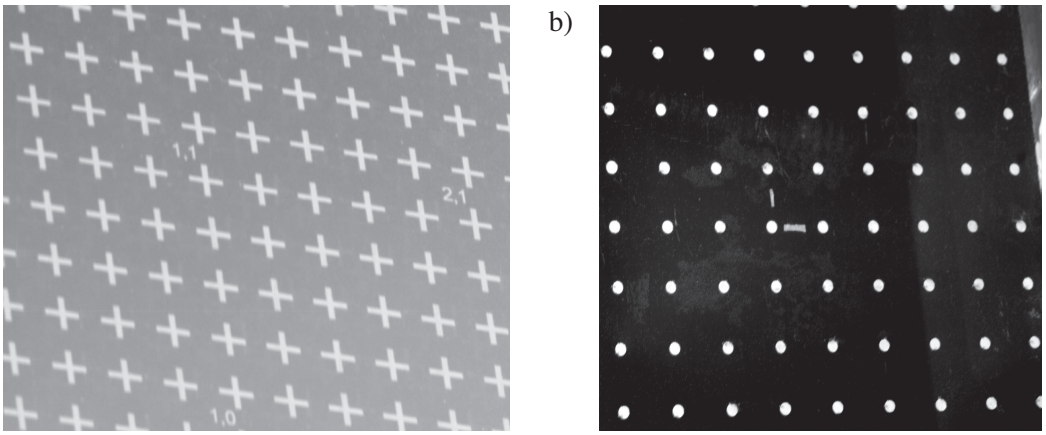

Figure B.1: Calibration Targets. (a) Calibration marks laminated between perspex sheets , and (b) In-house manufactured calibration plate.

B.2 Determination of the camera calibration matrix M

Tomographic PIV relies on the accurate camera calibration so that corresponding particle images have lines-of-sight that intersect when projected. In order to obtain this, a series of homogeneous, physical locations, $\mathbf{x} = (x, y, z)^T$, are mapped onto each camera system in pixel coordinates, $\mathbf{X} = (X, Y)^T$. The mapping is typically modelled with a standard pinhole model equation, which for each camera is

$$\begin{pmatrix} X \\ Y \\ S \end{pmatrix} = \mathbf{M} \begin{pmatrix} x \\ y \\ z \\ 1 \end{pmatrix} \tag{B.1}$$

where $\mathbf{M}$ is the 3×4 projection perspective calibration matrix and S is a scale factor. From Eq B.2, it can be seen that $\mathbf{M}$ is composed of the intrinsic matrix $\mathbf{A}$ (which considers the camera principal point, focal length and skewness between X and Y lengths), 3D rotation matrix $\mathbf{R}$, and translation matrix $\mathbf{t}$, so that

$$\mathbf{M} = \mathbf{A} \left(\mathbf{R} \mid \mathbf{t} \right) \tag{B.2}$$

The locations in $\mathbf{x}$ are set by traversing a calibration plate through the laser sheet volume. At incremental z locations, an image of the calibration plate by each camera is recorded. The imaged calibration points must then be identified on the images. To aid this, image processing is employed to remove background noise. The imaged calibration points are then identified and their centroid locations calculated. The results is that each point in $\mathbf{X}$ has a corresponding physical location $\mathbf{x}$. There are several ways to calculate $\mathbf{M}$ in Eq B.1, utilising a Levenberg-Marquardt or other least squares minimisation algorithm (see for example Soloff et al, 1997).

B.3 Re-Projection Errors

After determining $\mathbf{M}$ for each camera, the accuracy of the calibration can be verified. Projecting the calibration points $\mathbf{x}$ onto each camera, the back-projected coordinates (X', Y') can be compared to the expected coordinates (see Figure B.3 for definitions). For a perfect calibration, $\mathbf{X} - \mathbf{X}' = 0$. For real calibration conditions, errors in $\mathbf{M}$ arise. The sources of these errors include inaccurate translation of the calibration plate, inaccurate calibration markings, weak optical distortions (Wieneke, 2008), and errors from the centroid location of the imaged calibration points.

Figure B.2 shows the scatter plot of the re-projections $\mathbf{X} - \mathbf{X}'$ from an experimental calibrations (fountain experiments, Chapter 4). Figure B.2a shows the errors before volume self-calibration. The colours correspond to the z-coordinate of the calibration plate. There are *clumps* of like colours with randomly distributed error - this systematic error is due to translation inaccuracies of the calibration plate. The scale of the volume-self calibrated data (Figure B.2b) has changed as the errors have significantly reduced. The z locations in Figure B.2b correspond to centre of the sub-volume v. To ascertain whether there are optical distortions, the back-projection errors for corresponding calibration points should be considered (Figure B.4).

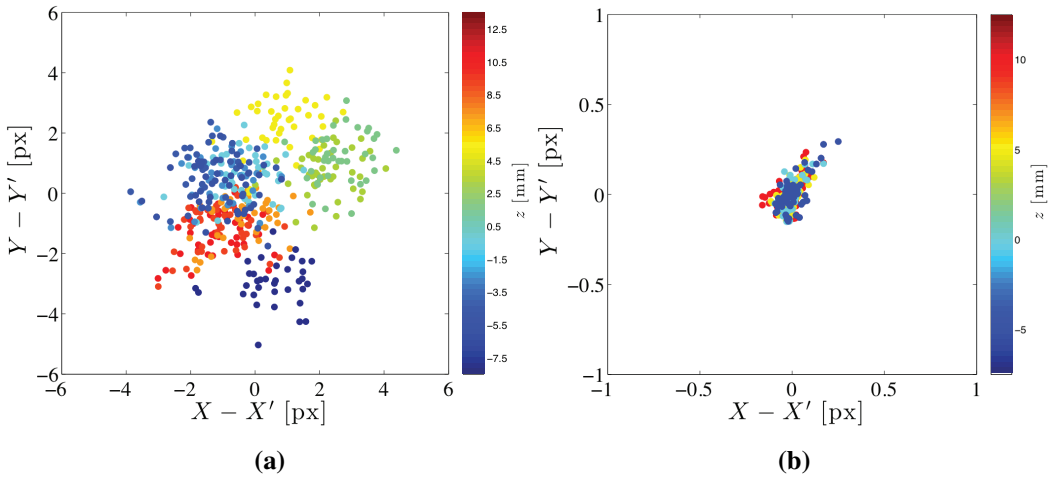

Figure B.2: Back-projection errors $\mathbf{X} - \mathbf{X}'$ from experimental data: (a) uncorrected calibration (variance = 2.46 px, max = 5.03 px), and, (b) after volume self-calibration (variance = 0.005 px, max = 0.35 px). Note the colour bar has changed for (b) as the volume self-calibration is corrected on four discrete planes and likewise the range of the axes have changed due to the correction.

B.4 Volume Self-Calibration

The volume self-calibration technique was introduced by Wieneke (2008). In addition to briefly reviewing the procedure, this section aims to add some best practice techniques based on using the program *Misalignment* by Lionel Thomas using the SLIP library (Tremblais et al, 2010). The self-calibration technique aims to improve the calibration accuracy achieved from the standard procedure described in section B.2, by calibrating on the imaged particles. The result is an updated perspective calibration matrix, $\mathbf{M}'$.

Volume self-calibration utilises triangulation, as performed in PTV (Maas et al, 1993). Imaged particles are identified, and corresponding particles are found by triangulation, utilising $\mathbf{M}$ from the calibration. Consider the three camera set up of Figure B.3, shown in a 2D view for simplicity. On each camera sensor, one set of corresponding particle images has been isolated. Due to naturally occurring misalignment errors (section B.3), the lines-of sight are not coincident. The point $P(x,y,z)$ is approximated by minimising d for all cameras: it is the best-fit world coordinate. $P(x,y,z)$ is projected back onto the cameras,

and the position $d = (X,Y) - (X',Y')$ is recorded.

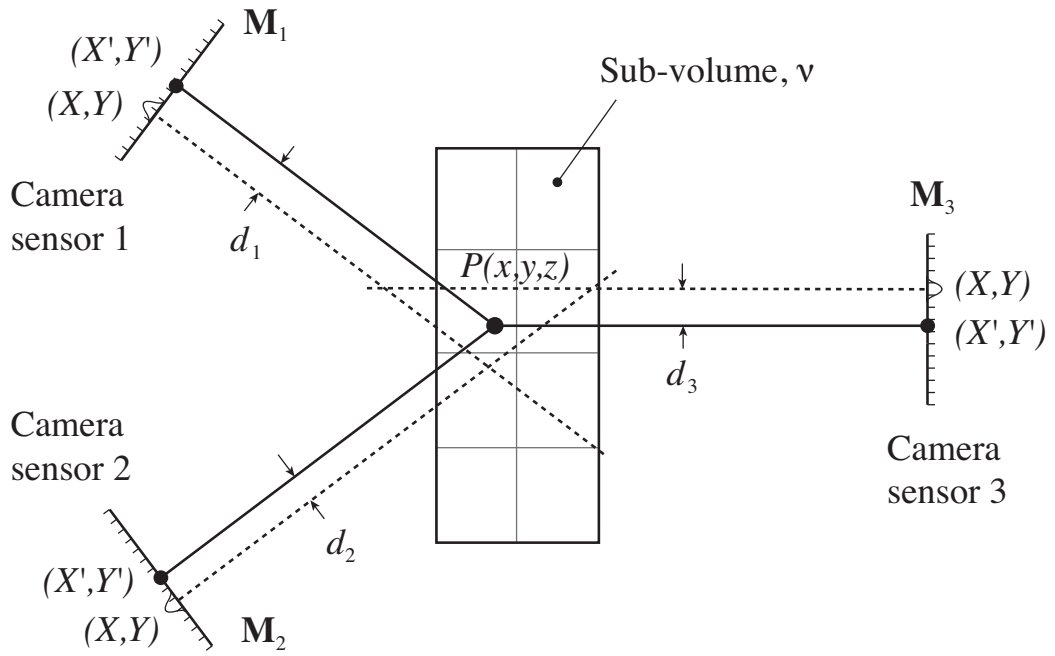

Figure B.3: Schematic showing the disparities d between projected particle images (X,Y) compared to the best-fit location of $P(x,y,z)$ onto the image at (X',Y').

Figure B.3 also shows that the volume is divided into a regular grid of sub-volumes, ν. In practice, thousands of P are considered for each realisation, however only so that the image densities are equivalent to PTV images (Wieneke, 2008). TPIV images are typically heavily filtered in order to keep the brightest, and this means that no ghost particles are included in the disparity calculation. For all $P \in \nu$, the disparity vector $\mathbf{d}_\nu = (X',Y')$ can be computed, by considering the average of d. The updated calibration matrix can then be determined from $\mathbf{M}' = \mathbf{M} - \mathbf{d}$.

The disparity maps can be represented as 2D images for each plane $\nu(z)$ (Figure B.4(a – c). These disparity maps were computed from 50 images and 7 iterations. In Figure B.4(a – c), the projections of P are shown as Gaussian disks with centre at (X',Y'), and at each grid location, $\mathbf{d}_\nu$ is calculated by finding the centre of area of the disks. The scale of each disparity image is shown. When calculating the disparity maps, a maximum search region

is set, a balance between being large enough to be able to correct large disparities, but not so large as to not be able to find unique particles. The scales shown in Figure B.4(a – c) are also equal to the search radius for that iteration, which decrease as the iterations progress.

In order to verify that real particles are being triangulated and not ghosts, the histogram of $P(z)$ is shown in Figure B.4d. The histogram shows that as $\mathbf{M}'$ improves, only particles within the laser sheet are found (for the experimental data shown, -5 mm $\leq \Delta z \leq 5$ mm. By the end of the 7th iteration of the self-calibration, the laser sheet profile has been retrieved). It is important that the laser sheet profile is obtained from the self-calibration process, as random errors appear to make valid disparity maps with a Gaussian distribution of d, but would not yield a laser sheet profile.

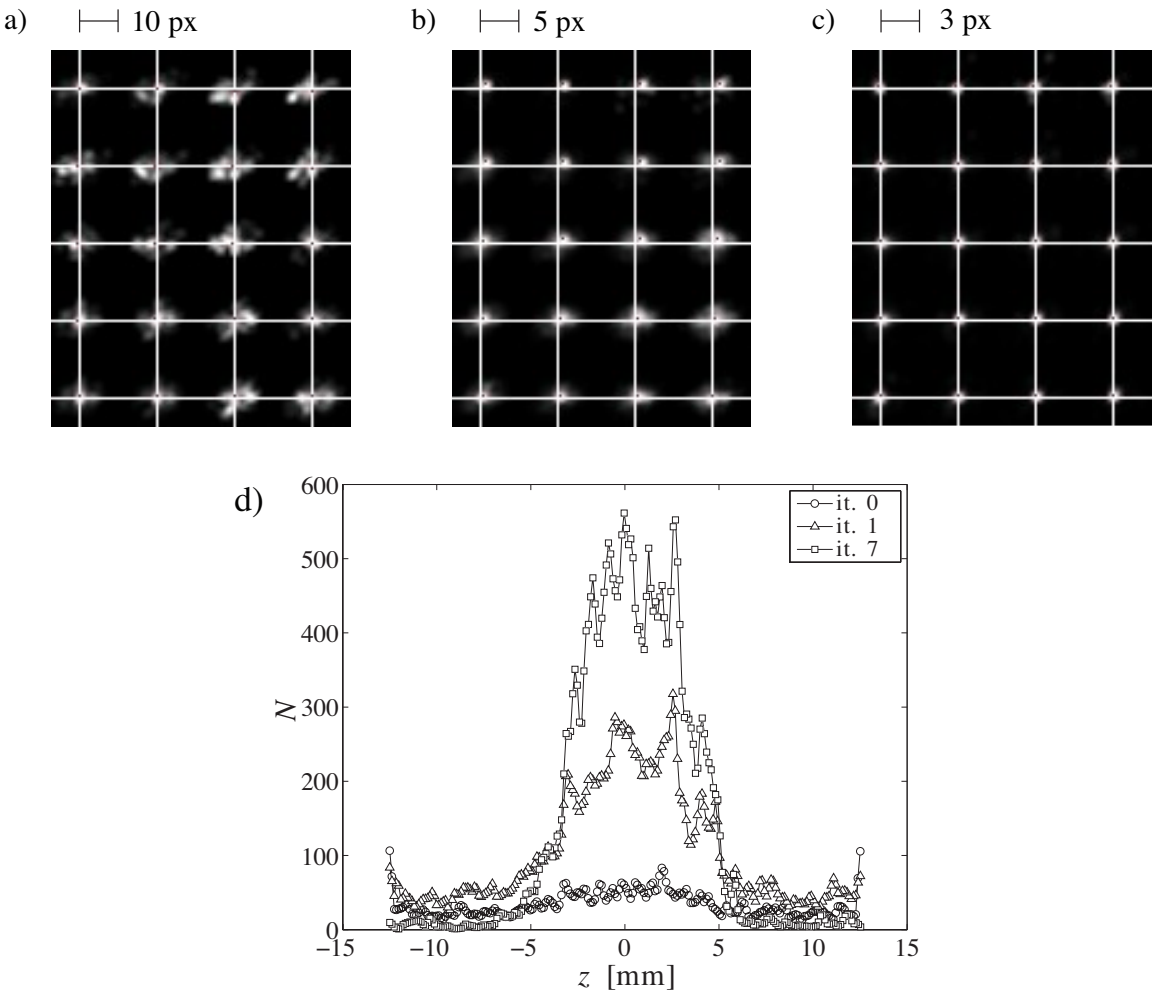

Figure B.4: Disparity maps calculated for the fountain experiment (Chapter 4). Images (a) to (c) show the disparity maps (iteration 0, 1 and 7 respectively), and (d) shows the corresponding histogram of the number of particles found at each location in z.

Appendix C

Vibration-Correction Implementations

To quantify the effect of vibration correction techniques, four variations of the volume self-calibration were applied[1]. These definitions are shown schematically in Figure C.1.

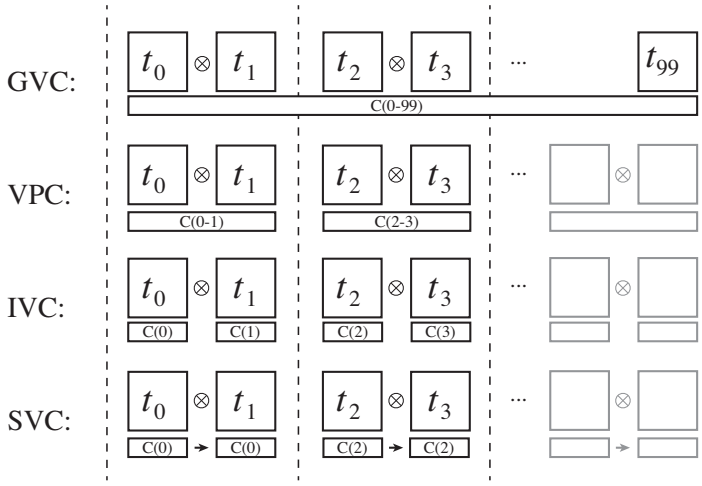

Figure C.1: Volume self-calibration methods. C(i) indicates the time-step t_i on which the volume self-calibration is performed and likewise, C($i_1 - i_2$) indicates the range of time-steps.

GVC Global Volume Correction: This is the standard implementation of the volume self calibration. The calibration model is generated by considering a large batch of im-

[1]This work has been published Earl et al (2015).

ages, in this case 100. The same calibration model is used for the reconstruction of all volumes as per the implementation of Wieneke (2008).

VPC Volume Pair Correction: Each *volume pair* that is cross-correlated to calculate a velocity field has a common calibration model determined by volume self-calibration applied over the pair of them. This method may be implemented to increase the number of valid particle matches for the self calibration combined with a vibration frequency $\ll 1/\Delta t$. This is the implementation of Michaelis and Wolf (2011)

IVC Individual Volume Correction: Each reconstructed volume has its own calibration model computed by computing the volume self-calibration for each time-step individually . This is the ideal case, each reconstruction is corrected, and suitable for when the vibration frequency is in the order of or greater than $1/\Delta t$.

SVC Single Volume Correction: For each volume pair that is cross-correlated to compute a velocity field, the calibration model is determined by applying the volume self-calibration applied over the first time step of a volume pair only. This implementation could be used where an assumption can be made that the vibration frequency is $\ll 1/\Delta t$

The volume self-calibration technique is an iterative process, whether applied globally or for individual volume corrections. For these comparisons, the GVC was used as the starting point for the other correction regimes. The GVC obtains the average (or reference) position of all the cameras with respect to the measurement volume. Once the domain of physical volume is known, its dimensions are fixed for the remaining correction regimes. This means that through each iteration of the vibration correction, the cameras move with respect to the volume (Figure C.2a).

Figure C.2b shows the evolution of the disparity maps for the IVC case. From the first iteration it is clear that the calibration model is not refined, and owing to the random position of the other cameras, the disparity distribution does not show one strong peak disparity (as would be the case in a non-vibrating experiment, Wieneke, 2008), but rather two or three disparity peaks. By the third iteration, the repeated application of the volume-self calibration resulted in disparity maps (hence camera models) that have converged.

Monitoring the disparities d_{ix} and d_{iy} allows for an optimum selection of $\varepsilon_{i,\max}$ to be determined for each iteration. Figure C.3b graphs the root mean square (rms) of the total disparity $d_{\text{rms}} = \sqrt{d_x^2 + d_y^2}$ for each camera against the iteration of the volume self-calibration. In Figure C.3b, d_{rms} is calculated over all sub-volumes and over 100 images of the first time-step for the IVC method. For the first iteration of the volume self-calibration, $0.3 \leq d_{\text{rms}} \leq 0.5$ px, which implies that the amplitude of relative vibration for one camera is within the average particle image diameter. As the cameras are vibrating independently of each other, the rms of the total combined disparity is 1 px. As will be seen, this small magnitude of vibration will enable an acceptable reconstruction without vibration correction, however the resulting velocity field and turbulence statistics are more severely affected.

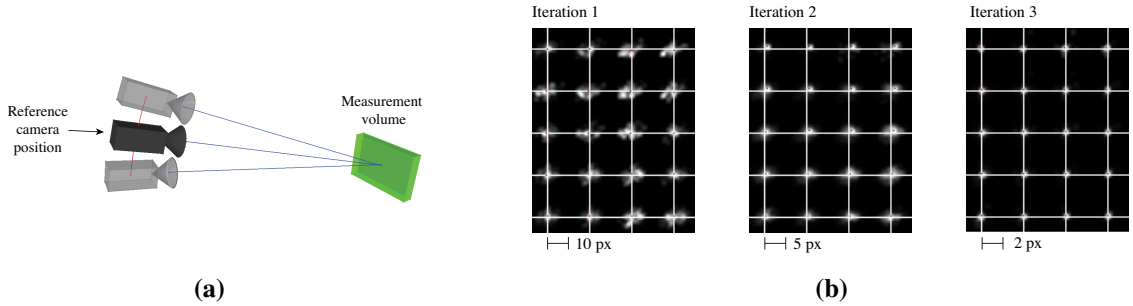

Figure C.2: (a) Physcial interpretation of vibration correction schemes. (b) Sample of disparity maps for the first three iterations of the IVC method

Additionally, a time history of the disparity errors is presented for the IVC case. Figure C.3a shows the average magnitude of the disparities for each time step. A time series analysis like this has the potential to uncover a dominant frequency of vibration. However, in this case, an evaluation of the frequency domain revealed no discernible frequency was obtained.

It was thus found that 4 iterations of the vibration correction schemes were required, and for the IVC only one iteration was required for the second time-step. It was found that $d_{\text{rms}} \approx 0.2$ px for the second time-step, and was corrected to within an equivalent range as the first time-step after one iteration. This indicates that the frequency of vibration is less than $1/\Delta t$. For each iteration, the $\varepsilon_{i,\max}$ was reduced, starting from 10 px for the first

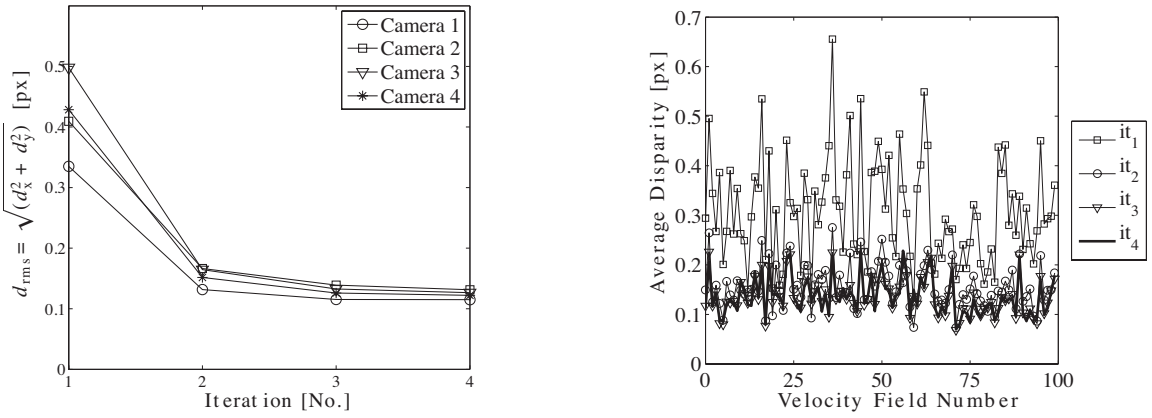

(a) **(b)**

Figure C.3: (a) Average reduction of ε over iterations of volume-self calibration for the IVC case. (b) History of average disparities of the entire volume for successive iterations of the volume-self calibration for a sequence of temporally spaced acquisitions.

iteration and finishing at 2 px for the fourth. In terms of computational effort, one iteration of the IVC/SVC was in the order of 40 s, and one iteration of the VPC was 50 s and thus the SVC case is 20% faster than the IVC and VPC. This time saving may become more significant with larger amplitudes of vibration, however in these experiments the time saved with respect to the reconstruction and cross correlation times was not significant.

C.1 Synthetic Model to Study Camera Vibration

C.1.1 Implementation

In order to further investigate the results presented in Section 3.4, a synthetic model was implemented to closely resemble the experimental conditions. A single realisation of a direct numerical simulation (DNS) velocity field was seeded with particles that were used to generate synthetic TPIV images, of which it was possible to extract four independent velocity fields. The synthetic image generator used was the same as that described in Thomas et al (2014); the key input parameters for this investigation are contained in Table C.1. Further details of the simulated homogeneous isotropic turbulence velocity field can be found

in Lecordier et al (2001).

Table C.1: Key parameters of synthetic TPIV model to simulate vibration.

Parameter	Description
Camera arrangement	4 cameras, inverted pyramid, 20° declination and subtended angle
Image size	All cameras: 512×512 px with no noise (perfect filtering), $N_s = 0.6$
d_τ	$\mathrm{d}\tau \approx 5.4$
TPIV algorithm	BiMart 3 iterations, $\mathscr{B} = 4$, identical to experimental implementation
Volume size (I:J:K)	512:512:128 vx
IV size	$64 \times 64 \times 64$
IV overlap	50%
Vector field dimensions	$15 \times 15 \times 3$
(max,rms) particle displacement	($\pm$5 vx, 1.5 vx)
Spatial resolution	7.5η

The vibration of a four camera system is complex, with combinations of independent and dependent camera translations and rotations of varying magnitudes and frequencies. The main affect of vibration on the tomographic reconstruction, regardless of complexity, is to cause a misalignment of the lines-of-sights of corresponding particle images. Thus, the aim of this section is to investigate the affects of camera vibration, or misalignment, in the simplest possible manner to fully describe the observations in the experimental results. Additionally, using a 'perfect' simulation allows the analysis to be free from contamination of experimental noise sources, such as non-uniform particle size, inhomogeneous illumi-

nation and optical aberrations. To this end, a systematic translation along the x-axis, and independently, a systematic rotation about the y-axis was applied to one camera in the model (Figure C.4). For the translation, an increasing displacement of 1 vx increments was applied, while for the rotation, an additional angle was applied so that the line of sight of the camera had a 1 vx shift at the out edges of the volume. For brevity, the remainder of this section will refer to this type of rotation as a rotation by a certain number of voxels.

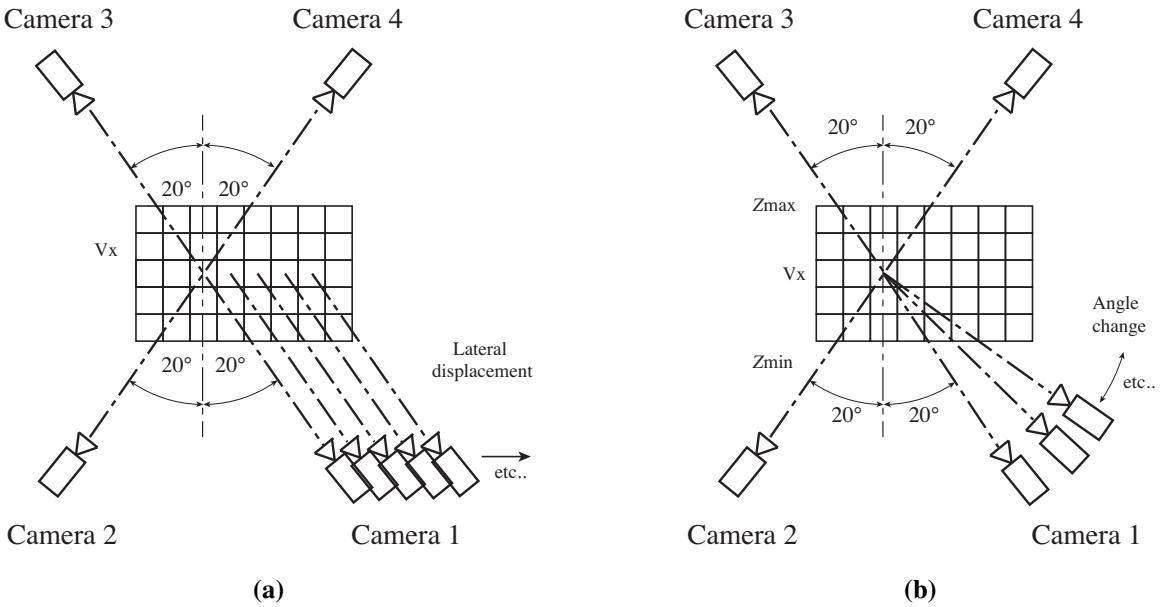

Figure C.4: Schematic of vibration implementation (a) Single camera translation (b) Single camera rotation

C.1.2 Reconstruction and Cross-Correlation Metrics

This section describes the effect that the translation and rotation of one camera has on tomographic reconstruction and cross-correlation metrics. Figure C.5 shows the affect of the shift and rotation on the laser sheet profile. In both cases, an increase in camera misalignment results in a reduction in a significant reduction in signal quality. Additionally, the rotation case introduces a dissymmetry, where the side of the laser sheet profile that the rotated camera is positioned (positive Z) has between 20 to 30% less intensity than the

opposite side of the volume. The SNR of the reconstruction (from Scarano, 2013) at 0 vx misalignment is approximately 30 and at 10 vx misalignment between 2 and 3.

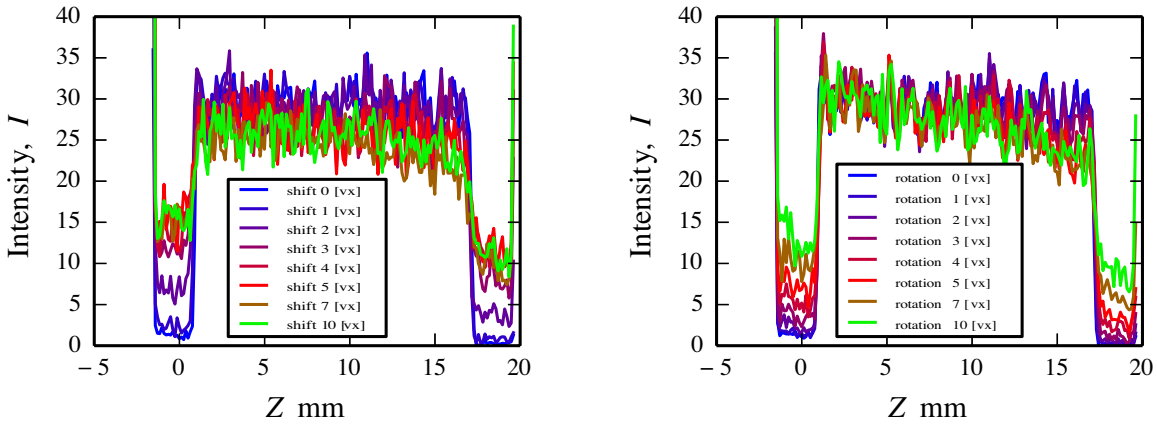

(a) Shifted **(b)** Rotated

Figure C.5: Laser sheet profiles for the synthetic case comparing the intensity on the camera model shift. (a) Shift, (b) rotation

Figure C.6 shows the effect of the translation misalignment on the reconstructed particles of a single interrogation volume (IV) located in the centre of the volume. The IV intensities have been projected onto one face to produce these two-dimensional images. Figure C.6(a) shows the intensities at 0 vx error, (b) at 2 vx shift, (c) at 5 vx shift and (d) at 10 vx shift. As the misalignment error increases, it can be seen that ghost particle production increases dramatically, until the projected image is dominated by intensities that are not present in the perfectly aligned case.

Figure C.7 shows the effect of the translation misalignment (Figure C.7a) and rotation (Figure C.7 b) on the cross-correlation SNR, number of local peaks per IV (NbP) and vector outlier detection by median filter flags (MFF). NbP is determined by calculating the number of local peaks in the IV, which corresponds to the number of reconstructed particles, ghosts or otherwise. Regarding the translation errors, the SNR decreases rapidly until hitting a plateau at a translation approximately equal to d_τ. The MFF peaks at the same level of translation. NbP tends to increase beyond a translation error of d_τ, and tapers off beyond this error. This metric would be sensitive to N_s and d_τ, however the full parametrisation of

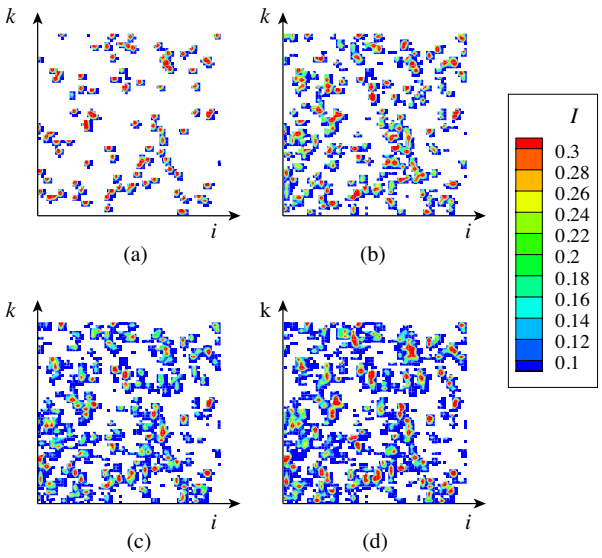

Figure C.6: 2D projections of reconstructed volume in a $64 \times 64 \times 64$ window at (a) 0 error, (b) 2 vx shift, (c) 5 vx shift, (d) 10 vx shift

these variables is beyond the scope of this study. The rotation errors yield similar trends, albeit more gradually. This is due to the line-of-sights of all cameras remaining error free in the central plane of the reconstruction domain.

C.1.3 Simulation of Vibration Correction Schemes.

The vibration correction schemes used for the experiment (Section 3.3.4) were recreated in the synthetic model. Figure C.8 shows a schematic of how the translation and rotation errors were combined to replicate the experimental conditions. The schematic shows the number of permutations tested for each correction scheme. The assumptions used for each case are outlined as follows:

IVC The correct implementation of the IVC scheme retrieves the correct camera models for both time steps, t_0 and t_1. Therefore, in the synthetic model, the IVC case has

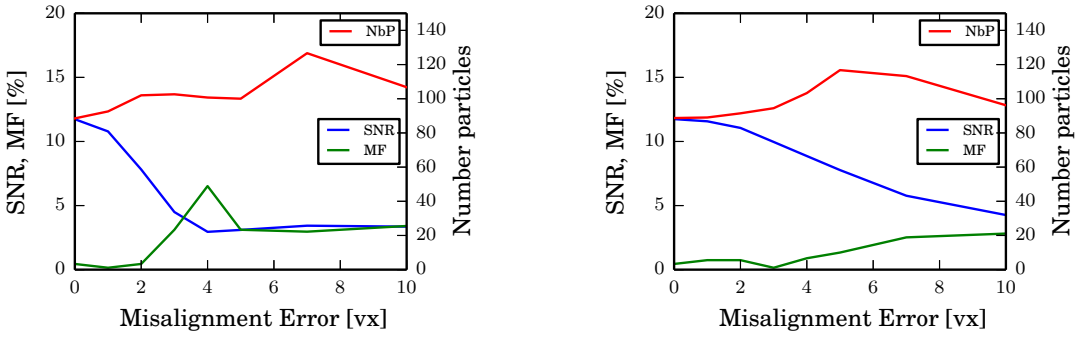

(a) Shifted

(b) Rotated

Figure C.7: Effect of camera error on the average SNR [%], MFF [%] and NbP, equivalent to number of particles, per IW. (a) shows the affect of translations, (b) for rotations

perfect camera models.

GVC It is highly improbable that t_0 has no calibration error for a GVC, therefore t_0 is assumed to have a misalignment of 2 vx. Then, t_1 is varied through the set of misalignment errors.

SVC t_0 is perfectly corrected (like the IVC), and then similar to the GVC, the second time step t_1 has a varying level of error.

VPC For misalignments not significantly greater than d_τ, disparity maps would not necessarily show two separate peaks. The resulting camera model would then be the average of perfect calibration and misalignment error.

As the IVC case only has one permutation, the several results in this section will be normalised by this case. It also represents the best possible reconstruction quality for this particular arrangement. This normalisation permits an analysis of the simulated effect of increasing vibration as the misalignment increase.

C.1.4 Correction Schemes and their Effect on Velocity

Figure C.9 shows the differences to local velocity field for each camera model, normalised by the standard deviation of the IVC case, σ_{ivc}. The translation error yields very similar

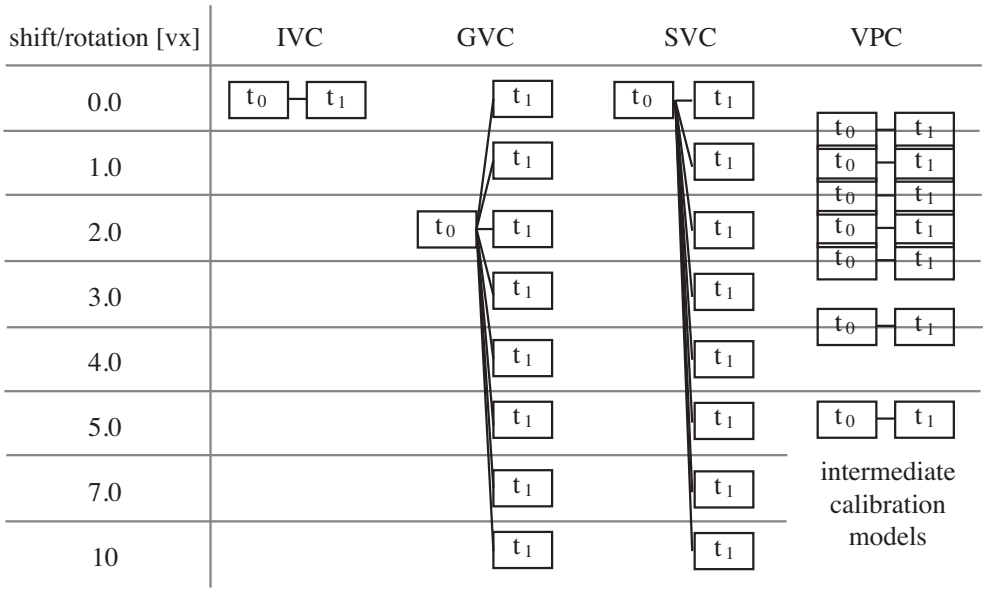

Figure C.8: Schematic representation of the synthetically created vibration implementation schemes.

results to the experimental results, where the velocity field is shown to be updated locally. A notable difference is the clear shift of velocity components that is not observed in the experimental results. This is believed to be an artefact of moving only one camera in the synthetic case, as opposed to all cameras vibrating in the experimental case. The rotation error also modifies the velocity field locally, however rather than randomly, the velocity correction has a dominate frequency at I vectors to the velocity field, which is particularly evident in the GVC and SVC case. This result rotation errors in the calibration models can cause a periodic type error in the velocity field.

It was then investigated to see whether this local correction could be due to local particle distributions. Figure C.10 plots the number of particles, again approximated by the number of local intensity peaks in an IV, compared to the magnitude of velocity difference chance, normalised by σ_{ivc}. The colours of the scatter markers indicate a different misalignment error. Despite three cameras maintaining perfect calibration, there is a weak trend that lends weight to support this hypothesis.

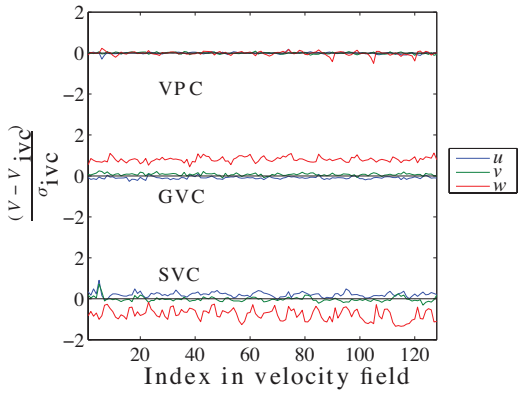

(a) Shifted

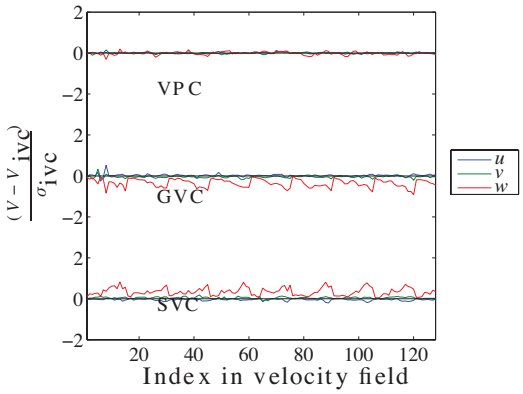

(b) Rotated

Figure C.9: Difference between velocity fields, normalised by the standard deviation σ of the velocity of the IVC case (a) 1 vx translation (b) 1 vx rotation

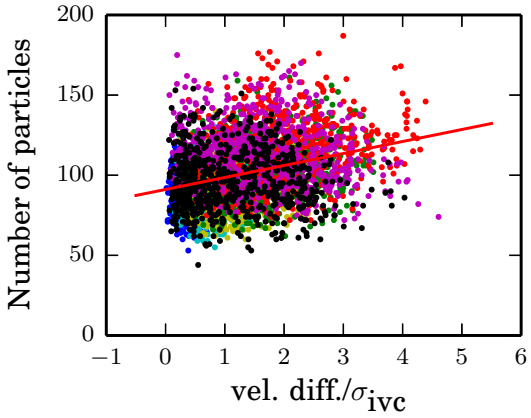

Figure C.10: Scatter plot of the number of detected particles in an IV and the magnitude of local velocity correction in the GVC. The velocity has been normalised by the standard deviation σ of the IVC scheme. The colour of the markers represent a level of misalignment. There is a weak correlation (R^2=0.2) between number of particles within an IV and the size of the velocity correction.

C.1.5 Correction Schemes and their Affect on Turbulence Statistics

Figure C.11 shows the evolution of TKE function of the misalignment error. The GVC case has an initial error owing to the 2 vx error imposed on its t_0 reconstructed volume.

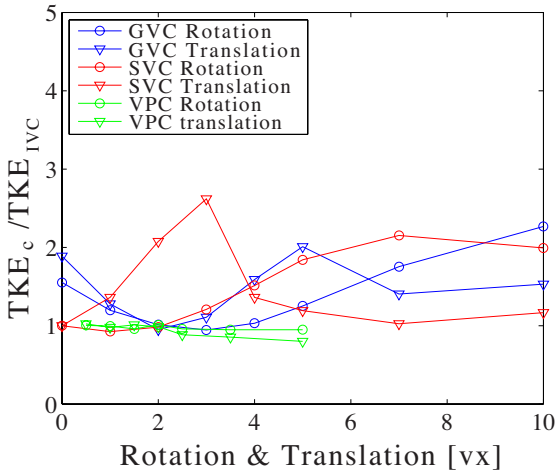

Figure C.11: Evolution of the turbulent kinetic energy (TKE) for each correction case c, normalised by the IVC case, with respect to increasing misalignment error.

Interestingly, the magnitude of TKE for the GVC case approaches the IVC level when its t_1 volume also has a 2 vx misalignment. The SVC correction case augments significantly within d_τ, after which its level drop off. For larger errors, the rotation errors are more significant for both the GVC and SVC case. The VPC case remains relatively constant, and its magnitude of TKE actually decreases to approximately 90% of the IVC case. These results indicate that the noise induced by the misalignment errors can significantly effect the TKE statistics, particularly the SVC and GVC cases. As VPC has identical error on both time steps, the ghost particles have the same relative motion and position in both time steps and act to smooth the velocity field and hence TKE, a result also reported by Elsinga et al (2010b).

Figure C.12 shows the evolution of the vorticity magnitude ω as it evolves as a function of the misalignment error. Similar to the TKE analysis, the VPC acts to smooth the velocity field and likewise ω. This is indeed the observation for the GVC case when the misalignment errors on t_1 are ± 1 vx of t_0. The GVC exhibits a maximum at the particle image diameter, and for larger errors appears to plate at 15% greater than the IVC vorticity magnitude. This figure shows that there can be a 20% fluctuation in ω magnitude averaged for the entire velocity field.

Figure C.13 shows the evolution of the energy dissipation ε as a function of the mis-

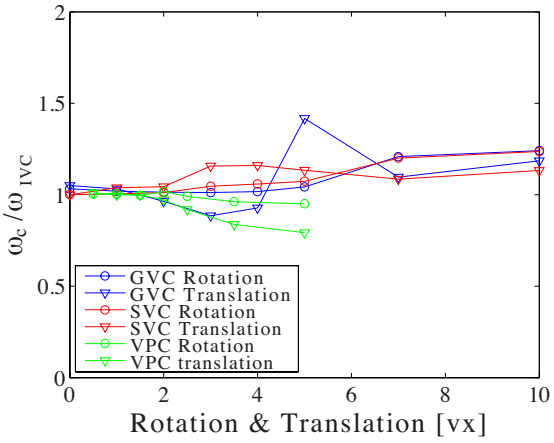

Figure C.12: Evolution of the magnitude of vorticity ω for each correction case c, normalised by the IVC case, with respect to increasing misalignment error.

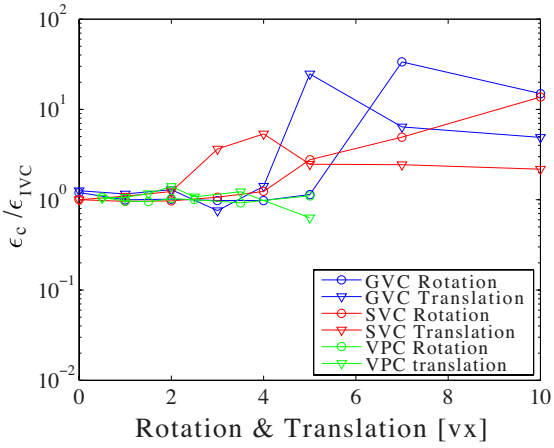

Figure C.13: Evolution of the energy dissipation ε for each correction case c, normalised by the IVC case, with respect to increasing misalignment error.

alignment error. Note that in this figure has a log scale on the ordinate axis of the graph. As ε is computed by a large combination of all velocity gradients in the velocity gradient tensor (Equation 3.10) can increase by an order of magnitude after approximately one particle diameter of shift/rotation. This result is of particular importance for experiments that wish to resolve the kolmogorov scale to calculate ε, that essentially undetectable vibrations within a particle diameter can cause significant errors on the calculation. For vibrations larger than d_τ, the GVC and SVC case exceed the IVC value by greater than an order of magnitude.

Appendix D

Programme that calculates the approximate lens mounted adapter settings to achieve Scheimpflug condition

For TPIV experiments, the Scheimpflug condition is met by rotating and/or tilting the lens with respect to the camera sensor. The Scheimpflug condition is met when the focal, lens and camera sensor plane intersect on a common line. Two-axis lens mounted Scheimpflug adapters require skill (and patience) to work with, as an adjustment in tilt or rotation to improve the focal plane alignment with the laser sheet also changes the camera's field-of-view. In a rather tedious process, the camera must be rotated so that it is viewing the measurement volume again, and further adjustments to the lens mounted adapter require again move the camera. In TPIV, the problem is exacerbated as there are typically four cameras to adjust.

In an effort to minimise this iterative procedure, a simple programme implemented in Octave (equivalent to Matlab) models the camera positions with respect to the centre of the measurement volume and calculates the theoretical rotation and tilt of the lens mounted adapters *a priori*. Although in practice additional camera adjustment is required, this code allows for a streamlining of the focus and lens tilting process. The code is as follows:

```
function main
% User inputs:  coordinates of the lens centres and flange focal length
% of the lenses

% Definitions:
% alpha = Rz (roll)
% beta = Rx (pitch) (elevation)
% theta = Ry (yaw) (azimuth)
clc;
% --------------------
% USER INPUT
% --------------------

% Camera coordinates in cartesian coordinates, [cam1 cam2 cam3 cam4]
camera.x = [205 205 205 205];
camera.y = [210 190 190 210];
camera.z = [715 715 715 715];

% Distance between lens and image plane (flange focal length)
plane.lens.z_shift = [46.5 46.5 46.5 46.5];

% --------------------
% END USER INPUT
% --------------------

printf('******************\n\n')
printf('SCHEIMPFLUG ADAPTER SETTINGS\n \n')
```

```
for cam = 1:4
printf('******************\n')
fprintf('camera %d settings:\n',cam)
fprintf('x = %3.0f\ny = %3.0f\nz = %3.0f\n', ...
   camera.x(cam),camera.y(cam),camera.z(cam))

beta = atand(camera.y(cam)/camera.z(cam)); % elevation angle
theta = atand(camera.x(cam)/camera.z(cam)); % azimuth angle
fprintf('azimuth = %2.1f deg\nelevation = %2.1f deg\n',theta,beta)

% Scheimpflug rotation angle
scheimpflug_rotate_angle = atand(theta/beta);
fprintf('scheimpflug_rotate_angle is %2.1f deg from horizontal\n', ...
   scheimpflug_rotate_angle)

% Plot results
% Set image (focal), lens and sensor plane dimensions:
plane.image.x = 2000; % width
plane.image.y = 2000; % height
plane.image.z = 0; % z location

plane.sensor.x = 1500; % width
plane.sensor.y = 1500; % height
plane.sensor.z = camera.z(cam); % z location

plane.lens.x = 1500; % width
plane.lens.y = 1500; % height
plane.lens.z = plane.sensor.z - plane.lens.z_shift(cam); % z location

% Generate plane coordinates
plane.image.coords = generate_plane_coordinates( ...
   plane.image.x, plane.image.y, 0);
```

```
plane.lens.coords = generate_plane_coordinates( ...
   plane.lens.x, plane.lens.y, 0);

plane.sensor.coords = generate_plane_coordinates( ...
   plane.sensor.x, plane.sensor.y, 0);

% beta correction is lens tilt angle to ensure intersection of 3 planes
beta_corr = atand((plane.lens.z_shift(cam)*sind(beta))/plane.sensor.z);

% Same again for Rx rotation
theta_corr = atand((plane.lens.z_shift(cam)*sind(theta))/plane.sensor.z);

% offset sensor by z_shift
plane.sensor.coords(:,3) = plane.sensor.coords(:,3)+plane.lens.z_shift(cam);

% apply lens rotation to sensor
plane.sensor.coords = ...
plane.sensor.coords*plane_rotation(0,beta_corr,theta_corr);

% apply additional offset to lens and sensor
plane.lens.offset = (plane.sensor.z - plane.lens.z_shift(cam)* ...
   cosd(beta))/cosd(beta-beta_corr);

plane.sensor.coords(:,3) = plane.sensor.coords(:,3)+plane.lens.offset;
plane.lens.coords(:,3) = plane.lens.coords(:,3)+plane.lens.offset;
```

```
% rotate matrices by beta - beta correction
plane.lens.coords = plane.lens.coords*plane_rotation( ...
   0,beta-beta_corr,theta-theta_corr);
plane.sensor.coords = plane.sensor.coords*plane_rotation( ...
   0,beta-beta_corr,theta-theta_corr);

% calculate the angle between the planes
%{
define normal vector of sensor plane
sensor.p1 = plane.sensor.coords(1,:);
sensor.p2 = plane.sensor.coords(2,:);
sensor.p3 = plane.sensor.coords(3,:);
plane.sensor.normal = cross(sensor.p1-sensor.p2, sensor.p1-sensor.p3);
% define normal vector of sensor plane
lens.p1 = plane.lens.coords(1,:);
lens.p2 = plane.lens.coords(2,:);
lens.p3 = plane.lens.coords(3,:);
plane.lens.normal = cross(lens.p1-lens.p2, lens.p1-lens.p3);
% calculate scheimpflug angle
scheimpflug_tilt_angle = 180/pi*atan2(...
   norm(cross(plane.sensor.normal,plane.lens.normal)),...
   dot(plane.sensor.normal,plane.lens.normal));
%}

scheimpflug_tilt_angle = sqrt(beta_corr^2+theta_corr^2);
fprintf('scheimpflug_tilt_angle is %1.1f deg\n',scheimpflug_tilt_angle)

%{
% plot planes
subplot(2,2,cam)
fill3(plane.image.coords(:,1),plane.image.coords(:,2),...
plane.image.coords(:,3),'g','FaceAlpha',1);
```

```
hold on
fill3(plane.lens.coords(:,1),plane.lens.coords(:,2),...
   plane.lens.coords(:,3),'b','FaceAlpha',0.2);
fill3(plane.sensor.coords(:,1),plane.sensor.coords(:,2), ...
   plane.sensor.coords(:,3),'r','FaceAlpha',0.2);
xlabel x
ylabel y
zlabel z
view(-50,20)
%}
end
printf('******************\n')

% --------------------------------
function output = generate_plane_coordinates(x,y,z)
% generate matrix of plane coordinates
output = [-x -y z; ...
   x -y z; ...
   x y z; ...
   -x y z; ...
   -x -y z];

% --------------------------------
function rotate_matrix = plane_rotation(alpha,beta,theta)
% alpha = Rz, beta = Ry, theta = Rx

rotate_matrix_alpha = ...
   [cosd(alpha) -sind(alpha) 0; sind(alpha) cosd(alpha) 0; 0 0 1];
rotate_m_beta = ...
   [cosd(beta) 0 sind(beta); 0 1 0; -sind(beta) 0 cosd(beta)];
rotate_m_theta = ...
   [1 0 0; 0 cosd(theta) -sind(theta); 0 sind(theta) cosd(theta)];
```

```
rotate_matrix = rotate_matrix_alpha*rotate_m_beta*rotate_m_theta;
```

For the inverted pyramid configuration of the cameras, Figure D.1 shows the orientation of the cameras' tilt axis.

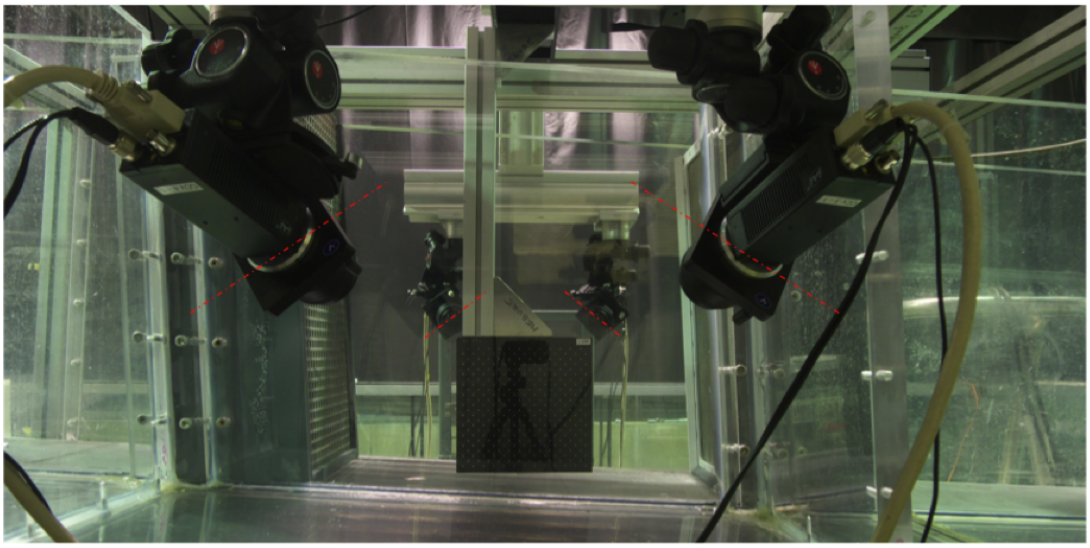

Figure D.1: The red dashed lines indicate the orientation of the tilt axes of the cameras in the inverted pyramid configuration so that the Schiemplfug condition can be met.

Appendix E

Short guide to batch processing TPIV experiments

This section provides a brief guide to batch processing the TPIV programmes of the SLIP Library. The reconstruction and correlation processes are covered with examples of the scripts used to batch process. The following folder tree was implemented for the batch files:

```
~/TESTS/TURBULENT_CHANNEL/
    ./camera_matrices
    ./camera_calibration
        ln -s <calibrate>
    ./raw_data
    ./filtered_data
    ./run0_misalignment
    ./run1_recon
        ln -s <volume_reconstruction>
    ./run2_recon
        ln -s <volume_reconstruction>
```

```
./run3_correl
    ln -s <correlate3d>
./results
./parameter_files
./scripts
```

In the above, $< \cdots >$ denotes the SLIP programme location to be linked to that directory and `./` denotes the folder is in the parent directory one indent to the left. There are two folders for reconstruction to allow more than one reconstruction programme to run. In the folder tree, `camera_matrices` contains all of the calibration matrices for the cameras. In the case of the open channel flow experiments, there was one camera matrix for each camera at every time step. `camera_calibration` is where the calibration images and analysis is undertaken, `parameter_files` contain the parameter files for the correlation and reconstruction programmes, and `results` are where the final velocity fields are stored and `scripts` where analysis scripts can be kept. `run0_misalignment` is a folder where the volume self calibration update occurs. Following is an example code derived from the reconstruction of two volumes followed by the correlation of the open channel experiments. The code is run in a Linux (or MAC) terminal window and is a `bash` script.

```
#!/bin/bash
############################
# change suffix of volume/image file
suf=G1G2_5p_Q34
suf2=G1G2

for num in {0..999}; do
let num2=$num+1 # for second volume
```

```
##########################
# RECONSTRUCTION
##########################

cd  /WORK/TESTS/TURBULENT_CHANNEL/$suf2/run1_recon

# variable name (equivalent to output name)
printf -v r1 'rec_vol_%s_%06d' $suf $num
printf -v r2 'rec_vol_%s_%06d' $suf $num2

echo $r1
echo "****************************************"

# Uncomment the following lines to prevent overwriting existing data
# if [ -a "../run3_correlation/"$r1".cdf" ]; then
# continue
# fi

# Reconstruct the first volume
./volume_reconstruction -p ../parameter_files/vol_rec_parameters.txt
-i "../filtered_data/cam%1d_"$suf"_"$num".tif"
-c "../camera_matrices/cam%1d_modified_pinhole_model_"$num".dat"
-o "../run3_correlation/"$r1".cdf" -threads 4

echo $r2
echo "****************************************"

# Reconstruct the second volume
./volume_reconstruction -p ../parameter_files/vol_rec_parameters.txt
-i "../filtered_data/cam%1d_"$suf"_"$num2".tif"
-c "../camera_matrices/cam%1d_modified_pinhole_model_"$num2".dat"
-o "../run3_correlation/"$r2".cdf" -threads 4
```

```
############################
# CORRELATION
############################

# Only correlate reconstruction pairs stating from even numbers
if [$(( $num % 2 )) -eq 1 ]; then
continue
fi

cd  /WORK/TESTS/TURBULENT_CHANNEL/$suf2/run3_correlation

echo "****************************************"
echo "vfield_"$r1"_"$num2"_".dat"
echo "****************************************"

./correlation3d -p ../parameter_files/correlation_parameters.txt
-i1 $r1".cdf" -i2 $r1".cdf" -o "../results/vfield_"$r1"_"$num2"_".dat"
-threads 4

############################
done # for num
```